CO_2-SELECTIVE POLYMER AND MIXED-MATRIX MEMBRANES FOR CO_2/N_2 AND CO_2/CH_4 SEPARATIONS

Raymond THÜR

Supervisor:
Prof. I. F. J. Vankelecom, KU Leuven

Members of the Examination Committee:
Prof. M. Maertens, KU Leuven, Chair
Prof. D. C. Nijmeijer, TU Eindhoven
Dr. P. Vandezande, Vito
Prof. R. Ameloot, KU Leuven
Prof. G. Koeckelberghs, KU Leuven

Dissertation presented in partial fulfilment of the requirements for the degree of Doctor of Bioscience Engineering (PhD)

November 2020

Doctoraatsproefschrift nr. 1666 aan de faculteit Bio-ingenieurswetenschappen van de KU Leuven

© 2020 KU Leuven, Science, Engineering & Technology

Uitgegeven in eigen beheer, THÜR RAYMOND, HEVERLEE

Alle rechten voorbehouden. Niets uit deze uitgave mag worden vermenigvuldigd en/of openbaar gemaakt worden door middel van druk, fotokopie, microfilm, elektronisch of op welke andere wijze ook zonder voorafgaandelijke schriftelijke toestemming van de uitgever.

All rights reserved. No part of the publication may be reproduced in any form by print, photoprint, microfilm, electronic or any other means without written permission from the publisher.

Table of Contents

Dankwoord ..... **V**

Abstract ..... **IX**

Samenvatting ..... **XI**

List of abbreviations and symbols ..... **XIII**

List of figures ..... **XV**

List of tables ..... **XXI**

List of publications ..... **XXIII**

Chapter 1 Introduction to membrane-based gas separation **1**

Abstract 2
Contributions 2
1.1 Problem definition 3
1.2 Membrane technology 3
1.2.1 Membrane terminology 3
1.2.2 A short history of membrane-based gas separation 4
1.2.3 Performance indicators 6
1.3 Mass transport in dense, polymeric membranes: the solution-diffusion model 7
1.3.1 Background and basics 7
1.3.2 Free volume theory 9
1.3.3 Solubility 10
1.3.4 Diffusivity 11
1.4 CO_2-selective polymer membranes 12
1.4.1 Conventional polymers for CO_2 separation 12
1.4.2 Problems to be solved for polymeric membranes 14
1.5 Towards better membranes 17
1.5.1 Surpassing the Robeson upper bound 17
1.5.2 Mixed-matrix membranes 18
1.5.3 Challenges for mixed-matrix membranes 19

Chapter 2 Scope of thesis and dissertation overview **25**

Chapter 3 Bipyridine-based UiO-67 as a novel filler in mixed-matrix membranes for CO_2-selective gas separation **27**

Abstract 28
Contributions 28
3.1 Introduction 29
3.2 Materials and methods 31
3.2.1 Chemicals 31
3.2.2 MOF synthesis 31

3.2.3 Membrane synthesis 31
3.2.4 Characterization 32
3.3 Results and discussion 35
3.3.1 MOF characterization 35
3.3.2 MMM characterization 37
3.3.3 Gas permeation experiments 40
3.3.4 Comparison with state-of-the-art 42
3.4 Conclusions 43
3.5 Acknowledgements 43
3.6 Supplementary information to Chapter 3 45

Chapter 4 Modulator-mediated functionalization of MOF-808 as a platform tool to create high-performance mixed-matrix membranes 49

Abstract 50
Contributions 50
4.1 Introduction 51
4.2 Materials and methods 53
4.2.1 Chemicals 53
4.2.2 MOF synthesis 53
4.2.3 Membrane synthesis 53
4.2.4 Characterization 54
4.3 Results and discussion 57
4.3.1 Modulator-mediated functionalization: fluorinated MOF-808 57
4.3.2 Increasing the fluorine concentration inside MOF-808 60
4.3.3 Comparison with state-of-the-art 64
4.4 Conclusions 66
4.5 Acknowledgements 66
4.6 Supplementary information to Chapter 4 67

Chapter 5 Towards more rational mixed-matrix membrane design: Correlation of MOF-808 parameters with mixed-matrix membrane CO_2 permeation 77

Abstract 78
Contributions 78
5.1 Introduction 79
5.2 Materials and methods 81
5.2.1 Chemicals 81
5.2.2 MOF synthesis 81
5.2.3 Membrane synthesis 82
5.2.4 Characterization 83
5.3 Results and discussion 87
5.3.1 Characterization of MOFs and membranes 87
5.3.2 Computational characterization of MOF-808 91
5.3.3 Gas permeation experiments 93
5.3.4 Correlation of MOF parameters with membrane CO_2 permeation 95
5.4 Conclusions 97

5.5 Acknowledgements 97
5.6 Supplementary information to Chapter 5 99

Chapter 6 Tuning 6FDA-DABA membrane performance for CO_2 removal by physical densification and decarboxylation cross-linking during simple thermal treatment 109

Abstract 110
Contributions 110
6.1 Introduction 111
6.2 Materials and methods 112
6.2.1 Chemicals 112
6.2.2 Membrane synthesis 112
6.2.3 Characterization 112
6.3 Results and discussion 116
6.3.1 Evidence for thermally induced cross-linking 116
6.3.2 Membrane dilation versus membrane tightening 118
6.3.3 Gas permeation experiments 121
6.3.4 Effect of plasticization and temperature on gas permeation 124
6.3.5 Comparison with state-of-the-art 126
6.4 Conclusions 127
6.5 Acknowledgements 127
6.6 Supplementary information to Chapter 6 129

Chapter 7 Second generation high-throughput set-up for testing of gas separation membranes under industrially relevant conditions 133

Abstract 134
Contributions 134
7.1 Introduction 135
7.2 Materials and methods 136
7.2.1 Chemicals 136
7.2.2 Membrane synthesis 136
7.3 Results and discussion 137
7.3.1 Equipment design 137
7.3.2 Set-up for proof testing 141
7.3.3 Mapping the permeability problem 145
7.3.4 Discussion 148
7.4 Conclusions 150
7.5 Acknowledgements 150
7.6 Supplementary information to Chapter 7 151

Chapter 8 General conclusions and future perspectives 153

8.1 General conclusions 154
8.2 Future work and outlook 158
8.2.1 Future work 158
8.2.2 Outlook 160

Bibliography…… 165

Dankwoord

Beste lezer,

Met gepaste trots presenteer ik u mijn doctoraatsschrift, het resultaat van vier jaren onderzoek waarin u vast en zeker een stukje hart en ziel van mij zult tegen komen. De afgelopen vier jaren zijn naar mijn gevoel voorbij gevlogen. Achteraf terugblikkend is dat meestal het geval maar ik heb het gevoel dat tijdens mijn doctoraat de klok effectief sneller tikte dan mij lief was. Ik heb een geweldig doctoraat gekend waarin ik mijn onderzoek heb kunnen invullen naar hartenwens, op de manier die ik zelf voor ogen had. Het was zeker niet zo dat die vier jaren enkel bestonden uit rozengeur en maneschijn. Integendeel, de momenten van frustratie en teleurstelling omdat er nog maar eens een lading ideeën of membranen de (spreekwoordelijke) vuilbak in kon waren talrijk. Toch blik ik terug met een ontzettend positief gevoel en zelfs een tikkeltje melancholie. Er van uitgaande dat u nog steeds geïnteresseerd bent om verder te lezen, zou ik graag overgaan tot het aanhalen van enkelen belangrijke en bewonderenswaardige personen aan wie ik een oprecht woordje van dank verschuldigd ben. Ik ben er van overtuigd dat ik het geluk heb gehad om omringd te zijn door de juiste mensen op het juiste moment, zowel in als buiten het labo.

In de eerste plaats zou ik graag mijn dank willen uitdrukken richting het Fonds Wetenschappelijk Onderzoek voor de financiering van mijn doctoraat waardoor ik gedurende mijn heel doctoraat zorgeloos membranen heb kunnen onderzoeken.

Ivo, mijn doctoraat start natuurlijk bij u. De keuze voor een doctoraat was makkelijk maar ik weet nog goed dat het niet evident was om te schakelen van FO naar gasscheiding en dat die beslissing uiteindelijk gevallen is in de modderpoel die Rock Werchter na vier dagen was. Al met al een geslaagde beslissing gebleken vind ik zelf. Bedankt om mij de mogelijkheid te bieden een doctoraat te starten, voor het vertrouwen en de vrijheid in mijn onderzoek. Ik heb vijf jaar met plezier in de Membrane Technology Group gewerkt. Over heel de lijn, een welgemeend dankuwel!

Verder zou ik de juryleden van mijn examencommissie willen bedanken voor hun kritische input tijdens de evaluatie van dit manuscript. Rob, Guy, Kitty en Pieter, bedankt om tijd en moeite te nemen om dit proefschrift onder het vergrootglas te leggen en waar nodig te verbeteren. Miet, bedankt voor de vlotte samenwerking en om alles in goede banen te leiden.

Achter elk doctoraat schuilt zoveel meer dan enkel het werk van de doctoraatsstudent zelf. Daarom zou ik de volgende paragraaf willen aanwenden om iedereen te bedanken die achter de schermen er voor heeft gezorgd dat alles (min of meer) op rolletjes bleef lopen en onder controle bleef. In de eerste plaats, zou ik graag mijn dank uitdrukken richting Johan, Stef, Werner en Paul voor hun technische deskundig- en bereidwilligheid. Verder mag ik natuurlijk niet vergeten om de dames van het secretariaat, Lieve, Inge, Birgit en uiteraard Annelies, heel erg te bedanken voor hun talrijke hulp. Mijn thesisstudenten Sam, Vincent, Daan en Simon: het

was een plezier om met jullie te mogen samenwerken. Ik heb het genoegen gehad om, stuk voor stuk, vier topstudenten te mogen begeleiden. Als één iemand van jullie ooit spontaan een liedje van Guus Meeuwis op zet, weet ik dat ik in mijn opzet ben geslaagd.

Evidemment, mon séjour chez CNETE au Canada était une expérience inoubliable de mon doctorat. Je voudrais remercier tous ceux qui y étaient impliqués. Merci à Nicholas et Nancy de m'avoir invité. Merci à mes amis, à Alexandre et sa femme Jeanne et à Joshua de m'y avoir accueilli et pour leur hospitalité.

Rhea en Jeroen, ik stel me hardop de vraag wat er van mij en mijn doctoraat geworden zou zijn zonder jullie hulp en dagelijkse motivering. Jeroen, ik herinner me de dag waarop ik bij u in de bureau binnenwaaide alsof het gisteren was. De tijden dat ik meer uren per week met u doorbracht dan met mijn vriendin zijn ondertussen voorbij maar dat neemt niet weg dat ik heel content ben dat het uw bureau was waar ik destijds bijna per ongeluk terecht kwam. Ik kan me eerlijk geen betere mentor inbeelden dan u. Voor uw (niet altijd oneindig) geduld, uw membraanhulp en niet-membraanhulp: een welgemeend bedankt. En ook nog een oprechte verontschuldiging voor het verstoppen van uw trui destijds. Op nog vele jaren vriendschap. Rhea, zelfde jaar beginnen, zelfde jaar afleggen. Onze loopjes, gesprekjes, fruitpauzes… Wat een avontuur is het geweest. Ik ben zelfs een tijdje vegetariër geworden door u. Ik weet dat ik af en toe iets te ver ging in mijn mopjes. En dat ik op sommige momenten, als ik u weer eens de spreekwoordelijke gordijnen had ingejaagd, een beetje tactischer had moeten zijn maar wat ben ik blij dat gij vier jaar lang een hoofdrolspeelster zijt geweest in mijn doctoraat. Ik zal u in ieder geval niet meer onverwacht Racoon's Oceaan laten luisteren. Maarten, Ines en Peter, van SEM en laboverantwoordelijken tot de broodnodige momenten van ontspanning. Jullie hebben de volledige weg met mij afgelegd waarvoor ik enkel dankbaar kan zijn. Furthermore, I would like to thank the membrane group in general and more specifically Katja, Daan, Maxime, Subha, Ayesha, Tan, Rosa, Bart, Angela, Yun for the nice moments and activities. Machiel, wat was ik blij toen ik ontdekte dat er in de Lage Landen nog onderzoekers bezig zijn met MMMs voor CO_2 scheiding!

Niels, ik kan het draaien of keren hoe ik wil maar drie van de zes hoofdstukken uit dit boekje komen voort uit het feit dat gij op een avond op de Oude Markt met een licht dubbele tong iets brabbelde over zirconium MOFs en bipyridine. Waarop ik met een even dubbele tong antwoordde in de trend van: 'MOFs? Die kunnen toch nergens tegen?' en dacht 'Dat ga ik nooit gebruiken.'. Kijk eens aan, vier jaar verder. Ik vond het heerlijk om met u samen te werken maar ben toch vooral blij dat we elkaar buiten het labo ook vonden en vinden. In dezelfde lijn wil ik Thijs, Jason en Thomas graag vermelden. Merci jongens!

Ik zou dit moment ook willen aangrijpen om enkele mensen te vernoemen die er voor zorgden dat de balans tussen werk en privé naar de juiste kant doorsloeg. Christof, in mijn masterthesis had ik het al over 'your foolishness' en uw intelligente input. Proficiat, ge (of je?) hebt ook de finale versie van het dankwoord van mijn doctoraat gehaald. Vijf jaar ouder, een significant deel van onze haren kwijt maar in de meeste aspecten nog geen haar veranderd. Ik kan me eerlijk gezegd al niet meer herinneren hoe het leven zonder u was. Nu er officieel een einde dreigt te

komen aan onze tijd samen in Leuven moet ik wel toegeven dat ik met wat weemoed en een zwaar hart terug kijk naar het begin. Wat een parcours hebben we gereden met de nodige horten en stoten. En wat hebben we gelachen. Ik koester de herinneringen en kijk al uit naar de volgende jaren waarin er ongetwijfeld weer het één en ander gebeuren gaat (om maar iets te zeggen: het moment dat e-sports populairder wordt dan voetbal). Het plezier was en is geheel voor mij. Lars, ook zonder u zou mijn tijd hier in Leuven niet geweest zijn wat het nu is geweest. Van Turkije tot Spanje en van Oxford tot Porto, half Europa hebben we doorkruist met Koolstof steeds in ons kielzog. De talrijke concerten, nachtjes uit, vakanties, de occasionele karaokebar, spellenavonden van heb-ik-jou-daar en zo veel meer. Ik heb er van genoten en ben klaar om de komende jaren net niks hieraan te veranderen. Ook de overige heren van de ponyclub met natuurlijk Jonas, Maarten, Tom, Thibaut, Martijn zou ik graag willen bedanken voor de talrijke avonden van vertier tot dusver.

Ten slotte ook nog een heel erg welgemeend woord van dank voor diegenen die het allemaal van de eerste rij hebben meegemaakt. Mijn lieve ouders die altijd voor me klaar stonden en staan, zowat alles voor mij overhebben, die me in eerste instantie de kans gaven om te gaan studeren in het verre Leuven en nooit goede raad tekort komen. Ik ben ontzettend dankbaar voor jullie in mijn leven. Broer, zus, jullie zijn twee van mijn favoriete personen. Een dikke kus om mijn quasi-eindeloos gezever steeds aan te willen horen (al dan niet vrijwillig).

Liefste Eva, waar moet ik beginnen? Ik kan nauwelijks bevatten dat het alweer meer dan drie jaar geleden is sinds de Vesper en kan nu enkel tot de conclusie komen dat ik ontzettend veel geluk heb gehad u daar tegen te komen. Ik zou u graag willen bedanken voor de fantastische jaren die we al samen hebben doorgebracht, voor uw geduld, uw luisterend oor en onvoorwaardelijke steun. Bedankt voor alles vanuit de grond van mijn hart. Mijn eigen woorden schieten eens te meer vreselijk tekort. Het mooiste aan Brabant ben jij, dat ben jij.

Rayminator over and out.

"The road goes ever on and on, down from the door where it began.

Now far ahead the road has gone, and I must follow if I can." – J.R.R. Tolkien

Abstract

The separation of CO_2 from energy streams such as raw natural gas and bio gas is of high importance in industry because CO_2 causes severe infrastructure corrosion and lowers the caloric value of the produced methane. Also in environmental context, CO_2 capture has gained increasing interest since CO_2 is a key greenhouse gas, strongly contributing to global warming. Over the past three decades, membrane-based gas separation has matured into an industrial standard technology for applications such as N_2 production, H_2 recovery during ammonia synthesis and CO_2 removal from natural gas. The polymeric membranes that are the industrial standard for these applications generally only have mediocre separation performance. Membranes with better performance would therefore increase the membrane market share in existing applications (e.g. natural gas sweetening) and/or unlock new application domains (e.g. membrane-based CO_2 capture). One way to improve membrane performance is to incorporate metal-organic frameworks (MOFs) in polymer matrices to form mixed-matrix membranes (MMMs). MMMs are hybrid materials that combine the advantages of polymers (e.g. good processability) with the excellent separation ability of MOFs.

In **Chapter 3**, the CO_2 affinity of zirconium-based UiO-67 MOFs was enhanced by replacing the standard linker with BPYDC (2,2'-bipyridine-5,5'-dicarboxylic acid) linkers in varying concentrations. At optimal conditions, incorporation of these MOFs in Matrimid membranes simultaneously improved the CO_2/CH_4 separation factor and the CO_2 permeability. However, at too high BPYDC concentrations, the MOF stability was compromised, thus limiting the practical applicability of the UiO-67-BPYDC MMMs.

As a response to the limited stability of UiO-67, MOF-808 was investigated as a far more stable alternative for MMM design in **Chapter 4**. Furthermore, the unique structure of MOF-808 allowed direct incorporation of monotopic modulator molecules in the MOF framework. Hence, selection of appropriate modulators bearing CO_2-philic chemical moieties led to an in-situ MOF functionalization towards enhanced CO_2 affinity (modulator-mediated functionalization, MoFu). The versatility of the MoFu concept was demonstrated by using a series of fluorinated and non-fluorinated carboxylic acid modulators. Outstanding CO_2 separation performance was obtained for the fluorinated MOF-808 MMMs, which consequently surpassed the state-of-the-art performance upper bounds.

Consistent structure-performance relationships for the rational design of MOF-based MMMs for gas separation are very scarce. A first step in finding such relationships could be the linking of intrinsic MOF parameters, such as the CO_2 uptake and the CO_2 adsorption enthalpy (Q_{st}), to the performance indicators of the MMM. Therefore, in **Chapter 5**, MOF-808 parameters were correlated with the CO_2/N_2 separation factor and CO_2 permeability of the corresponding MMMs. MOF-808 CO_2 uptake correlated poorly with MMM performance, which is in strong contrast to literature where CO_2 uptake is one of the dominant factors used to explain MMM separation behavior. Correlation coefficients of CO_2 Q_{st} with the separation factor were

significantly higher than for CO_2 uptake but were still considered only moderate. However, a strong correlation was found between Q_{st} and CO_2 permeability, indicating that Q_{st} can be considered as the most effective predictor for MMM CO_2 permeability amongst the MOF parameters. The surprising lack of correlation of membrane performance with CO_2 uptake and rather strong correlation with Q_{st} once more underlined the need for more research focused at finding consistent relationships between MOF and MMM structure and the ultimate membrane performance.

In **Chapter 6**, pure polymer (6FDA-DABA) membranes, bearing free carboxylic acid groups on the polymer backbone, were exposed to different annealing temperatures (100 °C, 180 °C, 250 °C, 350 °C and 400 °C) to evoke decarboxylation cross-linking. The separation performance of the 6FDA-DABA membranes was found to be governed by two counteracting mechanism. For 6FDA-DABA-350 and 6FDA-DABA-400, covalent links were formed between polymer chains as a result of decarboxylation cross-linking and a more open membrane structure was subsequently obtained, resulting in an enhanced permeability for all gases (CO_2, N_2 and CH_4). Next to decarboxylation cross-linking, an increased polymer chain packing efficiency (i.e. physical tightening of the polymer matrix) led to gradually improved CO_2/CH_4 separation factors with higher annealing temperatures (till 350 °C). 6FDA-DABA-350 displayed a synergy between the dilation effect of cross-linking and the tightening effect, causing a simultaneous, strong improvement of both CO_2/CH_4 separation factor (+100%) and CO_2 permeability (+40%). Moreover, the cross-linked 6FDA-DABA-350 showed an increased resistance to CO_2-induced plasticization thanks to covalent cross-linking.

In the final **Chapter 7**, a second generation high-throughput (HT) gas separation set-up (HTGS-2) was developed and assembled for conducting membrane gas filtration tests in industrially realistic conditions. HTGS-2 is equipped to test membranes with seven different gases or gas mixtures, relevant for e.g. CO_2 capture, natural gas/bio gas upgrading and olefin/paraffin separation. During proof testing, it was noticed that the membrane separation factors could be accurately determined in line with literature. On the contrary, the recorded membrane permeability on HTGS-2 was systematically higher than that of HTGS-1. Several potential solutions for the permeability offset were proposed, including minimizing the downstream volume, redesigning the measuring cylinder configuration and repositioning the pressure sensor.

Samenvatting

De scheiding van CO_2 uit industriële energiestromen zoals aardgas of biogas is belangrijk vanuit industrieel standpunt aangezien CO_2 (in combinatie met water) sterk corrosief is met schade aan transportinfrastructuur tot gevolg. Bovendien verlaagt CO_2 de calorische waarde van het geproduceerde methaan. Ook vanuit ecologische overwegingen heeft CO_2 scheiding (of CO_2 afvang) recent de nodige aandacht gekregen omdat CO_2 een belangrijk broeikasgas is en op die manier een prominente rol speelt in de opwarming van de aarde. In de afgelopen 30 jaar is membraantechnologie uitgegroeid tot een industriële standaardtechnologie voor verschillende gasscheidingstoepassingen zoals N_2 productie, het herwinnen van H_2 tijdens ammoniaksynthese en CO_2 verwijdering uit aardgasstromen. De industriële polymeermembranen die traditioneel gebruikt worden voor CO_2 scheidingen zijn goedkoop maar hebben doorgaans slechts een beperkte scheidingsefficiëntie. Membranen met betere scheidingsefficiëntie zouden het membraanmarktaandeel in reeds bestaande toepassingen (zoals CO_2 verwijdering uit aardgas) kunnen vergroten en/of nieuwe toepassingen kunnen ontsluiten (bijvoorbeeld CO_2 afvang). Eén manier om de membraanperformantie te verbeteren is door het inbouwen van metaal-organische roosters (MOFs) in polymeermatrices ter vorming van *mixed-matrix* membranen (MMMs). MMMs zijn hybride materialen die de voordelen van polymeermembranen (bv. goede verwerkbaarheid tot modules) combineren met de uitstekende scheidingseigenschappen van de MOFs.

In **Hoofdstuk 3** werd de CO_2 affiniteit van zirconium-gebaseerde UiO-67 MOF verbeterd door de standaard MOF linker te vervangen door BPYDC linkers (2,2'-bipyridine-5,5'-dicarboxylic acid) in variërende hoeveelheden. Bij optimale condities resulteerde incorporatie van deze gemodificeerde UiO-67 partikels in Matrimid membranen in een simultane stijging van CO_2/CH_4 selectiviteit en CO_2 permeabiliteit. Bij te hoge BPYDC concentraties werd de MOF echter instabieler wat de praktische toepasbaarheid van de MMMs met UiO-67-BPYDC sterk limiteerde.

In **Hoofdstuk 4** werd MOF-808 voorgesteld als stabieler alternatief voor UiO-67. Bovendien laat de unieke structuur van de MOF-808 cluster directe incorporatie toe van modulatormoleculen in het MOF geraamte. De selectie van geschikte modulatormoleculen, die CO_2-fiele chemische groepen dragen, opende op die manier de deur voor een in-situ MOF functionalisatiemethode voor het bekomen van een betere MOF CO_2 affiniteit (modulator-gedreven functionalisatie, MoFu). De veelzijdigheid van het MoFu concept werd gedemonstreerd door een reeks van gefluorideerde en niet-gefluorideerde carbonzuren met toenemende alkylketen aan te wenden als modulator. Uitstekende CO_2 scheidingsperformantie werd bekomen voor de gefluorideerde MOF-808 MMMs te vergelijken met de huidige state-of-the-art MMMs.

Consistente structuur-performantie relaties voor het rationeel ontwerp van MOF MMMs zijn momenteel erg schaars. Een eerste stap in het vinden van zulke relaties zou het linken van intrinsieke MOF parameters (zoals CO_2 opname en de CO_2 adsorptiewarmte (Q_{st})) met

membraanperformantie indicatoren kunnen zijn. Daarom werden in **Hoofdstuk 5** MOF-808 parameters gecorreleerd met de CO_2/N_2 selectiviteit en de CO_2 permeabiliteit van de overeenkomstige MMMs. De CO_2 opname correleerde slechts zwak met de MMM performantie, wat in schril contrast staat met de literatuur waar CO_2 opname vaak als een van de sleutelparameters wordt aangehaald voor het verklaren van MMM performantie. De beste correlaties met de CO_2/N_2 selectiviteit werden geobserveerd voor de CO_2 Q_{st}. Bovendien correleerde Q_{st} als enige MOF parameter sterk met de CO_2 permeabiliteit van het membraan. Het onverwachte gebrek aan correlatie van de membraanperformantie met CO_2 opname en de sterke correlatie met CO_2 Q_{st} onderstreepten nogmaals het belang van onderzoek naar relaties tussen de MOF en MMM structuur en de ultieme membraanprestatie.

In **Hoofdstuk 6** werden pure polymeer (6FDA-DABA) membranen, met een vrij carbonzuur op de polymeerketen, blootgesteld aan warmtebehandelingen op verschillende temperaturen (100 °C, 180 °C, 250 °C, 350 °C en 400 °C) om decarboxylatiecrosslinken uit te lokken. De performantie van de 6FDA-DABA membranen werd bepaald door twee, elkaar tegenwerkende, mechanismen. In de 6FDA-DABA-350 en 6FDA-DABA-400 membranen werden covalente links gevormd tussen de polymeerketens als gevolg van decarboxylatiecrosslinken. Hierdoor werd een meer open membraanstructuur bekomen wat resulteerde in een verhoogde permeabiliteit voor alle gassen (CO_2, N_2, CH_4). Naast decarboxylatiecrosslinken werd de membraanperformantie ook beïnvloed door zogenaamde fysieke verdichting van de polymeermatrix ten gevolge van een efficiëntere polymeerketenstapeling bij hogere behandelingstemperaturen (t/m 350 °C). Dit veroorzaakte een gradueel stijgende CO_2/CH_4 selectiviteit voor deze membranen. 6FDA-DABA-350 vertoonde synergie tussen beide mechanismen met als gevolg een gelijktijdige en sterke verbetering van zowel CO_2 permeabiliteit (+40%) als van CO_2/CH_4 separatiefactor (+100%). Daarboven toonden de 6FDA-DABA-350 membranen een betere weerstand tegen CO_2 plastificering.

Hoofdstuk 7 besprak de ontwikkeling en constructie van een tweede generatie *high-throughput* gasscheidingsset-up (HTGS-2) die toelaat om membraanfiltratietesten uit te voeren onder industrieel relevante testcondities. HTGS-2 is uitgerust om membranen te testen met 7 verschillende pure gassen of gasmengsels die relevant zijn voor CO_2 afvang, opzuivering van aard- of biogas en olefine/paraffinescheiding. Tijdens proeftesten werd duidelijk dat de membraanselectiviteit zeer nauwkeurig kon worden bepaald, volledig in lijn met literatuur. In tegenstelling tot de separatiefactor bleken de gemeten permeabiliteitswaarden voor alle gassen systematisch te hoog in vergelijking met eerder gerapporteerde literatuur en HTGS-1 resultaten. Verschillende potentiële oplossingen voor dit probleem werden voorgesteld waaronder het minimaliseren van het *downstream* volume, herontwerpen van de meetcilinderconfiguratie en herpositionering van de druksensor.

List of abbreviations and symbols

α	Ideal selectivity
α^*	Separation factor
6FDA	4,4’-(Hexafluoroisopropylidene)diphthalic anhydride
A	Membrane area
AA	Acetic acid
ATR-FTIR	Attenuated total reflection – Fourier transform infrared spectroscopy
b	Langmuir equilibrium constant
BA	Butyric acid
BDC	1,4-Benzenedicarboxylic acid
BET	Brunauer–Emmett–Teller
BPDC	Biphenyl-4,4’-dicarboxylic acid
BPYDC	2,2’-Bipyridine-5,5’-dicarboxylic acid
BTC	1,3,5-Benzenetricarboxylic acid
BTDA	3,3’-4,4’-benzophenone tetracarboxylic acid dianhydride
C	Concentration
CA	Cellulose acetate
D	Gas diffusivity
DABA	3,5-Diaminobenzoic acid
DAM	2,4-Diaminomesitylene
DAPI	Diaminophenylindane
DMF	N,N-Dimethylformamide
DMSO	Dimethylsulfoxide
DSC	Differential scanning calorimetry
EDX	Energy-dispersive X-ray spectroscopy
EO	Ethylene oxide
FFV	Fractional free volume
GS	Gas separation
GPU	Gas permeation units
HCl	Hydrochloric acid
HFBA	Heptafluorobutyric acid
HKUST	Hong Kong university of science and technology
HTGS	High-throughput gas separation
J	Flux
k	Henry constant
L	Membrane thickness
MMM	Mixed-matrix membrane
MOF	Metal-organic framework
MoFu	Modulator-mediated functionalization
MIL	Materials institute Lavoisier
MS	Mass spectroscopy
NF	Nanofiltration
NMR	Nuclear magnetic resonance
ODA	4,4’-oxydianiline
P	Permeability
p	Pressure
PA	Propionic acid

PAN	Polyacrylonitrile
PALS	Positron annihilation lifetime spectroscopy
PDMS	Polydimethylsiloxane
PEO	Polyethylene oxide
PFPA	Pentafluoropropionic acid
PI	Polyimide
PIM	Polymer of intrinsic microporosity
pKa	Acid dissociation constant
Q	Permeance
R	Universal gas constant
RO	Reverse osmosis
S	Gas solubility
SD	Solution-diffusion
SEM	Scanning electron microscopy
SI	Supporting information
T	Temperature
T_d	Decomposition temperature
T_g	Glass transition temperature
TEM	Transmission electron microscopy
TFAA	Trifluoroacetic acid
TGA	Thermogravimetric analysis
THF	Tetrahydrofuran
TR	Thermally rearranged
UiO	Universitetet i Oslo
V	Volume
V_m	Molar volume
XRD	X-ray diffraction
ZIF	Zeolitic imidazolate framework
Zr	Zirconium

List of figures

Figure 1-1: Schematic overview of the typical streams present in a membrane-based separation process: feed stream, retentate stream and permeate stream. 4
Figure 1-2: Historical timeline of important events for membrane-based gas separation. 5
Figure 1-3: Schematic representation of the pore flow model and the solution-diffusion model. Figure adapted from reference[24]. 9
Figure 1-4: Variation in specific volume as a result of temperature. Figure adapted from reference[11]. 10
Figure 1-5: Schematic representation of Henry sorption, Langmuir sorption and dual-mode sorption in glassy polymers. 11
Figure 1-6: Movement of a CO_2 molecule inside a free volume element in a 6FDA-4PDA polymer matrix (left) and molecular simulation of the position of the CO_2 molecule (right). Figure adapted from reference[30]. 12
Figure 1-7: Chemical structure of cellulose. 13
Figure 1-8: Chemical structure of Matrimid. 13
Figure 1-9: Chemical structure of a polysulfone (Udel®). 14
Figure 1-10: Chemical structure of Pebax. 14
Figure 1-11: Selectivity-permeability trade-off for CO_2/CH_4 separation for the conventional polymer membranes. 15
Figure 1-12: Effect of plasticization on permeability. 16
Figure 1-13: Thickness-dependency of physical ageing with regard to O_2 and N_2 permeability. Figure copied from reference[58]. 17
Figure 1-14: Schematic representation of an MMM. 18
Figure 1-15: Representation of the crystal structure of UiO-66 and UiO-67. 19
Figure 3-1: Left: the structure of UiO-67 with a large octahedral cage with a pore diameter of 21 Å and small tetrahedral cages with a pore diameter of 11.5 Å. Right: the BPYDC (top) and BPDC (bottom) linkers. 29
Figure 3-2: The molar percentage of actually incorporated BPYDC linker compared to the molar percentage of BPYDC added during the synthesis of the MOF. 35
Figure 3-3: SEM images of (A) UiO-67, (B) UiO-67-18, (C) UiO-67-33, (D) UiO-67-63, (E) UiO-67-83 and (F) UiO-67-100. 36
Figure 3-4: ATR-FTIR spectrum of UiO-67, UiO-67-33, UiO-67-63 and UiO-67-100 powders. 36
Figure 3-5: CO_2 uptake (left) and N_2 adsorption isotherms (right) of UiO-67 with 33%, 63% and 100% BPYDC. 37
Figure 3-6: SEM cross-sections of (A) Matrimid, (B) MMM with UiO-67, (C) MMM with UiO-67-33, (D) MMM with UiO-67-63, (E) MMM with UiO-67-83, and (F) MMM with UiO-67-100. 38
Figure 3-7: ATR-FTIR spectrum of MMMs with 10 wt.% filler (left) and of Matrimid and MMMs with different UiO-67-33 loadings (right). 38
Figure 3-8: Free-volume radius plot (left) and intensity plot (right) of the short and long o-Ps for blanc Matrimid membrane and MMMs with UiO-67-33 and with UiO-67-100. 40

Figure 3-9: Effect of BPYDC percentage in UiO-67 on CO_2 permeability and CO_2/CH_4 separation factor. Gas filtrations were performed at 5 bar feed pressure and 30 °C for a 50v%/50v% feed. For all MMMs, filler loadings were 10 wt.%. 41
Figure 3-10: Pressure dependency of the CO_2 permeability and CO_2/CH_4 separation factor for the pure Matrimid membrane and MMMs with UiO-67-33 and UiO-67-83. Gas filtrations were performed at 30 °C for a 50v%/50v% feed. 42
Figure 3-11: Comparison of obtained membrane performance with similar membranes in literature via a Robeson plot. 42
Figure S3-1: XRD patterns of all MOFs. 45
Figure S3-2: SEM cross-sections of (a) Matrimid, (b) MMM with UiO-67, (c) MMM with UiO-67-33, (d) MMM with UiO-67-63, (e) MMM with UiO-67-83, and (f) MMM with UiO-67-100. 45
Figure S3-3: DSC measurements of pristine Matrimid and filled Matrimid membranes. 45
Figure S3-4: TGA traces of all membranes. 46
Figure S3-5: Lifetime plot of Matrimid and MMMs with UiO-67-33 and UiO-67-100. 46
Figure S3-6: Effect of increasing the filler weight percentage on the CO_2 permeability and CO_2/CH_4 separation factor of the UiO-67-33 MMMs. Gas filtrations were performed at 5 bar feed pressure and 30 °C for a 50v%/50v% feed. 46
Figure S3-7: XRD spectra of Matrimid with 10 wt.% UiO-67-83 before and after filtration at 10 bar. 46
Figure 4-1: Comparison between TFAA modulated MOF-808 cluster and UiO-66 cluster. 52
Figure 4-2: XRD pattern (left) and ATR-FTIR spectrum (right) of MOF-TFAA-150. The IR spectrum for MOF-TFAA-150 is compared to that of AA modulated MOF-808 (MOF-AA). 57
Figure 4-3: SEM images of (A) MOF-TFAA-150, (B) MOF-TFAA-550 and (C) MOF-TFAA-1300. ..58
Figure 4-4: CO_2/CH_4 separation factor and CO_2 permeability of Matrimid and MMMs with different sizes of MOF-TFAA. Gas filtrations were performed at 30 °C, 5 bar feed pressure and 50v%/50v% CO_2/CH_4 feed. 59
Figure 4-5: Effect of increasing the loading of MOF-TFAA-150. Gas filtrations were performed at 30 °C, 5 bar feed pressure and 50v%/50v% CO_2/CH_4 feed. 60
Figure 4-6: Pressure dependency tests for Matrimid membranes and MMMs with 10 wt.% MOF-TFAA. Gas filtrations were performed at 30 °C and 50v%/50v% CO_2/CH_4 feed. 60
Figure 4-7: XRD patterns (top) and SEM images (bottom) of (A) MOF-AA, (B) MOF-PA, (C) MOF-BA. 61
Figure 4-8: XRD patterns (top) and SEM images (bottom) of (A) MOF-TFAA, (B) MOF-PFPA, (C) MOF-HFBA. 62
Figure 4-9: Left: CO_2/CH_4 separation factor comparison between MMMs made with MOF modulated by alkyl carboxylic acids (black, square) and by perfluoro carboxylic acids (orange, circles). Right: CO_2 permeability of Matrimid and MMMs. Gas filtrations were performed at 30 °C, 5 bar feed pressure and 50v%/50v% CO_2/CH_4 feed. 64
Figure 4-10: Comparison of prepared MMMs with literature in a selectivity-permeability plot. 65
Figure S4-1: XRD patterns of simulated MOF-808, MOF-TFAA-1300, MOF-TFAA-550 and MOF-TFAA-150. 67

Figure S4-2: Size distribution plots of MOF-TFAA-150, MOF-TFAA-550 and MOF-TFAA-1300 based on visual analysis of SEM images with ImageJ. 67
Figure S4-3: CO_2 uptake (left) and N_2 adsorption isotherms (right) of MOF-AA and MOF-TFAA. CO_2 uptake and N_2 adsorption were conducted at 0 °C and -196 °C, respectively. 68
Figure S4-4: TGA curves of Matrimid, MMM-TFAA-150, MMM-TFAA-550 and MMM-TFAA-1300. 68
Figure S4-5: SEM cross-section of (A,B) Matrimid, (C,D) MMM-TFAA-550 and (E,F) MMM-TFAA-1300. All MMMs contain 10 wt.% MOF. 69
Figure S4-6: SEM cross-section of (A,B, C) 20 wt.% MMM-TFAA-150 and (D,E,F) 30 wt.% MMM-TFAA-150. 70
Figure S4-7: TGA analysis of MOF-TFAA (top, left), MOF-PFPA (top, right) and MOF-HFBA (bottom, left). The plateaus, indicated by the dotted lines, correspond with the onset of the derivative weight curve. An approximation of the material composition is calculated by taking the difference in relative weight between plateau values. 71
Figure S4-8: ATR-FTIR spectra of MOF-AA and MOF-TFAA (top, left), MOF-PA and MOF-PFPA (top, right), and MOF-BA and MOF-HFBA (bottom). 71
Figure S4-9: N_2 adsorption isotherm of all MOFs. Experiment conducted at -196 °C. 72
Figure S4-10: Cumulative pore volume and incremental pore volume as a function of pore width for MOF-TFAA, MOF-PFPA and MOF-HFBA. 72
Figure S4-11: Cumulative pore volume and incremental pore volume as a function of pore width for MOF-AA, MOF-PA and MOF-BA. 72
Figure S4-12: CO_2 uptake of MOF-PA and MOF-PFFA. Experiment was conducted at 0 °C. 73
Figure S4-13: DSC curves of MMM-AA, MMM-PA and MMM-BA. 73
Figure S4-14: DSC curves of MMM-TFAA, MMM-PFPA and MMM-HFBA. 73
Figure S4-15: Specific volume of MMMs made with MOF modulated by alkyl carboxylic acids and by perfluoro carboxylic acids. C2, C3 and C4 indicates the number of carbon atoms in the carboxylic acid. 74
Figure S4-16: SEM cross-section of Matrimid MMMs with 10 wt.% MOF-PFPA. 74
Figure S4-17: SEM cross-section of Matrimid MMMs with 10 wt.% MOF-HFBA. 75
Figure S4-18: Membrane sorption isotherms of CO_2 and N_2 in MMM-TFAA and MMM-PFPA. 75
Figure S4-19: Membrane coupons of Matrimid, MMM-TFAA, MMM-PFPA and MMM-HFBA. .75
Figure 5-1: Overview of MOF-808 functionalization strategy. FA = formic acid, TFAA = trifluoroacetic acid, BA = benzoic acid, His = histidine, GA = glycolic acid. For clarity, Li-ions are not shown. 80
Figure 5-2: ATR-FTIR spectrum (left) and N_2 adsorption isotherms at 77 K (right) of all MOFs. 88
Figure 5-3: Experimental CO_2 adsorption enthalpies as a function of CO_2 loading for all MOFs. 90
Figure 5-4: CO_2 (left) and N_2 (right) sorption in the Matrimid reference membrane and all MMMs. 91
Figure 5-5: Two isosurfaces of the density of MOF-FA from GCMC simulations at 2 bar. The high density isosurface of sites 1 and 2 is shown in iceblue and a lower density isosurface is shown to encapsulate the metal cluster. 91
Figure 5-6: Density of the adsorbed CO_2 molecules in MOF-FA at 300 K projected on a plane orthogonal to the c-axis and the (a+b)-axis of the conventional unit cell. The CO_2 molecules are represented by the positions of the carbon atoms. 92

Figure 5-7: Density of the adsorbed CO_2 molecules in MOF-TFAA at 300 K projected on a plane orthogonal to the c-axis and the (a+b)-axis of the conventional unit cell. The CO_2 molecules are represented by the positions of the carbon atoms. 92
Figure 5-8: Simulated CO_2 adsorption enthalpies for MOF-FA, MOF-TFAA and MOF-FA with 1 and 3 defects, respectively (left). Simulated mixed-gas adsorption CO_2/N_2 selectivities for MOF-FA and MOF-TFAA (right). 93
Figure 5-9: CO_2 permeability (left) and CO_2/N_2 separation factor (right) for the 15v%/85v% and 50v%/50v% mixed-gas CO_2/N_2 experiment and the CO_2 pure gas experiment of all membranes. Gas filtrations were performed at 30 °C and 5 bar feed pressure. All MMMs contain 10 wt.% MOF. 94
Figure S5-1: XRD patterns of all MOF samples. 99
Figure S5-2: SEM images of all MOF particles: (A) MOF-FA, (B) MOF-GA, (C) MOF-His, (D) MOF-BA, (E) MOF-TFAA and (F) MOF-Li_2SO_4. 99
Figure S5-3: ATR-FTIR spectrum of MMM-His, Matrimid and MOF-His. 100
Figure S5-4: ^{1}H-NMR spectra for MOF-FA, MOF-BA, MOF-His and MOF-GA. 100
Figure S5-5: Incremental pore volume as a function of pore size for all MOFs. 101
Figure S5-6: CO_2 uptake of all MOFs at 273 K, 293 K and 313 K. 102
Figure S5-7: CO_2 adsorption isotherms of all MOFs in the low-pressure region (0-100 mbar) at 273 K. 102
Figure S5-8: Cluster models used in the derivation of the atomic charges of (a) MOF-FA-def1 and (b) MOF-TFAA. 105
Figure S5-9: Modelled CO_2 adsorption isotherms for MOF-FA and MOF-TFAA. For MOF-FA, the number of defects (i.e. absence of formate molecule) on the zirconium clusters has been varied from one (MOF-FA-def1) to three (MOF-FA-def3). 106
Figure S5-10: (a) Primitive unit cell of MOF-FA. (b) Conventional cubic unit cell of MOF-FA. 106
Figure S5-11: Density of the adsorbed CO_2 molecules in MOF-FA-def3 at 300 K projected on a plane orthogonal to the c-axis and the (a + b)-axis of the conventional unit cell. The CO_2 molecules are represented by the positions of the carbon atoms. 107
Figure 6-1: Chemical structure of 6FDA-DABA with weight average molecular weight M_w = 97 kD, number average molecular weight M_n = 41 kD and M_w/M_n = 2.37. 112
Figure 6-2: Color change at different annealing temperatures. From left to right: 6FDA-DABA annealed at 100 °C, 180 °C, 250 °C, 350 °C and 400 °C. Scale bar is 1 cm. 116
Figure 6-3: ATR-FTIR spectrum of 6FDA-DABA membranes. 117
Figure 6-4: TGA traces of 6FDA-DABA-100 and 6FDA-DABA-400 (left). MS output for the same membranes is given on the right. 118
Figure 6-5: XRD spectra of 6FDA-DABA-100 and 6FDA-DABA-350. 119
Figure 6-6: Emission fluorescence spectra for all membranes. Excitation wavelength is 510 nm. 120
Figure 6-7: N_2 and CO_2 sorption in 6FDA-DABA membranes annealed at 100 °C, 350 °C and 400 °C. 121
Figure 6-8: CO_2/CH_4 and CO_2/N_2 separation factor (left) and CO_2 permeability for the CO_2/CH_4 and CO_2/N_2 mixed-gas experiment (right) of 6FDA-DABA membranes annealed at different temperatures. Gas filtrations were performed at 30 °C, 5 bar feed pressure and 50v%/50v% CO_2/CH_4 and CO_2/N_2 feed. 122

Figure 6-9: Effect of feed pressure on CO_2/CH_4 separation factor (left) and CO_2 permeability (right). Gas filtrations were performed at 30 °C and 50v%/50v% CO_2/CH_4 feed.....125
Figure 6-10: Effect of measuring temperature on CO_2/CH_4 separation factor (left) and CO_2 permeability (right). Gas filtrations were performed at 10 bar feed pressure and 50v%/50v% CO_2/CH_4 feed. 125
Figure 6-11: Comparison of the obtained data with literature and state-of-the-art in a selectivity-permeability plot. The full black line represents the 2018 mixed-gas upper bound for CO_2/CH_4[61] while the dotted black line represents the 2008 Robeson upper bound[55]. 126
Figure S6-1: ATR-FTIR data of 6FDA-DABA membranes annealed at 100 °C (top, left), 180 °C (top, right), 250 °C (middle, left), 350 °C (middle, right) and 400 °C (bottom, left). 129
Figure S6-2: Cross-linking mechanism during decarboxylation as proposed by Qiu *et al.*[39]. ...130
Figure S6-3: DSC plot of 6FDA-DABA-100, 6FDA-DABA-350 and 6FDA-DABA-400. 130
Figure S6-4: XRD spectra of 6FDA-DABA membranes annealed at 100 °C, 180 °C, 250 °C, 350 °C and 400 °C. 130
Figure S6-5: Density and specific volume data for all 6FDA-DABA membranes. NA = not annealed. 130
Figure S6-6: CH_4 and N_2 mixed-gas permeability of 6FDA-DABA membranes annealed at different temperatures. Gas filtrations were performed at 30 °C, 5 bar feed pressure and 50v%/50v% CO_2/CH_4 and CO_2/N_2 feed. 131
Figure 7-1: Picture of the HTGS-2 set-up. 135
Figure 7-2: Simplified flow scheme of HTGS-2. MFC = mass flow controller, BP = back-pressure controller, RH = relative humidity sensor, GC = gas chromatograph, VP = vacuum pump, C2 = ethane and ethylene, C3 = propane and propylene. Set-up areas with temperature control are indicated in red. 138
Figure 7-3: Picture of the HTGS-2 membrane module. Eight membranes can be placed and tested at the same time. 139
Figure 7-4: Example of the determination of the dp/dt slope for calculation of the membrane permeability. 140
Figure 7-5: Left: Steady state separation factor for the 6FDA-DAM membrane is reached after approximately 60 min during a CO_2/CH_4 separation at 5 bar, 25 °C. For time = 0 till time = 84 min, sampling time between two measurements is 1.7 min. Afterwards, sampling time is 30 min. Right: Comparison of mixed-gas CO_2/CH_4 selectivity and CO_2 permeability between all 8 positions in HTGS-2. 6FDA-DAM membranes were used as test case. 142
Figure 7-6: Pressure dependency experiments performed on 6FDA-DAM membranes. Gas filtrations were performed with a 50v%/50v% CO_2/CH_4 feed composition at 30 °C.....143
Figure 7-7: Temperature dependency of the CO_2/CH_4 separation factor and CO_2 permeability of a 6FDA-DAM membranes. 144
Figure 7-8: Permeability offsets of three polysulfone coupons (A, B, C) for N_2, CH_4 and CO_2 pure gas filtrations at 2.5, 5 and 10 bar. 146
Figure 7-9: Permeability offsets of three 6FDA-DAM coupons (A, B, C) for N_2, CH_4 and CO_2 pure gas filtrations at 2.5, 5 and 10 bar.....147
Figure 7-10: Left: Permeance offsets of three PAN-PDMS coupons (A, B, C) for N_2 pure gas filtration at 2 bar. Right: average CO_2, N_2 and CH_4 permeability measured on HTGS-2 for PAN-PDMS membranes at 2.5, 5 and 10 bar.....148

Figure 7-11: Modified downstream configuration of HTGS-2. 149
Figure S7-1: Average CO_2, N_2 and CH_4 permeability measured on HTGS-1 (left) and HTGS-2 (right) for polysulfone membranes at 2.5, 5 and 10 bar. 151
Figure S7-2: CO_2/N_2 and CO_2/CH_4 ideal selectivities of three polysulfone coupons (A, B, C) for filtrations at 2.5, 5 and 10 bar. 151
Figure S7-3: Average CO_2, N_2 and CH_4 permeability measured on HTGS-1 (left) and HTGS-2 (right) for 6FDA-DAM membranes at 2.5, 5 and 10 bar. 151
Figure S7-4: CO_2/N_2 and CO_2/CH_4 ideal selectivities of three 6FDA-DAM coupons (A, B, C) for filtrations at 2.5, 5 and 10 bar. 152
Figure S7-5: N_2 permeance at 2 bar feed pressure measured on HTGS-1 (left) and HTGS-2 (right) of three PAN-PDMS coupons (A, B, C). Each measurement was repeated three times. 152

List of tables

Table 3-1: Glass transition and degradation temperatures of pristine Matrimid and the UiO-67 MMMs.....39
Table S3-1: Comparison of results with MMMs based on Zr-MOFs reported in literature. $\alpha^*_{CO2/CH4}$ is the separation factor, P_{CO2} the CO_2 permeability in Barrer, $\Delta\alpha^*$ and ΔP the increase in selectivity and permeability, respectively, compared to the pristine polymer membrane.....47
Table 4-1: Comparison of MOF-AA and MOF-TFAA-550 with regard to BET surface area, pore volume and CO_2 uptake. 58
Table 4-2: BET surface area, pore volume, average pore size, average number of modulator molecules per Zr_6 cluster (as determined by NMR). T_g of the corresponding 10 wt.% Matrimid MMM is given as well. Adsorption isotherms for N_2 and CO_2 are found in SI. .63
Table S4-1: T_g measured by DSC and T_{deg} measured by TGA of Matrimid and its MOF-TFAA MMMs with different particle sizes. MMMs contained 10 wt.% MOF. 68
Table S4-2: Density of Matrimid and 10 wt.% MOF MMMs. 74
Table S4-3: Overview of similar MMMs reported in literature. $\alpha^*_{CO2/CH4}$ is the separation factor, P_{CO2} the CO_2 permeability in Barrer, $\Delta\alpha^*$ and ΔP the increase in separation factor and permeability, respectively, compared to the pristine polymer membrane. 76
Table 5-1: Average number of ligand molecules per Zr_6 cluster, pore volume (cm^3), pore diameter (Å), BET value (m^2/g) and CO_2 uptake at 273 K and 1000 mbar for all MOFs. ..89
Table 5-2: Correlation coefficients between MOF-808 parameters (CO_2 uptake at 50 and 1000 mbar and Q_{st} at a coverage of 0, 15, 30 cm^3 (STP)/g) and the corresponding MMM parameters (α^* at 15v%/85v% and 50v%/50v% CO_2/N_2 feed, and CO_2 permeabilities for 15v%/85v% and 50v%/50v% CO_2/N_2 feed and the pure CO_2 feed ($P_{100/0}$)). Strong correlations are indicated in green and weak correlations in red. Intermediate correlations have no special markings. 96
Table S5-1: Average size of all MOFs calculated after ImageJ analysis. 30 samples were measured per MOF. 99
Table S5-2: ANOVA analysis of the MOF particle sizes. As the p-value is larger than the significance level (0.05), no statistically significant difference in size exists between the samples. 100
Table S5-3: Model parameters for the dual-site Langmuir fit on the CO_2 adsorption isotherm at 273 K. N is the amount of adsorbed gas (cm^3 (STP)/g), $N_{m,A}$ and $N_{m,B}$ the amount of adsorbed gas at saturation for sorption site A and B, respectively (cm^3 (STP)/g) and b_A and b_B the adsorption equilibrium constants for, respectively, sorption site A and B. R^2 is the correlation coefficient.....103
Table S5-4: CO_2 Q_{st} (kJ/mol) of all MOFs for different CO_2 loadings (0, 5, 15, 30 cm^3 (STP)/g). 103
Table S5-5: Solubility (S) of CO_2 and N_2 in the Matrimid reference membrane and the MMMs. S_{CO2}/S_{N2} constitutes the CO_2/N_2 solubility selectivity. Measurements were conducted at 30 °C and varying pressures (see table). 104

Table S5-6: Simulated adsorption enthalpies for MOF-FA, MOF-TFAA and MOF-FA with 1 and 3 defect(s), respectively. 107
Table 6-1: Solubility in THF, NMP and DMSO of the annealed membranes. + = soluble, - = not soluble. NA = not annealed. 116
Table 6-2: Oxygen and fluorine content of all 6FDA-DABA membranes, as determined by EDX. 118
Table 6-3: Degradation temperature (T_{deg}), d-spacing, density, specific volume and fractional free volume (FFV) of all membranes. 119
Table 6-4: Summary of pure gas permeabilities, ideal selectivities, mixed-gas permeability and separation factor of all membranes. Gas filtrations were performed at 30 °C, 5 bar feed pressure. 122
Table 6-5: Permeability P (Barrer), solubility S (cm^3 (STP)/cm^3 cmHg), diffusivity D ($x10^{-8}$ cm^2/s), ideal CO_2/N_2 selectivity α (-), CO_2/N_2 solubility selectivity S/S (-) and CO_2/N_2 diffusivity D/D (-) of 6FDA-DABA membranes annealed at 100 °C, 350 °C and 400 °C. 123
Table S6-1: Heating profiles of the different 6FDA-DABA membranes. 129
Table S6-2: Solubility (S) of CO_2 and N_2 in 6FDA-DABA-100, 6FDA-DABA-350 and 6FDA-DABA-400. S_{CO2}/S_{N2} constitutes the CO_2/N_2 solubility selectivity. Measurements were conducted at 30 °C and varying pressures (see table). 131
Table 7-1: Overview of the polymer membranes used for proof testing of HTGS-2. 136
Table 7-2: Overview of HTGS-2 features and comparison to HTGS-1. RT = room temperature, BTX = benzene, toluene, xylene. 137
Table 7-3: Thermal conductivity of all used gases in HTGS-2 (at 300 K)[270]. 140
Table 7-4: Overview of the anticipated stage-cut for all membranes used. 141
Table 7-5: CO_2/CH_4, CO_2/N_2 and propylene(C3=)/propane(C3) separation factor and CO_2 and propylene permeability of 6FDA-DAM, 6FDA-DABA and Pebax membranes as tested on HTGS-2. Gas filtrations were performed with 50v%/50v% CO_2/CH_4 and CO_2/N_2 mixtures at 5 bar and 30 °C. 143
Table 7-6: Comparison of separation factor ($\alpha^*_{CO2/CH4}$, $\alpha^*_{CO2/N2}$) and CO_2 permeability (Barrer) of dense 6FDA-DAM, 6FDA-DABA and Pebax membranes measured on HTGS-1 and HTGS-2 for CO_2/CH_4 and CO_2/N_2 mixed-gas filtrations. 144

List of publications

Publications related to this dissertation:

4. Towards more rational mixed-matrix membrane (MMM) development: correlating MOF-808 parameters with MMM CO_2 permeation, R. Thür, D. Van Havere, N. Van Velthoven, S. Smolders, A. Lamaire, J. Wieme, Veronique Van Speybroeck, D. De Vos, I.F.J. Vankelecom, Submitted to Journal of Materials Chemistry A

3. Tuning 6FDA-DABA membrane performance for CO_2 removal by physical densification and decarboxylation cross-linking during simple thermal treatment, R. Thür, V. Lemmens, D. Van Havere, M. van Essen, K. Nijmeijer, I.F.J. Vankelecom, Journal of Membrane Science 610, 2020, 118195

2. Modulator mediated Functionalization (MoFu) of MOF-808 as a platform tool to create high-performance mixed-matrix membranes., R. Thür, N. Van Velthoven, V. Lemmens, M. Bastin, S. Smolders, D. De Vos, I.F.J. Vankelecom, ACS Applied Materials & Interfaces 11, 2019 (47), 44792-44801

1. Bipyridine-based UiO-67 as novel filler in mixed-matrix membranes for CO_2-selective gas separation. R. Thür, N. Van Velthoven, S. Slootmaekers, J. Didden, R. Verbeke, S. Smolders, M. Dickmann, W. Egger, D. De Vos, I.F.J. Vankelecom, Journal of Membrane Science 576, 2019, 78-87

Publications not related to this dissertation:

2. Tuning the selectivity of thin film composite forward osmosis membranes: effect of co-solvent and different interfacial polymerization synthesis routes. R. Thür, M. Corvilain, C. Klaysom, Y. Hartanto, I.F.J. Vankelecom, Separation and Purification Technology 227, 2019, 115671

1. Blending PPO-based molecules with Pebax MH 1657 in membranes for gas separation. J. Didden, R. Thür, A. Volodin, I.F.J. Vankelecom, Journal of Applied Polymer Science 135, 2018 (27), 46433

Chapter 1

Introduction to membrane-based gas separation

Raymond Thür, Ivo F.J. Vankelecom

Centre for Membrane Separations, Adsorption, Catalysis and Spectroscopy for Sustainable Solutions (cMACS), KU Leuven, Celestijnenlaan 200F, Box 2454, 3001 Heverlee, Belgium

Abstract

A brief introduction to membrane-based gas separation is presented, including a historical overview of important membrane events, membrane performance indicators and relevant gas transport mechanisms in dense and porous membranes. Commonly used polymer membranes in industry and academia are shortly discussed along with possible new routes towards improved membranes. MMMs are introduced with special attention for their opportunities and challenges.

Contributions

Raymond Thür: writing and redaction. Ivo F.J. Vankelecom: correction.

1.1 Problem definition

The separation of carbon dioxide (CO_2) from industrial gas streams has gained increasing attention over the past years since CO_2 is an important greenhouse gas, strongly contributing to global warming[1]. CO_2 capture from power plants and industrial exhaust gas streams aims at reducing anthropogenic CO_2 emissions[2]. Within the European Union, the price for CO_2 emission has substantially risen from <10 EUR/ton in 2012 to 20-25 EUR/ton in 2020, as a result of the EU Emissions Trading System[3]. As the best pilot scale CO_2 capture membrane can remove CO_2 at a cost of 35 USD/ton CO_2[4], it seems probable that membrane-based CO_2 capture will become economical in the near future. Next to environmental reasons, CO_2 removal from energy streams, such as natural gas and biogas (e.g. CO_2/CH_4 separation), is imperative in industry to prevent transport infrastructure corrosion and to maintain high caloric value specifications of the produced methane[5]. Although conventional separation technologies for these applications (such as amine scrubbing and cryogenic distillation) definitely have their respective advantages, they are often highly energy-intensive and have a relatively large environmental footprint[6]. Membrane-based gas separation is considered a viable alternative for the traditional technologies as it offers lower energy consumption, reduced environmental impact and a modular design, which allows retrofitting in existing plants[7]. Membranes with improved separation capacity (i.e. higher selectivity and permeability) could unlock new application areas (e.g. membrane-based CO_2 capture) or expand the membrane market share in already existing industries and are thus highly desired[8]. In contrast to engineering of membrane materials for better membrane performance, membrane stability effects such as membrane plasticization, physical ageing and the effect of feed impurities are known to be a major concern for membrane commercialization[8]. However, academic testing often takes place at relatively low pressures and with binary gas mixtures or even pure gas streams, while industrial feed streams consist of complex mixtures, containing impurities (H_2S, H_2O, higher hydrocarbons, NO_x, SO_x) and are treated at pressures up to 80 bar for natural gas. There is a thus a pressing need to bridge the existing gap between lab-scale research and the actual industrial applications[9].

1.2 Membrane technology

1.2.1 Membrane terminology

A membrane is defined as a thin, semi-permeable barrier that selectively allows one component to permeate while other components are retained. A typical membrane separation process usually contains three separate streams: (1) the feed stream, which consists of a mixture of components that needs to be purified, (2) the permeate stream, which entails the molecules that permeate through the membrane and (3) the retentate stream, which is composed of the species that are retained by the membrane (Figure 1-1)[10]. As a result of the membrane's selectivity towards one component, both the permeate and the retentate will be enriched with one of the feed components. The driving force behind species permeation through the membrane is a gradient in chemical potential across the membrane, most often expressed in terms of a gradient in pressure, temperature, electric potential and/or concentration,

depending on the separation process[10]. Although this generic definition is applicable to all membrane types, the microscopic nature and the function of the membrane might vary drastically between the different separation processes[11].

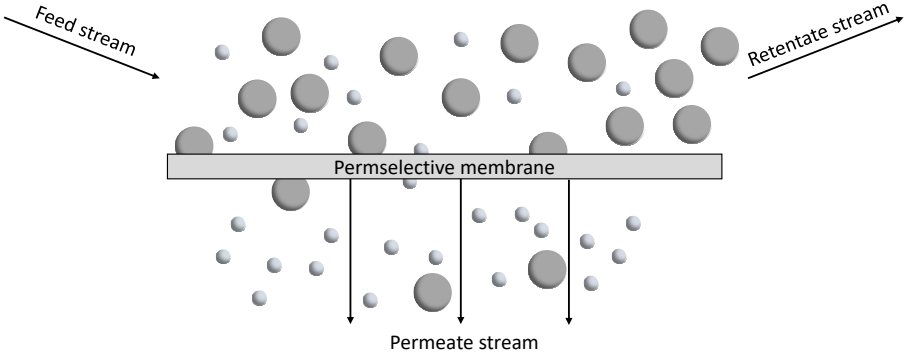

Figure 1-1: Schematic overview of the typical streams present in a membrane-based separation process: feed stream, retentate stream and permeate stream.

1.2.2 A short history of membrane-based gas separation

The first systematic study of the permeation behavior of different gasses through a membrane was performed by J.K. Mitchel in 1831[12]. He found that the permeation rate of different gases through natural rubber strongly varied, with carbon monoxide permeating one hundred times slower than ammonia. In addition, Mitchel observed that natural rubber was capable of adsorbing its own volume in CO_2 and linked this with the enhanced permeability of CO_2[12,13]. The next milestone was marked by the publication of a paper by Thomas Graham in 1866, in which he established the foundations for the later solution-diffusion (SD) model still used to date. Graham already tested the effect of various parameters on permeation such as cross-linking, membrane thickness, temperature and membrane type[14]. Furthermore, Graham formulated his law of diffusivity based on his work with porous membranes, which would later be used during the Manhattan project for the enrichment of uranium[13] (the first industrial scale, membrane-based gas separation application). In 1879, von Wroblewski demonstrated that the permeation rate of gases in a rubber is proportional to the product of gas solubility and diffusivity, building on previous results obtained by Exner and Stefan[15]. In the next decades, the SD model was modernized and further developed alongside other theories on gas transport through membranes. The time-lag method for determination of the gas diffusivity was developed in 1920 by Daynes and picked up later by Barrer[16]. Maeres was in 1954 the first to observe the discontinuity in Arrhenius plots at the glass transition temperature of polymers and to hypothesize the existence of two 'modes of sorption' in glassy polymers[17]. These observations eventually gave rise to the dual-mode sorption model as described by Michaels, Vieth and Barrie in 1963[12]. Despite the scientific progress made in the first half of the 20th century, the commercial breakthrough of gas separation membranes only took place by the 1980s, mostly as a result of the fact that the isotropic membranes before that time had too low gas

permeance. The development of the first asymmetric membranes (i.e. membranes with a selective skin layer and a highly permeable support layer) for reverse osmosis (RO) by S. Loeb and S. Sourirajan was a major breakthrough for the commercialization of large-scale membrane-based separations[18]. RO and nanofiltration (NF) matured into the industrial standard technology for desalination and water purification[19] and the technology and knowledge necessary to produce industrial-grade membranes could eventually be transferred to gaseous separations as well. The first industrial Prism© polysulfone membranes were then launched by Permea in 1980 for H_2 recovery from other gaseous components (Ar, CH_4, N_2) during the ammonia production process[20]. By the mid-1980s, the first (mostly cellulose acetate (CA) based) membranes were commercialized for sweetening of natural gas and N_2 separation from air[8]. After optimization of N_2/O_2 separation by Dow, Ube and Du Pont/Air Liquide, smaller applications such as dehydration of air and natural gas or vapor removal from air and N_2 streams were exploited[11]. Nowadays, four large commercial applications (H_2 recovery, N_2 production, natural gas treatment and vapor recovery from air) can be identified, from which N_2 production (800 million USD/year) and natural gas treatment (300 million USD/year) are the most important. Beside the already established industries, Galizia *et al.* defined three upcoming application areas, in which implementation of gas separation membranes can be economical: olefin/paraffin separation (e.g. propane/propylene), CO_2 capture (e.g. CO_2/N_2) and vapor/vapor separation (H_2O/ethanol). However, development of membranes with enhanced performance will be imperative to unlock these new applications. Furthermore, membranes with improved performance could also increase the membrane market share in already established markets such as natural gas processing, stressing the importance of on-going membrane development[8]. An historical overview of important membrane events is given in Figure 1-2.

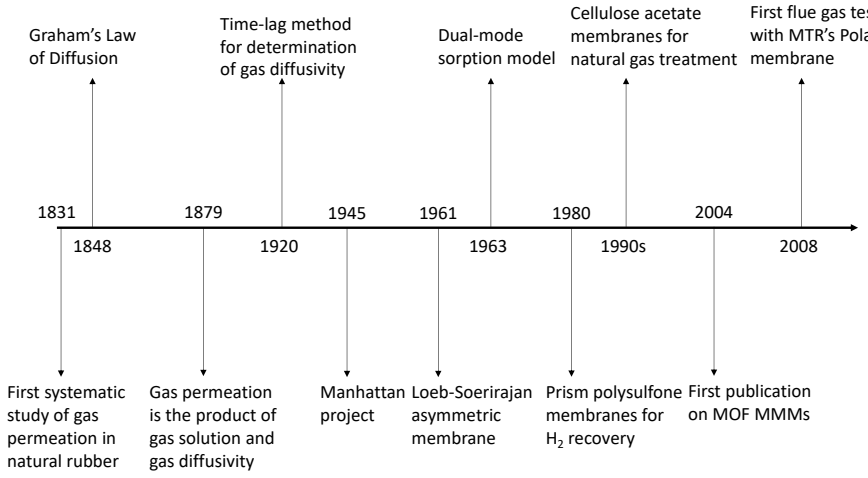

Figure 1-2: Historical timeline of important events for membrane-based gas separation.

1.2.3 Performance indicators

The performance of gas separation membranes is commonly mapped by a combination of four parameters. The gas permeability (P) and the gas permeance (Q) are a measure for the quantity of gas that is transported through the membrane per unit of time and area. The ability of the membrane to discriminate between two gases is probed by determination of the ideal selectivity (α) under pure gas testing conditions or by the separation factor (α^*) when the membrane is tested with a mixed-gas feed. Membrane permeability and ideal selectivity are intrinsic material properties and can thus be used for membrane comparison. The membrane permeance and separation factor are dependent on the testing conditions[21].

1.2.3.1 Permeability and permeance

The flux J is defined as the quantity of gas that passes through a membrane with area A in a time interval Δt (Equation 1.1):

$$J = \frac{V}{A \times \Delta t} \tag{1.1}$$

with J the flux, A the active membrane area, V the volume of the permeate gas and Δt the time interval in which a volume of gas V migrates through the membrane.

The permeability P can be defined as the pressure and thickness normalized flux (Equation 1.2):

$$P = \frac{J \times l}{\Delta p} \tag{1.2}$$

with P the gas permeability, J the gas flux, l the membrane thickness and Δp the pressure difference across the membrane.

Permeability is commonly expressed in units of Barrer, which is defined in Equation 1.3:

$$1\ Barrer = 10^{-10}\ \frac{cm^3\ (STP) \times cm}{cm^2 \times s \times cmHg} \tag{1.3}$$

Membranes used in industry often consist of a selective layer supported by a porous support or of asymmetric, skinned membranes. In either case, determination of the thickness of the selective layer is troublesome as the selective layer is deliberately kept very thin to ensure high flux while the chemical contrast between selective and support layer is often very low[22]. Therefore, the gas permeance is defined as (Equation 1.4):

$$Q = \frac{P}{l} \tag{1.4}$$

with Q the permeance, P the permeability, l the membrane thickness.

Permeance is expressed in terms of Gas Permeation Units (GPU, Equation 1.5):

$$1\ GPU = 10^{-6}\ \frac{cm^3\ (STP)}{cm^2 \times s \times cmHg} \tag{1.5}$$

1.2.3.2 Ideal selectivity and separation factor

The ideal selectivity $\alpha_{i/j}$ is defined as the ratio of the pure gas permeabilities of gas i and j, respectively, as given in Equation 1.6:

$$\alpha_{i/j} = \frac{P_i}{P_j} = \frac{D_i}{D_j} \times \frac{S_i}{S_j} \quad (1.6)$$

with P_i and P_j the pure gas permeability of gas i and j, respectively, D_i/D_j the diffusivity selectivity and S_i/S_j the solubility selectivity.

When using mixed-gas feed streams, the presence of one gas can affect the permeation of the other gas (e.g. competitive sorption). Therefore, the separation factor $\alpha^*_{i/j}$ takes into account non-ideal effects in mixed-gas conditions (Equation 1.7):

$$\alpha^*_{i/j} = \frac{y_i/y_j}{x_i/x_j} \quad (1.7)$$

with y_i and y_j the mole fraction of gas i and j in the permeate stream and x_i and x_j the mole fraction of gas i and j in the feed stream.

1.3 Mass transport in dense, polymeric membranes: the solution-diffusion model

1.3.1 Background and basics

Membranes are characterized by their capacity to separate components based on the difference in component permeation rate. Depending on the membrane type, gas permeation through the membrane can be described with two models. The pore flow model is commonly applied to predict gas flow through capillary or porous media such as finely microporous ceramic/carbon membranes[11,22] while non-porous membranes are mostly described with the solution-diffusion (SD) model. The pore flow model, originating from the modelling of porous, liquid filtration membranes, describes the transport of gas molecules as a pressure-driven convective flow through small pores. It entails various diffusion mechanisms, including Knudsen flow, capillary condensation, size sieving and surface diffusion, depending on the pore size and morphology[23]. However, the pore flow model fails to adequately describe the permeation of gases in dense, non-porous polymeric membranes as the pore diameter of these membranes falls within the range of the thermal motion of the polymer chains[24]. For transport through non-porous, polymeric membranes, the SD model has become the standard descriptive model, in which penetrant molecules dissolve in the polymeric matrix and consequently diffuse through the membrane. Separation takes place owing to the difference in permeant's solubility and diffusivity[21]. The major difference between both models lays in the definition of size and permanence of the pores[11]. Within the framework of the pore flow model, pores are relatively large and fixed in time and position while SD 'pores' consist of free-volume elements smaller than 5 Å, which are transient in time, appearing and disappearing between polymer chains as a result of the thermal motion of the chains. Generally, when speaking of pore sizes in the range

of 5-10 Å, the changeover between pore flow and solution-diffusion is made[10,11,21]. As is the case for all models, assumptions have to be defined for the SD and pore flow model as well to set the model boundaries[11]. Firstly, the gas on the feed and permeate side of the membrane is assumed to be in equilibrium with the membrane interface. As such, the adsorption and desorption rates at the interface are much higher than the rate of diffusion, making the latter the rate determining step for gas permeation. This can be physically rationalized by the dependency of molecule diffusion on the thermal motion of the polymer chains to form new free volume elements. A second assumption is related to the manifestation of the chemical potential gradient (i.e. the driving force for permeation) in the membrane, which differs for SD and pore flow membranes. The pore flow model presumes a uniform penetrant concentration along the membrane. As a result, the chemical potential gradient presents itself as a pressure gradient. On the other hand, the SD model assumes a uniform pressure at any point in the membrane, meaning that the chemical potential is merely a function of the concentration gradient over the membrane (Figure 1-3). This follows from the assumption that dense polymer membranes transmit pressure in the same way as liquids do[24]. Although this is an oversimplification (especially for glassy polymers), and small pressure losses over the membrane are expected in reality, the SD model has repeatedly proved its worth over time[11,24]. Evidence for the validation of the SD model is considered to originate primarily from the excellent agreement between theory and experimental findings[11]. Furthermore, direct experiments have been performed to validate specific predictions of the SD model, such as a decrease in permeants concentration on the membrane permeate side with increasing feed pressure. For a more detailed description of these experiments, the reader is referred to open literature[25–28]. Since the 1940s, the permeation through dense polymer films has been increasingly explained by the SD model and in the 1980s the debate was decisively concluded in favor of the SD model. According to Baker, '*currently only a few die-hard pore-flow modelers use this approach to rationalize transport through dense membranes*'[11].

The SD model entails three discrete steps that determine the permeation of the gas. First, the gas molecule adsorbs on the membrane surface and dissolves in the polymer matrix. The gas molecule then diffuses along the concentration gradient towards the downstream side where it will finally desorb from the membrane. Gas permeability is thus governed by the product of gas solubility (S) and diffusivity (D) as shown in Equation 1.8[24]. The solubility of the gas describes the relationship between the concentration of the gas in the feed stream and the concentration of the gas in the membrane while the diffusivity entails the effect of the chemical environment and the molecular motions of the polymer on the kinetics of gas transport[11,23].

$$P = D \times S \tag{1.8}$$

with P the gas permeability, D the gas diffusivity and S the gas solubility.

High gas permeabilities can thus be accomplished by a high diffusivity, a high solubility or a combination of both. Examples of gases with high diffusivity are hydrogen and helium, owing to their small kinetic diameter. CO_2 is an example of a gas with a relatively high solubility

coefficient, originating from its strong quadrupole moment. Water molecules tend to have both high D and S coefficients due to their small size and strong dipole moment[10].

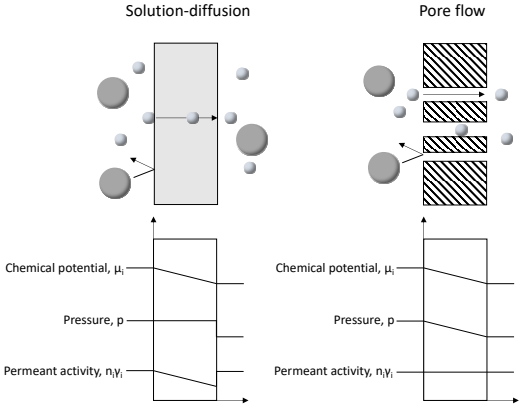

Figure 1-3: Schematic representation of the pore flow model and the solution-diffusion model. Figure adapted from reference[24].

1.3.2 Free volume theory

The local environment sensed by the gas molecule in the polymer matrix affects the permeation behavior of the molecule. Consequently, proper understanding of the polymer structure and the membrane permeation properties is desired to design or select the most suitable membrane for a certain application. However, such structure-performance relationships have so far not yet successfully been defined[11,21]. Nonetheless, a number of semi-empirical correlation tools have been established, from which the fractional free volume (FFV) is the most frequently applied (Equation 1.9). The FFV is defined as the ratio of the volume of the unoccupied space (i.e. free volume) and the total polymer volume[10].

$$FFV = \frac{v - v_0}{v} \tag{1.9}$$

with FFV the fractional free volume, v the specific volume and v_0 the occupied volume by the molecules themselves.

Several polymer properties (such as specific volume, free volume, tensile modulus, specific heat, permeability) heavily rely on the polymer state (i.e. rubbery or glassy) in which the polymer is found. In the rubbery state, molecular segments of the polymer backbone have enough thermal energy to freely rotate around the backbone axis. The glassy state implies a restriction in rotational movements of the polymer backbone segments. The distinction between the two states is made based on the glass transition temperature (T_g), which is the temperature at which the polymer chains and segments have just sufficient thermal energy to overcome the rotation restrictions, marking the transition from rubbery to glassy (or vice versa)[23]. Figure 1-4 shows the variation in specific volume as a function of the temperature of a

polymer. At temperatures above the T_g, the segments of the polymer backbone and side groups can rotate freely without sterical hindrance. The free volume appearing in rubbery polymers is the so-called interstitial or equilibrium free volume and is made up from the unoccupied space between the constantly moving polymer chains. This free volume is a result of random and imperfect polymer chain packing. However, when the temperature is lowered and passes the T_g, the polymer enters its glassy state, meaning that rotational movements of (rigid) backbone segments become restricted. The free volume decreases at lower temperatures but a slower-than-expected reduction in free volume is observed with decreasing temperature once the polymer has entered its glassy state. When the lack of rotational energy and the reduced free volume cause polymer segmental motions to stop, the residual free volume elements are kinetically frozen in the polymer structure. This type of free volume is called the excess or hole free volume and is typically only observed in glassy polymers. Consequently, two types of free volume (i.e. interstitial and excess free volume) exist in glassy polymers[10,11,23].

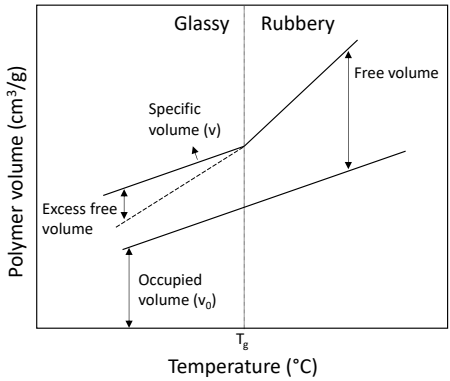

Figure 1-4: Variation in specific volume as a result of temperature. Figure adapted from reference[11].

1.3.3 Solubility

Sorption of a gas in a polymer matrix is an equilibrium process, meaning that conventional thermodynamics can be applied to quantitatively calculate sorption coefficients (e.g. by Flory-Huggings expressions). It was demonstrated by Baker that gas sorption in a membrane is inversely proportional with the gas saturation vapor pressure. More specifically, gas boiling temperature or critical temperature, which predict the condensability of a gas, can thus be applied as indicators for the gas solubility in the membrane[11]. The sorption of gases in ideal polymers (i.e. rubbers) tends to behave like sorption in liquids[29] and can thus be described by Henry's law[10,21]:

$$C_E = k \times p \tag{1.10}$$

with C_E the concentration of gas adsorbed in the equilibrium free volume of the polymer, k the Henry's law constant and p the gas pressure.

For non-ideal polymers such as glassy polymers, sorption behavior deviates from the ideal Henry sorption as glassy polymers also contain kinetically frozen, hole free volume elements, which significantly contribute to the sorption capacity of the polymer. The sorption behavior in these polymers can be adequately described by the dual-mode sorption model, which assumes that gas sorption in the polymer simultaneously occurs in two different sorption sites or 'modes', i.e. Henry sorption in equilibrium free volume elements and Langmuir sorption in hole free volume sites. The concentration of gases in glassy polymers can hence be described as the sum of the concentration in the individual modes[10,21]:

$$C = C_E + C_H = k \times p + C_{H,m} \times \frac{b \times p}{1 + b \times p} \tag{1.11}$$

With C_H the concentration of gas adsorbed in the hole free volume as described by Langmuir sorption, b the Langmuir equilibrium constant, p the pressure and $C_{H,m}$ the Langmuir maximum capacity.

Although the dual-mode sorption model often gives a good fit with experimental data (three parameter fit), the physical basis for the existence of two different sorption modes is difficult to rationalize (as it implies the presence of two different sorption populations) and should thus be approached with care[10]. An overview of the different sorption mechanisms is given in Figure 1-5. At low pressures, a strong increase in adsorption is observed as the Langmuir sites will determine the overall sorption behavior. After saturation of the hole free volumes (C_H approaching $C_{H,m}$), sorption will continue according to Henry's law. As a result, $C_{H,m}$ can be seen as a measure for the total hole free volume. The solubility coefficient S is defined as the pressure-normalized sorption (Equation 1.12)[23]:

$$S = \frac{C}{p} = k + C_{H,m} \times \frac{b}{1 + b \times p} \tag{1.12}$$

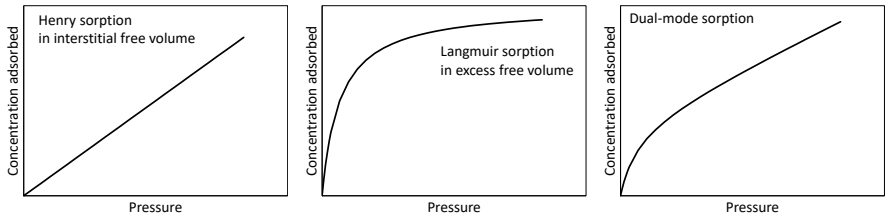

Figure 1-5: Schematic representation of Henry sorption, Langmuir sorption and dual-mode sorption in glassy polymers.

1.3.4 Diffusivity

In contrast to the solubility coefficient, diffusivity is a kinetic term subject to features of both the polymer and the gas molecule. Consequently, diffusivity cannot be predicted with simple thermodynamics and no quantitative link between polymer structure and diffusivity coefficient has yet been found[11,23]. However, based on the free volume theory, it is possible to rationalize

an approach to link polymer structure and diffusivity. Transport of gas molecules through a non-porous polymer membrane takes place based on migration of the molecule through unoccupied space between the polymer chains[21]. Figure 1-6 displays a simulation of a CO_2 molecule migrating through a polyimide matrix. The CO_2 molecule finds itself accommodated in a polymer cavity, moving not more than 5 Å. After 100 ps, the collective and random thermally-induced motion of the polymer chains will unlock the CO_2 molecule, enabling it to make a jump of roughly 10 Å and to move to the next polymer cavity[30]. Rubbery membranes tend to have higher diffusion coefficients than conventional glassy polymers because the polymer chains do not experience rotational restrictions, leading to faster opening and closing of the polymer cavities. Larger diffusion coefficients are expected for both rubbery and glassy polymers with higher temperature as more thermal energy allows more segmental rotation. In addition, specific polymer features such as side chain length, polymer-polymer interaction and polymer stacking affect the FFV and thus the diffusion coefficient. Finally, the size of the gas molecule itself is inversely proportional to the diffusion coefficient[10,11,23].

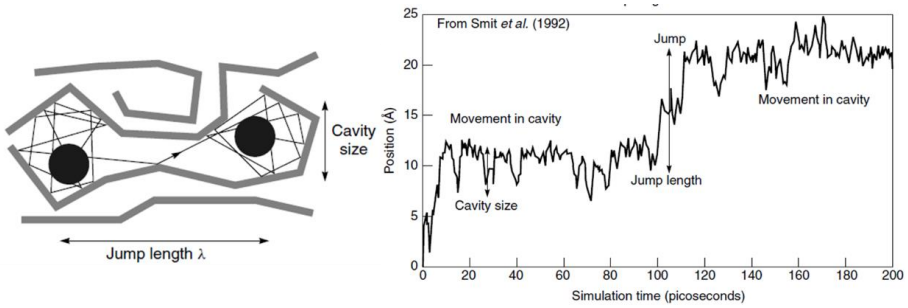

Figure 1-6: Movement of a CO_2 molecule inside a free volume element in a 6FDA-4PDA polymer matrix (left) and molecular simulation of the position of the CO_2 molecule (right). Figure adapted from reference[30].

1.4 CO_2-selective polymer membranes

Over the past two decades, a lot of time and effort has been dedicated to finding new polymer materials with enhanced separation performance[8]. Despite the designing and testing of numerous novel polymers, the majority of today's membrane materials is still made up by the same handful of polymers used 20 years ago. This paragraph provides an overview of some conventional polymeric membrane materials commonly used for CO_2 separation in both industry and academia.

1.4.1 Conventional polymers for CO_2 separation

Traditionally, cellulose acetate (CA, Figure 1-7) is a commonly used material for the fabrication of polymeric gas separation membranes[7]. Originally designed for desalination of seawater, asymmetric CA membranes are mainly used in treatment of sour natural gas (i.e. removal of CO_2 and H_2S) and in enhanced oil recovery applications[7,11]. Typically, the cellulose precursor is completely acetylated to form cellulose triacetate and subsequently hydrolyzed to obtain the

desired degree of acetylation. The degree of acetylation strongly affects solubility in organic solvents and CO_2 permeability as incorporation of acetate groups weakens hydrogen bonding between the polymer chains and disrupts polymer chain packing, causing higher gas permeability[31]. The main limitations of CA membranes are found in their separation performance. CA membranes intrinsically have only poor-moderate selectivity/permeability combinations, well below the Robeson upper bound[7]. In addition, they are prone to plasticization already at CO_2 partial pressures of 4-5 bar[32]. However, due to the combination of a cheap and readily available raw resource (cellulose) and a well-developed fabrication technology (phase inversion), CA membranes have been commercially available (e.g. Honeywell's UOP Separex membrane) for more than three decades now[7,11,33].

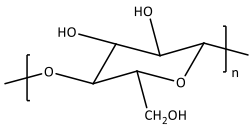

Figure 1-7: Chemical structure of cellulose.

Aromatic polyimides, classically synthesized by polycondensation of an aromatic dianhydride and an aromatic diamine, combine reasonable gas permeability with a relatively high intrinsic selectivity. These polymers generally have a very good compatibility with organic solvents and good thermal and mechanical stability with high T_g, making them attractive for membrane preparation[34]. Matrimid® (Matrimid, Figure 1-8) is a commercially available polyimide, consisting of 3,3'-4,4'-benzophenone tetracarboxylic acid dianhydride (BTDA) and diaminophenylindane (DAPI) monomers, which is often used as a benchmark in academic testing[35–38]. The past ten years, more attention has been payed to fluorinated polyimides and, more specifically, to polyimides containing -$C(CF_3)_2$- in the polymer backbone[39,40]. These 6FDA-based (hexafluoro isopropylidene diphthalic anhydride) polyimides often have increased polymer chain stiffness (higher T_g). Moreover, the hexafluoro groups disrupt chain packing and can act as a molecular spacer[7]. However, these membranes are still very costly, impeding large scale production. Also polyimides (in general) suffer from severe plasticization at elevated CO_2 partial pressure[41]. Multiple strategies to resolve the plasticization problem exist, including chemical[42] and thermal[40] cross-linking or filler addition[43]. Examples of commercial polyimide membranes are Evonik's P84® hollow fiber membrane and UBE's Upilex®, which are applied in natural gas treatment.

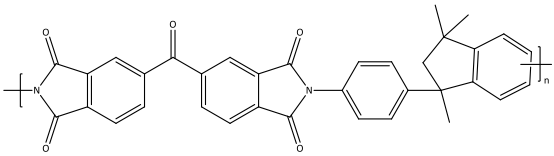

Figure 1-8: Chemical structure of Matrimid.

Polysulfones, typically containing a -Ar-SO_2-Ar'- repeat unit (Ar = aryl group), are an abundantly present group of materials for gas separations with comparable performance to polyimides and

CA[7] (Figure 1-9). Their main advantage lays with a good thermal and chemical stability and excellent mechanical and film forming properties, ensuring good processability into membrane modules[44]. Also for polysulfones, numerous reports are available on the chemical modification of the polymer backbone to optimize gas transport and minimize plasticization[7]. Fluorinated polysulfone was reported to reach a CO_2 plasticization pressure of 15.2 bar[45]. Although most polysulfone membranes are used in hydrogen recovery (e.g. Permea's Prism® membranes) and air separation, sporadic reports of polysulfone membranes for CO_2/CH_4 separation can be found in literature[46].

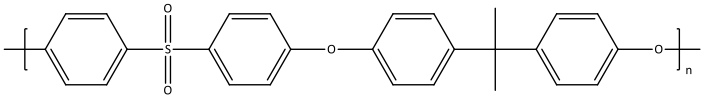

Figure 1-9: Chemical structure of a polysulfone (Udel®).

Ethylene oxide (EO)-based polymers have been extensively studied for gas separation membranes, owing to the high affinity of condensable gases such as CO_2 to the EO phase compared to light gases (e.g. N_2 or CH_4)[47–49]. However, a combination of poor film forming ability of poly(ethylene oxide) (PEO) and EO crystallization at molecular weights above 1 kDa makes designing of pure EO membranes extremely difficult. Block-copolymers are an interesting way of exploiting the very good EO CO_2 separation capacity. EO-based block-copolymers consist of soft, amorphous PEO segments (with good CO_2 affinity) connected to hard segments (giving mechanical strength to the membrane). For example, the commercially available Pebax® MH1657 (Pebax, Figure 1-10) alternates hard polyamide (PA) blocks with PEO segments while Polyactive® includes hard segments based on polybutylene terephthalate (PBT). Pebax membranes generally show high CO_2/N_2 selectivities around 40-50 combined with CO_2 permeabilities between 75-100 Barrer, while the CO_2/CH_4 selectivity is only around 15[47]. MTR's Polaris® membrane is the first commercially available membrane for carbon capture applications and is believed to consist of soft EO segments with a thin, active layer selective towards CO_2 and H_2O, although its exact chemical structure is unknown[50]. The first generation, commercial scale Polaris® membrane displays CO_2/N_2 ideal selectivities of around 50 combined with CO_2 permeance of ~1000 GPU[51].

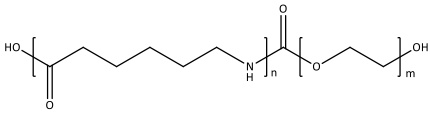

Figure 1-10: Chemical structure of Pebax.

1.4.2 Problems to be solved for polymeric membranes

1.4.2.1 Trade-off between permeability and selectivity

The commercial success of polymeric membranes can be explained by their relatively low cost compared to alternative technologies, their mechanical robustness and ease of processing and module making. Ideally, polymeric membranes with both high selectivity and permeability are

desirable as high selectivity renders higher product purity and lower operational costs while membranes with high permeability require less membrane area, lowering capital expenses[52]. However in 1991, Robeson first noticed and described the existence of an inverse relationship between permeability and selectivity for glassy polymers. He collected pure gas permeation data for various gas pairs and derived an empirical upper bound characterized by the following mathematic relationship (Equation 1.13)[53]:

$$P_i = \beta \times \alpha_{i/j}^{n} \tag{1.13}$$

with $\alpha_{i/j}$ the ideal selectivity of gas i and j, P_i the pure gas permeability of gas i, and β and n empirically determined constants.

The front factor β depends on multiple parameters including gas condensability, chain stiffness and the average distance between polymer chains while n is linked to the difference in kinetic diameters of the gases i and j[52]. The origin of this intrinsic performance trade-off can be found in the size-sieving nature of the rigid glassy polymer chains and has been ascribed to the inability to create larger free volume element sizes without broadening the free volume size distribution[54]. A higher permeability in glassy polymers can be accommodated by increasing the free volume element size, leading to higher gas diffusivity but at the expense of diffusivity selectivity as the size distribution becomes broader, causing overall a decreased selectivity. Over the past decades, the position of the selectivity-permeability upper bound has been revisited multiple times[55] and shifted towards more selective and more permeable membranes, showing the progress made in tailoring polymer membranes for specific separations[22]. The performance trade-offs of the traditional membranes described above are given in Figure 1-11 for CO_2/CH_4 separation.

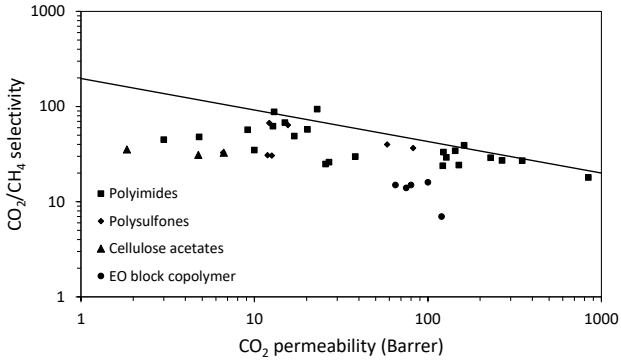

Figure 1-11: Selectivity-permeability trade-off for CO_2/CH_4 separation for the conventional polymer membranes.

1.4.2.2 Plasticization

Excessive sorption of highly soluble gases (e.g. CO_2, H_2S, organic vapors) in the membrane tends to swell the polymer chains, leading to enhanced free volume and polymer segmental mobility

or, said otherwise, an apparent decrease in T_g. Consequently, gas diffusivity selectivity decreases while gas diffusivity strongly increases, frequently resulting in enhanced permeability but lowered separation factor. This effect is known as membrane plasticization and mostly affects glassy polymers as their characteristic rigidity is compromised[7,23,56]. Rubbery polymers commonly suffer less from selectivity losses as they are already above their T_g[21]. Plasticization is usually dependent on the condensability of the penetrant, the filtration conditions (e.g. CO_2 partial pressure), exposure time and thickness of the membrane[57]. Typical plasticization behavior is shown in Figure 1-12. Initially, a decrease in permeability is observed with increasing pressure as a result of lowered solubility due to saturation of the excess free volume sites. After a certain threshold pressure (i.e. the plasticization pressure), an upturn in permeability is noticed as a result of plasticization[10].

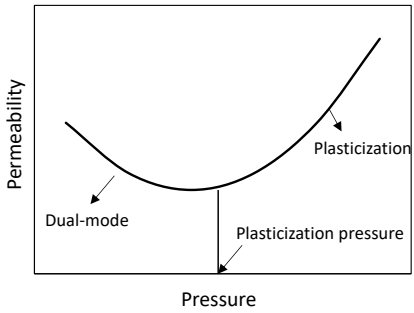

Figure 1-12: Effect of plasticization on permeability.

1.4.2.3 Physical ageing

Next to plasticization, physical ageing is another important factor, which can drastically influence membrane performance. Since glassy polymers below their T_g are inherently non-equilibrium materials due to the presence of 'kinetically frozen' excess free volume, the rearrangement of the polymer chains over time towards their thermodynamic equilibrium packing results in the gradual loss of excess free volume. This phenomenon is called physical ageing[10,22]. 'Diffusion' of the free volume elements is frequently suggested to be at the base of this behavior as free volume elements steadily migrate towards the membrane surface during chain rearrangement. Ageing depends on a range of parameters such as temperature, polymer type and membrane synthesis and post-synthesis conditions[7]. Furthermore, it is commonly accepted that thin films face accelerated aging compared to their thick film counterparts (Figure 1-13)[58]. The loss in free volume will often eventually lead to lower permeability and increased gas pair selectivity. Ageing thus results in an opposite effect on the membrane performance compared to plasticization. Mitigation of physical ageing can be done by nanoparticle addition to the polymer matrix, blending and cross-linking[59].

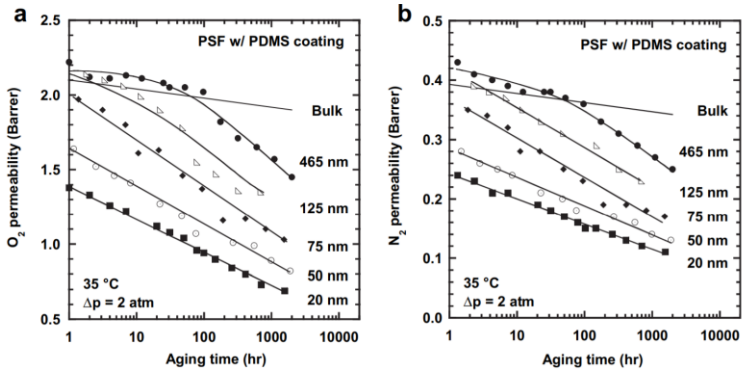

Figure 1-13: Thickness-dependency of physical ageing with regard to O_2 and N_2 permeability. Figure copied from reference[58].

1.5 Towards better membranes

1.5.1 Surpassing the Robeson upper bound

Membrane-related sales for gas separation applications have grown from 150 million USD/year to approximately 1.5 billion USD/year in less than 20 years[8,13]. However, the materials used 20-30 years ago still provide (close to) the best set of membrane properties for current membrane applications. Two decades of designing and redesigning conventional polymers has delivered valuable empirical structure-performance insights but failed to render groundbreaking new materials. Galizia and co-workers identified five novel routes to better membranes beyond the traditional polymers[8]:

- *Unconventional-conventional polymers,* such as fully fluorinated polymers (e.g. Hyflon AD and Teflon AF), which possess characteristics so different from conventional polymers that disruptive new results are possible[60].
- *Nanoporous polymers*: these polymers have high intrinsic porosity, resulting from their sterically hindered and contorted backbone[61]. Materials like polymer of intrinsic microporosity (PIM) define new selectivity-permeability upper bounds as their large pores allow to achieve both high solubility and diffusivity for various gases. The major challenge for this class of polymers lays with severe physical ageing[8]. Next to PIMs, thermally rearranged (TR) polymers, mostly based on polybenzoxazoles (PBOs), arise after rearrangement of polyimide precursors containing ortho-hydroxyl groups during thermal treatment at temperatures above 400 °C[62]. These cross-linked polymers are plasticization-resistant and are highly porous due to frustrated chain packing, leading to high gas permeabilities. At the same time, the narrow distribution of free volume elements often guarantees high selectivity as well. Main disadvantage for TR polymers is the high temperature required for rearrangement, which is often detrimental for mechanical properties of the membrane[8].

- *Facilitated transport membranes*: facilitated transport membranes circumvent the limitations of the traditional SD transport mechanism by chemically reacting the fast component with a mobile or fixed carrier. These membranes are extremely interesting for low pressure carbon capture applications (e.g. CO_2/N_2). Exceptional CO_2/N_2 performances have been reported with interfacially polymerized polyamine and polyamide membranes, owing to the selective, carrier-mediated targeting of CO_2 over N_2 and the extremely thin selective layers[63–65]. Facilitated transport membranes are mainly limited by carrier saturation, carrier degradation and/or the dependence on water in the feed to fuel the facilitated transport mechanism[66].
- *Inorganic membranes* generally display unique gas separation properties due to their precisely defined and uniform pore structure and chemistry. Despite this, almost no large scale commercial applications with inorganic membranes currently exists, which is mainly related to the poor mechanical properties (i.e. brittleness) of these materials and difficulties in up-scaling and with reproducibility, making it challenging and costly to fabricate large area membrane modules[23,67].
- *Mixed-matrix membranes (MMMs)* are hybrid membranes, which consist of a polymeric matrix, containing inorganic particles (so-called fillers) such as metal-organic frameworks (MOFs) or zeolites. MMMs are believed to combine the processability of cheap polymers with the excellent separation performance of the inorganic fillers, bypassing the mediocre performance of pure polymer membranes and the brittleness and high cost of purely inorganic membranes[23]. MOF-based MMMs are at the core of this dissertation and will be discussed in more detail in the next section.

1.5.2 Mixed-matrix membranes

Figure 1-14 depicts the hybrid nature of MMMs, containing fillers that are randomly embedded in a polymer matrix. Initially, these fillers mainly entailed inorganic materials (e.g. silica, alumina, zeolites) but more recently the research focus has shifted towards (partially) organic fillers because of their better compatibility with the polymeric phase. The seemingly endless combination possibilities of fillers and polymers has rapidly generated an extensive stream of novel MMMs over the past two decades. Numerous filler classes have been tried as potential filler, including zeolites[68], carbon nanotubes[69], covalent organic frameworks[70], graphene[8], carbon molecular sieves[71], activated carbon[72], 2D materials[73,74] and MOFs[67].

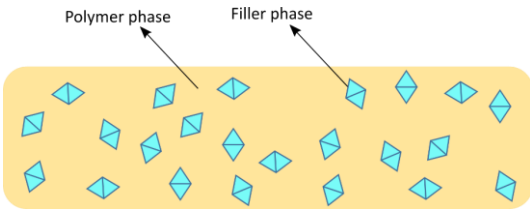

Figure 1-14: Schematic representation of an MMM.

Over the past years, MOFs in particular have gained a lot of attention in the academic research setting, owing to their chemical and structural diversity. MOFs are a class of microporous, crystalline materials and are based on the flexible coordination chemistry between metal ions/clusters and organic linkers. This flexibility in chemistry allows to fine-tune MOF physical and chemical properties towards a specific gas separation application. MOFs can be synthesized with very high porosity and surface area up to 10 000 m^2/g, specific pore size and pore functionality and good mechanical, thermal and chemical stability[8]. Furthermore, the partly organic nature of MOFs generally improves the polymer-filler compatibility, causing better interfacial adhesion. To date, numerous MOFs based on various metals and linkers have been developed and applied in MMMs. Conventional MOFs that are frequently studied include ZIF-8, zirconium-based UiO-66, HKUST-1 and MIL-53[67]. General conclusions that can be drawn from filtration experiments with these MMMs are that incorporation of the MOFs for most cases causes an increase in membrane permeability at a constant or lower selectivity while roughly 10-15% of the MOFs results in a simultaneous improvement of both permeability and selectivity. Furthermore, almost all MMMs display increased plasticization resistance compared to the pristine polymer membrane[67]. Among the wide variety of MOFs, zirconium-based MOFs are a noteworthy family of MOFs due to their good stability features (including water and acid stability) combined with high specific surface area and pore volume. Two renown MOFs in this family are UiO-66, consisting of a $Zr_6O_4(OH)_4$ cluster linked by various 1,4-benzenedicarboxylate (BDC^{2-}) linkers and its isoreticular nephew UiO-67, having the same zirconium cluster but biphenyl-4,4'-dicarboxylate ($BPDC^{2-}$) linkers instead of BDC^{2-} (Figure 1-15).

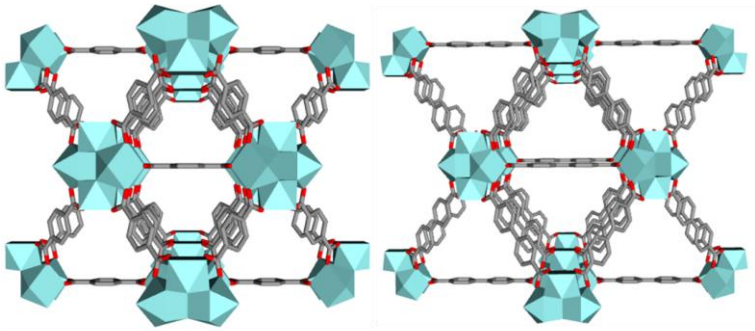

Figure 1-15: Representation of the crystal structure of UiO-66 and UiO-67.

1.5.3 Challenges for mixed-matrix membranes

As mentioned before, MMMs have often been reported to improve the membrane performance, either by increasing gas permeability, gas pair selectivity or, more rarely, a combination of both. Furthermore, better plasticization and ageing resistance has been observed as an unexpected (but welcome) side-effect of filler incorporation. Besides the improvement of the overall membrane performance, the hybrid nature of these membranes brings with it some important challenges for MMMs, including interfacial adhesion and

compatibility between filler and polymer phase, membrane processability, gas transport mechanisms and the absence of structure-performance relationships. Some of these are briefly highlighted below.

1.5.3.1 MOF-polymer interphase

Good interfacial adhesion between the filler and the polymer is of high importance to guarantee good membrane separation performance[75]. Commonly, four different interface types are theoretically identified next to the ideal interface in which the fillers are perfectly wetted by the polymer. When the interaction between polymer and filler is too strong, this can cause a rigidified polymer layer surrounding the filler. Rigidified polymer layers often result in a slightly increased membrane selectivity due to enhanced local diffusivity selectivity. Furthermore, a high affinity between polymer and filler combined with an easily accessible pore can lead to pore blocking by polymer intrusion. When the compatibility is too low, the polymer can detach from the filler, creating so-called interfacial voids between polymer and filler (i.e. sieve-in-a-cage morphology). These interfaces typically cause a substantial increase in membrane permeability and a reduction in membrane size selectivity. When the interfacial voids are in the range of the size of the permeating gases, selectivity can be retained and a mild increase in permeability is often observed (i.e. leaky interface)[75,76]. Although MOF fillers dispose of a proven track-record of having better compatibility with polymers compared to completely inorganic particles (such as zeolites or silica), the overly optimistic approach of MOF/polymer adhesion has often led to an underappreciated and underreported importance of interfacial defects for MOF MMMs[77].

Experimental sealing strategies

Various experimental strategies have been proposed to improve the interfacial adhesion. Most of these entail surface modification of the filler or the polymer to enhance physical interaction or to allow chemical cross-linking between filler and polymer. Improved physical interaction has been acquired by Tien-Binh and co-workers by preparing MMMs based on hydroxyl-functionalized polymers and MIL-53-NH_2. Improved adhesion followed from hydrogen bonding between the polymer hydroxyl groups and the amino groups on the MOF outer surface[78]. The use of MOF-oligomer composites has also been explored to seal the MOF-polymer interface. It was found that surface-functionalizing UiO-66 particles with Durene oligomers resulted in 6FDA-Durene MMMs with higher MOF loadings and less defects at the interface[79]. Next to the use of hydrogen bonding and MOF-oligomer composites, also enhanced π-π interaction has been exploited to improve physical interaction between filler and polymer[80]. Additionally, chemical cross-linking has been applied to improve the MOF-polymer interface. The bulk of these approaches rely on functionalization of the filler and/or polymer, resulting in formation of covalent bonds between the polymer and the filler[81]. A third mitigation strategy for weak interfacial interactions is the use of tertiary components (so-called compatibilizers), which are designed to display good interaction with both filler and polymer[82]. In this context, ionic liquids (ILs) are a very interesting choice of sealing agent as they can act as a wetting and binding phase

(i.e. glue) between MOF and polymer and can be designed to have high CO_2 affinity themselves[77]. Also in-situ synthesis of MOF MMMs has been considered and already applied[35].

Interphase characterization

Besides varying experimental synthesis strategies, the experimental characterization of interfacial defects remains notoriously challenging. Traditional techniques such as scanning electron microscopy and differential scanning calorimetry fall short of adequately characterizing the polymer-MOF interface as they probe bulk transport properties of the composite material and not the properties at the interface[83]. Positron annihilation lifetime spectroscopy is used to characterize the free volume elements in MMMs but most often lacks sufficient resolution to make a clear distinction between interfacial voids, free volume elements of the polymer and the MOF free volume. Recently, FIB-SEM and Raman infrared spectroscopy have been proposed as alternative analysis techniques to evaluate the dispersion and embedding of the fillers in the polymer matrix[77].

Owing to the limitations of traditional characterization techniques, there seems to be an important role to play for molecular modelling in understanding the interfacial interactions between MOF and polymer. Especially in combination with state-of-the-art characterization, modelling at the microscopic level can expose interesting aspects about the MOF-polymer interphase. A combination of solid-state NMR and molecular modelling was applied to demonstrate that PEO penetrates into UiO-66 cages more easily than polyvinylidene fluoride (PVDF)[83]. Ozcan *et al*. performed microsecond-scale concentration gradient molecular dynamics simulations of H_2 and CH_4 transport through PIM-1/ZIF-8 MMMs. This allowed the authors to determine the density and residence time of the permeating H_2 and CH_4 gases along the membrane. They found that poor compatibility between polymer and MOF results in the presence of non-selective microvoids, causing the composite material to have lower performance than expected based on the performance of pure PIM-1 and ZIF-8[84]. Another noteworthy study, in which modelling was combined with IR spectroscopy microimaging, visualized the transient concentration gradient of CO_2 in a 6FDA-DAM/ZIF-8 MMM. It was shown that ZIF-8 acts as a transport highway towards the surrounding polymer phase. Furthermore, Grand Canonical Monte Carlo (GCMC) simulations revealed that CO_2 is preferably accommodated in the microvoids between polymer and MOF, hence causing CO_2 accumulation at the interface[85]. General conclusions that can be drawn from these modelling studies reveal that selecting compatible MOF/polymer pairs is of utmost importance to reach acceptable performance and remains one of the biggest challenges in the field[86].

1.5.3.2 MMM processability

Processability remains an important concern for MMMs, especially towards development of industrial applications. Even though MMMs have better mechanical properties than purely inorganic membranes, the mechanical properties of the membrane are substantially affected by filler incorporation. For example, it was observed that ZIF-8 loadings above 15 wt.% in Matrimid reduces the toughness and tensile strength of the MMMs. In addition, high temperature treatments and even higher filler loadings were shown to have a strong negative

impact on the brittleness of the MMMs[87,88]. It is not unreasonable to assume that these effects become even more pronounced when MMMs are produced as thin-films rather than dense, stand-alone membranes. Some asymmetric MMMs with good selectivity have been reported but most up-scaled asymmetric MMM attempts failed to produce defect-free selective layers[89–93]. A key aspect for thin-film MMM preparation is ensuring colloidal stability of the filler dispersion during synthesis[71]. Filler particle size is in this regard an important parameter, although there is no consensus in literature on the ideal particle size[94,95]. Ideally, smaller particle sizes should lead to better incorporation in the membrane but at a higher risk of agglomeration. Larger particles tend to agglomerate less, but are more difficult to incorporate defect-free in polymer films. Currently, mitigation strategies for particle agglomeration include nanoparticle priming[67], MMM 'wet synthesis' (i.e. MOF is not dried during MMM synthesis)[96] and particle functionalization for better compatibility with the solvent[97].

1.5.3.3 Gas sorption and transport mechanisms in MMMs

Finding a universal and unified description of the mechanistic transport of gas through MMMs remains a complex challenge. While compelling evidence for the validation of the SD model in polymer membranes has been delivered through various experiments[24,27,98], validation studies of the legitimacy of the SD model in MOF-based MMMs are currently still unaccounted for. It may be anticipated that the SD model can be applied in ultramicroporous MOFs, which contain similar free volume element sizes as in many polymers, but MMMs containing MOFs with free volume elements larger than 5 Å require more advanced approaches[98]. Since the transport through MMMs is a net result of the transport mechanisms of both polymeric (SD) and inorganic materials, the traditional polymer-based dual-mode sorption model (Equation 1.11) is not able to give a satisfactory description of sorption in these hybrid materials[99]. Modelling at the micro and macroscale can play a central role in unravelling the complexity of the gas transport mechanisms in MMMs. Macroscopic modelling based on either the effective medium approach (EMA) or resistance model approach (RMA) has led to a series of permeability prediction models[99]. Although the majority of these models (such as Maxwell, Bruggeman, Lewis-Nielsen) assume an ideal interphase (which is difficult to obtain), they can be applied to fit experimental data and estimate MMM and MOF properties at low MOF loadings (<15 vol%)[100]. Molecular simulations have been instrumental for determination of the MOF-polymer interphase but also for penetrant binding mechanisms in MMMs. Molecular computations such as GCMC and molecular dynamics (MD) are becoming increasingly popular to evaluate adsorption isotherms and selectivities in MOF membranes and MMMs[75,98,99]. An overview of various modelling studies can be found elsewhere[98].

Chapter 2 Scope of thesis and dissertation overview

As described in the introduction, membranes with enhanced separation performance are predicted to unlock new application areas and/or expand the membrane market share in existing industries. Development of new polymer membranes and MOF MMMs with improved separation performance therefore remains relevant and essential for the field. Even though the concept behind MMMs is relatively straightforward, its practical implementation involves a number of challenges. One of them is the lack of distinct structure-property relationships, which currently impedes the rational preparation of tailor-made MMMs for specific gas separation applications. In addition, testing of MMMs and, by extension, membranes in general under industrially relevant testing conditions is of high importance to gain insight in the true potential of the membrane. Yet, membrane developers still remain overly fixated on researching thick free-standing membrane films tested under pure gas conditions or, at best, a binary mixture of gases, whereas this is only the first stage of membrane development.

In face of these challenges, the aim of this dissertation is threefold: **(1) research new membrane materials with enhanced separation properties** for CO_2/CH_4 and CO_2/N_2 model mixtures, respectively representing natural gas/bio gas and flue gas streams. The focus in this part of the thesis will be on designing both novel polymeric membrane materials as well as hybrid MMMs in an attempt to circumvent the trade-off between membrane selectivity and permeability that most traditional polymeric membranes suffer from. The potential of decarboxylation cross-linking of a polyimide bearing carboxylic acid groups (6FDA-DABA) is investigated as a way to tune membrane performance. Furthermore, two types of MOF-based MMMs, consisting of UiO-67 and MOF-808, will be developed and discussed; **(2) initiate a systematic approach for a more rational design of MMMs**. More specifically, this section builds on findings from the first part of the thesis; and **(3) the design and assembly of a second generation high-throughput gas separation** (HTGS-2) set-up for membrane testing under industrially relevant conditions.

Chapter 3 entails the synthesis and description of a novel MMM based on zirconium UiO-67 MOF. In this section, the standard biphenyl-4,4'-dicarboxylic acid (BPDC) linker of UiO-67 is replaced by 2,2'-bipyridine-5,5'-dicarboxylic acid (BPYDC) linkers, containing two heterocyclic nitrogen atoms, in order to improve the CO_2 affinity of the MOF and membrane. Moreover, the effect of BPYDC concentration in the MOF on membrane performance is investigated.

Chapter 4 addresses the shortcomings of the MOF-polymer systems in Chapter 3. More specifically, UiO-67 is replaced by the far more stable MOF-808. A novel and straightforward MOF synthesis method (modulator-mediated functionalization) is introduced to perform cheap, in-situ MOF functionalization during synthesis. Series of fluorinated and non-fluorinated carboxylic acids are used as modulator during MOF-808 synthesis as a proof-of-concept. The fluorinated and non-fluorinated MOFs are incorporated in Matrimid membranes and studied for their CO_2/CH_4 separation performance.

Chapter 5 involves an attempt to correlate intrinsic MOF parameters with MMM performance indicators. Testing of various MMMs during this PhD gave rise to the question which MOF parameters can be used as performance indicators for the corresponding MMMs. A key element in this research was the availability of MOF-808, which can be used as a platform MOF due to its unique cluster composition.

Next to MOF incorporation in polymer membranes, **Chapter 6** elaborates on a purely polymeric pathway to improved membrane performance. Membranes made from a polyimide bearing carboxylic acid groups (6FDA-DABA) are exposed to thermal treatment at various temperatures. The effect of different annealing temperatures on the membrane structure and performance is thoroughly characterized and underlying mechanisms of the membrane performance are elucidated. Two counteracting mechanisms are identified to be responsible for the membrane performance: physical tightening due to enhanced polymer stacking efficiency and polymer dilation as a result of decarboxylation cross-linking.

Finally, **Chapter 7** describes the development and assembly of HTGS-2 for testing of membranes under industrially relevant conditions and with a broad range of gases. Compared to the original set-up, HTGS-2 is designed to test at higher temperatures (100 °C), higher pressures (34 bar), with 7 different gases and in presence of gas impurities, such as water.

Chapter 3

Bipyridine-based UiO-67 as a novel filler in mixed-matrix membranes for CO_2-selective gas separation

Raymond Thür[a], Niels Van Velthoven[a], Sam Slootmaekers[a], Jeroen Didden[a], Rhea Verbeke[a], Simon Smolders[a], Werner Egger[b], Marcel Dickmann[c], Dirk De Vos[a], Ivo F.J. Vankelecom[a]

*Based on *Journal of Membrane Science 2019, 576, 78–87*

[a] Centre for Membrane Separations, Adsorption, Catalysis and Spectroscopy for Sustainable Solutions (cMACS), KU Leuven, Celestijnenlaan 200F, Box 2454, 3001 Heverlee, Belgium

[b] Heinz Maier-Leibnitz Zentrum (MLZ) and Physik Department E21, Technische Universität München, Lichtenbergstraße 1, 85748 Garching, Germany

[c] Institut für Angewandte Physik und Messtechnik, Universität der Bundeswehr München, 85577 Neubiberg, Germany

*https://doi.org/10.1016/j.memsci.2019.01.016

Abstract

Bipyridine-based UiO-67 MOFs were for the first time successfully applied as filler material in Matrimid MMMs. Extensive characterization of fillers (via XRD, NMR, SEM, ATR-FTIR, CO_2 and N_2 physisorption) and membranes (via XRD, SEM, ATR-FTIR, DSC, TGA and PALS) was performed to gain insight in the MMM separation behavior. Incorporation of BPYDC linkers increased the CO_2 affinity of the MOFs and corresponding MMMs, owing to the presence of nitrogen heteroatoms in the linker. As a result, the CO_2/CH_4 separation factor improved from 38 for pristine Matrimid to 75 for the MMM with 10 wt.% UiO-67-33 while the CO_2 permeability was simultaneously enhanced from 16 Barrer (Matrimid) to 26 Barrer. The concentration of the filler inside the membrane could be increased to 30 wt.%, resulting in a permeability improvement of 350% compared to the reference Matrimid membrane, however at the expense of the membrane selectivity. Use of N-heterocyclic ligands proved to be an interesting strategy and good alternative for functionalization of MOF surfaces to obtain improved membrane performance.

Contributions

Raymond Thür: design and coordination of experiments, membrane and MOF preparation, characterization (SEM, ATR-FTIR, TGA, DSC), gas permeation experiments, data analysis, manuscript writing and redaction. Niels Van Velthoven: MOF preparation, characterization (XRD, NMR), data analysis, manuscript correction and redaction. Sam Slootmaekers: membrane and MOF preparation, gas permeation experiments, data analysis. Jeroen Didden: design of experiments, manuscript correction and redaction. Rhea Verbeke: PALS experiments and data analysis, manuscript correction and redaction. Simon Smolders: physisorption experiments and data analysis, manuscript correction and redaction. Werner Egger: PALS experiments and data analysis. Marcel Dickmann: PALS experiments and data analysis. Dirk De Vos: manuscript correction and redaction. Ivo F.J. Vankelecom: design of experiments, manuscript correction and redaction.

3.1 Introduction

One of the main limitations of pure polymeric membranes for gas separation is the trade-off between permeability and selectivity, as described in 1991 and revisited in 2008 by Robeson[53,55]. In an attempt to exceed the Robeson upper bound, the easy processability of cheap polymers and the superior gas separation characteristics of inorganic particles have been combined into so-called MMMs, constituted of a dispersed filler in a continuous, polymeric phase. MOFs are a family of crystalline fillers particularly interesting for gas separation, as they show high specific surface area, ease of modification, adjustable porosity, and broad chemical composition in a variety of framework topologies[101,102].

Zirconium-based MOFs (Zr-MOFs) are considered to be among the most promising materials for practical applications, mostly due to their excellent thermal and chemical stability (including outstanding water stability), large surface area and porosity[103,104]. The most renowned member of the Zr-MOFs is UiO-66 ($Zr_6O_4(OH)_4BDC_6$), which consists of $Zr_6O_4(OH)_4$ clusters connected by BDC^{2-} ligands[105]. Next to UiO-66, UiO-67, which is the isoreticular analogue of UiO-66, consists of the same $Zr_6O_4(OH)_4$ cluster but connected by $BPDC^{2-}$ linkers (Figure 3-1)[105]. Compared to UiO-66, UiO-67 has a higher theoretical BET surface area and larger pore window but lowered thermal and mechanical stability[106]. Many examples of the use of (modified) UiO-66 in membrane-based gas separation can be found[107–109]. Anjum *et al.* successfully prepared MMMs based on amino-functionalized UiO-66 (UiO-66-NH_2). Their modulation approach, combined with the use of amino-functionalized linkers (BDC-NH_2), led to an improved particle-polymer interface and significantly enhanced the separation performance[81]. By in-situ cross-linking of UiO-66-NH_2 particles with PIM-1, Tien-Binh *et al.* managed to significantly boost both permeability and ideal selectivity of the resulting MMM[110].

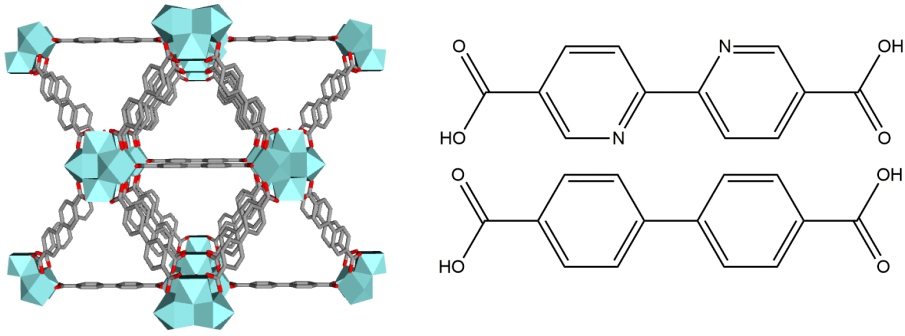

Figure 3-1: Left: the structure of UiO-67 with a large octahedral cage with a pore diameter of 21 Å and small tetrahedral cages with a pore diameter of 11.5 Å. Right: the BPYDC (top) and BPDC (bottom) linkers.

Although UiO-67 and its bipyridine derivatives have already been extensively tested in catalysis[111], their use in membrane-based separations has been rather limited so far. Cu(II) loaded UiO-67 with BPYDC linkers has been applied for desulfurization of gasoline, while UiO-67 was incorporated in poly(vinyl alcohol) membranes for ethanol dehydration[112,113]. Only one

report on the use of UiO-67 as filler in MMMs for CO_2 separation could be found in open literature[67,77,114]. In 2012, Nik *et al.* incorporated several MOFs, including UiO-67, in a fluorinated polyimide matrix (6FDA-ODA), reporting a CO_2/CH_4 separation factor of 15 when using the UiO-67 MMM and of 42 for the pristine 6FDA-ODA membrane. The reduced performance of the UiO-67/polyimide membrane was attributed to poor adhesion between polymer and MOF. Moreover, it was shown that amino-functionalized fillers improved the MOF-polymer interaction but could, at the same time, result in polymer rigidification at the interface with a decreased CO_2 permeability and increased CO_2/CH_4 selectivity as a result[115]. Even though immobilizing functional groups on the MOF surface is a promising strategy to enhance the CO_2 affinity, it also often reduces pore volume and surface area, which is undesirable for gas permeation. Following this reasoning, the use of linkers, which contain heterocyclic functionalities instead of immobilized functional groups (e.g. BDC-NH_2) was investigated as this could be an interesting way to incorporate heteroatom functionality in the MOF without compromising its structural features, while still improving both CO_2 affinity and permeability[104,116]. Therefore, the standard $BPDC^{2-}$ linkers in UiO-67 are replaced by N-heterocyclic $BPYDC^{2-}$ linkers in different ratios. For the first time, UiO-67 and its bipyridine derivatives are now successfully incorporated in a membrane, exemplified here by using the Matrimid polymer, and applied for CO_2/CH_4 separations.

3.2 Materials and methods

3.2.1 Chemicals

Polyimide (Matrimid) was kindly provided by Huntsman (Switzerland). Trichloromethane (chloroform, >99%) and *N,N*-dimethylformamide (DMF, >99%) were purchased from Acros. CO_2 and CH_4 were acquired from Air Liquide (Belgium). $ZrCl_4$ (99.95%) was purchased from ABCR and hydrochloric acid (HCl, 37 wt.% solution in water) was supplied by Fisher. Acetic acid (glacial), BPDC (97%) and BPYDC (97%) were supplied by Sigma-Aldrich.

3.2.2 MOF synthesis

UiO-67 and its bipyridine derivatives were prepared by a standard solvothermal method. 1.27 mmol linker (BPDC, BPYDC or a combination) was dissolved in 100 mL DMF in a 250 mL Schott bottle and sonicated for 15 min. Next, 1.27 mmol $ZrCl_4$ was added, followed by 2.15 mL acetic acid and 0.5 mL 37% HCl. The mixture was then placed in an oven at 120 °C for 48 h. After MOF formation, the MOF was washed 3 times with DMF and 3 times with ethanol. After each washing step, the MOF mixture was centrifuged for 30 min at 4000 rpm. Eventually, the MOFs were dried overnight in an oven at 80 °C.

3.2.3 Membrane synthesis

3.2.3.1 Preparation of pristine Matrimid membranes

Matrimid (0.42 g) was dried at 100 °C overnight in an oven, then dissolved in chloroform (5.58 g) to form a 7 wt.% polymer solution. The solution was stirred overnight and eventually cast in a Teflon Petri dish (diameter 6 cm) in a nitrogen bag at room temperature. In order to slow down the solvent evaporation, a plastic funnel wrapped with paper or aluminum foil was inversely placed over the Petri dish. After solidification of the membrane due to solvent evaporation, the Matrimid membrane was annealed in an oven. The temperature was raised from room temperature to 110 °C in 17 min and kept constant for 1 h. Next, the temperature was gradually increased to 180 °C at 5 °C/min and kept constant for 6 h.

3.2.3.2 Preparation of MMMs

MMMs were prepared by dispersing fillers in varying weight percentages in chloroform (5.58 g). The filler suspension was then stirred for 30 min and sonicated for 60 min in a sonication bath. After sonication, dried Matrimid (0.42 g) was added following a priming protocol (see supporting information). The resulting polymer/filler suspensions were stirred overnight. Prior to casting in a nitrogen bag, the suspensions were again sonicated for 45 min. After casting in a Teflon Petri dish, a plastic funnel wrapped with paper or aluminum foil was inversely placed over the Petri dish. The same annealing protocol was used as for pristine Matrimid. After annealing, the membrane was allowed to cool down naturally to room temperature. The filler loading of the membrane was calculated as follows:

$$filler\ loading\ (wt.\%) = 100 \times \left(\frac{m_{filler}}{m_{filler} + m_{polymer}}\right) \quad (3.1)$$

3.2.4 Characterization

3.2.4.1 X-ray diffraction

X-ray diffraction (XRD) patterns of both membranes and MOFs were recorded on a STOE STADI P COMBI diffractometer with an image plate position sensitive detector (IP PSD) in the 2θ region from 5° to 60°, with internal resolution of 0.03° and counting time of 1200 s. The measurements were performed in transmission mode by using CuKα1 radiation (λ=1.54056 Å) created through a Ge (111) monochromator.

3.2.4.2 Scanning Electron Microscopy

Membrane and particle morphology were analyzed by scanning electron microscopy (SEM, Philips XL30 FEG). Particle dispersion in the membrane and membrane cross-sections were observed. Before measurement, all membranes were frozen and broken in liquid nitrogen. All samples were coated with a gold/palladium film.

3.2.4.3 Thermogravimetric Analysis

Thermal stability of the membranes was investigated by thermogravimetric analysis (TGA). TGA analysis was performed on a TA instruments TGA Q500. Samples were heated at a rate of 10 °C min^{-1} to 550 °C under N_2 flow.

3.2.4.4 Attenuated Total Reflectance – Fourier Transform Infrared Spectroscopy

Attenuated total reflectance – Fourier transform infrared spectroscopy (ATR-FTIR) was applied to identify functional groups of all MOF and membrane samples. Before measurement, all samples were dried. A Bruker Alpha instrument with a diamond ATR crystal was used to perform 32 scans at a resolution of 4 cm^{-1}.

3.2.4.5 Differential Scanning Calorimetry

Differential scanning calorimetry (DSC) measurements were performed on all membrane samples to study the effect of MOF addition and BPYDC content on membrane glass transition temperature (TA instruments DSC Q2000). The membrane samples were heated up and cooled down under nitrogen atmosphere at 10 °C min^{-1}. Thermal history of the polymer was erased by heating up to 350 °C. Afterwards, the actual measurement entailed the cooling down from 350 °C to 150 °C and reheating up to 350 °C. The obtained data were analyzed with Universal Analysis software.

3.2.4.6 N_2 and CO_2 physisorption

Gas sorption measurements were performed on a Micromeritics 3Flex surface analyzer at -196 °C (N_2) and 0 °C (CO_2). Prior to measurements, samples were evacuated under vacuum at 100 °C for 16 h. Surface areas were calculated using the multi-point Brunauer–Emmett–Teller (BET) method applied to the isotherm adsorption branch, taking into consideration the BET surface area rules defined by Rouquerol[117] and the consistency criteria described by Walton and Snurr[118].

3.2.4.7 Nuclear Magnetic Resonance

In order to determine the relative ratio of built-in linkers in the mixed-linker UiO-67 samples, ^{1}H liquid phase nuclear magnetic resonance (NMR) was applied on UiO-67 and its BPYDC derivatives. The samples were dissolved in 600 µL deuterated dimethyl sulfoxide (DMSO) with addition of 40 µL of a 40 wt.% hydrofluoric acid solution. The spectra were recorded on a Bruker AMX-300 spectrometer at 300 MHz (16 scans) and analyzed using SpinWorks 4.2 software.

3.2.4.8 Positron Annihilation Lifetime Spectroscopy

Positron annihilation lifetime spectroscopy (PALS) is a technique to determine free volume in polymer membranes. It is based on the lifetime of the ortho-positronium (o-Ps), which is trapped inside free volume elements until it annihilates with an electron from the surroundings. This so-called pick-off lifetime is then used to calculate the free volume element size by the Tao-Eldrup model[119,120]. The intensity of the o-Ps annihilation, being a product of Ps formation probability and the concentration of free volume holes, can be used in some cases to estimate relative changes in the hole concentration. A more thorough explanation of the use of PALS on polymeric membranes can be found elsewhere[121].

Implantation energies of 2 keV were applied, corresponding to a median implantation depth of ca. 100 nm (for a polymer density of 1 g/cm³) to ensure the bulk of the MMM is probed. For all measured spectra, 4x10^6 counts were collected with a counting rate of about 10^4 cts/s and a time resolution of about 250 ps. The resolution function was determined via p-doped SiC, a material with known lifetimes. All spectra were evaluated with PALSfit[122] and deconvoluted into two or three lifetime components, leading to good overall fit variances below 1.2.

3.2.4.9 Gas permeation

Membrane permeability and CO_2/CH_4 separation factor were measured in a custom-built High-Throughput Gas Separation (HTGS) set-up, described elsewhere[47,123]. HTGS allows the simultaneous measurement of 16 membrane coupons with an effective permeation area of 1.91 cm^2, using variable feed compositions, pressures and temperatures.

Gas permeability was measured by accumulating gas permeate in an auxiliary cylinder of 75 cm³. The pressure increase in the cylinder (dp/dt) was measured to calculate the gas permeability of the membrane:

$$P_i = 10^{10} \times \frac{y_i \times V \times V_m \times L}{x_i \times p_{up} \times A \times R \times T} \times \frac{dp}{dt} \quad (3.2)$$

with P_i the gas permeability (Barrer), y_i the mole fraction of the component in the permeate, x_i the mole fraction of the component in the feed, V the downstream volume (cm³), V_m the molar volume (L/mol), A the membrane permeation area (1.91 cm^2), L the membrane thickness (µm), T the operating temperature (K), p_{up} the upstream pressure (bar), R the gas constant (0.082 L atm/mol K) and dp/dt the pressure increase (Torr/s).

Mixed-gas separation factors $\alpha^*_{i/j}$ were calculated by the ratio of the downstream (y) and upstream (x) mole fraction of the two gases by the following equation:

$$\alpha^*_{i/j} = \frac{y_i / y_j}{x_i / x_j} \quad (3.3)$$

with y_i and y_j the mole fractions of components i and j in the permeate, x_i and x_j the mole fractions of the components i and j in the feed. During gas chromatography analysis, y_i/y_j is determined from peak areas linked to mole fractions in the permeate, while x_i/x_j is determined by the feed settings.

3.3 Results and discussion

3.3.1 MOF characterization

Figure 3-2 shows the actual incorporation of BPDC and BPYDC linkers, determined by NMR. A non-linear correlation can be observed, demonstrating that the BPYDC linkers are preferentially incorporated in the MOF framework, e.g. a synthesis mixture with 25% BPYDC and 75% BPDC linker results in a MOF with 33% BPYDC linker incorporated. As both linkers are of similar size, the difference in incorporation is probably not due to steric effects, but due to a difference in carboxylic acid acidity. Indeed, the (predicted) pK_a of BPYDC (1.95) is slightly lower than that of BPDC (3.77), indicating a more deprotonated linker and thus higher probability of incorporation in the MOF framework. The MOFs with different BPYDC concentration are denoted as UiO-67-*x* with *x* being the molar percentage of actual incorporated BPYDC. For example, UiO-67 with 33% BPYDC incorporated linker is denoted as UiO-67-33.

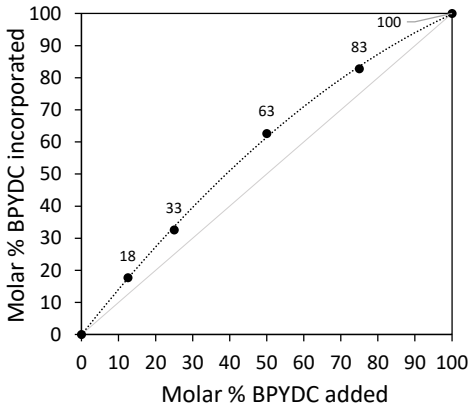

Figure 3-2: The molar percentage of actually incorporated BPYDC linker compared to the molar percentage of BPYDC added during the synthesis of the MOF.

As shown in Figure S3-1, the diffraction patterns of both UiO-67 and the bipyridine MOFs match well with literature[124,125]. When compared to the simulated UiO-67 pattern, the same reflections can be seen for the synthesized UiO-67 and the bipyridine-based isoreticular series. For the samples with 18%, 33%, and 83%, a peak broadening is observed at very low 2θ. These scattering artefacts are generally attributed to MOF morphology and domain size. A possible explanation for this could be clustering and agglomeration of the particles during drying. SEM images of all MOF powders used in membrane preparation are displayed in Figure 3-3. In general, a spherical particle morphology is observed, with strongly varying domain sizes. For UiO-67-33 and UiO-67-83, particle size seems to be larger, probably due to clustering after drying.

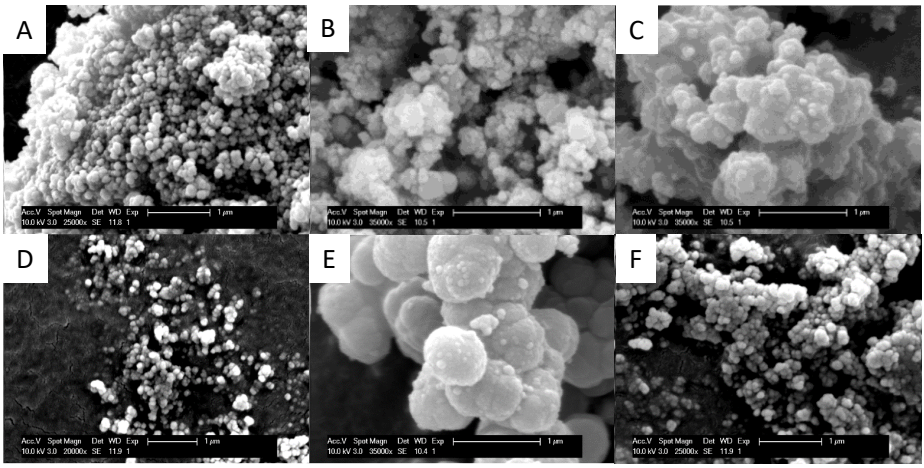

Figure 3-3: SEM images of (A) UiO-67, (B) UiO-67-18, (C) UiO-67-33, (D) UiO-67-63, (E) UiO-67-83 and (F) UiO-67-100.

IR spectra of the as-synthesized MOFs are shown in Figure 3-4. IR bands are visible around 458 cm^{-1} (Zr-μ_3-OH stretching), 671 cm^{-1} (Zr-μ_3-O stretching), 1409 cm^{-1} (C=O stretching) and 1593 cm^{-1} (C=C stretching), matching previous literature[126]. The low frequency of the carbonyl stretching band, usually found around 1750 cm^{-1} for free carbonyls, can be explained by the coordination of the linker -COO^- to high molecular weight Zr atoms. At 1366 cm^{-1}, a peak appears for all BPYDC MOFs, agreeing with C-N/C=N stretching in the aromatic BPYDC linker. This peak has slightly shifted to lower wavenumbers compared to normal imide stretching[127], due to the hybrid character of the C-N bond in the aromatic ring.

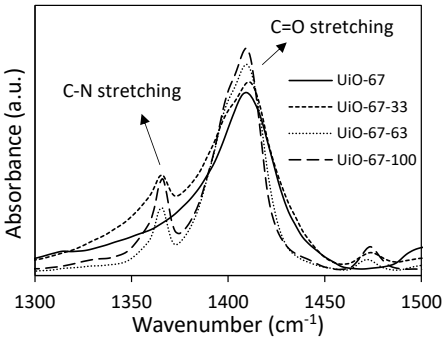

Figure 3-4: ATR-FTIR spectrum of UiO-67, UiO-67-33, UiO-67-63 and UiO-67-100 powders.

As can be seen in Figure 3-5, the CO_2 uptake increased from 40 cm^3/g for UiO-67-33 to 51 cm^3/g for UiO-67-100. In addition, the type II N_2 sorption isotherms indicate a microporous material for all measured MOFs. A higher BET surface area was observed with increasing BPYDC concentration: 1570 m^2/g, 1600 m^2/g, 1800 m^2/g for 33%, 63% and 100% BPYDC, respectively, which are in the same range as described in literature[126,128,129] and comparable to BET values

reported for UiO-66[81] and UiO-67[126]. The 15% gain in specific surface area thus not fully accounts for the steeper rise in CO_2 uptake (25%), indicating that also the CO_2 affinity of the MOF is improved at higher BPYDC concentrations. In accordance with these results, Li *et al.* reported an increased CO_2 storage capacity for UiO-BPYDC compared to traditional UiO-67, owing to the bipyridine sites, which function as CO_2 docking sites[130].

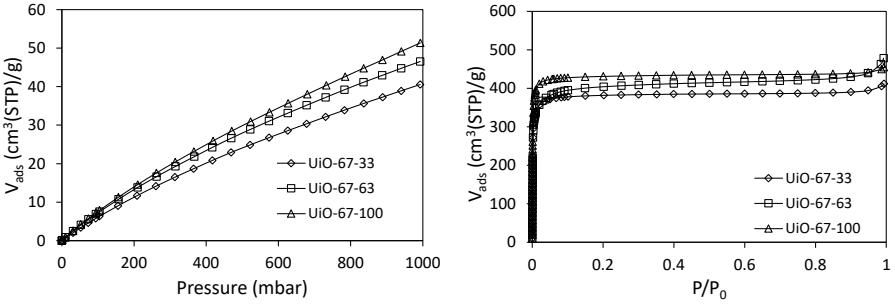

Figure 3-5: CO_2 uptake (left) and N_2 adsorption isotherms (right) of UiO-67 with 33%, 63% and 100% BPYDC.

3.3.2 MMM characterization

Figure 3-6 shows the SEM cross-sections of the MMMs with 10 wt.% MOF loading. Upon MOF addition, the cross-sections seem to transform from relatively smooth for the Matrimid cross-section (A) to a more nodular and interconnected network for MMMs (B-F). This nodular structure arises from interfacial stress between particle and polymer and is, in general, observed when a filler (not only MOF) is introduced in the polymer matrix[37,131]. For all MMMs, good dispersion and homogeneity of UiO-67 particles in the Matrimid matrix can be seen (also Figure S3-2). SEM images of the dried powders suggested that (especially) UiO-67-33 and UiO-67-83 showed more agglomeration than the other MOFs (Figure 3-3). Although a certain degree of clustering can be observed for all MMMs, the difference in agglomeration with the other MOFs seems to be far less pronounced for the MMM samples than it was for the dried powder samples, suggesting that at least part of the clustering can be reversed during preparation of the MMM (i.e. via extensive sonication).

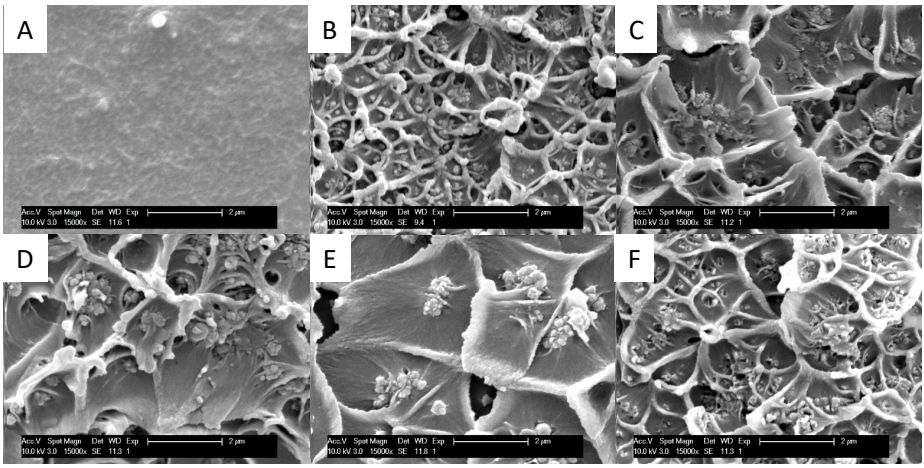

Figure 3-6: SEM cross-sections of (A) Matrimid, (B) MMM with UiO-67, (C) MMM with UiO-67-33, (D) MMM with UiO-67-63, (E) MMM with UiO-67-83, and (F) MMM with UiO-67-100.

IR analyses of the membranes are shown in Figure 3-7. For all membranes, the typical polyimide peaks at 2957 cm^{-1}, 2862 cm^{-1} (both C-H stretch aliphatic), 1777 cm^{-1} (C=O asymmetric stretch), 1715 cm^{-1} (C=O symmetric stretch), 1618 cm^{-1} (C=C stretch) and 1362 cm^{-1} (C-N stretch) were clearly visible[81,127,132]. The MMMs also showed MOF specific peaks at 458 cm^{-1} corresponding to Zr-μ_3-OH stretching, while other typical MOF bands were not visible due to the low concentration of MOF.

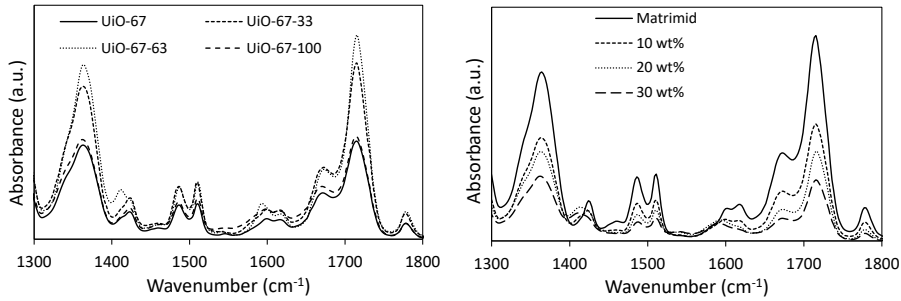

Figure 3-7: ATR-FTIR spectrum of MMMs with 10 wt.% filler (left) and of Matrimid and MMMs with different UiO-67-33 loadings (right).

T_g and decomposition temperature (T_d) of all MMMs with 10 wt.% filler are presented in Table 3-1. A higher T_g can be observed upon addition of filler, indicating more rigid polymer chains near the filler surface and thus proving a good interaction between MOF and polymer[81,133] (Figure S3-3). Furthermore, TGA results suggest that the MMMs showed a high level of thermal stability, similar to the unfilled Matrimid membrane (Figure S3-4).

Table 3-1: Glass transition and degradation temperatures of pristine Matrimid and the UiO-67 MMMs.

	T_g (°C)	T_d (°C)
Pristine Matrimid	315	510
MMM – UiO-67	n.a.	512
MMM – 33% BPYDC	325	513
MMM – 63% BPYDC	322	514
MMM – 83% BPYDC	321	514
MMM – 100% BPYDC	323	513

n.a. = not available

Additionally, PALS was used to investigate the free-volume elements of Matrimid and the MMMs with UiO-67-33 and UiO-67-100. From the lifetime plots, one can directly observe that the intensities of the o-Ps species, which can be related to free-volume characteristics of the membrane (see materials and methods), are very low (Figure 3-8). This is due to the fact that the polymer matrix consists of a polyimide, which is known to strongly inhibit positronium formation[134]. Nevertheless, small differences between the spectra are observed, with the UiO-67-33 MMM showing a slightly higher intensity and a higher apparent background signal (Figure S3-5). This visual observation is backed by the outcome of the multi-exponential fit. For UiO-67-33, 2 o-Ps lifetimes were required to adequately describe the spectra. The short o-Ps lifetime component corresponds to free-volume elements with an average radius of 0.34 nm, while the long o-Ps lifetime could be fixed at 21 ns, corresponding to the large cages of the modified UiO-67 (i.e. radius of 1.05 nm), maintaining a good overall fit variance. For Matrimid and the MMM with UiO-67-100, the spectra could be described by only one o-Ps lifetime, giving rise to a radius of about 0.31 nm for both samples. The cavities in UiO-67-100 were thus not detected, either because of the low amount of filler, or because of the strong inhibition of the polymer matrix. Alternatively, it could be hypothesized that pore collapse may have occurred during PALS measurements under high vacuum (10^{-8} mbar).

Regarding the intensity of the observed o-Ps lifetimes, being the product of the o-Ps formation probability and the concentration of the free-volume elements (Figure 3-8), Matrimid shows the lowest intensity, followed by UiO-67-100, followed by UiO-67-33. Even though one should be careful when correlating intensity with porosity, all the more because the intensities are very low for these samples, the PALS results suggest that the UiO-67-33 MMM has larger and more free-volume elements than the MMM with UiO-67-100 and the reference Matrimid sample. When comparing UiO-67-100 with Matrimid, the intensity for UiO-67-100 is twice as high, which might imply that the latter has a higher concentration of free-volume elements of 0.6 nm diameter. PALS hence suggests that UiO-66-33 has the least dense structure, followed by UiO-66-100, followed by pure Matrimid.

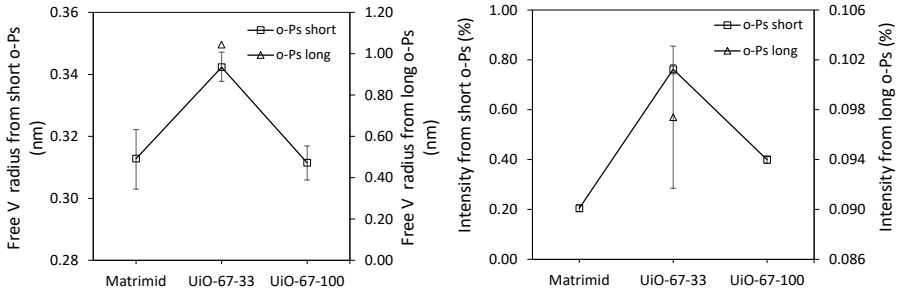

Figure 3-8: Free-volume radius plot (left) and intensity plot (right) of the short and long o-Ps for blanc Matrimid membrane and MMMs with UiO-67-33 and with UiO-67-100.

3.3.3 Gas permeation experiments

The separation factors for Matrimid and the corresponding MMMs are shown in Figure 3-9. The unfilled Matrimid membrane displays a CO_2/CH_4 separation factor of 38, in good agreement with literature[81,133]. Incorporation of UiO-67 leads to an enhancement in separation factor of almost 45%, resulting in a CO_2/CH_4 selectivity of 55. The highest separation factor is registered for UiO-67-33 (75), representing a 37% increase compared to the MMM with UiO-67. Additionally, it is observed that higher BPYDC concentrations in the MOF do not further improve the CO_2/CH_4 separation factor. The strong increase in separation factor for MMMs containing bipyridine UiO-67 can be explained by the improved CO_2 affinity of the BPYDC MOF as confirmed by CO_2 physisorption experiments, which showed an increased amount of CO_2 adsorbed with increasing BPYDC content (Figure 3-5). Furthermore, also polymer rigidification can contribute to the higher separation factor as confirmed by the higher T_g for the MMMs as detected by DSC. All MMMs exhibit an augmented permeability compared to the Matrimid membrane, which can be ascribed to two factors: (1) a higher gas diffusion thanks to the introduction of permanent MOF-pores, and (2) disruption of polymer chain packing by the filler, resulting in enhanced free volume between the polymer chains[135,136]. This was also confirmed by PALS, suggesting a higher concentration of free volume elements for UiO-67-33 MMM > UiO-67-100 MMM > Matrimid. While there is no perceptible trend among the UiO-BPYDC MMMs, the highest permeabilities were measured upon addition of UiO-67 and UiO-67-33 (+69%). MMMs with UiO-67-83 and UiO-67-100 showed a substantially lower permeability, which might point towards (partial) pore collapse of the MOFs. A similar observations was made for UiO-67-100 during PALS measurement, suggesting a lowered stability for MOFs with high bipyridine content. Multiple interactions contribute to the ameliorated CO_2 adsorption properties of the BPYDC functionalized UiO-67. First of all, CO_2 can readily interact with the bipyridine C-N/C=N dipole through its quadrupole[130,137,138]. Moreover, interaction with possibly exposed clusters and aromatic linkers (through favorable π-π interactions with CO_2) might additionally contribute to the selectivity enhancement[139,140]. Further increasing the filler loading to 20 wt.% and 30 wt.% resulted in a decline in separation factor and a substantial improvement in CO_2 permeability, as

shown in Figure S3-6. Typically, this is an indication for the occurrence of non-selective voids at the interface between filler and polymer[141].

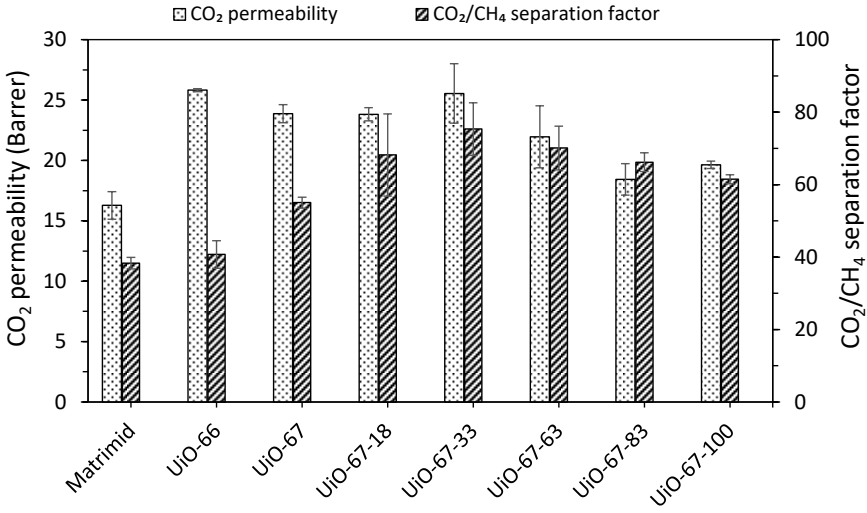

Figure 3-9: Effect of BPYDC percentage in UiO-67 on CO_2 permeability and CO_2/CH_4 separation factor. Gas filtrations were performed at 5 bar feed pressure and 30 °C for a 50v%/50v% feed. For all MMMs, filler loadings were 10 wt.%.

Additionally, pressure dependency experiments were conducted for the pure Matrimid membrane and MMMs with UiO-67-33 and UiO-67-83 (Figure 3-10). CO_2 permeability in the Matrimid membrane and the MMMs decreases with increasing feed pressure, in accordance with the solution-diffusion model[21]. Furthermore, upon increasing the feed pressure from 2 to 5 bar, the separation factor of both the Matrimid membrane and the MMMs with bipyridine MOF remains constant at around 40 and 70-75, respectively. However, at 10 bar feed pressure, the MMMs lose a large portion of their selectivity, while the Matrimid separation factor does not change. XRD patterns of Matrimid with 10 wt.% UiO-67-83 taken before and after filtration at 10 bar (Figure S3-7) display a considerable loss in crystallinity after filtration. This suggests that partial pore collapse at 10 bar might be a reasonable explanation for the loss in selectivity as this would make the bipyridine sites (partly) inaccessible for CO_2. Additionally, the observed permeability and PALS results further support this hypothesis.

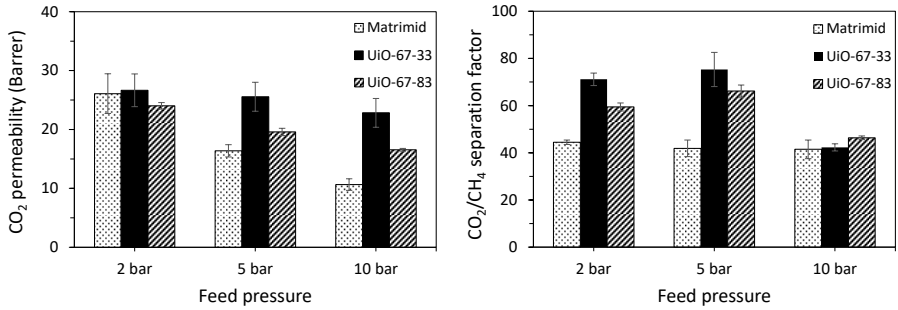

Figure 3-10: Pressure dependency of the CO_2 permeability and CO_2/CH_4 separation factor for the pure Matrimid membrane and MMMs with UiO-67-33 and UiO-67-83. Gas filtrations were performed at 30 °C for a 50v%/50v% feed.

3.3.4 Comparison with state-of-the-art

The prepared membranes were compared to MMMs recently reported in literature, which were tested under similar conditions (Figure 3-11 and Table S3-1). Although the Robeson plot mainly originates from pure gas permeability and ideal selectivity data, plotting mixed-gas data on this graph still allows for a useful comparison and benchmarking. From Figure 3-11, it can be observed that the synthesized MMMs perform well in line with similar membranes in the field and that the distinct improvement in membrane performance upon incorporation of UiO-BPYDC MOFs directs the MMMs past the 2018 mixed-gas upper limit but below the 2008 Robeson upper bound.

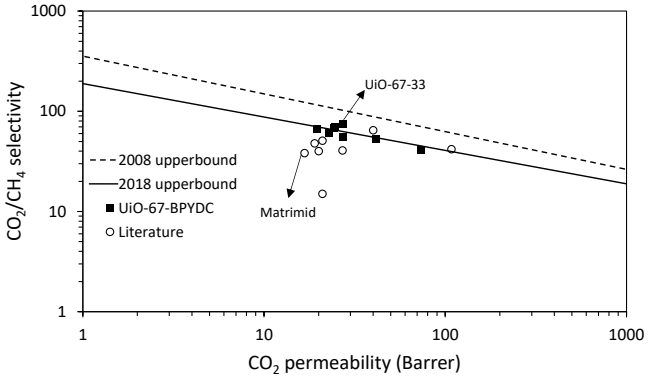

Figure 3-11: Comparison of obtained membrane performance with similar membranes in literature via a Robeson plot.

3.4 Conclusions

UiO-67 and its BPYDC derivatives were for the first time successfully incorporated in Matrimid, resulting in MMMs with good CO_2/CH_4 separation performance. At an optimal BPYDC concentration of 33%, the MOF increased both membrane selectivity (96%) and permeability (63%), compared to the unfilled polyimide membrane. This was attributed to the excellent interaction between CO_2 and the bipyridine N sites, which function as docking sites for CO_2. Increasing the BPYDC concentration in the MOF did not further improve the MMM performance. Although the MMMs at high filler loading (30 wt.%) suffered from interfacial defects between polymer and MOF, reasonable performance was still achieved (equal selectivity and 350% increase in CO_2 permeability). A comparison with similar MMMs in literature pointed out that the improvement in CO_2/CH_4 separation factor is among the highest reported in literature for MMMs with Zr-MOFs. In general, the use of N-heterocyclic ligands proved to be a good strategy for enhancing the membrane CO_2 affinity and thus can be considered as an alternative for standard immobilization of functional groups on MOFs. However, MOF stability issues were observed during filtrations at elevated feed pressure.

3.5 Acknowledgements

R.T. would like to thank Research Foundation-Flanders (FWO) for a SB-PhD fellowship (1S63317N). N.V.V. thanks FWO for a SB-PhD fellowship (1S32917N). J.D. thanks the Agency for Innovation by Science and Technology (IWT Vlaanderen) for funding through an SBO-STW grant (131720). R.V. would like to thank FWO for a SB-PhD fellowship (1S00917N). S.S. is grateful to FWO for funding through an Aspirant grant (1104118N). PALS data were obtained through experiments performed at the NEPOMUC PLEPS instrument operated by FRM-II at the Heinz Maier-Leibnitz Zentrum (MLZ), Garching, Germany.

3.6 Supplementary information to Chapter 3

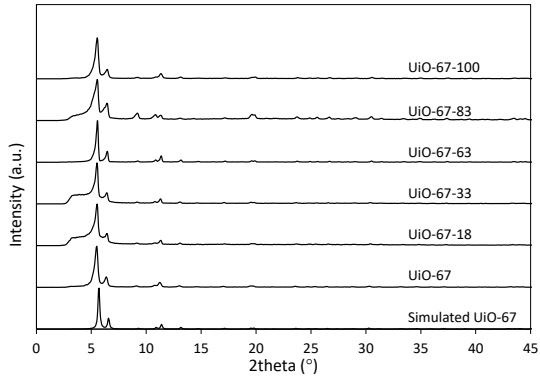

Figure S3-1: XRD patterns of all MOFs.

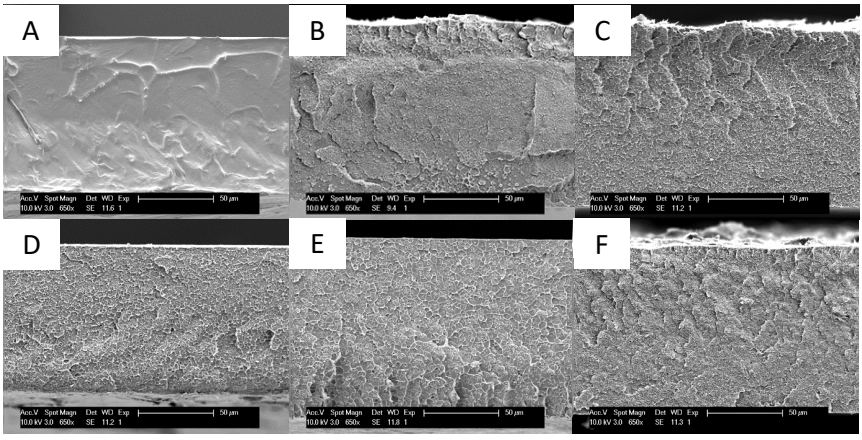

Figure S3-2: SEM cross-sections of (a) Matrimid, (b) MMM with UiO-67, (c) MMM with UiO-67-33, (d) MMM with UiO-67-63, (e) MMM with UiO-67-83, and (f) MMM with UiO-67-100.

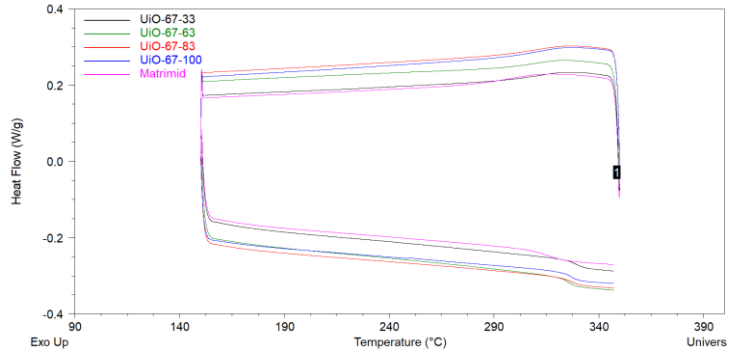

Figure S3-3: DSC measurements of pristine Matrimid and filled Matrimid membranes.

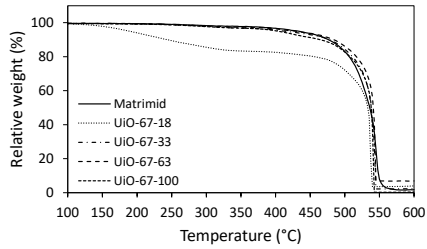

Figure S3-4: TGA traces of all membranes.

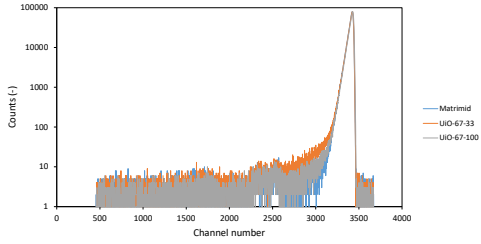

Figure S3-5: Lifetime plot of Matrimid and MMMs with UiO-67-33 and UiO-67-100.

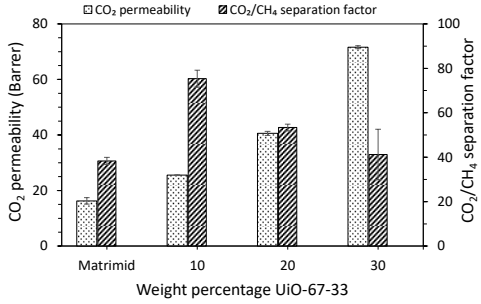

Figure S3-6: Effect of increasing the filler weight percentage on the CO_2 permeability and CO_2/CH_4 separation factor of the UiO-67-33 MMMs. Gas filtrations were performed at 5 bar feed pressure and 30 °C for a 50v%/50v% feed.

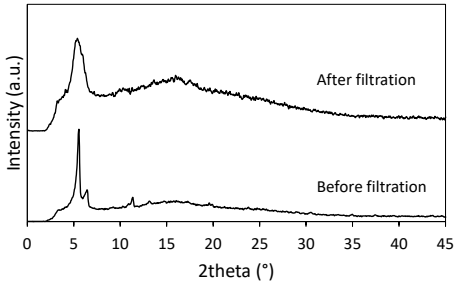

Figure S3-7: XRD spectra of Matrimid with 10 wt.% UiO-67-83 before and after filtration at 10 bar.

Priming protocol

- Dispersion of 0.105 g MOF in $CHCl_3$
- Sonication 60 min
- Addition of 0.105 g Matrimid
- Stirring 30 min
- Sonication 30 min
- Stirring overnight
- Addition of 0.105 g Matrimid
- Stirring 30 min
- Sonication 30 min
- Addition of 0.210 g Matrimid
- Stirring overnight
- Sonication 15 min
- Casting

Table S3-1: Comparison of results with MMMs based on Zr-MOFs reported in literature. $\alpha^*_{CO2/CH4}$ is the separation factor, P_{CO2} the CO_2 permeability in Barrer, $\Delta\alpha^*$ and ΔP the increase in selectivity and permeability, respectively, compared to the pristine polymer membrane.

Polymer	Filler	$\alpha^*_{CO2/CH4}$	$\Delta\alpha^*$	P_{CO2} (Barrer)	ΔP	Reference
Matrimid	UiO-67-33	75	+100%	27	+69%	This work
Matrimid	UiO-66	40	+6%	26	+63%	This work
Matrimid	Modulated UiO-66	48	+50%	19	+440%	[81]
6FDA-ODA	UiO-67	15	-65%	21	+44%	[115]
Matrimid	UiO-66-GO	51	+42%	21	+160%	[107]
Matrimid	ZIF-8	40	+20%	20	+150%	[133]
6FDA-DAM	UiO-66-$COCH_3$	33	+14%	1263	+23%	[142]
6FDA-BisP	UiO-66	42	+52%	108	+217%	[143]
Matrimid	UiO-66-NH_2@ICA	65	+115%	40	+120%	[144]
PIM-1	UiO-66-$(COOH)_2$	11*	-5%	~6000	+20%	[145]

*pure gas permeability

Chapter 4

Modulator-mediated functionalization of MOF-808 as a platform tool to create high-performance mixed-matrix membranes

Raymond Thür, Niels Van Velthoven, Vincent Lemmens, Maarten Bastin, Simon Smolders, Dirk De Vos, Ivo F.J. Vankelecom

*Based on *ACS Appl. Mater. Interfaces 2019, 11, 47, 44792-44801*

Centre for Membrane Separations, Adsorption, Catalysis and Spectroscopy for Sustainable Solutions (cMACS), KU Leuven, Celestijnenlaan 200F, Box 2454, 3001 Heverlee, Belgium

*https://doi.org/10.1021/acsami.9b19774

Abstract

Modulator-mediated functionalization (MoFu) is introduced as a new and versatile platform tool to improve the separation performance of MOF-based membranes, exemplified here by the creation of MMMs with enhanced CO_2 separation efficiency. The unique structure of MOF-808 allows incorporation of CO_2-philic modulators in the MOF framework during a one-pot synthesis procedure in water, thus creating a straightforward way to functionalize both MOF and corresponding MMM. As a proof of concept, a series of fluorinated carboxylic acids (trifluoroacetic acid (TFAA), pentafluoropropionic acid (PFPA) and heptafluorobutyric acid (HFBA)) and non-fluorinated alkyl carboxylic acids (acetic acid (AA), propionic acid (PA) and butyric acid (BA)) were used as modulator during MOF-808 synthesis. In general, crystalline and microporous MOF-808 could be obtained for all modulator types, except for HFBA. The use of fluorinated modulators increased the MOF-808 CO_2 affinity compared to their non-fluorinated counterparts. As a result, the performance of MMMs based on fluorinated MOF-808 improved substantially with two of the best MMMs prepared with 30 wt.% MOF-TFAA and 10 wt.% MOF-PFPA performing very close to the 2008 and 2018 upper bound limits for CO_2/CH_4. Compared to the MMM with MOF-TFAA, an improved solubility selectivity seemed to be at the base of the excellent separation performance of PFPA-based MMM. For the MMM containing MOF-HFBA, it was hypothesized that reduced interfacial compatibility between the MOF and the polymer chains compromised the MMM performance. Due to its facile functionalization (and its subsequent excellent performance), MOF-808 is proposed as an alternative for the widely used UiO-66, which is, from a functionalization point-of-view and despite its widespread use, a rather limited MOF.

Contributions

Raymond Thür: design and coordination of experiments, membrane and MOF preparation, characterization (XRD, ATR-FTIR, TGA, DSC, density measurements), gas permeation experiments, data analysis, manuscript writing and redaction. Niels Van Velthoven: design of experiments, NMR and physisorption data acquisition and analysis, manuscript correction and redaction. Vincent Lemmens: design of experiments, membrane and MOF preparation, characterization, gas permeation experiments, data analysis, manuscript correction and redaction. Maarten Bastin: SEM and TGA data acquisition and analysis, manuscript correction and redaction. Simon Smolders: physisorption data acquisition and analysis, manuscript correction and redaction. Dirk De Vos: manuscript correction and redaction. Ivo F.J. Vankelecom: design of experiments, manuscript correction and redaction.

4.1 Introduction

Combination of the advantages of organic polymers and inorganic fillers has been extensively studied as a means to create more efficient membranes, resulting in the development of MMMs for gas separation applications. The main target here is to move the MMM separation performance towards both high fluxes and high selectivities[55]. Especially for the separation of CO_2 from CH_4, a lot of effort has been dedicated to finding new polymer-filler combinations with enhanced separation performance[35,79,133,146–148]. In this context, MOFs were proposed as a new filler material for MMM preparation about a decade ago[35,38,79,142,149–152]. For example, UiO-66 (and its functionalized derivatives), consisting of hexanuclear $Zr_6O_4(OH)_4$ clusters connected by 12 BDC^{2-} linkers, is one of the most reported fillers in MMM literature to improve membrane permeability[67,81]. It has a good porosity and specific surface area and shows excellent thermal, chemical and mechanical stability, following from the high coordination number of the Zr-oxo cluster[105]. Although UiO-66 definitely has its respective advantages, one can expect from novel MOF materials for MMM applications to not only increase the membrane's permeability but also simultaneously the selectivity. In this sense, UiO-66 faces some serious limitations. As the cluster coordination sphere is theoretically fully occupied by BDC^{2-} linkers, few additional coordination sites are available for introducing functional ligands, besides a limited number of missing-linker defects[153]. Especially with regard to creating functionality inside the MOF framework (to enhance CO_2-philicity), a lot of progress can be realized compared to traditional functionalization methods (e.g. through linker functionalization or grafting) of UiO-66, which often entail the use of expensive organic linkers in addition to potential negative consequences regarding porosity and surface area[81,154]. Bearing this in mind, MOF-808 is here proposed as an alternative to UiO-66 for future MMM development. Almost a decade after the discovery of UiO-66, MOF-808 was first synthesized by the Yaghi group[155] and has been used in e.g. catalysis and gas detection[156–159]. Compared to UiO-66, MOF-808 exhibits a higher surface area and larger pore volume, but at the same time, equally excellent thermal, chemical and mechanical stability[160]. Both UiO-66 and MOF-808 are based on the same $Zr_6O_4(OH)_4$ clusters, respectively linked by ditopic BDC^{2-} and tritopic benzenetricarboxylate (BTC^{3-}) linkers. Whereas the UiO-66 Zr-cluster is theoretically coordinatively saturated with 12 BDC^{2-} linkers, the coordination sites on the Zr-cluster in MOF-808 are occupied by only 6 linker carboxylate groups (three at opposing vertices of the cluster), leaving the 6 remaining equatorial sites available for coordination with modulators or other ligands (Figure 4-1)[153,160]. This unique feature allows to introduce functionalized moieties in the MOF framework by selecting a specific modulator (e.g. trifluoroacetic acid) without having to apply expensive and difficult-to-synthesize functionalized organic linkers.

In this work, MOF-808 is introduced as a new platform MOF for membrane-based CO_2 removal and as a versatile alternative for UiO-66. Advantages of MOF-808 entail easy one-pot synthesis in water[161], low cost components and facile upscaling[161], large pore volume and specific surface area[155], and most importantly, straightforward and cheap functionalization by modulation. To illustrate the principle of functionalization by modulation, trifluoroacetic acid (TFAA) was selected for the role of modulator based on the excellent anticipated affinity between

fluorinated compounds and CO_2[162]. The fluorine content in the MOF pore was then systematically enhanced by using pentafluoropropionic acid (PFPA), heptafluorobutyric acid (HFBA) as modulator. MOF-808 modulated with acetic acid (AA), propionic acid (PA) and butyric acid (BA) were synthesized and applied as reference materials. The fluorinated and reference MOFs were incorporated in Matrimid membranes and tested for their use in membrane-based CO_2/CH_4 separation.

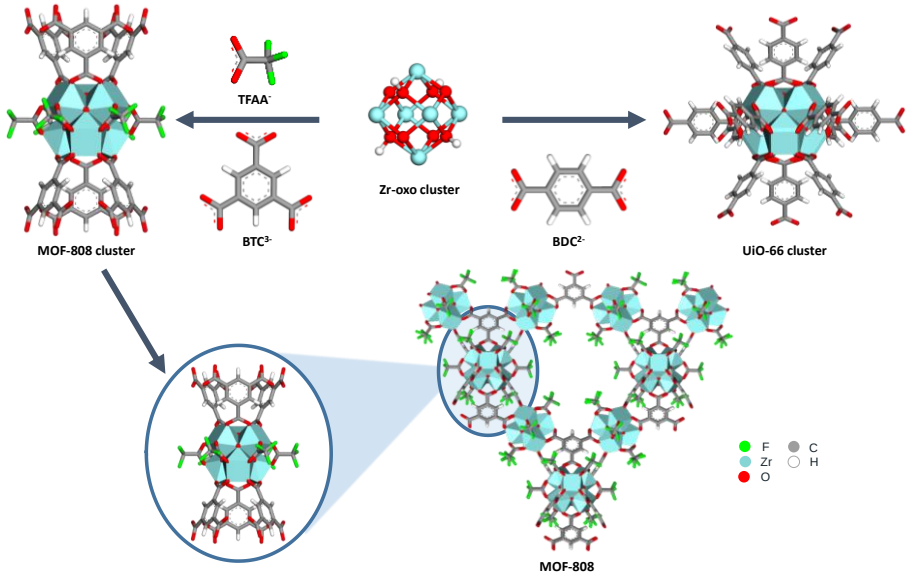

Figure 4-1: Comparison between TFAA modulated MOF-808 cluster and UiO-66 cluster.

4.2 Materials and methods

4.2.1 Chemicals

Polyimide (Matrimid) was kindly provided by Huntsman (Switzerland). THF (>99%) was purchased from Acros. Ethanol (pure) was purchased from Fischer. CO_2 and CH_4 gases were purchased from Air Liquide (Belgium). AA, PA, BA, PFPA, HFBA were supplied by Sigma-Aldrich. TFAA was purchased from Merck-Schuchardt while zirconylchloride octahydrate ($ZrOCl_2.8H_2O$) was supplied by Abcr GmbH. BTC was purchased from J&K Chemicals.

4.2.2 MOF synthesis

MOF-AA, MOF-PA, MOF-BA, MOF-TFAA, MOF-PFPA and MOF-HFBA were synthesized following a recipe described in reference[161] but with variation of the modulator type. First, 0.605 mmol (0.127 g) BTC and 1.815 mmol (0.585 g) $ZrOCl_2.8H_2O$ were added to a 10 mL crimp cap vial. Subsequently, 4.55 mL demi-H_2O and 17.8 mmol modulator (being AA, PA, BA, TFAA, PFPA or HFBA) were added. The mixture was then heated to 100 °C in a heating block with stirring for 24 h. Afterwards, the MOF sludge was washed with water (3 times) and with THF (3 times). After each washing step, the samples were centrifuged. The washed MOF was stored in THF until further use. Different particle sizes for MOF-TFAA were obtained by adding different amounts of solvent during MOF synthesis: 4 mL H_2O for MOF-TFAA-1300, 2 mL H_2O for MOF-TFAA-550, 1 mL H_2O for MOF-TFAA-150.

UiO-66 was prepared by adding 1.82 mmol (0.58 g) $ZrOCl_2.8H_2O$, 1.82 mmol (0.30 g) BDC, 5 mL water and 5 mL acetic acid to a 10 mL crimp cap vial. The mixture was then heated under stirring at 100 °C for 24 h. Afterwards, the MOF sludge was washed with water (3 times) and with THF (3 times). After each washing step, the samples were centrifuged. The washed MOF was stored in THF until further use.

4.2.3 Membrane synthesis

4.2.3.1 Preparation of pristine Matrimid membranes

0.42 g of Matrimid was dissolved in THF (5.58 g). The polymer solution was then stirred overnight and poured by hand into a Teflon Petri dish (diameter 6 cm) under N_2 atmosphere at room temperature. A plastic funnel was placed on top to slow down the solvent evaporation rate. When the solid membrane film was formed, it was annealed in a muffle oven according to the following temperature profile: heating to 110 °C at 5 °C/min, 2 h at 110 °C, heating to 180 °C at 5 °C/min and 6 h at 180 °C.

4.2.3.2 Preparation of MMMs

Since a wet synthesis method was applied[96], the MOF quantity was determined by using a calibration curve. 1, 2 and 3 mL of the MOF in THF suspension were transferred with a pipette to glass beakers and dried overnight at 100 °C. The used volume of MOF suspension was then correlated with the actual MOF mass. Using the calibration curve, the desired amount of wet MOF (in THF) was determined and further diluted with 5.58 g THF. After stirring and sonication,

0.42 g polymer was added in three portions according to a priming protocol[154]. Before polymer addition, the polymer/MOF suspensions were sonicated for 30 min and continuously stirred. Prior to casting, the suspensions were again sonicated. Casting and annealing of the MMM films occurred according to the same procedure as for the unfilled membranes. Filler loading was determined with the following equation:

$$filler\ loading\ (wt.\%) = 100 \times \left(\frac{m_{filler}}{m_{filler} + m_{polymer}}\right) \quad (4.1)$$

4.2.4 Characterization

4.2.4.1 XRD

Powder XRD of MOFs and membranes were recorded on a Malvern PANalytical Empyrean diffractometer in transmission mode over a 1.3-45° 2θ range, using a PIXcel3D solid state detector and Cu anode (Cu Kα1: 1.5406 Å; Cu Kα2: 1.5444 Å).

4.2.4.2 SEM

Membrane cross-sections and MOF particle morphologies were studied with SEM (Philips XL30 FEG). Membrane cross-sections were prepared by breaking the membranes in liquid nitrogen and a gold/palladium coating was applied on all samples before measurement.

4.2.4.3 TGA

TGA (TA instruments TGA Q500) was performed to study the thermal degradation of membranes and MOF when heated to high temperatures. Both membrane and MOF samples were heated in presence of O_2 at a heating rate of 5 °C/min.

4.2.4.4 ATR-FTIR

A Bruker Alpha instrument equipped with a diamond ATR crystal was used to perform ATR-FTIR and to study chemical changes and functional groups in membranes and MOFs. 32 scans were collected at a resolution of 4 cm^{-1}.

4.2.4.5 DSC

DSC (TA instruments DSC Q2000) experiments were conducted on the polymer membranes and MMMs. Membranes were first heated to 375 °C to erase the thermal history of the polymer. This was followed by the measurement cycle, which comprised of cooling down to 275 °C and reheating to 375 °C. The membrane samples were heated up and cooled down under nitrogen atmosphere at 10 °C min^{-1}. TA Universal Analysis was used for data analysis.

4.2.4.6 N_2 and CO_2 physisorption

A Micromeritics 3Flex surface analyzer was used for gas sorption experiments. Experiments were conducted at -196 °C (liquid N_2). Before measuring, all MOFs were activated under vacuum at 100 °C for 16 h. Surface areas were calculated via the multi-point BET method applied to the isotherm adsorption branch, taking into account surface area criteria as given by Rouquerol[117] and the consistency criteria described by Walton and Snurr[118].

4.2.4.7 NMR

^{1}H and ^{19}F liquid phase NMR were performed on MOF samples. For ^{1}H NMR, 600 µL deuterated dimethylsulfoxide was used to dissolve 3 mg MOF-808 by addition of 40 µL of a 40 wt.% hydrofluoric acid solution. The samples for ^{19}F NMR were prepared in a similar way with the addition of 10 µL fluorobenzene as internal standard. A recycle delay time (d1) of 30 s was used for ^{19}F NMR. The spectra were recorded on a Bruker AMX-300 spectrometer at 300 MHz (for ^{1}H NMR) and at 400 MHz (for ^{19}F NMR) (16 scans) and analyzed using SpinWorks 4.2 software.

4.2.4.8 Density measurements

Density measurements were carried out on all membranes. The buoyancy method was applied to determine the experimental density with help of a Sartorius YDK 01 Density Determination Kit. Water was selected as the buoyancy liquid. The weight of the membrane sample was first measured in air and then in water. The resulting values were used in Equation 4.2:

$$\rho = \frac{W(a)}{0.99983} \times \left[\frac{\rho(fl) - 0.0012\ g/cm^3}{W(a) - W(fl)}\right] + 0.0012\ g/cm^3 \quad (4.2)$$

with W(a) and W(fl), the weight of the sample in air and water, respectively. The density of water, ρ(fl), is taken to be 0.99821 g/cm^3 at 20.1 °C while the density of air is 0.0012 g/cm^3. 0.99983 is a correction factor for the buoyancy of the set-up wires.

4.2.4.9 Membrane gas sorption

High pressure sorption of N_2 and CO_2 was measured at 30 °C up to pressures of 25 bar for MMM-TFAA and MMM-PFPA membranes. The measurements were performed on a Rubotherm series IsoSORP© instrument. The membrane weight and volume were calculated by performing helium pycnometry on all membranes. The additional weight due to sorption of the selected gas in the membrane over time was measured with a magnetically suspended balance. The weight was corrected for the buoyancy of the measurement gases (Equation 4.3):

$$m_{corrected} = m_{measured} + \rho_{gas} \times V_{sample} \quad (4.3)$$

with $m_{corrected}$ the corrected weight (g), $m_{measured}$ the measured weight (g), ρ_{gas} the measuring gas density (g/cm^3) and V_{sample} the sample volume (cm^3).

The N_2 and CO_2 solubility in the membranes can be calculated with Equation 4.4:

$$S = \frac{C}{p} \quad (4.4)$$

with S the gas solubility (cm^3(STP)/cm^{3}cmHg), C the quantity of adsorbed gas (cm^3(STP)/cm^3) and p the pressure (cmHg).

4.2.4.10 Gas permeation

Membrane performance characteristics (permeability and separation factor) were determined in our in-house developed HTGS set-up[47,123]. Membrane coupons had a permeation area of 1.91 cm^2. A constant-volume varying-pressure method was used to measure gas permeability. The membrane permeate is accumulated in an auxiliary cylinder of 75 cm^3. A vacuum sensor is then

used to measure the increase in pressure as a function of time (dp/dt). Gas permeability (P) of the membrane is calculated via:

$$P_i = 10^{10} \times \frac{y_i \times V \times V_m \times L}{x_i \times p_{up} \times A \times R \times T} \times \frac{dp}{dt} \quad (4.5)$$

with P_i the gas permeability (Barrer), y_i the mole fraction of the component in the permeate, x_i the mole fraction of the component in the feed, V the downstream volume (cm^3), V_m the molar volume (L/mol), A the membrane permeation area (1.91 cm^2), L the membrane thickness (µm), T the operating temperature (K), p_{up} the upstream pressure (bar), R the gas constant (0.082 L atm/mol K) and dp/dt the pressure increase (Torr/s).

Mixed-gas separation factors $\alpha^*_{i/j}$ were determined as the ratio of the downstream (y) and upstream (x) mole fraction of the two gases by the following equation:

$$\alpha^*_{i/j} = \frac{y_i / y_j}{x_i / x_j} \quad (4.6)$$

with y_i and y_j the mole fractions of i and j in the permeate, x_i and x_j the mole fractions of i and j in the feed. During gas chromatography analysis, y_i/y_j is determined from peak areas linked to mole fractions in the permeate, while x_i/x_j is determined by the feed settings.

4.3 Results and discussion

4.3.1 Modulator-mediated functionalization: fluorinated MOF-808

4.3.1.1 Characterization of MOFs and membranes

As mentioned before, the unsaturated coordination sphere of the Zr-oxo cluster of MOF-808 allows to introduce functionalized modulator molecules. In this way, modulation of MOF-808 can be used as a versatile approach towards creating MOFs with a high CO_2 preference over other gases, such as N_2 and CH_4. With this concept of "modulator-mediated functionalization" (MoFu) in mind and knowing that CO_2 shows excellent quadrupole-dipole interaction with polarized C-F bonds, TFAA modulated MOF-808 samples with different particle sizes (ranging on average from 150 nm to 1300 nm) were synthesized and incorporated in Matrimid membranes. The different MOF samples are denoted as MOF-TFAA-*x* and the corresponding Matrimid MMMs as MMM-TFAA-*x*, with *x* being the average particle size in nm.

XRD data show that highly crystalline MOF-808 particles can be made by using TFAA as modulator and that there is a good agreement with the simulated XRD pattern of MOF-808 (Figure 4-2 and Figure S4-1). Furthermore, ATR-FTIR confirmed the appearance of an intense doublet signal at ~1170 and ~1205 cm^{-1}, indicating the presence of symmetrical and anti-symmetrical C-F stretching vibrations[163].

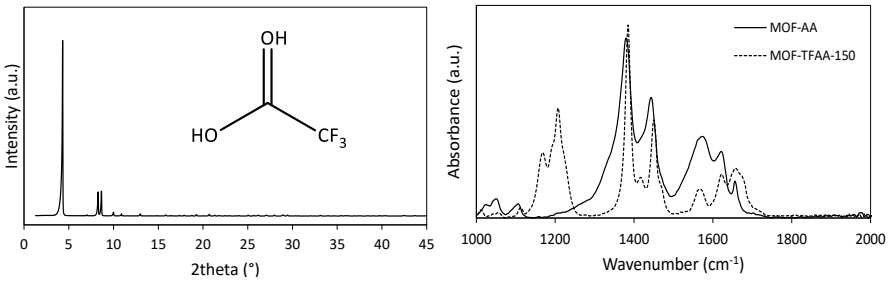

Figure 4-2: XRD pattern (left) and ATR-FTIR spectrum (right) of MOF-TFAA-150. The IR spectrum for MOF-TFAA-150 is compared to that of AA modulated MOF-808 (MOF-AA).

Octahedral MOF crystals were successfully synthesized with particle sizes ranging from 150 to 1300 nm (Figure 4-3). Visual analysis of the SEM images of the different sized MOFs with ImageJ resulted in size distribution plots given in Figure S4-2. Relatively homogeneous size distributions were obtained for MOF-TFAA-150 and MOF-TFAA-550 while synthesis of MOF-TFAA-1300 was found to result in particles with a higher polydispersity. For the 150 nm and 550 nm particles, low solvent concentrations caused a highly concentrated synthesis mixture, which quickly formed a homogeneous gel[164]. This hindered the supply of fresh reactants to the MOF nuclei, slowing down the crystal growth rate relative to the nucleation rate and resulting in small, homogeneous particles. In more diluted reaction mixtures such as those used for MOF-TFAA-1300, reactant diffusion was not impeded and the crystal growth rate overcame the nucleation rate[165]. Furthermore, N_2 physisorption showed a decreased BET surface area and pore volume upon switching from AA to TFAA (Table 4-1 and Figure S4-3), following from a higher number of

modulator molecules on the cluster in the MOF-TFAA sample (Table 4-2). Despite a loss of 32% in pore volume, the TFAA modulated MOF exhibited an almost equal CO_2 uptake compared to that of MOF-AA (Figure S4-3). In addition, the steeper initial slope of the CO_2 sorption isotherm confirms that the use of fluorinated modulator enhances the CO_2 affinity of the MOF since the isotherm slope in the low-pressure region is believed to correlate primarily with the MOF-CO_2 interaction strength rather than pore volume or BET[166,167]. Deria *et al.* attributed similar behavior in fluorinated NU-1000 to a synergistic effect of the C-F bond and defects on the cluster, which contribute to the formation of a polarized environment[162].

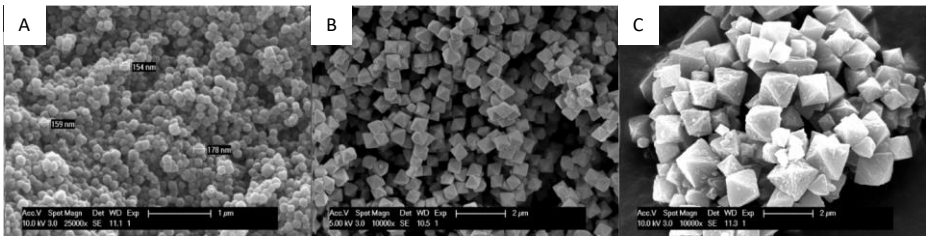

Figure 4-3: SEM images of (A) MOF-TFAA-150, (B) MOF-TFAA-550 and (C) MOF-TFAA-1300.

After MOF synthesis, MMMs with the differently sized MOFs were prepared. Table S4-1 shows a thermal stability for all membranes in the same range as that of the unfilled membrane. A slight decline in thermal stability can be observed for MMMs with increasing particle size. DSC shows an elevated T_g for all MMMs compared to pristine Matrimid after incorporation of 10 wt.% MOF, which can be explained by reduced polymer chain mobility due to presence of the MOF particles and thus a certain extent of polymer rigidification[37]. Furthermore, SEM cross-sections (Figure S4-5) suggest a good incorporation of the particles without evidence for sieve-in-a-cage morphology or severe particle clustering. MMM-TFAA-1300 shows a less uniform incorporation of the fillers, probably due to size effects.

Table 4-1: Comparison of MOF-AA and MOF-TFAA-550 with regard to BET surface area, pore volume and CO_2 uptake.

	BET surface area (m^2/g)	Pore volume (cm^3/g)	CO_2 uptake (cm^3/g)
MOF-AA	1982	0.65	49.2
MOF-TFAA	1239	0.49	46.0

4.3.1.2 Gas permeation experiments

Gas permeation experiments (Figure 4-4) show that incorporation of MOF-TFAA-150 increases the membrane separation factor with 93% from 40 (Matrimid) to 77, while the CO_2 permeability is almost doubled due to MOF incorporation[168]. Figure 4-4 clearly shows that the fluorinated MMM reaches higher CO_2/CH_4 separation factors and similar CO_2 permeabilities when compared to MMM-AA. Electrostatic dipole-quadrupole interactions between C-F and CO_2 lay at the base of this excellent performance as the C-F bond is intensely polarized due to the large difference in electronegativity between C and F[169]. This results in an enhanced CO_2 affinity of

the fluorinated MOF as confirmed by CO_2 physisorption data (Table 4-1). Fried *et al.* reported with help of molecular orbital calculations a maximum quadrupole-dipole interaction energy of -11.5 kJ/mol between CO_2 and $CF_3CH_2CH_3$, situating the quadrupole-dipole interaction strength between London dispersion and hydrogen bonding[170]. Furthermore, it is observed that with decreasing particle size, the MMMs display a small improvement of the separation factor combined with a minor increase in permeability. The lower separation factor of MMM-TFAA-1300 can be explained by a less successful incorporation of the large MOF particles in the polymer matrix (as shown by SEM). In contrast with our findings, a constant or a decreasing separation factor with decreasing ZIF-71 particle size was observed by Japip *et al.*[141] while a worse performance was found for smaller ZIF-8 particles by Sánchez-Lainez *et al.* The latter was attributed to a higher degree of clustering when using particles below 150 nm[94]. In our case however, particle clustering is largely avoided by using a MMM synthesis method that avoids drying (and thus clustering) of the MOF particles.

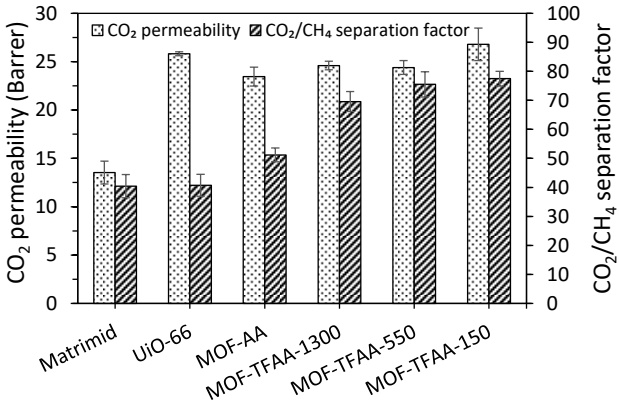

Figure 4-4: CO_2/CH_4 separation factor and CO_2 permeability of Matrimid and MMMs with different sizes of MOF-TFAA. Gas filtrations were performed at 30 °C, 5 bar feed pressure and 50v%/50v% CO_2/CH_4 feed.

When the MOF-TFAA loading is increased, no statistical difference in CO_2/CH_4 separation factor can be observed between the MMMs with varying MOF loading while a substantial gain in CO_2 permeability is observed (Figure 4-5). Based on the rise in separation factor for 10 wt.% MMMs, one could expect a similar improvement for 20 and 30 wt.% MMMs. However, gas separation data show that the separation factor only slightly increases for 30 wt.% and even slightly decreases for 20 wt.%. Nevertheless, due to overlapping standard deviations, the separation factor for all three loadings has to be considered statistically constant, hence suggesting to a certain extent the presence of interfacial defects at higher MOF loading, which would allow unselective gas flow past the MOFs. This could also explain the extremely steep enhancement in CO_2 permeability for the MMMs with 30 wt.% MOF. SEM cross-sections of 20 and 30 wt.% MMMs support this hypothesis as particle aggregation can be observed at higher loadings, resulting in a higher probability of interfacial defects (Figure S4-6).

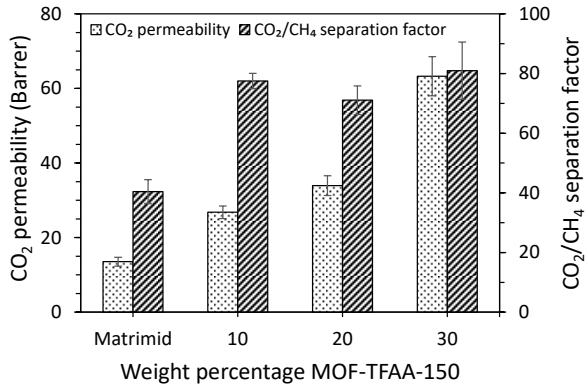

Figure 4-5: Effect of increasing the loading of MOF-TFAA-150. Gas filtrations were performed at 30 °C, 5 bar feed pressure and 50v%/50v% CO_2/CH_4 feed.

Varying the feed pressure (Figure 4-6) predominantly impacts the CO_2 permeability, whereas CO_2/CH_4 separation factor remains largely unaffected for both the unfilled and the 10 wt.% MOF-TFAA loaded membrane. By increasing the feed pressure, the permeability of the reference membranes and the MMM steadily drops. This can be considered as typical solution-diffusion behavior since the dual-sorption model predicts a decreased gas solubility in the membrane with increasing pressure and thus, as a consequence, a lowered gas permeability[21,171]. While the separation factor of the MMMs is relatively stable over the entire pressure range (with exception of the MMM separation factor at 10 bar, probably an experimental outlier), the Matrimid membrane loses a substantial part of its separation factor at 15 bar. As the plasticization pressure of Matrimid is believed to be at around 7-8 bar CO_2 partial pressure[37], this loss in separation factor probably originates from starting plasticization although not yet visible in the permeability result.

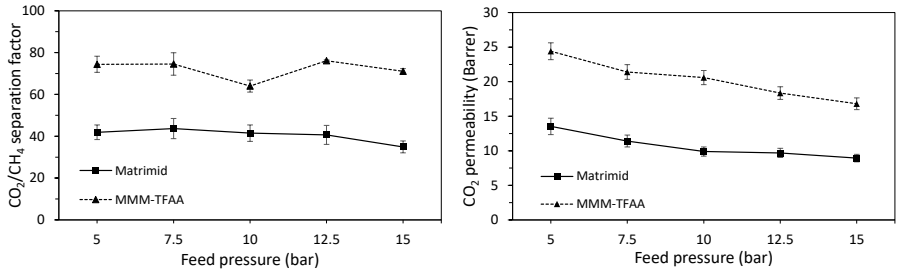

Figure 4-6: Pressure dependency tests for Matrimid membranes and MMMs with 10 wt.% MOF-TFAA. Gas filtrations were performed at 30 °C and 50v%/50v% CO_2/CH_4 feed.

4.3.2 Increasing the fluorine concentration inside MOF-808

4.3.2.1 Characterization of MOFs and membranes

As the incorporation of a fluorinated modulator (TFAA) in the first part of this work strongly improved the membrane performance, it was hypothesized that an additional rise in fluorine

content might even further enhance the CO_2 separation efficiency of the membrane. Therefore, a series of fluorinated alkyl carboxylic acids were applied as MOF modulators for better CO_2-philicity of the resulting MMMs. Their non-fluorinated analogues were also used as reference materials. A MOF prepared with modulator *x* is simply denoted as MOF-*x*, while the corresponding MMM is named MMM-*x*. For example, Matrimid with MOF-AA will be denoted as MMM-AA.

Figure 4-7 displays the SEM images and XRD patterns of MOF-808 modulated with AA, PA and BA. All MOFs are highly crystalline and correspond well with the simulated diffractogram of MOF-808. Additionally, SEM images show that the average particle size of the synthesized MOFs decreases with increasing length of the alkyl chain: 850 nm for AA, 650 nm for PA and <100 nm for BA. A decline in particle size with increasing size of the modulator was also observed by Zhan *et al.* for their Zr-fumarate MOF[172].

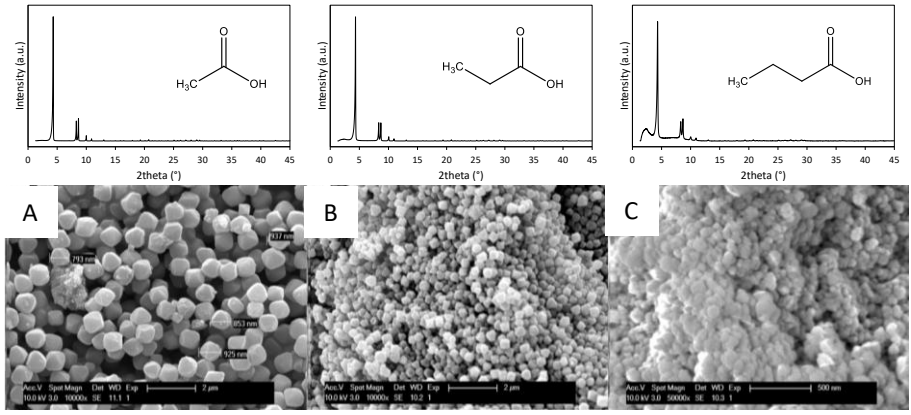

Figure 4-7: XRD patterns (top) and SEM images (bottom) of (A) MOF-AA, (B) MOF-PA, (C) MOF-BA.

Likewise, XRD and SEM data of the perfluoro-compounds are presented in Figure 4-8. Whereas the use of TFAA and PFPA still results in highly crystalline particles, modulation with HFBA creates a MOF with lower crystallinity. Although the XRD pattern still corresponds with that of MOF-808, significant peak broadening is observed, which is a strong indication for the presence of extremely small particles. Calculations based on the Debye-Scherrer equation indicate a crystallite size of ~15 nm. Therefore, it is hypothesized that the hydrophobic HFBA tails repulse the aqueous synthesis medium during MOF nucleation and growth, preventing connection and further growth of first-stage MOF clusters.

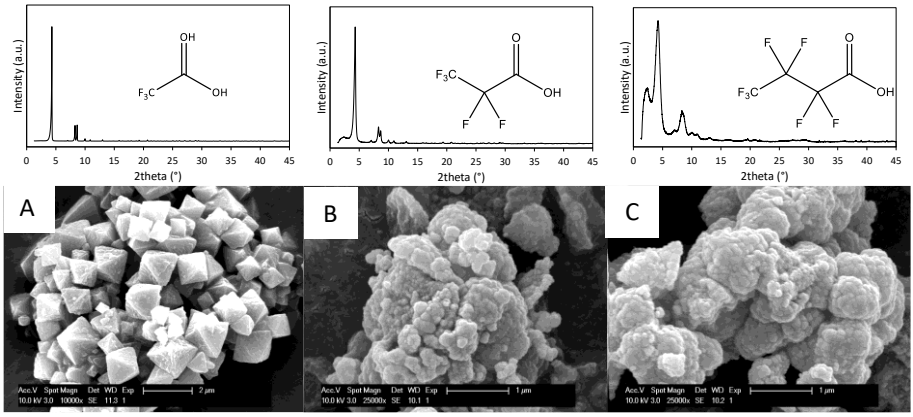

Figure 4-8: XRD patterns (top) and SEM images (bottom) of (A) MOF-TFAA, (B) MOF-PFPA, (C) MOF-HFBA.

NMR shows that AA, PA and BA modulated MOF-808 contained respectively 3.8, 3.2 and 3.9 modulator molecules per Zr-cluster while 4.9 TFAA, 4.2 PFPA and 3.9 HFBA molecules were on average incorporated per cluster for the fluorinated MOFs (Table 4-2). To validate the obtained NMR results, TGA data were taken for MOF-TFAA, MOF-PFPA and MOF-HFBA (Figure S4-7). Although less accurate than NMR, thermogravimetric analysis suggests approximatively 3.6, 3.4 and 2.9 molecules of TFAA, PFPA and HFBA, respectively, per Zr-cluster and thus confirms the trend obtained by NMR[102]. IR analysis further confirmed the presence of fluorine groups inside the different MOFs. For TFAA, PFPA and HFBA modulated MOF, typical C-F stretching and bending vibrations are seen in Figure S4-8. Peaks at 1170 cm^{-1} and 1215 cm^{-1} belong respectively to symmetric and asymmetric stretching of $-CF_3$ groups. $-CF_2$ stretching becomes visible at 1040 cm^{-1} in the PFPA spectrum. Furthermore, MOF-HFBA shows two extra peaks at 1090 and 1125 cm^{-1}, which Crowder *et al.* attributed to C-F vibrations of CF_2[173].

Finally, a reduction in specific surface area of both the non-fluorinated and the fluorinated series with increasing alkyl chain length is observed: 1982 m^2/g (MOF-AA), 1468 m^2/g (MOF-PA) and 739 m^2/g (MOF-BA) for the regular MOFs and 1239 m^2/g (MOF-TFAA), 1089 m^2/g (MOF-PFPA) and 622 m^2/g (MOF-HFBA) for the fluorinated MOFs (Figure S4-9). A similar trend was perceived when functionalizing NU-1000 using perfluoroalkane ligands with varying chain length[162]. Moreover, the lower values for the fluorinated MOFs can be attributed to a higher modulator occupation of the cluster. The MOF pore diameters are well in agreement with literature[155] (Figure S4-10 and Figure S4-11). The small cage with pore diameter of 5-6 Å remains unchanged by varying the modulator while the average pore diameter of the large, adamantine cage gradually decreases with increasing the modulator size for both fluorinated and standard modulators (Table 4-2). As mentioned above, modulation with TFAA instead of AA had a substantial, positive effect on the CO_2 affinity of the MOF, although not reflected in a higher absolute CO_2 uptake. A similar observation is made for MOF-PFPA, which displays a 33% lower pore volume but a 6% increase in CO_2 uptake with respect to MOF-PA. Compared to MOF-TFAA, a comparable decrease in pore volume (23%) and CO_2 uptake (21%) is noticed for MOF-PFPA. Furthermore, an enhancement in T_g of roughly 10 °C was detected by DSC measurements

(Figure S4-13 and Figure S4-14) for all MMMs, indicating a reduced polymer chain mobility. Although a minor reduction in T_g is observed for both the fluorinated and non-fluorinated series with smaller MOF particles, the particle size does not seem to have a large effect on polymer rigidity. Table S4-2 shows that the density of the pristine Matrimid membrane was 1.23 g/cm^3, which is in good agreement with literature[37]. Upon MOF incorporation, the density of the MMMs (with exception of MMM-HFBA) increased slightly compared to that of pure Matrimid[41,174,175]. A notable rise in specific volume was observed for MMM-HFBA (Figure S4-15) compared to the other MMMs. SEM images indicate that TFAA and PFPA modulated MOF are well embedded in the polymer matrix (Figure S4-16) while the SEM cross-sections of MMM-HFBA show a rather irregular MOF incorporation (Figure S4-17).

Table 4-2: BET surface area, pore volume, average pore size, average number of modulator molecules per Zr_6 cluster (as determined by NMR). T_g of the corresponding 10 wt.% Matrimid MMM is given as well. Adsorption isotherms for N_2 and CO_2 are found in SI.

	BET surface area (m^2/g)	CO_2 uptake (cm^3/g)	Pore volume (cm^3/g)	Pore size (Å)	Modulators per Zr_6 cluster	T_g of corresponding MMM (°C)
MOF-AA	1982	49.8	0.65	18.4	3.8	326
MOF-PA	1468	35.7	0.53	16.7	3.2	325
MOF-BA	739	-	0.27	15.6	3.9	325
MOF-TFAA	1239	46.0	0.49	18.4	4.9	326
MOF-PFPA	1089	37.8	0.40	16.7	4.2	324
MOF-HFBA	622	-	0.21	13.8	3.9	324

4.3.2.2 Gas permeation experiments

Figure 4-9 demonstrates that, for the series of MOF modulated with alkyl carboxylic acids, CO_2/CH_4 separation factor was found to be relatively constant with increasing modulator chain length, ranging from 41 (for PA) till 51 (for AA). Both AA and BA MOFs caused a similar gain in permeability of roughly 60%, while PA modulation led to only a minor increase. The use of fluorinated MOFs boosted the MMM performance (both separation factor and CO_2 permeability): the MMM containing TFAA modulated MOF-808 denotes a 50% higher separation factor and comparable CO_2 permeability with respect to MOF-AA and an optimal separation factor of 97 is observed for MOF-PFPA combined with a CO_2 permeability of 29 Barrer. CO_2 physisorption data demonstrated that the fluorinated modulator improved the CO_2 affinity of the MOF (Table 4-1 and Table 4-2). Furthermore, N_2 physisorption showed that the pore size gradually decreases with increasing modulator chain length. For HFBA and BA modulated MOF, the pore size still remains 13.8 and 15.8 Å, respectively, which largely excludes the possibility of size sieving by the MOF, considering the kinetic diameters of CO_2 (3.3 Å) and CH_4 (3.8 Å)[9]. Additionally, DSC revealed an increased T_g for all MMMs and thus a certain degree of polymer rigidification at the polymer-particle interface (Table 4-2). This may contribute to an enhanced separation factor but a similar degree of polymer rigidification should be assumed for incorporation of all MOFs as no notable differences in T_g were observed between the individual samples. It is not completely clear why MOF-PFPA shows such a substantial increase in separation factor compared to MOF-TFAA. N_2 and CO_2 adsorption experiments on the MOF

predicted no large difference in CO_2 affinity between both MOFs (Table 4-2). Membrane sorption experiments also showed very similar CO_2 adsorption for MMM-TFAA and MMM-PFPA at 5 bar but a lower N_2 sorption for MMM-PFPA. Consequently, MMM-PFPA denotes a higher CO_2/N_2 solubility selectivity than MOF-TFAA (S_{CO2}/S_{N2} = 12.9 vs 10.6) (Figure S4-18). The incorporation of a longer fluorinated modulator chain thus seems to exclude N_2 rather than cause more CO_2 adsorption. Even though no sorption measurements could be performed for CH_4, it is anticipated that similar sorption can be expected for CH_4[11]. Possibly, this effect becomes more pronounced in mixed-gas conditions since mixed-gas conditions may lead to competitive sorption of CO_2 over CH_4. An additional factor which might contribute to the observed separation behavior is the fact that the longer PFPA chains create a more confined pore environment and thus increase the polarization effect perceived by the gas molecules during permeation[176]. Finally, a substantial decrease in separation factor is observed when MOF-HFBA is used, possibly caused by interfacial defects (as suggested by SEM and density measurements), which may arise from low compatibility between the highly fluorinated MOF and the non-fluorinated polymer. The strongly augmented permeability (higher than expected) for MMM-HFBA further adds to this hypothesis of existing molecular voids between polymer and filler. This is also visible in Figure S4-19, which shows the change in membrane morphology and structure upon incorporation of HFBA modulated MOF.

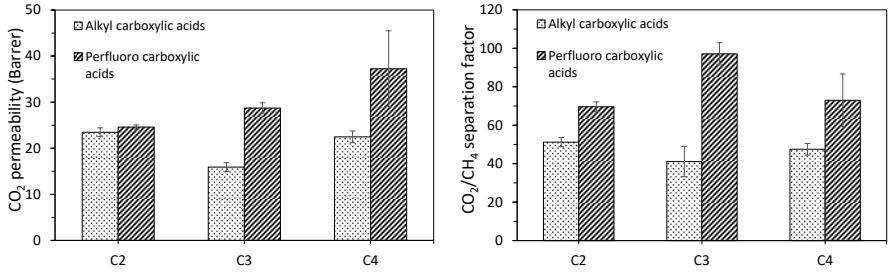

Figure 4-9: Left: CO_2/CH_4 separation factor comparison between MMMs made with MOF modulated by alkyl carboxylic acids (black, square) and by perfluoro carboxylic acids (orange, circles). Right: CO_2 permeability of Matrimid and MMMs. Gas filtrations were performed at 30 °C, 5 bar feed pressure and 50v%/50v% CO_2/CH_4 feed.

4.3.3 Comparison with state-of-the-art

In Figure 4-10 and Table S4-3, the MMMs obtained in this study are compared to literature and the upper bounds determined by Robeson in 2008[55] and by Wang in 2018[61]. All MMMs containing MOFs modulated by fluorinated carboxylic acids cross the mixed-gas upper bound, while MMMs based on MOF-AA, MOF-PA and MOF-BA all fall under this limit. The 30 wt.% MMM-TFAA and 10 wt.% MMM-PFPA MMMs even cross the 2008 Robeson upper bound with their performance. This is especially remarkable when considering that the starting material, Matrimid, is only a moderately performing polymer with a separation factor-permeability combination far below both upper bounds. When comparing to literature (Table S4-3), it can be concluded that MMMs based on regular MOF-808 show similar or improved performance

compared to UiO-66 based MMMs, while Matrimid MMMs with fluorinated MOF-808 clearly outperform these UiO-66 MMMs.

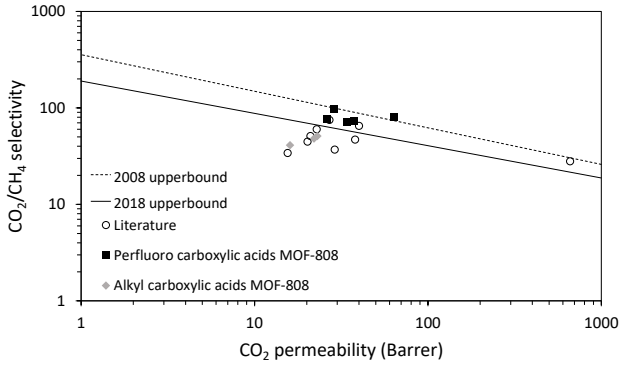

Figure 4-10: Comparison of prepared MMMs with literature in a selectivity-permeability plot.

4.4 Conclusions

MOF-808 holds promise as a highly versatile MOF for MMM design due to its low preparation cost, excellent intrinsic features (stability, porosity, specific surface) and, most importantly, simple functionalization. MOF-808 can be very easily tuned in terms of particle morphology and inner and outer surface functionalities by playing with MOF synthesis parameters and (cheap) modulator types. Furthermore, the MOF can be prepared in water, excluding the use of toxic organic solvents (e.g. DMF) traditionally used in MOF synthesis. "Modulator-Mediated Functionalization" (MoFu) is a novel and straightforward tool to tune the separation potential of MOFs, exemplified here for the CO_2-philicity of MOF-808. In a first section, the use of a fluorinated modulator (TFAA) instead of AA increased the MOF CO_2 affinity, resulting in a substantially better membrane performance of MOF-TFAA compared to MOF-AA. Furthermore, the effect of MOF-TFAA particle size on membrane performance was studied. It was shown that smaller MOF particles result in a minor improvement of CO_2/CH_4 separation factor, which was attributed to the prevention of MOF particle agglomeration during synthesis. Next, fluorinated and non-fluorinated carboxylic acid modulators with increased alkyl chain lengths were used for MOF synthesis and functionalization. Crystalline, microporous MOF-808 particles could be obtained as confirmed by XRD and N_2 physisorption. The observed CO_2 separation performance of the prepared fluorinated MOF-808 MMMs was outstanding. Two of the best MMMs prepared with 30 wt.% MOF-TFAA and 10 wt.% MOF-PFPA improved the CO_2/CH_4 separation factor with 100% and 140%, respectively. At the same time, both MOFs significantly enhanced the CO_2 permeability (+350% and +100%). Compared to MOF-TFAA, an improved solubility selectivity seemed to be at the base of the excellent separation behavior of MMM-PFPA, possibly enforced by a more confined polarized environment in the MOF-PFPA pore. Further increasing the chain length of the fluorinated modulator (HFBA) resulted in reduced interfacial compatibility between MOF-HFBA surface and the polymer chains, resulting in a (partly) compromised performance. Although here demonstrated for CO_2/CH_4 separation, the presented MoFu-concept is in theory applicable to all separation domains (both gas and liquid) that involve MOF-based membranes.

4.5 Acknowledgements

R.T. and N.V.V. are grateful to the FWO for their SB-PhD fellowships (1S63317N and 1S32917N). S.S. thanks FWO for funding through an Aspirant grant (1104118N). The authors would like to thank Kristien van der Flaas for help with the DSC measurements and Machiel van Essen for conducting the membrane sorption experiments.

4.6 Supplementary information to Chapter 4

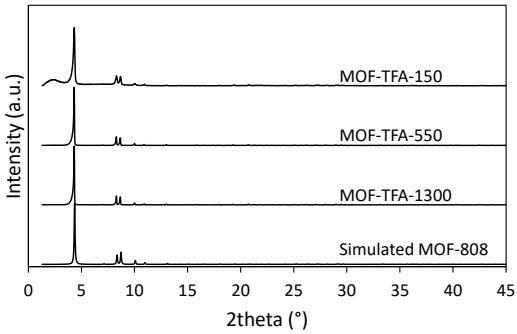

Figure S4-1: XRD patterns of simulated MOF-808, MOF-TFAA-1300, MOF-TFAA-550 and MOF-TFAA-150.

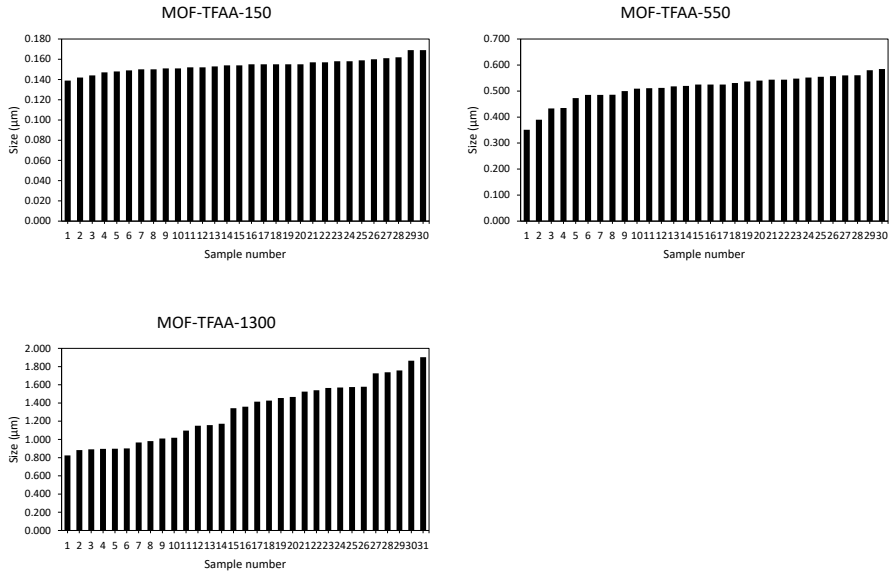

Figure S4-2: Size distribution plots of MOF-TFAA-150, MOF-TFAA-550 and MOF-TFAA-1300 based on visual analysis of SEM images with ImageJ.

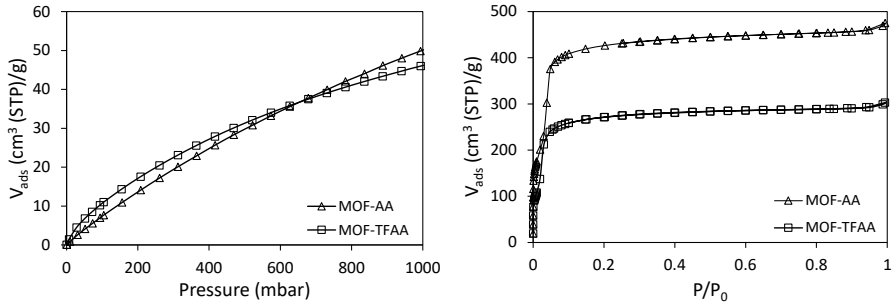

Figure S4-3: CO_2 uptake (left) and N_2 adsorption isotherms (right) of MOF-AA and MOF-TFAA. CO_2 uptake and N_2 adsorption were conducted at 0 °C and -196 °C, respectively.

Table S4-1: T_g measured by DSC and T_{deg} measured by TGA of Matrimid and its MOF-TFAA MMMs with different particle sizes. MMMs contained 10 wt.% MOF.

	T_g (°C)	T_{deg} (°C)
Matrimid	314	546
MMM-TFAA-150	325	540
MMM-TFAA-550	326	532
MMM-TFAA-1300	326	527

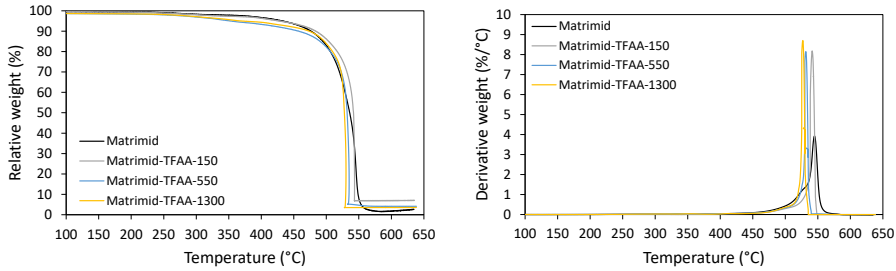

Figure S4-4: TGA curves of Matrimid, MMM-TFAA-150, MMM-TFAA-550 and MMM-TFAA-1300.

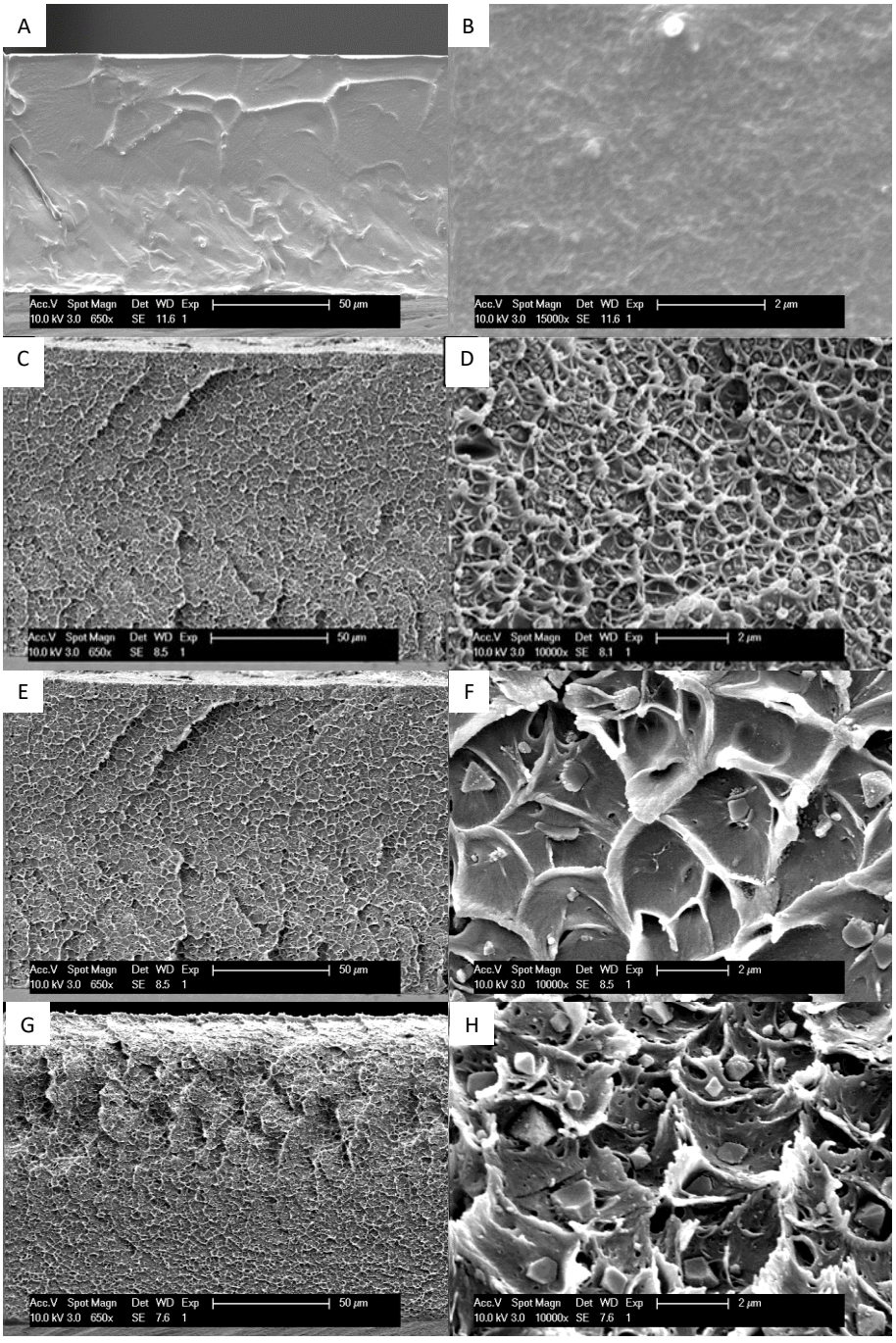

Figure S4-5: SEM cross-section of (A,B) Matrimid, (C,D) MMM-TFAA-550 and (E,F) MMM-TFAA-1300. All MMMs contain 10 wt.% MOF.

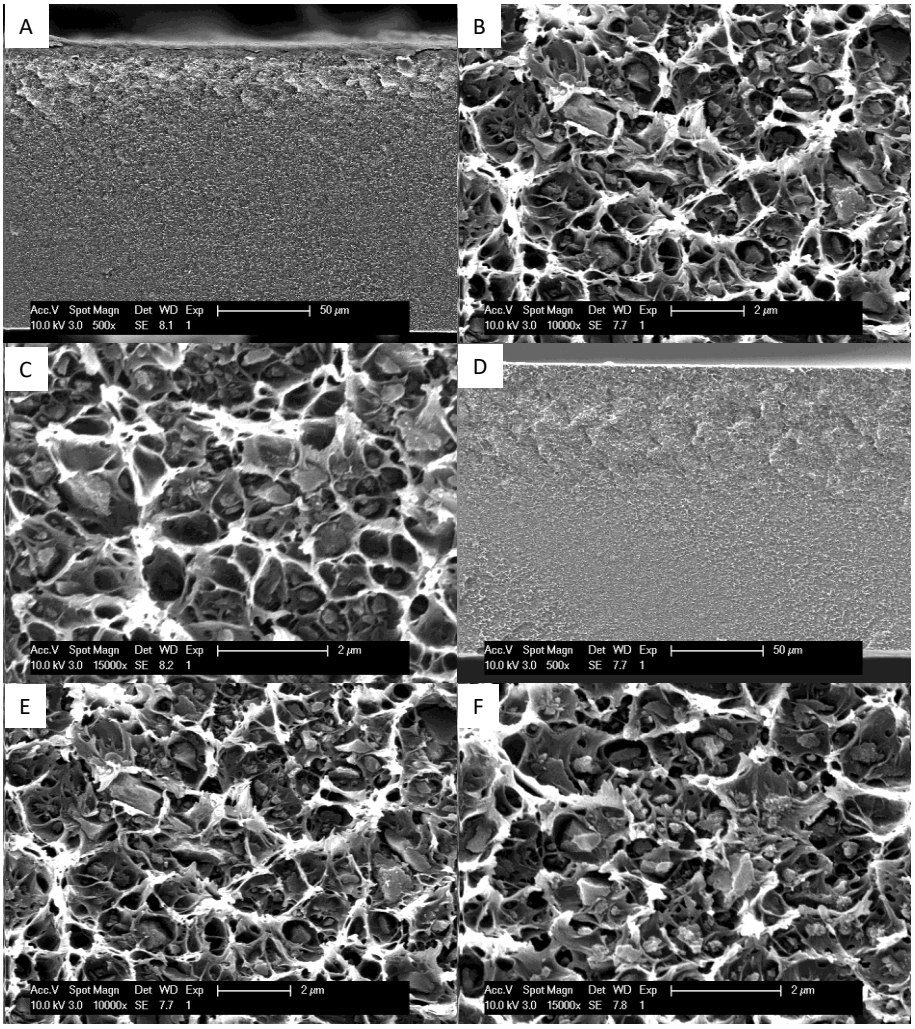

Figure S4-6: SEM cross-section of (A,B, C) 20 wt.% MMM-TFAA-150 and (D,E,F) 30 wt.% MMM-TFAA-150.

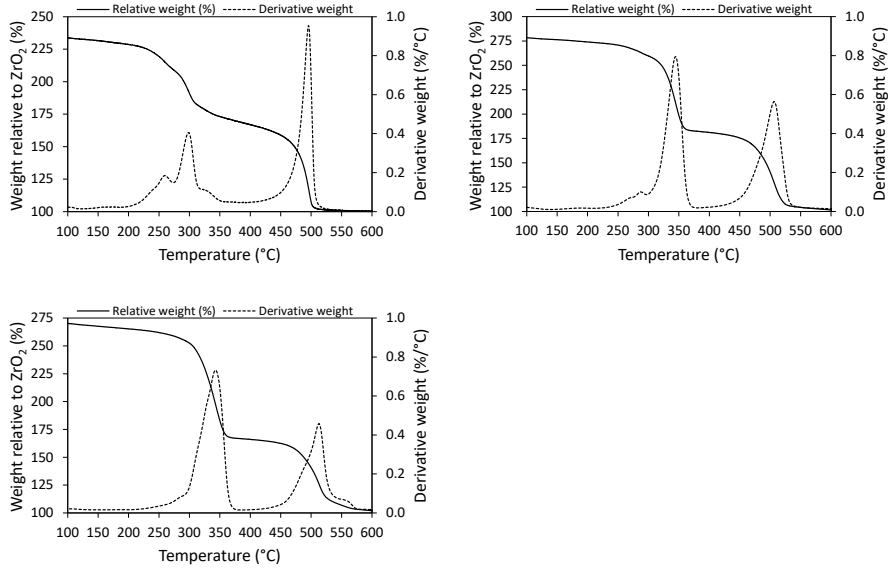

Figure S4-7: TGA analysis of MOF-TFAA (top, left), MOF-PFPA (top, right) and MOF-HFBA (bottom, left). The plateaus, indicated by the dotted lines, correspond with the onset of the derivative weight curve. An approximation of the material composition is calculated by taking the difference in relative weight between plateau values.

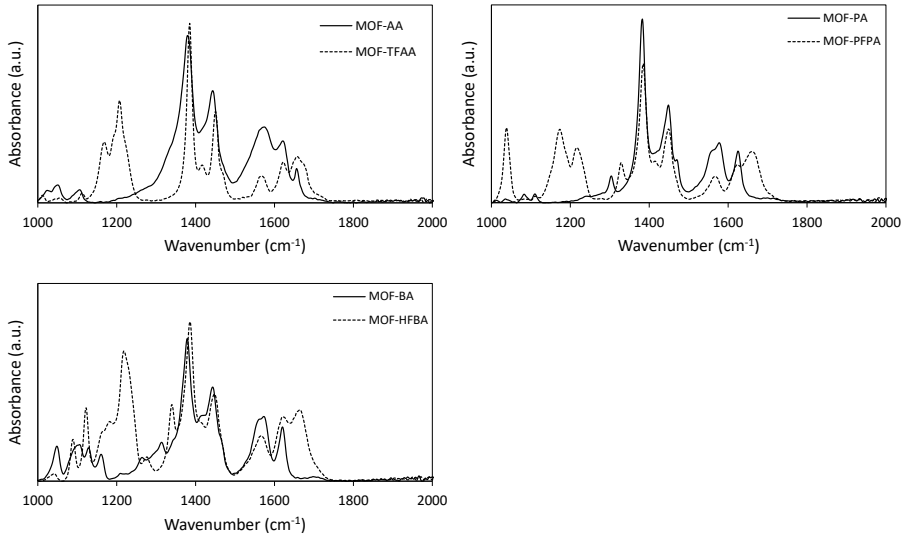

Figure S4-8: ATR-FTIR spectra of MOF-AA and MOF-TFAA (top, left), MOF-PA and MOF-PFPA (top, right), and MOF-BA and MOF-HFBA (bottom).

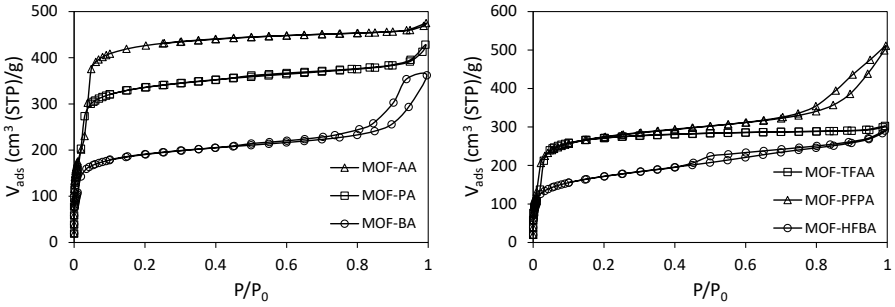

Figure S4-9: N_2 adsorption isotherm of all MOFs. Experiment conducted at -196 °C.

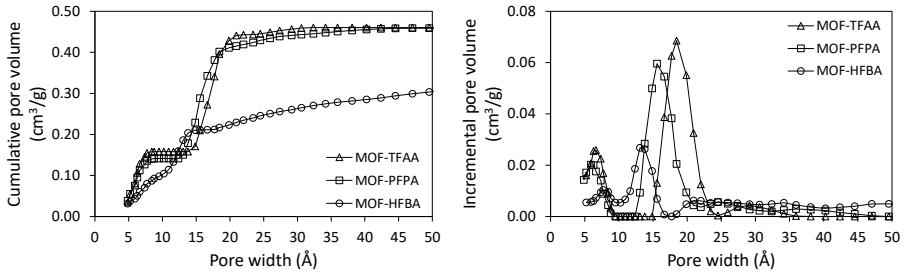

Figure S4-10: Cumulative pore volume and incremental pore volume as a function of pore width for MOF-TFAA, MOF-PFPA and MOF-HFBA.

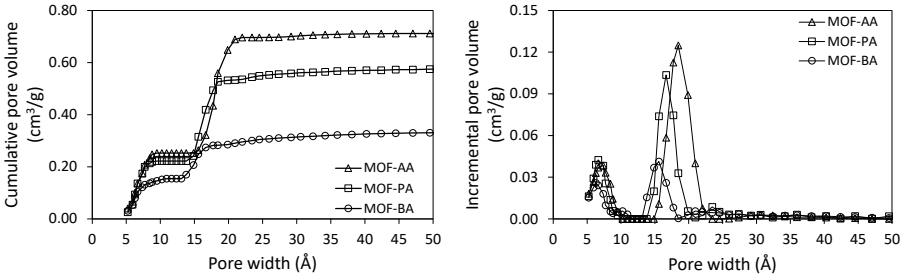

Figure S4-11: Cumulative pore volume and incremental pore volume as a function of pore width for MOF-AA, MOF-PA and MOF-BA.

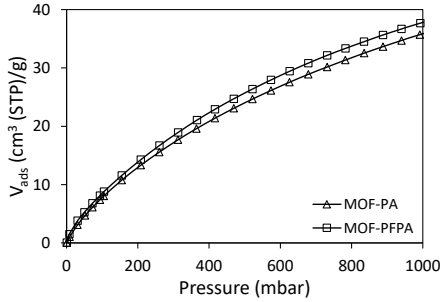

Figure S4-12: CO_2 uptake of MOF-PA and MOF-PFFA. Experiment was conducted at 0 °C.

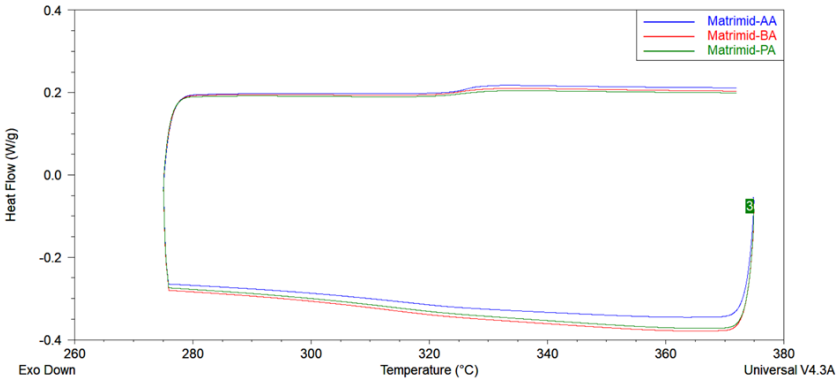

Figure S4-13: DSC curves of MMM-AA, MMM-PA and MMM-BA.

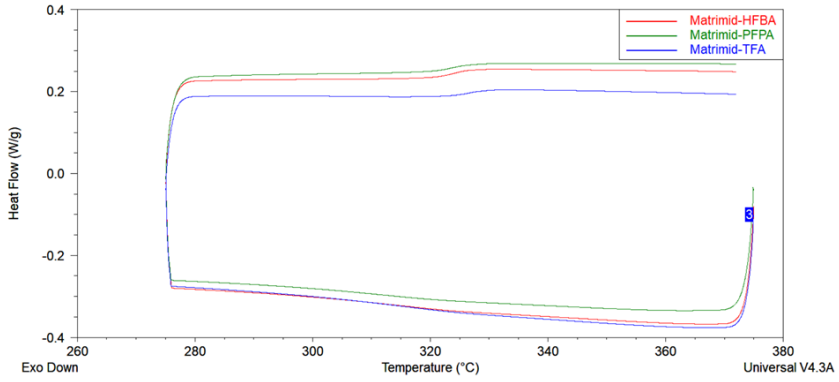

Figure S4-14: DSC curves of MMM-TFAA, MMM-PFPA and MMM-HFBA.

Table S4-2: Density of Matrimid and 10 wt.% MOF MMMs.

	Density (g/cm³)
Matrimid	1.23 ± 0.01
MMM-AA	1.27 ± 0.02
MMM-PA	1.28 ± 0.01
MMM-BA	1.28 ± 0.01
MMM-TFAA	1.28 ± 0.01
MMM-PFPA	1.26 ± 0.00
MMM-HFBA	1.22 ± 0.02

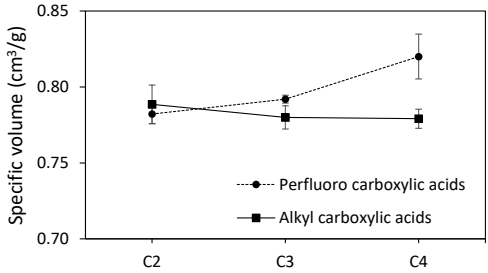

Figure S4-15: Specific volume of MMMs made with MOF modulated by alkyl carboxylic acids and by perfluoro carboxylic acids. C2, C3 and C4 indicates the number of carbon atoms in the carboxylic acid.

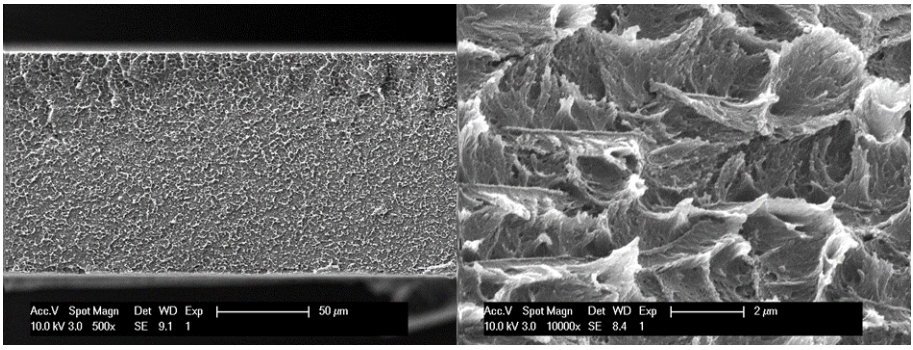

Figure S4-16: SEM cross-section of Matrimid MMMs with 10 wt.% MOF-PFPA.

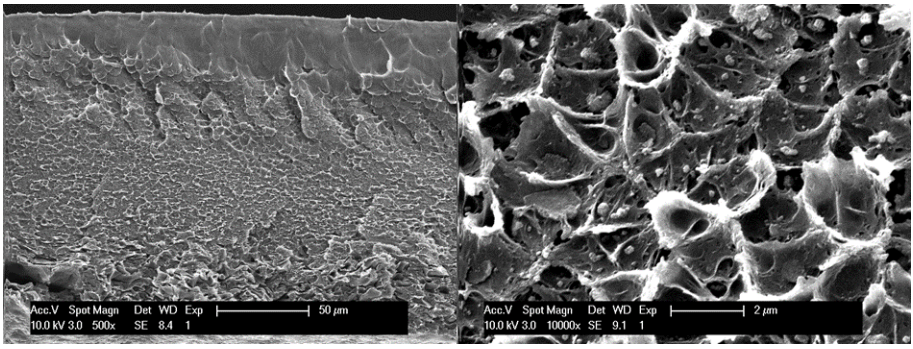

Figure S4-17: SEM cross-section of Matrimid MMMs with 10 wt.% MOF-HFBA.

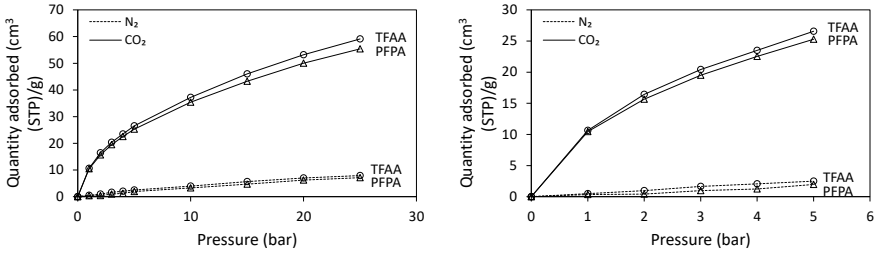

Figure S4-18: Membrane sorption isotherms of CO_2 and N_2 in MMM-TFAA and MMM-PFPA.

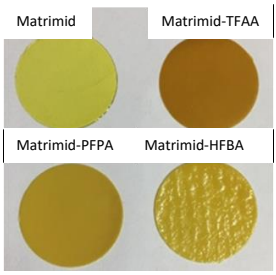

Figure S4-19: Membrane coupons of Matrimid, MMM-TFAA, MMM-PFPA and MMM-HFBA.

Table S4-3: Overview of similar MMMs reported in literature. $\alpha^*_{CO2/CH4}$ is the separation factor, P_{CO2} the CO_2 permeability in Barrer, $\Delta\alpha^*$ and ΔP the increase in separation factor and permeability, respectively, compared to the pristine polymer membrane.

Polymer	Filler	$\alpha^*_{CO2/CH4}$	$\Delta\alpha^*$	P_{CO2} (Barrer)	ΔP	Reference
Matrimid	MOF-TFAA	70	+75%	25	+78%	This work
Matrimid	MOF-PFPA	97	+140%	29	+107%	This work
Matrimid	MOF-HFBA	71	+77%	38	+171%	This work
Matrimid	UiO-67-BPYDC	75	+87%	27	+42%	[154]
Matrimid	UiO-66-NH_2	47	+52%	38	+530%	[81]
Matrimid	UiO-66-GO	51	+46%	21	+160%	[107]
Matrimid	UiO-66	39	-2%	26	+63%	[154]
Matrimid	NH_2-MIL-53(Al)	28	-7%	660	+4300%	[177]
Matrimid	ZIF-8	34	-	16	-	[178]
Matrimid	UiO-66-NH-PA	37	-	29	-	[80]
Matrimid	UiO-66-NH_2-@ICA	75	+117%	40	+120%	[144]

Chapter 5

Towards more rational mixed-matrix membrane design: Correlation of MOF-808 parameters with mixed-matrix membrane CO_2 permeation

Raymond Thür[a], Daan Van Havere[a], Niels Van Velthoven[a], Simon Smolders[a], Aran Lamaire[b], Jelle Wieme[b], Veronique Van Speybroeck[b], Dirk De Vos[a], Ivo F.J. Vankelecom[a]

Manuscript submitted to Journal of Materials Chemistry A

[a]Centre for Membrane Separations, Adsorption, Catalysis and Spectroscopy for Sustainable Solutions (cMACS), KU Leuven, Celestijnenlaan 200F, Box 2454, 3001 Heverlee, Belgium

[b]Center for Molecular Modeling, Ghent University, Tech Lane Ghent Science, Park Campus A, Technologiepark 46, 9052 Zwijnaarde, Belgium

Abstract

Consistent structure-performance relationships for the design of MOF (metal-organic framework)-based mixed-matrix membranes (MMMs) for gas separation are currently scarce in MMM literature. A first step in finding such relationships could be the linking of intrinsic MOF parameters, such as CO_2 uptake and the CO_2 adsorption enthalpy (Q_{st}), to the separation performance indicators of the MMM (i.e. separation factor and permeability). Such a study presumes the availability of a platform MOF, which allows systematic comparison of the relevant MOF parameters. MOF-808 can take up the role of such platform MOF, owing to its unique cluster coordination and subsequent ease of introducing additional functional molecules. For this purpose, formic acid (FA) modulated MOF-808 (MOF-FA) was post-synthetically functionalized with five different ligands (histidine (His), benzoic acid (BA), glycolic acid (GA), lithium sulfate (Li_2SO_4) and trifluoroacetic acid (TFAA)) to create a series of isostructural MOFs with varying structural properties. CO_2 uptake and CO_2 Q_{st} of the MOFs were determined with CO_2 sorption experiments and a Clausius-Clapeyron analysis. Both MOF properties were subsequently linked to the CO_2/N_2 separation factor and CO_2 permeability of the corresponding MMM. Unlike many literature reports, MOF-808 CO_2 uptake proved to be a poor indicator for MMM performance. In contrast, a strong correlation was observed between Q_{st} at high CO_2 loadings (15 and 30 cm^3 (STP)/g) on one hand and CO_2 permeability under varying feed conditions on the other hand. Furthermore, correlation coefficients of $Q_{st,15}$ and $Q_{st,30}$ with the separation factor were significantly better than those calculated for CO_2 uptake. The surprising lack of correlation between membrane performance and CO_2 uptake and the strong correlation with Q_{st} once more underlines the difficulty to rationally design MMMs and, more importantly, stresses the need for more research focused on finding consistent relationships between the filler properties and the eventual membrane performance.

Contributions

Raymond Thür: design and coordination of experiments, membrane and MOF preparation, characterization, gas permeation experiments, data analysis, manuscript writing and redaction. Daan Van Havere: design of experiments, membrane and MOF preparation, characterization, gas permeation experiments, data analysis, manuscript correction and redaction. Niels Van Velthoven: NMR, manuscript correction and redaction. Simon Smolders: physisorption data acquisition and analysis, manuscript correction and redaction. Aran Lamaire: computational modelling, manuscript correction and redaction. Jelle Wieme: computational modelling, manuscript correction and redaction. Dirk De Vos: manuscript correction and redaction. Veronique Van Speybroeck: manuscript correction and redaction. Ivo F.J. Vankelecom: manuscript correction and redaction.

5.1 Introduction

MMMs consist of a continuous polymer matrix containing dispersed nanoparticles (so-called fillers)[67,137]. While polymeric membranes show good processability but rather moderate gas separation performance[34,179], purely inorganic membranes can reach high selectivity/permeance combinations due to their particular size sieving abilities or strong affinity for the target component[180]. However, inorganic membranes are often uneconomical to produce as they are brittle, making it challenging to prepare up-scaled membranes with large specific surface[181]. MMMs are believed to profit from the best of both worlds, having improved separation capacity due to nanoparticle addition while maintaining the good film-forming properties of the polymer. Much research has been dedicated in the past 10 years to find better combinations of polymers and MOFs with enhanced performance compared to the state-of-the-art[71,95,137,182–186]. A lot of these literature reports focus on the use and modification of conventional MOFs, frequently employing a trial-and-error approach for developing novel MMMs. Although the membrane performance can indeed often be boosted by incorporation of MOFs in terms of higher permeability or gas pair selectivity, the theoretical understanding behind the MMM concept remains rather poor while consistent structure-performance relationships for the design of MMMs are currently very scarce[84,187]. A first step towards finding such structure-performance relationships could be the linking of intrinsic MOF parameters to the gas permeation behavior of the MMM (thus determining indicators for the MMM separation performance based on MOF parameters). For example, Seoane and co-workers proposed a method to quantify polymer-MOF compatibility based on the Hansen solubility parameters of MOF and polymer[67]. With respect to the membrane selectivity and permeability, MOF parameters such as pore volume and CO_2 uptake are often identified as key drivers in the ultimate MMM performance, where good MMM separation performance goes hand in hand with high pore volume and CO_2 uptake[79,154,188–191]. However, no study has been devoted so far to the systematic correlation between MOF and MMM parameters for a series of isostructural MOFs. This is understandable since such a study presumes the availability of a platform MOF, which allows systematic comparison of the relevant MOF parameters. Furthermore, the overall gas permeation through the MMM is the result of a subtle interplay between polymer and MOF-related factors, which complicates the identification of one-on-one correlations and causalities between parameters.

MOF-808, consisting of the same $Zr_6O_4(OH)_4$ cluster as UiO-66 but linked through six BTC^{3-} linkers, can take up the role of such platform MOF since it can be simply modified to change intrinsic MOF properties while preserving the same MOF structure and topology[95]. Next to the six BTC^{3-} linkers occupying the binding sites (at opposing vertices of the cluster), the six equatorial binding sites can theoretically be occupied by up to six modulator or ligand molecules[158] (Figure 5-1), which can be easily attached via solvent-assisted ligand exchange[192]. As shown in previous work, it is possible to create isostructural MOF-808 derivatives with subtly changed BET surface area, pore volume, CO_2 uptake and CO_2 affinity[95]. Moreover, other appealing features of MOF-808 include its excellent thermal, chemical and mechanical stability,

following from the high coordination number of the Zr_6-cluster, and the easy up-scaling of the synthesis in non-toxic solvents such as water[161].

In this work, post-synthetic functionalization of MOF-808 was applied to create a series of isostructural MOF-808 with systematically varying CO_2 uptake and CO_2 isosteric heat of adsorption (Q_{st}). For this purpose, a single batch of MOF-FA was produced to guarantee a uniform starting material for all functionalizations, hence avoiding differences in MOF morphology or particle size due to batch variations. Five different functional molecules were selected based on their anticipated interaction with CO_2. TFAA has previously been proven to enhance the CO_2 affinity of MOF-808 particles for MMM design[95]. Histidine and GA were selected for the presence of (heterocyclic) N and O heteroatom functionality in their chemical structure while the use of BA could result in enhanced compatibility with the polymer phase due to π-π stacking between the aromatic compounds of MOF and polymer and, secondly, improved interaction with CO_2 through quadrupole-quadrupole interaction[80]. Li_2SO_4 was chosen based on the knowledge that Li is the hardest metal ion available and should thus, according to Pearson's hard-soft-acid-base (HSAB) theory, result in good interaction with CO_2[193]. Furthermore, sulfate groups are known for their good affinity towards Zr-clusters and should thus ensure stable incorporation of the Li-ions[157]. The obtained CO_2 uptake and Q_{st} values were then correlated with the MMM performance parameters (CO_2/N_2 separation factor, pure gas permeability (PGP) and mixed-gas permeability) in an attempt to determine whether or not CO_2 uptake and CO_2 Q_{st} can be used as predictors for the MMM permeation behavior.

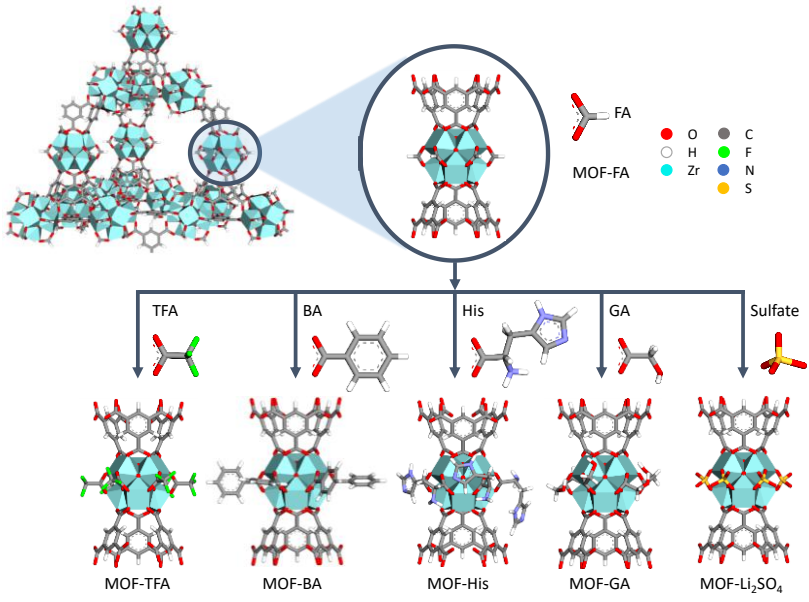

Figure 5-1: Overview of MOF-808 functionalization strategy. FA = formic acid, TFAA = trifluoroacetic acid, BA = benzoic acid, His = histidine, GA = glycolic acid. For clarity, Li-ions are not shown.

5.2 Materials and methods

5.2.1 Chemicals

Polyimide (Matrimid) was kindly provided by Huntsman (Switzerland). Sulfuric acid (99.9%), $Li_2SO_4.H_2O$ (>98.5%), BA (>99.5%), GA (99%) and histidine (L, >99%) were purchased from Sigma-Aldrich. TFAA (99%) was acquired from Merck-Schuchardt. FA (99%), THF (>99%), dimethylsulfoxide (DMSO, 99%), acetone (technical grade) and ethanol (pure) were supplied by Acros. Zirconylchloride octahydrate ($ZrOCl_2.8H_2O$) was acquired from Abcr GmbH and BTC from J&K Chemicals. CO_2 (>99.999%) and N_2 (>99.999%) were purchased from Air Liquide and used as delivered.

5.2.2 MOF synthesis

The different MOF-808 samples are denoted as MOF-*x*, with x being the ligand type, e.g. MOF-808 functionalized with BA is denoted as MOF-BA. A single batch of MOF-FA was prepared (yield 12.6 g) to prevent differences between functionalized samples due to batch variations of the starting material. All functionalized MOFs were synthesized using MOF-FA as starting material.

5.2.2.1 Synthesis of MOF-FA

The MOF synthesis recipe used in previous work[95] was adapted for using FA as modulator and subsequently scaled up. 5.08 g (24.2 mmol) BTC and 23.4 g (72.8 mmol) $ZrOCl_2.8H_2O$ were dissolved in 182 mL H_2O in a 500 mL round-bottom flask. Subsequently, 26.8 mL FA (712 mmol) was added and the mixture was thoroughly stirred for 15 min. The reaction mixture was then heated to 100 °C under reflux for 5 h in an oil bath. The formed MOF sludge was transferred into Falcon tubes and washed with distilled water (30 mL). After 8 h, the MOF samples were centrifuged (4000 rpm, 30 min) and the supernatant was decanted. This was repeated 4 times with distilled water and 3 times with ethanol. After the last washing step, a clean, white powder (12.6 g) was obtained by drying in a vacuum oven at 70 °C overnight.

5.2.2.2 Synthesis of MOF-BA

MOF-BA was functionalized according to the method developed by Baek *et al.*[194]. 250 mg of MOF-FA was suspended in a 50 mL DMSO solution with 1.12 g (9.251 mmol) BA in a 100 mL Schott bottle. The bottle was then placed in an oil bath at 100 °C under constant stirring. After 24 h, the reaction was stopped and the reaction mixture poured into Falcon tubes and washed with DMSO (3 times, 30 mL) and acetone (3 times, 30 mL), similar to the washing procedure of MOF-FA. After washing, the MOF was dried at 70 °C and stored for further use.

5.2.2.3 Synthesis of MOF-His, MOF-TFAA and MOF-GA

MOF-FA (250 mg) was suspended in a 50 mL aqueous solution of 0.005 mol ligand (0.78 g histidine, 0.57 g TFAA, 0.38 g GA) in a 100 mL Schott bottle. The bottle was placed on a stirring plate for 24 h at room temperature. Afterwards, the functionalized MOFs were washed 3 times with water and 3 times with acetone, similar to the washing procedure of MOF-FA. Finally, the MOFs were dried at 70 °C and stored for further use.

5.2.2.4 Synthesis of MOF-Li_2SO_4

An aqueous solution of sulfuric acid (0.1 M, 50 mL) was prepared in a 100 mL Schott bottle by mixing 0.268 mL sulfuric acid with 49.732 mL water, in which 250 mg of MOF-FA was suspended to form MOF-SO_4. The mixture was stirred for 24 h at room temperature. Next, MOF-SO_4 was washed with water and acetone, dried and re-suspended in a 50 mL aqueous solution containing 0.64 g (0.005 mol) $Li_2SO_4.H_2O$ for 24 h under continuous stirring. The resulting MOF was washed with water (3 times) and with acetone (3 times), dried at 70 °C and stored for further use.

5.2.3 Membrane synthesis

The different Matrimid MMMs are denoted as MMM-*x*, with x being the ligand type. For example, the Matrimid MMM containing MOF-TFAA is denoted as MMM-TFAA.

5.2.3.1 Preparation of pristine Matrimid membranes

Matrimid membranes were prepared by dissolving 0.42 g of polymer in 5.58 g THF. After stirring overnight, the polymer solution was poured into a Teflon Petri dish (d = 6 cm) in a nitrogen bag. Evaporation of the solvent was slowed down by placing a plastic funnel over the Petri dish. Once the membrane had solidified due to solvent evaporation, the polymer film was removed from the Petri dish and annealed in a muffle oven by heating from room temperature to 110 °C at 5 °C/min. The membrane remained at this temperature for 2 h. Next, the membrane was heated at 5 °C/min to 180 °C for 6 h. Subsequently, the membranes were allowed to cool down naturally.

5.2.3.2 Preparation of MMMs

10 wt.% MMMs were prepared by dispersing 0.047 g of dried MOF in 5.58 g THF. The dispersion was then thoroughly sonicated for 15 min. Following an adapted priming protocol[154], 0.42 g polymer was added to the dispersion in three steps (0.14 g per turn). All samples were continuously stirred on a magnetic stirring plate. Before and after polymer addition, the samples were sonicated for 15 min. After the final polymer addition, the polymer/MOF dispersion was stirred overnight and cast into a Petri dish (d = 6 cm) in a nitrogen bag. Evaporation of the solvent was slowed down by placing a plastic funnel over the Petri dish. Once the membrane had solidified due to solvent evaporation, the polymer film was removed from the Petri dish and annealed in a muffle oven by heating from room temperature to 110 °C at 5 °C/min. The membrane remained at this temperature for 2 h. Next, the membrane was heated at 5 °C/min to 180 °C for 6 h. The membranes were finally allowed to cool down naturally. Filler loading was determined with the following equation:

$$filler\ loading\ (wt.\%) = 100 \times \left(\frac{m_{filler}}{m_{filler} + m_{polymer}}\right) \quad (5.1)$$

with m_{filler} and $m_{polymer}$ the weight of the filler and polymer, respectively.

5.2.4 Characterization

5.2.4.1 XRD

MOF crystallinity was analyzed with XRD. XRD diffractograms were measured by a Malvern PANanlytical Empyrean diffractometer in transmission mode over a 1.3 – 45° 2θ range. A PIXcel3D solid-state detector and Cu anode (Cu Kα1: 1.5406 Å; Cu Kα2: 1.5444 Å) were used for detection and X-ray generation.

5.2.4.2 SEM

Particle morphology was examined with SEM (Philips XL30 FEG). To avoid sample charging, all samples were coated with a layer of gold/palladium. Particle size distribution was analyzed with ImageJ and statistical analysis (one-way ANOVA) to determine whether differences in size occurred between the MOFs.

5.2.4.3 ATR-FTIR

ATR-FTIR measurements on MOF and MMM samples were conducted to identify functional groups. All samples were dried prior to the measurement. A Bruker Alpha instrument containing a diamond ATR crystal was used to collect 32 scans at a resolution of 2 cm^{-1}.

5.2.4.4 N_2 and CO_2 physisorption

N_2 and CO_2 physisorption experiments were performed with a Micromeritics 3Flex surface analyzer. Prior to the measurement, all MOFs were activated under vacuum at 100 °C for 16 h. N_2 physisorption was conducted at -196 °C. Surface areas were calculated via the multi-point BET method applied to the isotherm adsorption branch, taking into account surface area criteria as given by Rouquerol[117] and the consistency criteria described by Walton and Snurr[118]. CO_2 sorption was measured at three different temperatures (273 K, 293 K, 313 K) to allow determination of the CO_2 Q_{st} of the different MOFs with the Clausius-Clapeyron equation (Equation 5.2)[195]:

$$\frac{\partial\, ln(p)}{\partial\, (\frac{1}{T})} = \frac{-Q_{st}}{R} \tag{5.2}$$

with p the equilibrium pressure (mbar), T the temperature (K), R the universal gas constant (J/mol K).

The sorption data were first fitted with the dual-site Langmuir model (Equation 5.3)[195]:

$$N = N_{m,A} \times \frac{b_A \times p}{1 + b_A \times p} + N_{m,B} \times \frac{b_B \times p}{1 + b_B \times p} \tag{5.3}$$

with N the amount of adsorbed gas (cm^3 (STP)/g), $N_{m,A}$ and $N_{m,B}$ the amount of adsorbed gas at saturation for sorption site A and B respectively (cm^3 (STP)/g), b_A and b_B the adsorption equilibrium constants for respectively sorption site A and B and p the pressure (mbar).

The Clausius-Clapeyron data points were then interpolated based on the fit values. Next, for a range of different CO_2 loadings, Q_{st} can be calculated from the slope of a ln(p) vs 1/T plot, according to Equation 5.2.

5.2.4.5 NMR

^1H and ^{19}F NMR measurements were carried out to determine the average number of ligand molecules per Zr_6 cluster. First, 3 mg MOF-808 was dispersed in 600 µL deuterated DMSO. Next, 25 µL of a 40 wt.% hydrofluoric acid (HF) solution was added for MOF digestion. For ^{19}F NMR, 10 µL fluorobenzene was added to the mixture as an internal standard. NMR spectra were recorded on a Bruker AMX-300 spectrometer at 300 MHz for ^1H NMR and at 400 MHz for ^{19}F NMR (16 scans). A recycle delay time of 30 s was applied for ^{19}F NMR. The output was analyzed with SpinWorks 4.2 software.

5.2.4.6 Membrane gas sorption

Sorption of N_2 and CO_2 was measured at 30 °C up to pressures of 15 bar for all membranes. A Rubotherm series IsoSORP© instrument was used to conduct the measurements. First, helium pycnometry was carried out on all membranes to determine the membrane weight and volume. The additional weight resulting from gas sorption in the membrane over time was determined with a magnetically suspended balance. The buoyancy of the measurement gases was taken into account to calculate the correct weight of the sample (Equation 5.4):

$$m_{corrected} = m_{measured} + \rho_{gas} \times V_{sample} \tag{5.4}$$

with $m_{corrected}$ the corrected weight (g), $m_{measured}$ the measured weight (g), ρ_{gas} the measuring gas density (g/cm^3) and V_{sample} the sample volume (cm^3).

The N_2 and CO_2 solubility in the membranes can be calculated with Equation 5.5:

$$S = \frac{C}{p} \tag{5.5}$$

with S the gas solubility (cm^3(STP)/cm^{3}cmHg), C the quantity of adsorbed gas (cm^3(STP)/cm^3) and p the pressure (cmHg).

5.2.4.7 Grand Canonical Monte Carlo (GCMC) simulation of CO_2 adsorption behavior in MOF-808

The input structures for the GCMC simulations were obtained by optimizing the primitive unit cell of the different MOF-808 structures using CP2K[196]. The optimizations were performed at the PBE-D3(BJ)[197–199] level of theory, combined with Gaussian TZVP-MOLOPT[200] basis sets, a plane wave basis set with a cut-off of 800 Ry and a relative cut-off of 60 Ry, and Goedecker-Teter-Hutter (GTH) pseudopotentials[201], allowing for a relaxation of both the atomic positions and the unit cell. The GCMC simulations were performed with RASPA[202], using a fixed framework and rigid CO_2 and N_2 adsorbate molecules described by the TraPPE force field[203]. The atomic framework charges were derived from cluster calculations using the Minimal Basis Iterative Stockholder (MBIS) partitioning scheme[204] (see Supporting Information for more details), while the Lennard-Jones interaction parameters are taken from the DREIDING model[205]

(except for zirconium, which was taken from UFF[206,207]. The temperature was set to 300 K. Each GCMC simulation consists of 10^7 cycles, with equal probabilities for translation, rotation, and (re)insertion moves. The first 10^5 cycles are regarded as equilibration steps and are not taken into account in any analysis.

The CO_2 enthalpy of adsorption can be determined from the GCMC simulations using Equation 5.6:

$$\Delta H_{ads} = \frac{\langle U \cdot N \rangle_\mu - \langle U \rangle_\mu \langle N \rangle_\mu}{\langle N^2 \rangle_\mu - \langle N \rangle_\mu^2} - \langle U_{host} \rangle - \langle U_{guest} \rangle - k_B T \quad (5.6)$$

with U the total energy of the host framework and the adsorbed molecules, N the number of adsorbed molecules, $\langle U_{host} \rangle$ the average energy of the adsorbent, $\langle U_{guest} \rangle$ the average energy of the adsorbate molecule in the gas phase, k_B the Boltzmann constant, and T the absolute temperature.

$\langle \dots \rangle_\mu$ denotes an average in the grand-canonical ensemble. As the host framework and the adsorbed molecules are described as rigid molecular systems, $\langle U_{host} \rangle = \langle U_{guest} \rangle = 0$.

The mixed-gas CO_2/N_2 selectivities of MOF-FA and MOF-TFAA were determined from a separate set of GCMC simulations in which both CO_2 and N_2 molecules can be inserted or deleted. The mole fractions were set to 0.5, so that the selectivity can be calculated from the ratio of the number of adsorbed CO_2 molecules to the number of adsorbed N_2 molecules.

5.2.4.8 Gas permeation

An in-house developed HTGS was used to examine the gas permeation behavior of the synthesized membranes. A detailed set-up description is given elsewhere[47,123,208]. HTGS allows simultaneous pure gas and mixed-gas testing of 16 membrane coupons at varying membrane temperatures and feed pressures. The active membrane area is 1.91 cm^2. CO_2 pure gas and mixed-gas permeability and the CO_2/N_2 separation factor were measured for all membranes.

CO_2/N_2 mixed-gas separation factors (α^*) were measured by a GC analysis of the permeate composition. The ratio of the feed and permeate mole fraction of CO_2 and N_2 then renders the separation factor (Equation 5.7):

$$\alpha^*_{CO2/N2} = \frac{y_{CO2} \,/\, y_{N2}}{x_{CO2} \,/\, x_{N2}} \quad (5.7)$$

where y_{CO2} and y_{N2} are the mole fractions of CO_2 and N_2 in the permeate, x_{CO2} and x_{N2} the mole fractions of gas CO_2 and N_2 in the feed. The ratio y_{CO2}/y_{N2} is determined from chromatogram peak areas of the permeate, while x_{CO2}/x_{N2} is determined by the feed settings.

Determination of the pure gas and mixed-gas permeabilities of CO_2 and N_2 was performed with a constant-volume-varying-pressure method. A pressure sensor (MKS Baratron) measures the change in pressure in a 75 cm^3 measuring cylinder while permeate gas is accumulated in the cylinder. The change in pressure as a function of time (dp/dt) is then used to calculate the

permeability P (Barrer) with Equation 5.8. For pure gas measurements, the mole fraction of the gas in permeate and feed is 1.

$$P_i = 10^{10} \times \frac{y_i \times V \times V_m \times L}{x_i \times p_{up} \times A \times R \times T} \times \frac{dp}{dt} \quad (5.8)$$

with P_i the gas permeability (Barrer), y_i the mole fraction of the component in the permeate, x_i the mole fraction of the component in the feed, V the downstream volume (cm^3), V_m the molar volume (L/mol), A the membrane permeation area (1.91 cm^2), L the membrane thickness (µm), T the operating temperature (K), p_{up} the upstream pressure (bar), R the gas constant (0.082 L atm/mol K) and dp/dt the pressure increase (Torr/s).

5.3 Results and discussion

5.3.1 Characterization of MOFs and membranes

Functionalization of the starting material MOF-FA does not change the crystal structure of the MOF since all its functionalized derivatives show a high degree of crystallinity (Figure S5-1), in good agreement with literature[95,192,194]. The variation in relative intensity between the large diffraction peak at 4.3° and the two smaller peaks at 8.3° and 8.7° can be attributed to the varying pore filling of the different MOFs[209–211]. Furthermore, post-synthetic functionalization does not affect the particle size nor morphology as confirmed by SEM (Figure S5-2). All MOFs have the same, lumped octahedral shape and a uniform, average MOF size of around 350 nm, originating from the starting material. A one-way analysis of variance (ANOVA) suggested no statistical difference in particle size between the MOFs (Table S5-1 and Table S5-2).

ATR-FTIR was used to further confirm the presence of the different ligands in the MOFs (Figure 5-2). In all spectra, peaks situated at 453 cm^{-1} (Zr-μ_3-OH stretch) and 660 cm^{-1} (Zr-μ_3-O stretch) are associated with the Zr-oxide cluster[154]. Likewise, clearly distinguishable peaks are observed at 760 cm^{-1}, 1385 cm^{-1}, 1572 cm^{-1} and 1620 cm^{-1}, corresponding to vibrations of the BTC linker[212]. No signal was found between 1715-1750 cm^{-1}, which corresponds with the C=O stretch of uncoordinated ligands or BTC, hence indicating that the MOF pores do not contain physisorbed ligands[212]. Specific peaks belonging to the ligand were found for all samples. Additional bands for MOF-His are visible at 822 cm^{-1} and 1067 cm^{-1}, resulting from mixed -NH_3^+ and -CH bending. Together with the higher relative absorbance of the signal at 1574 cm^{-1} (-NH_3^+ deformation), these absorptions suggests that histidine is present in its (partially) protonated form[132,144,213]. Specific absorption bands for MOF-TFAA were recorded at 1170 and 1208 cm^{-1}, attributed to -CF symmetrical and anti-symmetrical stretch, respectively[95]. Signals for MOF-BA and MOF-GA were less pronounced as their characteristic bands mostly coincide with linker peaks. For MOF-BA, the signal at 718 cm^{-1} has a higher absorbance (associated with an increased out-of-plane -CH stretching of the benzene ring) while a new peak occurs at 1178 cm^{-1} (-CH bending ring)[214]. MOF-GA shows a weak signal increase at 1000-1075 cm^{-1} (C-O stretch) but, most importantly, a broad signal at 3300 cm^{-1} due to -OH stretch (from GA, ethanol or water)[132]. Finally, an enhanced absorbance intensity in the 900-1200 cm^{-1} region has previously been associated with effective SO_4 functionalization of MOF-808[157].

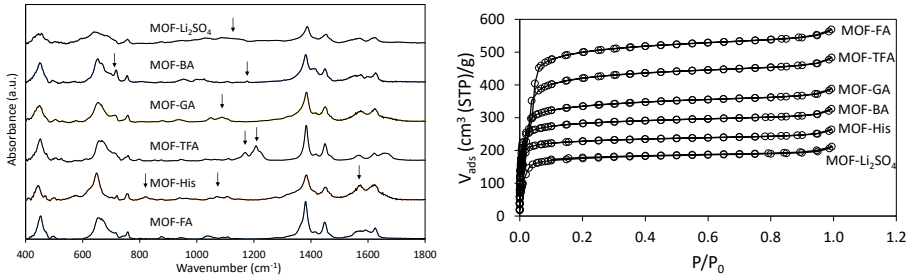

Figure 5-2: ATR-FTIR spectrum (left) and N_2 adsorption isotherms at 77 K (right) of all MOFs.

Further confirmation of successful post-synthetic functionalization was performed with ^{1}H NMR and ^{19}F NMR (Figure S5-4). A higher ligand loading on the cluster was detected in the following order: MOF-TFAA = MOF-His (3.3) > MOF-BA (3.2) > MOF-GA (2.3) > MOF-FA (2.2), as can be seen in Table 5-1. The difference in loading seems to roughly increase with decreasing pK_a of the carboxylic acid functional group (in water): TFAA (0.23) > His (1.78) > GA (3.83) ~ FA (3.75)[215,216]. A lower pK_a results in a larger concentration of deprotonated ligand at equal pH and thus a higher probability of incorporation in the MOF framework. MOF-BA deviates from this trend as it has the highest pK_a (4.20) but, at the same time, a loading of 3.2 BA per Zr_6 cluster. Due to the limited solubility of BA in water, BA functionalization took place in DMSO, whereas the other functionalizations were water-based, making it difficult to draw conclusions with regard to BA. None of the functional ligands had a cluster loading equal to the theoretical maximum of six, indicating that the remaining vacant sites were occupied by other charge compensating moieties (i.e. $-OH^-$, $-Cl^-$)[194].

CO_2 and N_2 physisorption experiments were conducted to determine characteristic MOF-808 parameters, such as pore volume and diameter, BET value and CO_2 uptake (Table 5-1). N_2 adsorption isotherms are given in Figure 5-2. Substantial differences in BET surface area and pore volume exist between the functionalized MOFs. For the starting material MOF-FA, BET and pore volume correspond well with literature[95,161,217]. The BET surface area, pore volume and pore diameter (Figure S5-5) all decrease with increasing size of the ligand (MOF-TFAA > MOF-GA > MOF-BA > MOF-His). Although Li_2SO_4 is considerably smaller in size than histidine and BA, MOF-Li_2SO_4 denotes the lowest BET and pore volume measured. As MOF-Li_2SO_4 retained its crystalline structure after functionalization, the low BET and pore volume suggest that the MOF pores might be partially blocked by salt deposition. Furthermore, functionalization strongly affects the CO_2 uptake of the different MOFs as well (Figure S5-6). At 1000 mbar and 273 K, the MOF-FA starting material displays the highest uptake (65.9 cm^3 (STP)/g), indicating that functionalization reduced the uptake capacity of the MOFs. The CO_2 uptake follows a decreasing trend from MOF-FA > MOF-His > MOF-TFAA > MOF-GA > MOF-BA > MOF-Li_2SO_4. However, only small differences in uptake (ranging from 48.1-55.2 cm^3 (STP)/g) are observed between the functionalized MOFs, except for MOF-Li_2SO_4, which loses more than 40% of uptake capacity compared to MOF-FA, further pointing towards the deposition of Li_2SO_4, blocking adsorption sites[218]. Besides the total CO_2 uptake capacity of the MOF, the initial slope of the CO_2 adsorption

isotherm in the low-pressure region also reveals qualitative information about the MOF CO_2-philicity as it is governed by the sorption equilibrium constant (b-value)[166,167,219,220]. Hence, adsorption in this pressure region is expected to correlate primarily with the MOF-CO_2 binding strength rather than with the specific surface area or pore volume. The slope in the lower pressure region (0-100 mbar, Figure S5-7) increases in the order MOF-BA < MOF-Li_2SO_4 < MOF-GA < MOF-FA ≈ MOF-His < MOF-TFAA, which was further confirmed by the b-values obtained from the dual-site Langmuir model (Table S5-3). The observed trends in CO_2 uptake and initial slope (b-value) indicate that MOF-TFAA has the highest affinity for CO_2, although this is eventually not reflected in the highest total CO_2 uptake since the MOF starting material (i.e. MOF-FA) can adsorb up to 28% more CO_2. While this observation seems to contradict at first sight, it can be explained by the larger pore volume and surface area of MOF-FA. Furthermore, an almost linear CO_2 adsorption isotherm is observed for MOF-BA in the low-pressure region, which has previously been associated with a lack of high-affinity bindings sites in the MOF[220,221]. At higher pressures, the difference between the isotherms of the other MOFs is less pronounced (Figure S5-6).

Table 5-1: Average number of ligand molecules per Zr_6 cluster, pore volume (cm^3), pore diameter (Å), BET value (m^2/g) and CO_2 uptake at 273 K and 1000 mbar for all MOFs.

	Ligands per Zr_6 cluster[#]	Pore volume (cm^3)	Pore diameter (Å)	BET value (m^2/g)	CO_2 uptake (cm^3 (STP)/g)[*]
MOF-FA	2.2	0.76	18.4	2304	65.9
MOF-TFAA	3.3	0.68	17.7	1946	51.2
MOF-GA	2.3	0.55	15.6	1421	50.9
MOF-BA	3.2	0.46	13.8	1119	48.1
MOF-His	3.4	0.37	10.9	901	55.2
MOF-Li_2SO_4	-	0.28	15.6	727	37.2

[#]as determined by NMR, [*]at 273 K and 1000 mbar

To obtain a more accurate and quantitative measure of the effect of functionalization on the MOF CO_2 affinity, the loading-dependent CO_2 Q_{st} was calculated for each MOF with the Clausius-Clapeyron method based on a dual-site Langmuir model (Figure 5-3). Table S5-4 gives the MOF Q_{st} values at different loadings. At zero coverage, the diverse functionalizations result in a difference of ~15 kJ/mol between the highest Q_{st} (MOF-TFAA, 39.2 kJ/mol) and the lowest Q_{st} (MOF-BA, 23.9 kJ/mol). The curve of the graphs of MOF-FA, MOF-TFAA, MOF-GA, MOF-Li_2SO_4 and (to a lesser extent) MOF-His all display a substantial Q_{st} reduction with increasing coverage. Comparable behavior has been associated with the saturation of high-affinity gas binding sites inside the MOF[162,222]. For the higher coverages, the Q_{st} appears to approach a pseudo-constant value of roughly 21-22 kJ/mol, with only small differences in the adsorption enthalpy between the MOFs, corresponding with the occupation of the low-affinity adsorption sites in the isostructural MOFs[162]. The change in Q_{st} of MOF-BA remains rather limited, suggesting a larger binding site homogeneity (as was also concluded from the CO_2 adsorption isotherm). CO_2 Q_{st} values in this work are comparable to the Q_{st} values reported in literature for similar MOFs. Plonka *et al.* found a Q_{st} of 32 kJ/mol for FA modulated MOF-808, well in line with our

findings[223]. Very similar values were reported for perfluoroalkane functionalized NU-1000 (which contains the same Zr_6 cluster as MOF-808) with $Q_{st,0}$ between 20 and 34 kJ/mol while the pristine NU-1000 gave a CO_2 $Q_{st,0}$ of 17 kJ/mol[162,224]. For UiO-66, CO_2 adsorption enthalpies at zero coverage vary between 26 and 38 kJ/mol, depending on the type of functionalization[225,226]. The highest Q_{st} in this work was noted for MOF-TFAA over the entire range of CO_2 loading. It is assumed that this high Q_{st} value of MOF-TFAA mainly follows from the strong dipole moment in the TFAA molecule, owing to the highly electronegative fluorine atoms[170].

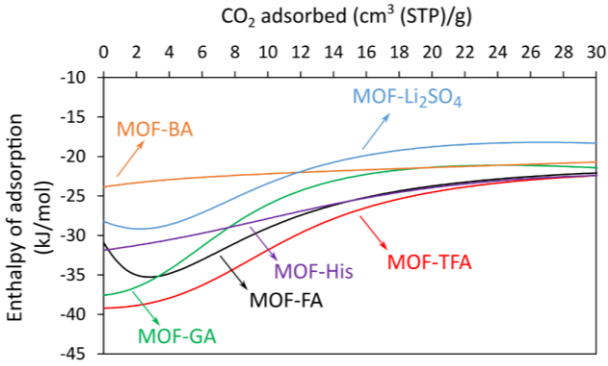

Figure 5-3: Experimental CO_2 adsorption enthalpies as a function of CO_2 loading for all MOFs.

Finally, N_2 and CO_2 sorption were measured for all membranes (Figure 5-4) and the corresponding solubility values were calculated in Table S5-5. With increasing pressure, the sorption of both N_2 and CO_2 in the membranes logically increases for all membrane types while the solubility decreases. CO_2 sorption in the membranes increases from Matrimid < MMM-GA < MMM-His < MMM-BA < MMM-FA < MMM-Li_2SO_4 < MMM-TFAA while an opposite trend can be observed for N_2 sorption, which decreases from MMM-GA > MMM-His > Matrimid > MMM-BA > MMM-FA > MMM-Li_2SO_4 > MMM-TFAA. In general, a strong improvement in solubility selectivity is observed for FA, BA, TFAA and Li_2SO_4 functionalized MOF-808 compared to the pristine Matrimid membrane while MOF-GA and MOF-His only modestly affect the CO_2/N_2 solubility selectivity. At 5 bar, the highest solubility selectivities are measured for MOF-TFAA (17.8) and MOF-Li_2SO_4 (18.4), which represent an 54% and 59% increase compared to Matrimid, respectively.

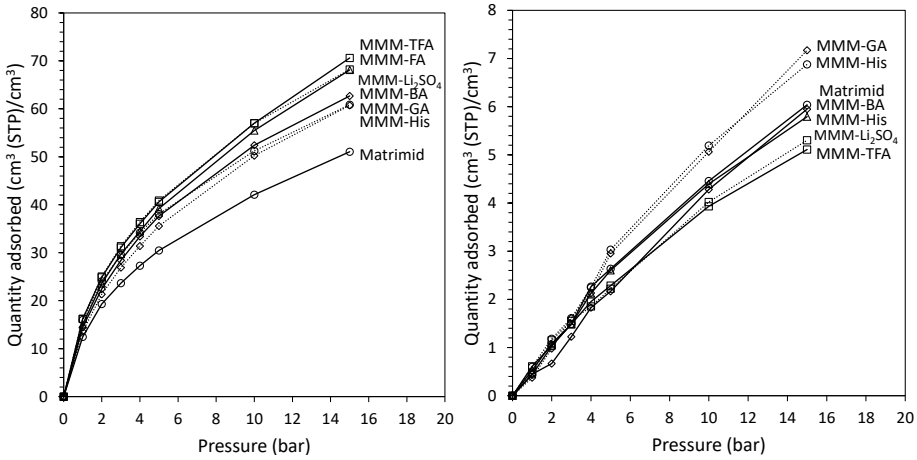

Figure 5-4: CO_2 (left) and N_2 (right) sorption in the Matrimid reference membrane and all MMMs.

5.3.2 Computational characterization of MOF-808

GCMC simulations were applied on MOF-FA and MOF-TFAA to acquire the MOF CO_2 adsorption sites, adsorption enthalpy and mixed-gas CO_2/N_2 adsorption selectivity. Additionally, the CO_2 adsorption isotherms were simulated and are available in Figure S5-9.

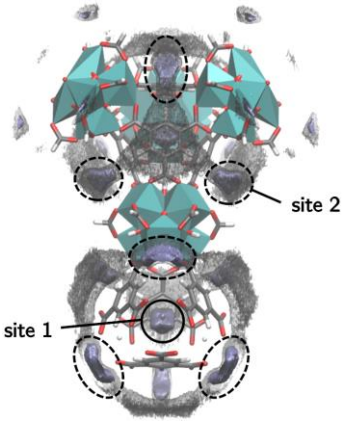

Figure 5-5: Two isosurfaces of the density of MOF-FA from GCMC simulations at 2 bar. The high density isosurface of sites 1 and 2 is shown in iceblue and a lower density isosurface is shown to encapsulate the metal cluster.

The adsorption densities of the CO_2 molecules at different pressure for MOF-FA are displayed in Figure 5-6, in which the primitive unit cell was expanded to the conventional cubic cell for ease of interpretation (Figure S5-10). At low pressures, the CO_2 molecules are primarily located within the cages formed by the four benzene rings of the linker, yielding a square grid of adsorption sites when viewing MOF-808 along the c-axis (marked as site 1 in Figure 5-5 and

Figure 5-6). A second type of adsorption sites that gain importance with increasing pressure are located in between the zirconium clusters, covering the open sides of the linkers (marked as site 2 in Figure 5-5 and Figure 5-6)[223]. At higher pressures, the linkers eventually become fully encapsulated by CO_2 with increasing pressure.

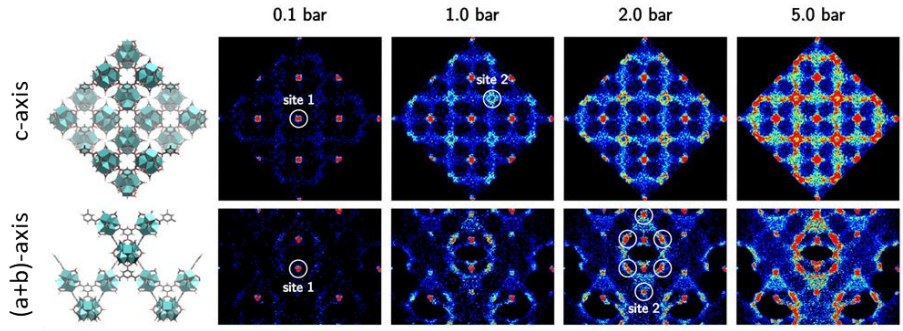

Figure 5-6: Density of the adsorbed CO_2 molecules in MOF-FA at 300 K projected on a plane orthogonal to the c-axis and the (a+b)-axis of the conventional unit cell. The CO_2 molecules are represented by the positions of the carbon atoms.

Although the adsorption sites for MOF-TFAA are similar, the filling pattern is different due to the presence of the TFAA functional groups, which results in a higher degree of localization of the adsorbed CO_2 molecules (Figure 5-7). After filling the tetragonal cages at the lowest pressures, the CO_2 molecules further adsorb onto the linkers. In contrast to MOF-FA, the adsorption sites located above the benzene rings of the linkers are also significantly occupied for mid-range pressures, implying that the surrounding TFAA functionalizations enhance the adsorption energy of these sites (more negative adsorption enthalpy).

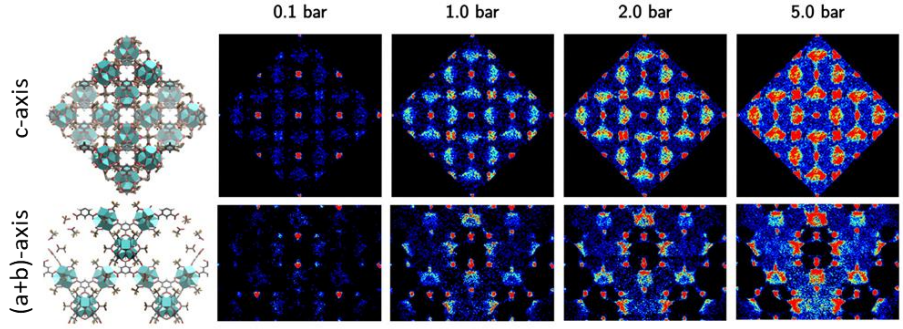

Figure 5-7: Density of the adsorbed CO_2 molecules in MOF-TFAA at 300 K projected on a plane orthogonal to the c-axis and the (a+b)-axis of the conventional unit cell. The CO_2 molecules are represented by the positions of the carbon atoms.

This is also confirmed by the calculated enthalpies of CO_2 adsorption for both MOFs (Figure 5-8, also Table S5-6). At the lowest pressures, the enthalpy of adsorption is completely dominated by the host-adsorbate interaction. Initially, the enthalpy values for MOF-FA and MOF-TFAA are

hence very similar as CO_2 first adsorbs in the tetragonal cages (site 1). Once adsorption sites on the linker molecules (site 2) become relevant, MOF-TFAA shows significantly lower adsorption enthalpies (stronger host-adsorbate interaction), in good agreement with the experimentally determined isosteric CO_2 adsorption enthalpy. A more moderate difference is observed at higher pressures as the adsorbate-adsorbate interactions also start to contribute to the adsorption enthalpy. Eventually, this is reflected in higher mixed-gas CO_2/N_2 selectivities for MOF-TFAA, confirming the experimental trends. Finally, the influence of open metal site defects (i.e. as a result of missing modulators) on the enthalpy of adsorption was also investigated for MOF-FA, by creation of a MOF-FA structure with 1 defect (MOF-FA-def1) and 3 defects (MOF-FA-def3), respectively (Figure S5-11 and Table S5-6). As can be seen in Figure 5-8, no difference in CO_2 adsorption enthalpy is observed between MOF-FA and MOF-FA-def1 while the CO_2 adsorption enthalpy of MOF-FA-def3 is slightly lower than that of MOF-FA but still significantly higher than the adsorption enthalpy of MOF-TFAA, indicating that the sole effect of defects on the CO_2 adsorption is rather limited in MOF-FA.

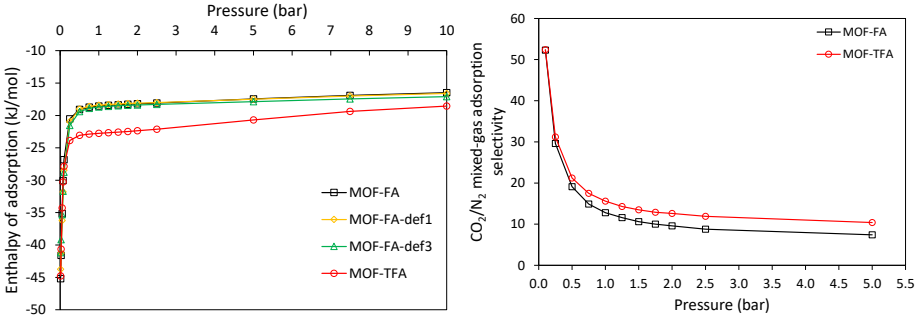

Figure 5-8: Simulated CO_2 adsorption enthalpies for MOF-FA, MOF-TFAA and MOF-FA with 1 and 3 defects, respectively (left). Simulated mixed-gas adsorption CO_2/N_2 selectivities for MOF-FA and MOF-TFAA (right).

5.3.3 Gas permeation experiments

CO_2 permeability of the mixed-gas experiments with 15v%/85v% and 50v%/50v% CO_2/N_2 feed compositions and of the CO_2 pure gas experiment is given in Figure 5-9. All MMMs show a significantly higher CO_2 permeability for all feed compositions compared to the pristine Matrimid membrane, owing to the incorporation of the MOF[135,136]. For the 15v%/85v% CO_2/N_2, the 50v%/50v% CO_2/N_2 and the pure CO_2 data, respectively, the smallest permeability increase was observed for MMM-Li_2SO_4 (+23%, +20%, +15%) while the most substantial increase was recorded for MMMs containing MOF-TFAA (+52%, +72%, +72%) as a result of a substantially increased CO_2 solubility upon incorporation of the TFAA functionalized MOF (+33%). The low MMM-Li_2SO_4 permeability can be linked to the above-mentioned pore blockage by Li_2SO_4 deposition. Furthermore, a similar trend can be seen for the various feed conditions with the CO_2 permeability increasing in the order Matrimid < MMM-Li_2SO_4 < MMM-His ≈ MMM-GA ≈ MMM-BA ≈ MMM-FA < MMM-TFAA. Finally, the CO_2 permeability is reduced when the CO_2 content in the feed is increased from 15% to 50% and eventually to 100%. A similar trend was

observed for UiO-66-NH_2 MMMs based on various fluorinated polyimides[79,150,185]. These observations are in line with the dual-mode sorption model, which predicts saturation of polymer excess free volume elements at elevated CO_2 pressure, resulting in a lowered CO_2 solubility[21,24].

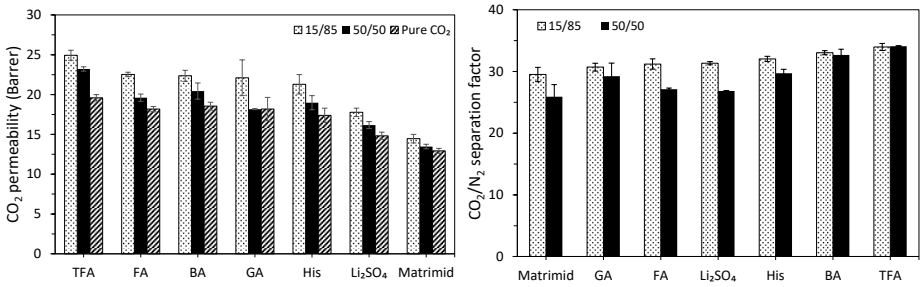

Figure 5-9: CO_2 permeability (left) and CO_2/N_2 separation factor (right) for the 15v%/85v% and 50v%/50v% mixed-gas CO_2/N_2 experiment and the CO_2 pure gas experiment of all membranes. Gas filtrations were performed at 30 °C and 5 bar feed pressure. All MMMs contain 10 wt.% MOF.

The CO_2/N_2 separation factors of Matrimid (Figure 5-9) for the 15v%/85v% (29.5) and the 50v%/50v% feed (25.9) are similar to literature[227,228]. In general, incorporation of the functionalized MOFs leads to a small enhancement in CO_2/N_2 separation factor for both feed mixtures compared to the pristine Matrimid membrane, but only small differences can be noticed between the MMMs. Polymer rigidification at the particle/polymer interface might (partially) explain the higher MMM separation factor. Previously, no large variations in T_g were detected for Matrimid MMMs containing MOF-808 with different functional groups, indicating that the degree of polymer rigidification upon particle incorporation was equal for all MMMs[95]. Since this work entails almost identical MMMs and no differences in particle morphology or particle size were observed with SEM (as all MOFs were synthesized starting from the same MOF-FA batch), it is reasonable to assume that polymer rigidification is equal for all MMMs. Similar to the permeability measurements, MOF-TFAA causes the largest improvement of the separation factor of all MOFs, while MOF-GA, MOF-Li_2SO_4 and MOF-FA do not significantly affect the 15v%/85v% and 50v%/50v% separation factor. Functionalization with TFAA (+9%, +25%) results in the best performance (compared to MMM-FA), which can be explained by the improved CO_2/N_2 selectivity for MOF-TFAA (as was confirmed by the GCMC simulations) and the resulting increasing in solubility selectivity for MMM-TFAA. As mentioned earlier, it is believed that the strongly polarized C-F bonds in MOF-TFAA and the consequent higher CO_2 affinity are at the base of the good separation factor for MMM-TFAA[95]. This was confirmed by both experimental and simulated CO_2 adsorption enthalpies, which were significantly lower (stronger MOF-CO_2 interaction) upon functionalization with TFAA and eventually resulted in an enhanced CO_2/N_2 mixed-gas adsorption selectivity for MOF-TFAA compared to MOF-FA (Figure 5-8). For the BA functionalized MOF, MMM-BA probably profits from enhanced π-π interaction between phenyl groups at the MOF surface and aromatic moieties of the polymer chains, which has previously been reported to improve polymer-MOF compatibility and, as a result, the

separation factor[80]. It can be hypothesized that a higher CO_2 Q_{st} might lead to a higher selectivity for the MMM based on MOF-TFAA, but observations for MOF-BA (with the lowest $Q_{st,0}$ but second highest α^*) contradict this. Finally, a lowered CO_2/N_2 selectivity for the 50v%/50v% feed is expected based on the dual-sorption model as the N_2 partial pressure is reduced (higher N_2 permeability), while the CO_2 partial pressure is enhanced (lower CO_2 permeability)[21].

5.3.4 Correlation of MOF parameters with membrane CO_2 permeation

Overall, the effect of ligand type on the MMM CO_2 permeability and CO_2/N_2 separation factor strongly varies when compared to the MOF-FA starting material. Only functionalization with TFAA and Li_2SO_4 causes the MMM permeability to change significantly while improved separation factors with respect to MOF-FA are only observed for BA and TFAA functionalization. To quantify the relationship between the examined MOF properties and the MMM permeation behavior, correlation coefficients between these parameters have been calculated in Table 5-2. Results were interpreted based on statistic guidelines defined by Ross *et al.*[229]. Correlation coefficients lower than 0.30 are considered as weak correlations, between 0.30 and 0.80 as moderate and higher than 0.80 as strong.

The conventional MOF parameters (BET surface area and pore volume) display a moderate linear correlation with the obtained permeabilities. This seems reasonable, owing to the positive relationship between gas diffusivity and MMM free volume[21]. In addition, a weak correlation is observed between these parameters with the CO_2/N_2 separation factor. Unexpectedly, also CO_2 uptake in both the low (at 50 mbar) and high (at 1000 mbar) pressure region correlates very poorly with both separation factors, while only moderate correlations were noted with permeability in 15v%/85v%, 50v%/50v% and pure CO_2 feed. This strongly contrasts with literature, where a high CO_2 uptake is very frequently used to explain MMM permeation observations[98,230]. The correlation of Q_{st} on one hand with CO_2 permeability and CO_2/N_2 separation factor on the other hand is less straightforward to interpret. The adsorption enthalpy at zero coverage ($Q_{st,0}$) shows moderate correlation with the CO_2 permeabilities, comparable to the CO_2 uptake values. Similarly, only weak correlations are observed for $Q_{st,0}$ and the different separation factors. Interestingly, strong correlations are observed between $Q_{st,15}$ and $Q_{st,30}$ on one hand and $P_{15/85}$, $P_{50/50}$ and $P_{100/0}$ on the other hand while correlation coefficients of $Q_{st,15}$ and $Q_{st,30}$ with the $\alpha^*_{15/85}$ and $\alpha^*_{50/50}$ are higher than for CO_2 uptake but are still considered only moderate. As such, Q_{st} can be considered as the most effective predictor for MMM CO_2 permeability amongst all MOF parameters.

A possible explanation for the difference in correlation strength of the Q_{st} at low loading and the ones at high loading might be found in the existence of mobile and immobile gas species in the membrane[231]. $Q_{st,0}$ represents the adsorption enthalpy of the high affinity sorption sites in the MOF and can possibly be linked to the tetragonal cages, which, at very low CO_2 pressure, are the primary CO_2 sorption sites (marked as site 1 in Figure 5-6 and Figure 5-7). These sites correspond with highly negative CO_2 adsorption enthalpies (very strong MOF-CO_2 interaction) and the highest CO_2/N_2 mixed-gas adsorption selectivity values observed (up to 60, Figure 5-8). Moreover, they are present in both MOF-FA and MOF-TFAA (and, by extension, in all

functionalized MOF-808 samples), explaining the very similar enthalpy and selectivity values for both MOFs at low CO_2 pressures. At relatively higher CO_2 pressures (starting from 0.25 bar in Figure 5-8), the GCMC simulations show substantial differences in adsorption enthalpy and CO_2/N_2 adsorption selectivities between MOF-FA and MOF-TFAA caused by the increased influence of the second type of adsorption sites (marked as site 2 in Figure 5-6 and Figure 5-7). It can thus be hypothesized that these sites (partially) immobilize gas molecules through (too) strong binding interaction[8] and thus do not (or to a lesser extent) contribute to gas permeation through the membrane. Although this hypothesis should be proven by performing time-lag experiments, it would explain the observed difference in correlation coefficients for $Q_{st,0}$ and $Q_{st,30}$[231].

As the overall gas permeability through the MMM is a net result of both MOF and polymer properties and their mutual interactions, it is not unexpected that none of the MOF parameters can predict the trends in MMM permeability one-on-one. Nonetheless, the unanticipated lack of correlation for CO_2 permeability with CO_2 uptake and its strong correlation with $Q_{st,15}$ and $Q_{st,30}$ once more underline the difficulty to formulate strong and general guidelines to steer MMM design and, more importantly, the need for more research focused at finding consistent relationships between MOF and MMM structures and ultimate membrane performance.

Table 5-2: Correlation coefficients between MOF-808 parameters (CO_2 uptake at 50 and 1000 mbar and Q_{st} at a coverage of 0, 15, 30 cm^3 (STP)/g) and the corresponding MMM parameters (α^* at 15v%/85v% and 50v%/50v% CO_2/N_2 feed, and CO_2 permeabilities for 15v%/85v% and 50v%/50v% CO_2/N_2 feed and the pure CO_2 feed ($P_{100/0}$)). Strong correlations are indicated in green and weak correlations in red. Intermediate correlations have no special markings.

	CO_2 uptake (50 mbar)	CO_2 uptake (1000 mbar)	BET surface area	Pore volume	$Q_{st,0}$	$Q_{st,15}$	$Q_{st,30}$
$\alpha^*_{15/85}$	0.079	0.053	0.123	0.173	0.056	0.414	0.291
$\alpha^*_{50/50}$	0.010	0.106	0.126	0.230	0.222	0.368	0.423
$P_{15/85}$	0.431	0.658	0.722	**0.800**	0.513	0.756	**0.834**
$P_{50/50}$	0.532	0.558	0.681	0.733	0.473	**0.844**	0.793
$P_{100/0}$	0.352	0.665	0.622	0.716	0.433	0.715	**0.866**

5.4 Conclusions

An attempt was made to correlate MOF-808 parameters with the CO_2/N_2 separation performance indicators of the corresponding MMMs. More specifically, MOF CO_2 uptake, CO_2 Q_{st}, pore volume and BET surface area were correlated with the MMM CO_2/N_2 separation factor and CO_2 permeability under varying feed conditions. Post-synthetic functionalization of FA modulated MOF-808 with different ligands (i.e. TFAA, BA, GA, histidine and Li_2SO_4) proved to be a successful tool to influence this set of MOF parameters, leading to a broad range of systematically varying parameter values for BET surface area, pore volume, CO_2 uptake and CO_2 Q_{st}. For the different MOF-808 MMMs tested in this work, MOF CO_2 uptake was a poor predictor for MMM performance, showing a very weak correlation with CO_2/N_2 separation factor and only moderate correlation with CO_2 permeability. This is in contrast to literature where CO_2 uptake is one of the dominant factors used to explain MMM separation behavior. The loading-dependent CO_2 Q_{st} correlates substantially better with the membrane performance indicators than CO_2 uptake. Correlation coefficients of $Q_{st,15}$ and $Q_{st,30}$ with the separation factor were higher than for CO_2 uptake but were still considered only moderate. A strong correlation was found between $Q_{st,15}$ and $Q_{st,30}$ on one hand and $P_{15/85}$, $P_{50/50}$ and $P_{0/100}$ on the other hand, indicating that Q_{st} can be considered as the most effective predictor for MMM CO_2 permeability amongst the MOF parameters. Interestingly, Q_{st} at zero coverage did not show a strong correlation with the MMM performance indicators. GCMC simulations on MOF-FA and MOF-TFAA revealed the existence of 2 types of adsorption sites in MOF-808. The first type of adsorption type is independent of cluster functionalization (e.g. TFAA instead of FA) and corresponds with the tetragonal cage, resulting in very strong MOF-CO_2 interaction (highly negative adsorption enthalpies) even at low CO_2 pressures while the second type of adsorption site was shown to be susceptible to TFAA functionalization. Finally, the existence of different adsorption sites with varying adsorption enthalpies was linked to the observed difference in correlation coefficients for $Q_{st,0}$ and $Q_{st,30}$ with CO_2 permeability.

5.5 Acknowledgements

R.T., N.V.V. and A.L. acknowledge the FWO for their support through a(n) (SB-)PhD fellowship (1S63317N, 1S32917N and 11D2220N). A.L. and V.V.S. would also like to thank the Research Board of Ghent University (BOF) for their support and the European Union's Horizon 2020 Research and Innovation Programme [ERC Consolidator Grant Agreement 647755 – DYNPOR (2015-2020)] for the received funding. The computational resources (Stevin Supercomputer Infrastructure) and services used in this work were provided by the VSC (Flemish Supercomputer Center), funded by Ghent University, FWO and the Flemish Government – department EWI.

5.6 Supplementary information to Chapter 5

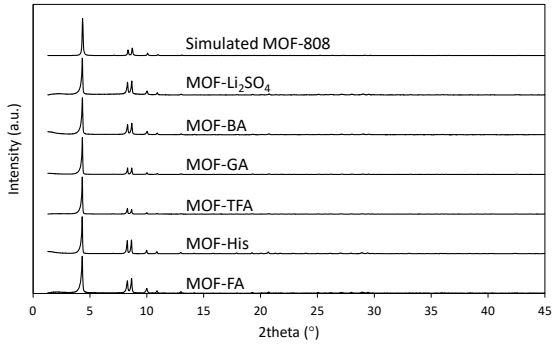

Figure S5-1: XRD patterns of all MOF samples.

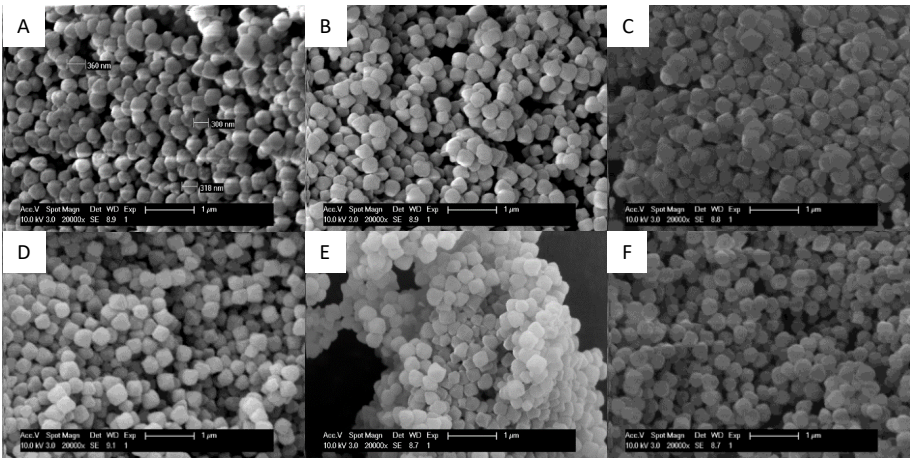

Figure S5-2: SEM images of all MOF particles: (A) MOF-FA, (B) MOF-GA, (C) MOF-His, (D) MOF-BA, (E) MOF-TFAA and (F) MOF-Li_2SO_4.

Table S5-1: Average size of all MOFs calculated after ImageJ analysis. 30 samples were measured per MOF.

	Number	Average size (nm)	Variance
MOF-BA	30	362.7	2132.1
MOF-FA	30	346.6	1080.2
MOF-GA	30	352.1	813.32
MOF-His	30	355.5	1786.3
MOF-Li_2SO_4	30	336.7	1131.8
MOF-TFAA	30	347.8	914.24

Table S5-2: ANOVA analysis of the MOF particle sizes. As the p-value is larger than the significance level (0.05), no statistically significant difference in size exists between the samples.

ANOVA

Source of Variation	SS	df	MS	F	p-value	F crit
Between Groups	11680.1	5	2336	1.7837	0.1185	2.2661
Within Groups	227882	174	1310			
Total	239562	179				

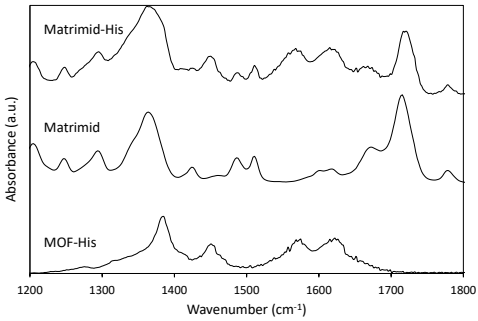

Figure S5-3: ATR-FTIR spectrum of MMM-His, Matrimid and MOF-His.

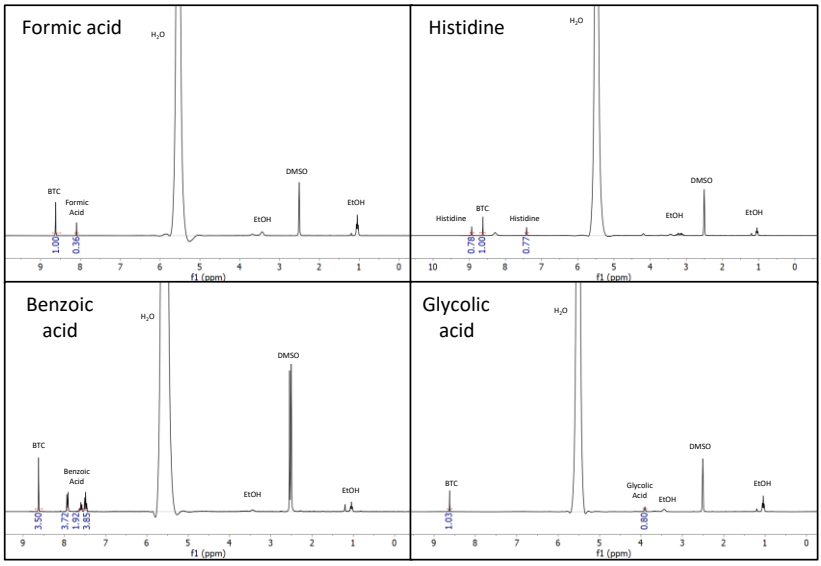

Figure S5-4: ^{1}H-NMR spectra for MOF-FA, MOF-BA, MOF-His and MOF-GA.

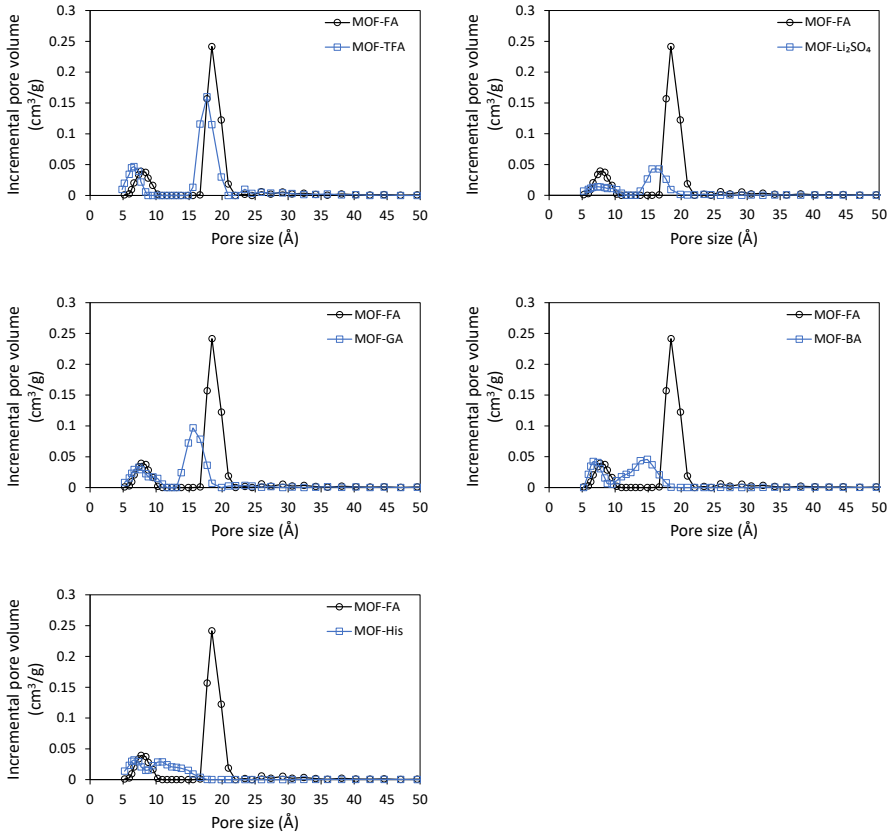

Figure S5-5: Incremental pore volume as a function of pore size for all MOFs.

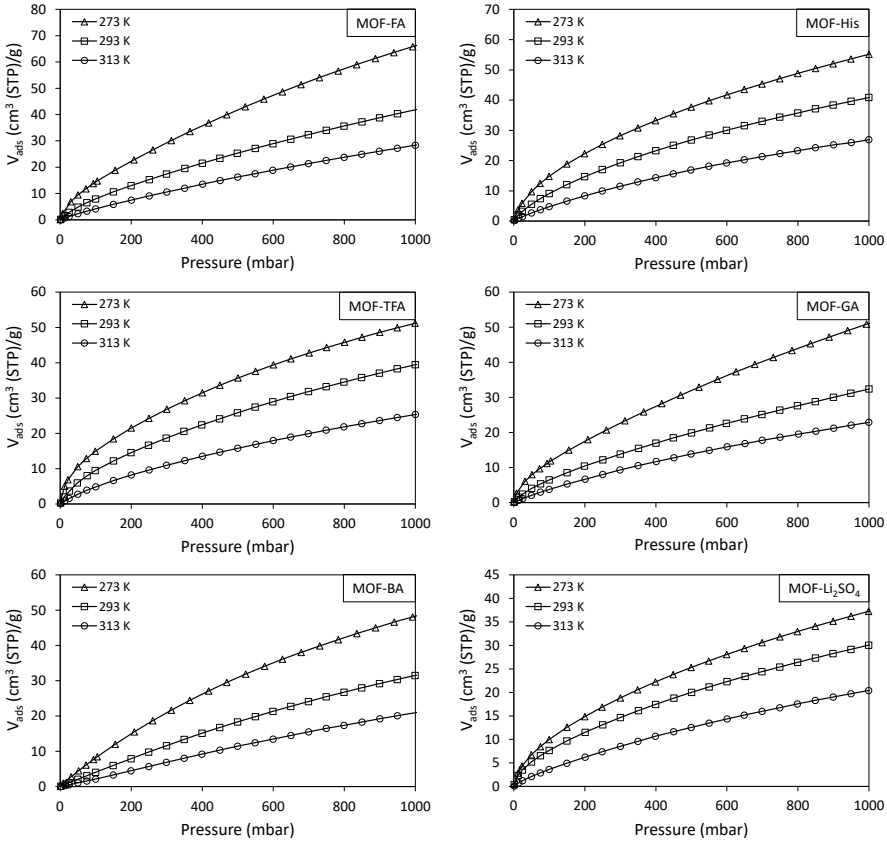

Figure S5-6: CO_2 uptake of all MOFs at 273 K, 293 K and 313 K.

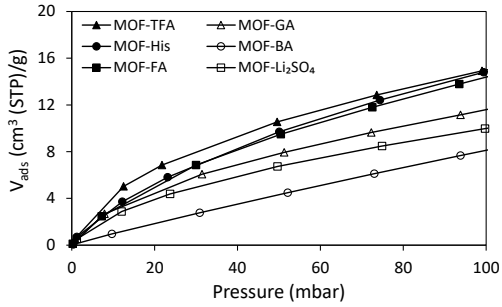

Figure S5-7: CO_2 adsorption isotherms of all MOFs in the low-pressure region (0-100 mbar) at 273 K.

Table S5-3: Model parameters for the dual-site Langmuir fit on the CO_2 adsorption isotherm at 273 K. N is the amount of adsorbed gas (cm^3 (STP)/g), $N_{m,A}$ and $N_{m,B}$ the amount of adsorbed gas at saturation for sorption site A and B, respectively (cm^3 (STP)/g) and b_A and b_B the adsorption equilibrium constants for, respectively, sorption site A and B. R^2 is the correlation coefficient.

	$N_{m,A}$	$N_{m,B}$	b_A	b_B	R^2
MOF-FA	0.34	8.74	0.046	0.00042	1.0000
MOF-GA	0.32	8.14	0.048	0.00031	1.0000
MOF-BA	0.04	4.95	0.014	0.00073	1.0000
MOF-TFAA	0.43	4.44	0.056	0.00070	1.0000
MOF-His	0.59	5.59	0.020	0.00050	0.9999
MOF-Li_2SO_4	0.35	3.87	0.028	0.00051	0.9999

Table S5-4: CO_2 Q_{st} (kJ/mol) of all MOFs for different CO_2 loadings (0, 5, 15, 30 cm^3 (STP)/g).

	CO_2 adsorbed (cm^3 (STP)/g)			
	0	**5**	**15**	**30**
MOF-FA	30.9	34.1	25.6	22.1
MOF-His	31.8	30.1	25.6	22.4
MOF-TFAA	39.2	37.2	27.7	22.5
MOF-GA	37.6	32.9	22.6	21.4
MOF-BA	23.9	22.8	21.8	20.7
MOF-Li_2SO_4	28.2	28.0	20.3	18.3

Table S5-5: Solubility (S) of CO_2 and N_2 in the Matrimid reference membrane and the MMMs. S_{CO2}/S_{N2} constitutes the CO_2/N_2 solubility selectivity. Measurements were conducted at 30 °C and varying pressures (see table).

Pressure (bar)	Membrane	S_{N2}	S_{CO2}	S_{CO2}/S_{N2}
5	Matrimid	0.00703	0.08125	11.6
	MMM-GA	0.00788	0.09487	12.0
	MMM-His	0.00809	0.10152	12.5
	MMM-FA	0.00694	0.10454	15.1
	MMM-BA	0.00578	0.10036	17.4
	MMM-TFAA	0.00609	0.10828	17.8
	MMM-Li_2SO_4	0.00592	0.10901	18.4
10	Matrimid	0.00594	0.05615	9.45
	MMM-GA	0.00675	0.06699	9.92
	MMM-His	0.00692	0.06833	9.87
	MMM-FA	0.00586	0.07399	12.6
	MMM-BA	0.00571	0.06989	12.2
	MMM-TFAA	0.00524	0.07603	14.5
	MMM-Li_2SO_4	0.00536	0.07594	14.2
15	Matrimid	0.00537	0.04539	8.46
	MMM-GA	0.00637	0.05398	8.46
	MMM-His	0.00611	0.05410	8.85
	MMM-FA	0.00515	0.06053	11.8
	MMM-BA	0.00529	0.05572	10.5
	MMM-TFAA	0.00454	0.06277	13.8
	MMM-Li_2SO_4	0.00472	0.06062	12.9

Force fields

To perform static GCMC (Grand Canonical Monte Carlo) simulations for the differently functionalized MOF-808 structures, each structure was parametrized by a non-covalent force field that contains both electrostatic and van der Waals interactions:

$$V = V_{ei} + V_{vdW} \qquad \text{(Equation 5.9)}$$

The electrostatic interactions are modelled by a Coulomb interaction between Gaussian charge distributions, which are derived from cluster models of the MOF-808 $Zr_6O_8H_x$ brick, using phenyl terminations at the positions of the six BTC^{3-} linkers (Figure S5-8). After a geometry optimization with Gaussian 16[232], using the B3LYP functional[233] and 6-311g(d,p) basis sets[234] for all atoms but zirconium, for which the LanL2DZ basis set and pseudopotential are used[235], the electron density of the cluster is determined with gpaw[236] using the PBE functional[197]. Finally, the atomic charges q_i are derived with the Minimal Basis Iterative Stockholder (MBIS) partitioning scheme[237], so that the electrostatic interaction is given by

$$V_{ei} = \frac{1}{2}\sum_{\substack{i,j=1 \\ (i\neq j)}} \frac{q_i q_j}{4\pi\epsilon_0 r_{ij}} \operatorname{erf}\left(\frac{r_{ij}}{d_{ij}}\right) \quad \text{(Equation 5.10)}$$

with r_{ij} the distance between atoms i and j, and q_i and d_i respectively the total charge and the radius of the Gaussian charge distribution[238] centered on atom i. The mixed radius d_{ij} of the Gaussian charges is given by $\sqrt{d_i^2 + d_j^2}$.

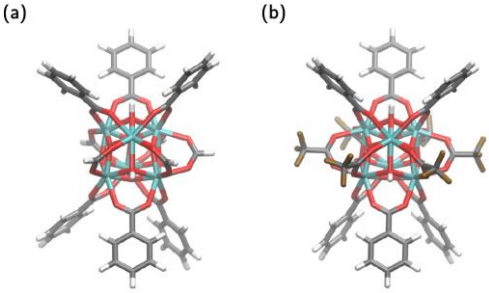

Figure S5-8: Cluster models used in the derivation of the atomic charges of (a) MOF-FA-def1 and (b) MOF-TFAA.

The van der Waals interactions are modelled by a Lennard-Jones potential:

$$V_{vdW} = \sum_{i<j} 4\epsilon_{ij}\left[\left(\frac{\sigma_{ij}}{r_{ij}}\right)^{12} - \left(\frac{\sigma_{ij}}{r_{ij}}\right)^{6}\right] \quad \text{(Equation 5.11)}$$

for which the parameters σ_{ij} and ϵ_{ij} between atom i and j are derived from the atomic DREIDING parameters[205] (and UFF parameters[207] for zirconium), using the Lorentz-Berthelot mixing rules:

$$\sigma_{ij} = \frac{\sigma_i + \sigma_j}{2} \text{ and } \epsilon_{ij} = \sqrt{\epsilon_i \epsilon_j} \quad \text{(Equation 5.12)}$$

In the GCMC simulations, the Lennard-Jones interactions are truncated at 10.1 Å and complemented by the appropriate tail corrections.

Modelled CO_2 isotherms

The CO_2 adsorption isotherms obtained from GCMC simulations at different pressures for MOF-FA and MOF-TFAA are given in Figure S5-9. The isotherms for both MOF-FA and MOF-TFAA are similar to the experimental ones, although small differences can be observed. These can be attributed to the different number of modulator molecules on the zirconium cluster and the slightly higher temperature at which CO_2 adsorption was simulated. For MOF-FA, two defect structures with, respectively, one and three missing formate groups per zirconium cluster are modelled next to the pristine MOF-FA (containing six formate groups per cluster). The absolute differences (i.e. the number of adsorbed CO_2 molecules per unit cell) between the pristine and defects structures are small and only significant at higher pressures. However, per unit of mass,

this results in a slightly larger uptake for MOF-FA with three defects in comparison to pristine MOF-FA.

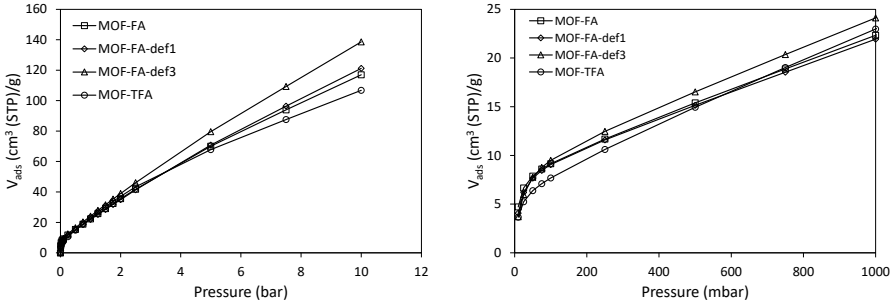

Figure S5-9: Modelled CO_2 adsorption isotherms for MOF-FA and MOF-TFAA. For MOF-FA, the number of defects (i.e. absence of formate molecule) on the zirconium clusters has been varied from one (MOF-FA-def1) to three (MOF-FA-def3).

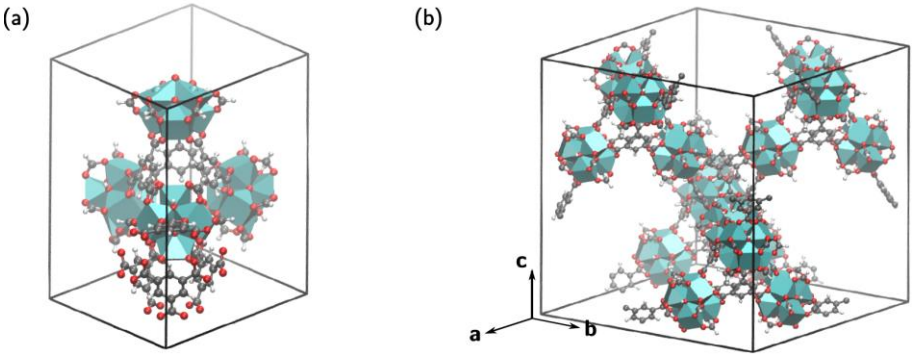

Figure S5-10: (a) Primitive unit cell of MOF-FA. (b) Conventional cubic unit cell of MOF-FA.

The CO_2 density in MOF-FA-def1 exhibits only small differences in comparison with the pristine MOF-FA. MOF-FA-def3, on the other hand, does show some interesting differences (Figure S5-11). Similar to MOF-FA, the CO_2 molecules are first adsorbed in the cages of the linkers, yielding a square grid of adsorption sites when viewing MOF-808 along the c-axis. The second type of adsorption sites, covering the open sides of the linkers, become more prominently occupied with increasing pressure, but do not longer give rise to a square grid of adsorption sites. This is due to the fact that an additional type of adsorption sites is present in MOF-FA-def3, located on the open metal sites of the zirconium clusters (marked as site 3 in Figure S5-11). These adsorption sites are observed to be more favorable than the adsorption sites located at the linkers. With increasing pressure the MOF-808 structure exhibits a different encapsulation, which is primarily formed by the adsorption sites at the open metal sites and the adsorption sites at the open sides of the linkers. The adsorption sites above the benzene rings of the linkers are not as significantly occupied as in pristine MOF-FA, not even at the highest pressures.

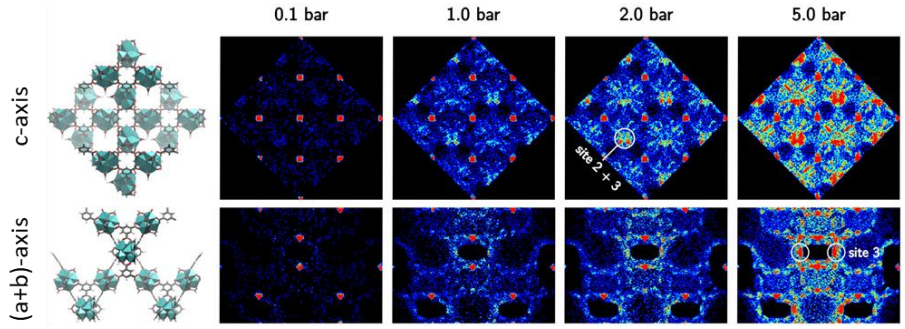

Figure S5-11: Density of the adsorbed CO_2 molecules in MOF-FA-def3 at 300 K projected on a plane orthogonal to the c-axis and the (a + b)-axis of the conventional unit cell. The CO_2 molecules are represented by the positions of the carbon atoms.

Table S5-6: Simulated adsorption enthalpies for MOF-FA, MOF-TFAA and MOF-FA with 1 and 3 defect(s), respectively.

Pressure (bar)	MOF-FA	MOF-FA-def1	MOF-FA-def3	MOF-TFAA
0.010	-45.2	-43.7	-41.2	-44.8
0.025	-41.6	-41.2	-39.2	-40.6
0.050	-35.2	-36.2	-35.3	-34.3
0.075	-30.1	-31.8	-31.7	-30.3
0.10	-26.8	-28.5	-28.8	-27.9
0.25	-20.5	-21.0	-21.5	-23.9
0.50	-19.1	-19.0	-19.4	-23.1
0.75	-18.7	-18.6	-18.9	-22.9
1.00	-18.6	-18.4	-18.7	-22.8
1.25	-18.4	-18.3	-18.6	-22.7
1.50	-18.4	-18.2	-18.5	-22.6
1.75	-18.3	-18.2	-18.4	-22.5
2.00	-18.2	-18.1	-18.4	-22.4
2.50	-18.1	-18.0	-18.3	-22.1
5.00	-17.4	-17.5	-17.9	-20.7
7.50	-16.9	-17.0	-17.5	-19.4
10.0	-16.5	-16.6	-17.1	-18.6

Chapter 6

Tuning 6FDA-DABA membrane performance for CO_2 removal by physical densification and decarboxylation cross-linking during simple thermal treatment

Raymond Thür[a], Vincent Lemmens[a], Daan Van Havere[a], Machiel van Essen[b], Kitty Nijmeijer[b], Ivo F.J. Vankelecom[a]

*Based on *Journal of Membrane Science, 2020, 610, 118195*

[a]Centre for Membrane Separations, Adsorption, Catalysis and Spectroscopy for Sustainable Solutions (cMACS), KU Leuven, Celestijnenlaan 200F, Box 2454, 3001 Heverlee, Belgium

[b]Membrane Materials and Processes, Department of Chemical Engineering and Chemistry, Eindhoven University of Technology, P.O. Box 513, 5600 MB Eindhoven, the Netherlands

*https://doi.org/10.1016/j.memsci.2020.118195

Abstract

Thermally induced decarboxylation cross-linking of carboxylic acid bearing polyimides has been recently introduced to create cross-linked polymer membranes with enhanced gas permeability. The main focus has been on the cross-linking of high permeability/low selectivity 6FDA co-polymers with a relatively low amount of carboxylic acid groups. In contrast, decarboxylation cross-linking was applied in this work on a low permeability/high selectivity polymer with a large amount of –COOH groups (pure 6FDA-DABA). 6FDA-DABA membranes were thermally treated at different temperatures (100 °C, 180 °C, 250 °C, 350 °C and 400 °C), tested for CO_2/CH_4 and CO_2/N_2 separation and thoroughly characterized by ATR-FTIR, TGA-MS, DSC, EDX, XRD, density measurements, fluorescence spectroscopy and gas sorption measurements. Two counteracting mechanisms defined the overall performance of the cured membranes. Physical tightening of the membrane significantly enhanced the CO_2/CH_4 separation factor with increasing annealing temperature due to an improved polymer chain packing efficiency, which was confirmed by fluorescence spectroscopy and membrane density experiments. In contrast, cross-linking through decarboxylation of the –COOH groups occurred from 330 °C onward and induced a more open polymer structure for 6FDA-DABA-350 and 6FDA-DABA-400. The more open polymer structure resulted in an increase in permeability of all gases. For 6FDA-DABA-350, a synergy was observed between the dilation effect of cross-linking and the tightening effect, causing a simultaneous, strong improvement of both separation factor (+100%) and permeability (+40%). As a result, the membrane performance crossed the 2018 mixed-gas upper bound and scored very close to the 2008 Robeson upper bound. Moreover, the cross-linked 6FDA-DABA-350 showed an increased resistance to CO_2-induced plasticization thanks to covalent cross-linking.

Contributions

Raymond Thür: design and coordination of experiments, membrane preparation, characterization (ATR-FTIR, TGA, DSC, XRD, density measurements), gas permeation experiments, data analysis, manuscript writing and redaction. Vincent Lemmens: design of experiments, membrane preparation, gas permeation experiments, data analysis, manuscript correction and redaction. Daan Van Havere: fluorescence experiments, manuscript correction and redaction. Machiel van Essen: gas sorption experiments, manuscript correction and redaction. Kitty Nijmeijer: manuscript correction and redaction. Ivo F.J. Vankelecom: manuscript correction and redaction.

6.1 Introduction

Aromatic polyimide (PI) membranes have been extensively studied for the sweetening of sour gas streams such as raw natural gas[9] and bio gas[146] because they combine an acceptable CO_2/CH_4 separation performance with excellent thermal, mechanical and chemical stability. Moreover, aromatic PIs are economically viable to synthesize and show good processability (solvent compatibility and thin-film processing)[34]. However, PI membranes are also prone to plasticization by highly condensable gases, such as CO_2 and organic vapors, with a loss in performance as a result[95,239]. To mitigate the effect of plasticization and also to further improve the membrane performance, thermal treatments have been frequently applied[40,127,240–245]. For example, thermally rearranged (TR) polybenzoxazole (PBO) polymers, first described in 2007[245], were prepared by exposing a PI precursor with an ortho-positioned hydroxyl group (i.e. 2,2'-bis(3-amino-4-hydroxylphenyl) hexafluoropropane) to temperatures up to 450 °C, leading to a rearrangement of the molecular structure of the polymer[62,239]. These membranes can reach gas permeabilities up to several orders of magnitude higher than the original polymer and often have improved resistance to plasticization. Next to TR membranes, thermally induced decarboxylation cross-linking of carboxylic acid bearing polymers has emerged as a relatively straightforward way of creating covalently bound polymer chains, resulting in plasticization resistance[241,246,247]. Furthermore, decarboxylation cross-linking can also induce a beneficial effect on permeability[39] or selectivity[246]. It is of importance to execute the thermal treatment at temperatures below the polymer glass transition temperature (T_g) to prevent pore collapse of the support layer and to retain the polymer's good processability (e.g. flexibility)[39]. The past years, the main focus has been on the cross-linking of high permeability/low selectivity 6FDA ((i.e. 4,4'-(hexafluoroisopropylidene)-diphthalic anhydride) copolymers with a relatively low amount of carboxylic acid groups. 6FDA-DAM:DABA (2:1) and 6FDA-DAM:DABA (3:2) copolymers were cross-linked by Koros and coworkers, resulting in plasticization-resistant membranes, several times more permeable for CO_2 at the cost of only a small loss in selectivity[39,241]. Furthermore, bulky carboxylated diamines were combined with 6FDA, 3,3',4,4'-benzophenonetetracarboxylic acid (BTDA) and 3,3',4,4'-diphenyl-sulfonetetracarboxylic dianhydride (DSDA) moieties to generate larger interchain distances compared to DABA-based cross-linking. For the different membranes tested, a relatively stable or slightly lower CO_2/CH_4 ideal selectivity with enhanced CO_2 permeability was achieved[240]. Tian *et al.* synthesized triptycene-based 6FDA PIs with low carboxylic acid content and obtained similar trends in selectivity and CO_2 permeability after sub-T_g annealing[40].

In contrast to the high permeability/low selectivity polymers with relatively few –COOH groups that have been studied so far in literature, decarboxylation cross-linking was applied in this work on a low permeability/high selectivity polymer with a large amount of –COOH groups (pure 6FDA-DABA). The hypothesis was that, since decarboxylation cross-linking generally enhances the membrane permeability and since membranes with high selectivity become desirable (at an adequate CO_2 permeance) for gas streams with elevated CO_2 concentration[248], the choice for 6FDA-DABA as a highly selective starting material can render a membrane with beneficial combination of high CO_2/CH_4 selectivity and enhanced CO_2 permeability.

6.2 Materials and methods

6.2.1 Chemicals

6FDA-DABA (Figure 6-1) was kindly provided by Fujifilm Manufacturing Europe B.V. (Tilburg, the Netherlands). Tetrahydrofuran (THF, 99.5%), N-methylpyrrolidone (NMP, 99.5%) and dimethylsulfoxide (DMSO, 99.8%) were purchased from Acros and used as delivered. CO_2 (>99.999%), N_2 (>99.999%) and CH_4 (>99.9995%) gases were purchased from Air Liquide (Belgium) and used as delivered.

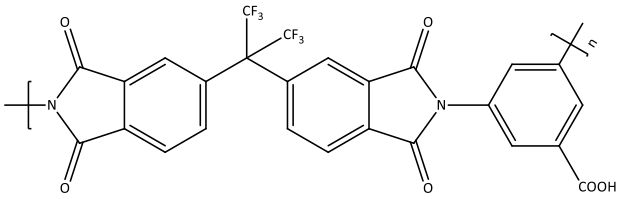

Figure 6-1: Chemical structure of 6FDA-DABA with weight average molecular weight M_w = 97 kD, number average molecular weight M_n = 41 kD and M_w/M_n = 2.37.

6.2.2 Membrane synthesis

7 wt.% polymer (0.42 g) was dissolved in THF (5.58 g) and stirred overnight. The polymer solution was cast in a Teflon petri dish in a nitrogen bag and covered with a plastic funnel to slow down solvent evaporation. Next, the solidified film was removed from the petri dish and annealed in a muffle oven at 5 °C/min at different temperatures, according to the heating protocol in Table S6-1.

6.2.3 Characterization

6.2.3.1 Solubility tests

Solubility tests in THF, NMP and DMSO were performed to verify whether annealed membranes were still soluble after thermal treatment.

6.2.3.2 ATR-FTIR

ATR-FTIR was performed with a Bruker Alpha instrument containing a diamond ATR crystal. A collection of 32 scans at a resolution of 2 cm^{-1} was measured.

6.2.3.3 XRD

XRD patterns were measured by using a Malvern PANalytical Empyrean diffractometer in transmission mode over a 1.3-45° 2θ range (PIXcel3D solid state detector and Cu anode (Cu Kα1: 1.5406 Å; Cu Kα2: 1.5444 Å)).

6.2.3.4 TGA

Thermogravimetric analysis of all membranes was done with a TA instruments TGA Q500. Samples were heated in N_2 atmosphere at a heating rate of 5 °C/min till 700 °C. A mass

spectrometer (MS, Hiden HPR-20 QIC-EGA) with a secondary electron multiplier detector was used to identify elution of CO_2 (m/z = 44) in the specified temperature range.

6.2.3.5 DSC

DSC was performed on a DSC Q2000 (TA instruments). In a first heating cycle, the polymer thermal history was erased at 400 °C. The measurement cycle consisted of cooling down to 300 °C at 10 °C/min and reheating to 400 °C at 10 °C/min. DSC data were analyzed with TA Universal Analysis.

6.2.3.6 Density measurements

Membrane density was determined with the buoyancy method by using a Sartorius YDK 01 Density Determination Kit with water as the buoyancy liquid. The membranes were first weighed in air and then in water. Equation 6.1 was used to calculate the membrane density:

$$\rho = \frac{W(a)}{0.99983} \times \left[\frac{\rho(fl) - 0.0012\ g/cm^3}{W(a) - W(fl)}\right] + 0.0012\ g/cm^3 \quad (6.1)$$

with W(a) and W(fl), the weight of the sample in air and water, respectively, ρ(fl) the density of water (0.99821 g/cm^3 at 20.1 °C) and 0.0012 g/cm^3 the density of air. A correction factor of 0.99983 was used for buoyancy of the set-up wires.

6.2.3.7 Energy dispersive x-ray spectroscopy

Energy dispersive x-ray (EDX) spectroscopy was performed on a Philips/FEI XL-30-FEG SEM (10 kV) on membrane cross-sections, which were broken in liquid nitrogen. An average value of three different data points was used in Table 6-2.

6.2.3.8 Fluorescence spectroscopy

Fluorescence excitation and emission spectra were measured using an Edinburgh photonics FL980 spectrofluorometer. First, an excitation scan was performed at an emission wavelength of 532 nm while varying excitation from 320 nm to 580 nm. This spectrum revealed a maximal emission at excitation wavelength of 510 nm. Next, the membrane samples were excited at 510 nm and an emission spectrum was recorded between 530 nm (20 nm red shift relative to the excitation wavelength) and 800 nm. The maximum emission appeared at 600 nm. For each sample, an excitation scan was then performed at an emission wavelength of 600 nm to generate the final excitation spectra. The settings of the spectrofluorometer were determined by adjusting the most fluorescent sample to 10^6 counts per second raw signal.

6.2.3.9 Gas sorption

High pressure gas sorption of N_2 and CO_2 was measured at 30 °C up to pressures of 25 bar for 6FDA-DABA-100, 6FDA-DABA-300 and 6FDA-DABA-400 membranes (Rubotherm series IsoSORP© instrument). First, helium pycnometry was performed on all membranes to determine the weight and volume of the samples. A magnetically suspended balance was then used to measure the weight increase in time due to sorption of the selected gas. The weight was corrected for the buoyancy of the measurement gases (Equation 6.2):

$$m_{corrected} = m_{measured} + \rho_{gas} \times V_{sample} \quad (6.2)$$

with $m_{corrected}$ the corrected weight (g), $m_{measured}$ the measured weight (g), ρ_{gas} the measuring gas density (g/cm^3) and V_{sample} the sample volume (cm^3).

The N_2 and CO_2 solubility in the membranes can be calculated with Equation 6.3:

$$S = \frac{C}{p} \tag{6.3}$$

with S the gas solubility (cm^3 (STP)/cm^{3}cmHg), C the quantity adsorbed (cm^3 (STP)/cm^3) and p the pressure (cmHg).

Combination of the CO_2/N_2 solubility selectivity data in Table S6-2 with the permeability data in Table 6-4 allows calculation of the CO_2/N_2 diffusivity selectivity (D_{CO2}/D_{N2}) with Equation 6.4:

$$\alpha_{CO2/N2} = \frac{P_{CO2}}{P_{N2}} = \frac{D_{CO2} \times S_{CO2}}{D_{N2} \times S_{N2}} = \frac{D_{CO2}}{D_{N2}} \times \frac{S_{CO2}}{S_{N2}} \tag{6.4}$$

with $\alpha_{CO2/N2}$ the CO_2/N_2 ideal selectivity, P_{CO2}, D_{CO2} and S_{CO2} the CO_2 pure gas permeability (Barrer), diffusivity (cm^2/s) and solubility (cm^3 (STP)/cm^{3}cmHg), respectively, and P_{N2}, D_{N2} and S_{N2} the N_2 permeability (Barrer), diffusivity (cm^2/s) and solubility (cm^3 (STP)/cm^{3}cmHg), respectively.

6.2.3.10 Gas permeation

CO_2, N_2 and CH_4 permeation were analyzed in a custom-made HTGS, as described elsewhere[47,123]. Both mixed-gas and single gas permeation were evaluated at varying pressures and temperatures. Membrane coupons with an active area of 1.91 cm^2 were used. One data point consists of the average value of three coupons.

CO_2/CH_4 and CO_2/N_2 mixed-gas separation factors (α^*) were determined by GC analysis of the permeate and calculated by the ratio of the downstream and upstream mole fraction of the respective gases:

$$\alpha^*_{i/j} = \frac{y_i / y_j}{x_i / x_j} \tag{6.5}$$

where y_i and y_j are the mole fractions of gas i and j in the permeate, x_i and x_j the mole fractions of gas i and j in the feed. The ratio y_i/y_j is determined from chromatogram peak areas of the permeate, while x_i/x_j is determined by the feed settings.

A constant-volume-varying-pressure method was applied for determination of the pure and mixed-gas permeability. A 75 cm^3 cylinder was used to accumulate the permeate while a pressure sensor (MKS Baratron) monitored the change in pressure as a function of time (dp/dt). Permeability of the gas i (P_i, Barrer) was determined with:

$$P_i = 10^{10} \times \frac{y_i \times V \times V_m \times L}{x_i \times p_{up} \times A \times R \times T} \times \frac{dp}{dt} \tag{6.6}$$

with P_i the gas permeability (Barrer), y_i the mole fraction of the component in the permeate, x_i the mole fraction of the component in the feed, V the downstream volume (75 cm^3), V_m the

molar volume (L/mol), A the membrane permeation area (1.91 cm^2), L the membrane thickness (µm), T the operating temperature (K), p_{up} the upstream pressure (bar), R the gas constant (0.082 L atm/mol K) and dp/dt the pressure increase (Torr/s). For pure gas experiments y_i and x_i equal 1.

6.3 Results and discussion

6.3.1 Evidence for thermally induced cross-linking

6FDA-DABA membranes were annealed at 100 °C, 180 °C, 250 °C, 350 °C and 400 °C. With increasing annealing temperature, it was observed that the membrane color changed from transparent to black and that 6FDA-DABA-350 and 6FDA-DABA-400 membrane coupons had significantly shrunk, as can be seen in Figure 6-2.

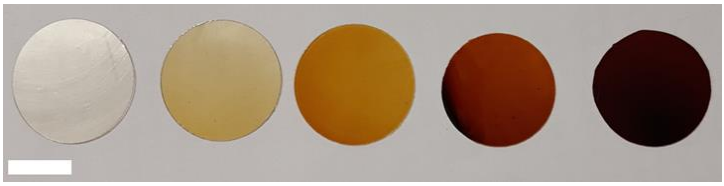

Figure 6-2: Color change at different annealing temperatures. From left to right: 6FDA-DABA annealed at 100 °C, 180 °C, 250 °C, 350 °C and 400 °C. Scale bar is 1 cm.

The annealed membranes were immersed in an excess amount of THF (the solvent that was originally used to dissolve the polymer) and two other conventional organic solvents (NMP, DMSO) to verify whether the solubility had changed after the curing process. Whereas the polymer films annealed below 250 °C readily dissolved in all solvents (with exception of 6FDA-DABA-250 in DMSO), 6FDA-DABA-350 and 6FDA-DABA-400 membranes could not be dissolved in any of the solvents (Table 6-1), which suggests a structural change in polymer chemistry at elevated temperatures.

Table 6-1: Solubility in THF, NMP and DMSO of the annealed membranes. + = soluble, - = not soluble. NA = not annealed.

Solvent	6FDA-DABA-NA	6FDA-DABA-100	6FDA-DABA-180	6FDA-DABA-250	6FDA-DABA-350	6FDA-DABA-400
THF	+	+	+	+	-	-
NMP	+	+	+	+	-	-
DMSO	+	+	+	-	-	-

ATR-FTIR data (Figure 6-3 and Figure S6-1) confirm the preservation of the PI molecular structure after thermal annealing below 400 °C: strong signals at 1351 cm^{-1} (C-N stretching), 1719 cm^{-1} (C=O symmetric stretching) and 1786 cm^{-1} (C=O asymmetric stretching) for all membranes show that the typical imide bonds remain intact[39,249]. Additionally, IR provides evidence for the occurrence of interchain cross-linking. A doublet signal at 1719 cm^{-1} in the spectra of the membranes annealed at or below 250 °C corresponds with C=O stretching of the imide and the aryl carboxylic acid group, respectively. However, for the samples treated at 350 °C and 400 °C, the doublet peak at higher wavenumbers disappeared, indicating that the carboxylic acid group is, at least partially, removed. In addition, the signal at approximately 1400 cm^{-1}, which corresponds with the O-H bending of the carboxylic acid group[132], is strongly reduced for 6FDA-DABA-350 and even completely disappears for 6FDA-DABA-400. This is

further confirmed by the characteristic O-H stretching peak between 3200 and 3400 cm^{-1} (related to the free carboxylic acid group[250]), which decreases in intensity with higher annealing temperatures (Figure S6-1). In addition, when decarboxylation occurs, a phenyl-phenyl C-C bond is formed (Figure S6-2). This signal is clearly visible at 1495 cm^{-1} but only for 6FDA-DABA-350 and 6FDA-DABA-400, suggesting that cross-linking did not occur for the membranes annealed below 350 °C, which is in good agreement with literature[39,251]. Although cross-linking possibly also evokes changes in -CF_3 signal peaks at ~650 cm^{-1}, ~1050 cm^{-1} and ~1160 cm^{-1} (as has been proposed in literature[39]), no significant conclusions can be drawn from the ATR-FTIR spectra with regard to this[249]. Finally, a somewhat irregular IR spectrum is observed for 6FDA-DABA-400, which might indicate structural changes due to starting carbonization of the polymer. As often reported, the thermal rearrangement of (ortho-hydroxy containing) PI to PBO can take place at this temperature. However, since 6FDA-DABA does not carry an ortho-positioned hydroxyl group and no clear PBO signals (at 1054 cm^{-1} and 1550 cm^{-1}) could be distinguished in the spectrum (while the imide peaks largely remained intact), it is considered unlikely that 6FDA-DABA-400 has been (partially) converted to a PBO.

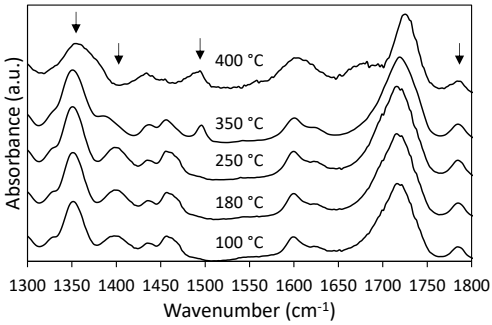

Figure 6-3: ATR-FTIR spectrum of 6FDA-DABA membranes.

Further evidence for interchain cross-linking is given by thermal analysis of the membranes with TGA-MS (Figure 6-4) and DSC (Figure S6-3). Figure 6-4 shows an intense signal around 560 °C, corresponding with the backbone degradation of the polymer. Interestingly, a secondary peak is detected with a smaller maximum in mass loss at 470 °C. The signal intensity of this peak strongly decreases for 6FDA-DABA-400. When correlated with the MS output, this higher weight loss is (at least partially) due to the removal of the carboxylic acid group in the form of CO_2 (m/z = 44). Similar behavior was observed for other membranes based on DABA moieties[39,240] and other polymers with acid group moieties[252,253]. This is further supported by the fact that no secondary CO_2 signal is observed for 6FDA-DABA-400, in which the decarboxylation already occurred during annealing. Furthermore, the CO_2 intensity signal only starts to increase at roughly 330-340 °C, suggesting that the decarboxylation cross-linking is initiated at this temperature. The initial weight loss observed for 6FDA-DABA-100 at low temperature can most likely be attributed to the presence of residual solvent, which did not yet evaporate during the annealing process. Finally, DSC measurements reveal an enhanced T_g when increasing annealing

temperature from 100 °C to 350 °C, while no T_g could be detected for 6FDA-DABA-400. This further points towards an enhanced restriction in polymer chain mobility due to cross-linking.

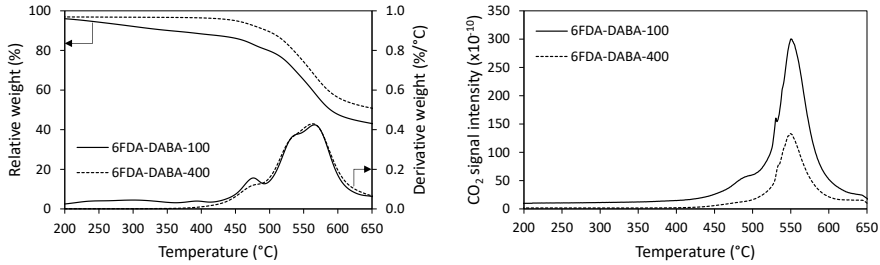

Figure 6-4: TGA traces of 6FDA-DABA-100 and 6FDA-DABA-400 (left). MS output for the same membranes is given on the right.

In addition, EDX measurements were performed to estimate the oxygen and fluorine content of the membranes. Although EDX is considered less accurate than X-ray photoelectron spectroscopy (XPS) for elemental analysis of light elements, it does allow to determine a trend in elemental content in a series of membranes. Table 6-2 shows that, while the fluorine content remains largely constant, a clear decline in oxygen content can be observed for annealing temperatures of 350 °C and 400 °C. This is in line with the occurrence of decarboxylation cross-linking, which results in the removal of oxygen in the form of H_2O, CO and CO_2[240]. Complete decarboxylation of 6FDA-DABA would theoretically lead to a loss in oxygen content of 33%. However, the oxygen loss for 6FDA-DABA-400 amounts to approximately 60%, indicating that part of the backbone (e.g. carbonyl bond) has been oxidized and removed as CO/CO_2[254].

Table 6-2: Oxygen and fluorine content of all 6FDA-DABA membranes, as determined by EDX.

	Oxygen	Fluorine	O/F ratio
6FDA-DABA-100	19,0	21,5	0,88
6FDA-DABA-180	17,7	21,2	0,84
6FDA-DABA-250	20,6	24,7	0,83
6FDA-DABA-350	14,5	23,0	0,63
6FDA-DABA-400	8,1	24,3	0,33

6.3.2 Membrane dilation versus membrane tightening

XRD and density experiments confirmed that, as a result of the decarboxylation cross-linking, a more open membrane structure was obtained at curing temperatures of 350 °C and 400 °C in comparison with the membranes annealed below 350 °C. XRD patterns can reveal information on the interchain distance between polymer chains by using Bragg's law ($n\lambda = 2d \sin\theta$) to calculate the interchain distance or d-spacing. Although the d-spacing does not indicate the actual distance between the polymer chains, it can be considered as a measure for the available unoccupied volume between the chains[255]. Only a small shift in d-spacing was observed in Figure S6-4 from 5.15 Å (100 °C) > 5.14 Å (180 °C) > 5.12 Å (250 °C), suggesting a denser polymer packing with increasing annealing temperature. However, after annealing at 350 °C, the d-spacing increased to 5.44 Å (350 °C) and, upon further annealing, to 5.52 Å (400 °C). Hence, a

more open polymer structure is expected after annealing above 350 °C. This was also observed by Qiu *et al.* when annealing 6FDA-DAM:DABA co-polyimides and was related to the formation of cross-links between adjacent –COOH groups induced by thermal decarboxylation[39]. In addition, Figure 6-5 shows the appearance of a shoulder peak at a 2θ value of 13° in 6FDA-DABA-350, indicating the formation of micropore-like structures[243].

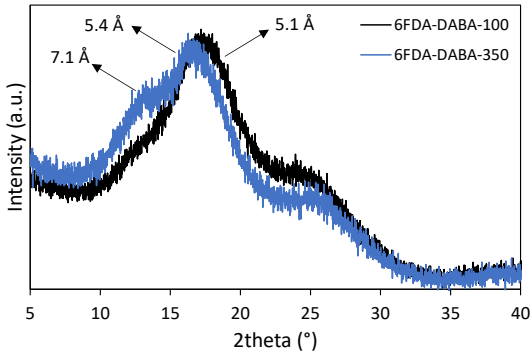

Figure 6-5: XRD spectra of 6FDA-DABA-100 and 6FDA-DABA-350.

Density and specific volume of all 6FDA-DABA membranes are presented in Table 6-3. The specific volume of the 6FDA-DABA membranes can be used to approximately calculate the fractional free volume (FFV) with the Bondi method[256–258]. As can be seen in Table 6-3, the FFV gradually decreases with higher annealing temperature to reach a minimum at 250 °C. When the annealing temperature is further increased, the FFV increases to a maximum for 6FDA-DABA-400, confirming that a more open structure is obtained after high-temperature annealing, well in agreement with the XRD data.

Table 6-3: Degradation temperature (T_{deg}), d-spacing, density, specific volume and fractional free volume (FFV) of all membranes.

	T_{deg} (°C)	d-spacing (Å)	Density (g/cm³)	Specific volume (cm³/g)	FFV
6FDA-DABA-100	566	5.15	1.47	0.68	0.198
6FDA-DABA-180	565	5.14	1.51	0.66	0.176
6FDA-DABA-250	558	5.12	1.59	0.62	0.131
6FDA-DABA-350	564	5.44	1.51	0.66	0.176
6FDA-DABA-400	563	5.52	1.44	0.70	0.215

Aromatic PIs are known to have weak but distinctive fluorescence emission as a result of improved chain packing during thermal annealing. A combination of multiple molecular, attractive interactions (such as Van der Waals, π-stacking, hydrogen bonding and, possibly, charge transfer) stabilizes the formed polymer-polymer complex, which can be studied with fluorescence spectroscopy[259–261]. Figure 6-6 depicts the fluorescence emission spectra used to investigate the thermal effect on chain packing in 6FDA-DABA membranes. Two spectral changes can be observed with increasing annealing temperature. First, the signal intensity

considerably increases with higher curing temperature for samples annealed at 100 °C, 180 °C and 250 °C as the elevated temperatures allow for a more energy-efficient arrangement of the polymer chains. The intensity signals for 6FDA-DABA-250 and 6FDA-DABA-350 are very similar, while a strong reduction in intensity is observed for 6FDA-DABA-400. Secondly, the signal maxima shift to higher emission wavelengths with higher temperature (red shift). The increased emission intensity confirms the densification of the membrane up to 250 °C, which is in good agreement with XRD and FFV data obtained earlier. When decarboxylation cross-linking takes place at elevated temperatures, packing is sterically disrupted, which is reflected in lowered fluorescence intensities for 6FDA-DABA-400. Although decarboxylation cross-linking also occurs for 6FDA-DABA-350, the intensity spectrum of 6FDA-DABA-350 is still very similar to that of 6FDA-DABA-250. This suggests that decarboxylation cross-linking has a much smaller effect on the polymer packing efficiency in 6FDA-DABA-350 than it has in 6FDA-DABA-400.

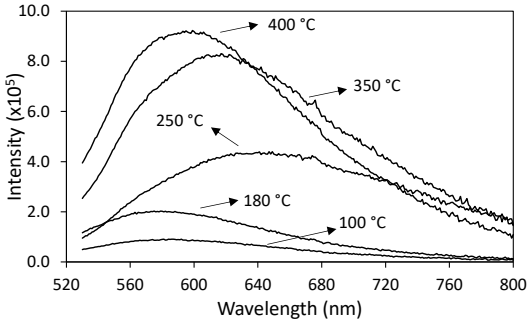

Figure 6-6: Emission fluorescence spectra for all membranes. Excitation wavelength is 510 nm.

Finally, N_2 and CO_2 sorption were measured for 6FDA-DABA-100, 6FDA-DABA-350 and 6FDA-DABA-400 membranes (Figure 6-7) and the corresponding solubility values were calculated in Table S6-2. While the gas sorption logically increases at higher pressure, a reduced solubility for CO_2 and N_2 is observed for all membranes with increasing pressure, in good agreement with predictions based on the dual-mode sorption model[11,21,24]. Furthermore, higher curing temperatures cause higher sorption and solubility for both gases. These results correspond well with the FFV calculations in Table 6-3 for 6FDA-DABA-400 as a higher FFV would allow more sorption and thus a higher solubility. However, this reasoning would predict a higher gas sorption for 6FDA-DABA-100 than for 6FDA-DABA-350 as the FFV of these membranes are 0.198 and 0.176, respectively. A possible explanation for this behavior would be the blockage of adsorption sites in 6FDA-DABA-100 by residual solvent (as indicated by TGA as well).

The effect of pressure and curing temperature on the CO_2/N_2 solubility selectivity is given in Table S6-2. A clear decline in solubility selectivity can be observed with increasing pressure, which suggests that the solubility of the more condensable gas (i.e. CO_2) is relatively more affected than the N_2 solubility. Additionally, a trend for the solubility selectivity can be observed when the annealing temperature is increased. In the entire pressure range, the solubility selectivity decreases in the following order: 6FDA-DABA-100 > 6FDA-DABA-400 > 6FDA-DABA-350. For example, at 10 bar, the solubility selectivity first decreases with 23% from

100 °C to 350 °C only to increase again with almost 10% when the membrane is heated to 400 °C, indicating that for the membrane treated at 350 °C the sorption of N_2 has increased relative to the CO_2 sorption.

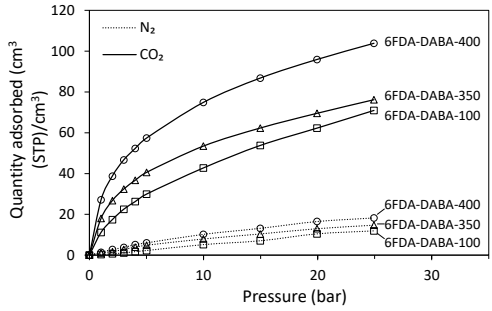

Figure 6-7: N_2 and CO_2 sorption in 6FDA-DABA membranes annealed at 100 °C, 350 °C and 400 °C.

6.3.3 Gas permeation experiments

Mixed-gas CO_2/CH_4 and CO_2/N_2 experiments were conducted with all 6FDA-DABA membranes. While the CO_2/N_2 separation factor only marginally improves for higher annealing temperatures, Figure 6-8 shows a steady improvement of the CO_2/CH_4 separation factor from 100 °C to 350 °C. 6FDA-DABA-350 reaches a CO_2/CH_4 separation factor of 94, which means an increase of almost 100% compared to 6FDA-DABA-100. This can be explained by so-called "physical tightening" of the membrane due to rearrangement of the polymer chains and improved packing efficiency[39], confirmed by density and fluorescence experiments. Annealing is known to cause an accelerated membrane ageing effect, resulting in higher selectivity and lower permeability[249]. For 6FDA-DABA-400 however, a steep decline in separation factor is observed, returning to the level of the membrane annealed at 100 °C, suggesting that a secondary effect counteracts the tightening of the membrane at very high annealing temperature. The evolution of the mixed-gas CO_2, CH_4 and N_2 permeability as a function of annealing temperature further supports this hypothesis (Figure 6-8 and Figure S6-6). Whereas the permeability of all gases gradually decreases till 250 °C, annealing at 350 °C and 400 °C results in a sudden (and strong) enhancement of the gas permeability. The CO_2 permeability of 6FDA-DABA-350 is 40% higher than the pristine membrane while 6FDA-DABA-400 reaches a CO_2 permeability of roughly 160 Barrer (at the same selectivity level as 6FDA-DABA-100). This was explained by XRD and density experiments, which suggested a more open polymer structure for 6FDA-DABA-350 and 6FDA-DABA-400, possibly with the presence of micropores. Formation of this open structure is a result of decarboxylation cross-linking, as proven by combination of the results of ATR-FTIR (Figure 6-3), TGA-MS (Figure 6-4), EDX (Table 6-2). Furthermore, the higher T_g for membranes cured at higher temperatures, as measured with DSC, also supports this (Figure S6-3). Although the separation behavior of 6FDA-DABA-400 resembles that of TR polymers (steep enhancement of permeability with no or a small loss in selectivity), no conclusive evidence for PBO formation was found in ATR-FTIR, as mentioned above.

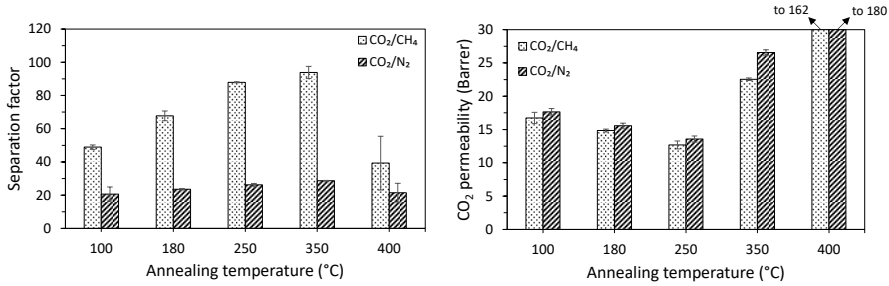

Figure 6-8: CO_2/CH_4 and CO_2/N_2 separation factor (left) and CO_2 permeability for the CO_2/CH_4 and CO_2/N_2 mixed-gas experiment (right) of 6FDA-DABA membranes annealed at different temperatures. Gas filtrations were performed at 30 °C, 5 bar feed pressure and 50v%/50v% CO_2/CH_4 and CO_2/N_2 feed.

Table 6-4 summarizes the pure gas permeabilities and ideal selectivities of the 6FDA-DABA membranes for CO_2, CH_4 and N_2. The data obtained here for 6FDA-DABA-180 are well in agreement with earlier results[262]. Overall, the pure gas data trends are similar to the mixed-gas data: higher annealing temperatures initially produce membranes with lower gas permeability and higher selectivity, while an increased permeability is observed for all gases for annealing temperatures of 350 °C and 400 °C. When compared to the mixed-gas results, ideal selectivities are consistently lower, suggesting competitive sorption by CO_2 at the expense of the less condensable gases CH_4 and N_2[262,263].

Table 6-4: Summary of pure gas permeabilities, ideal selectivities, mixed-gas permeability and separation factor of all membranes. Gas filtrations were performed at 30 °C, 5 bar feed pressure.

		Permeability (Barrer)			Selectivity	
		CO_2	CH_4	N_2	CO_2/CH_4	CO_2/N_2
6FDA-DABA-100	Pure gas	18.6	0.44	0.83	42.3	22.3
	Mix(CO_2/CH_4)	16.7	0.34	-	48.9	-
	Mix(CO_2/N_2)	17.7	-	0.91	-	20.6
6FDA-DABA-180	Pure gas	12.5	0.21	0.77	60.2	16.2
	Mix(CO_2/CH_4)	14.8	0.22	-	67.8	-
	Mix(CO_2/N_2)	15.6	-	0.66	-	23.5
6FDA-DABA-250	Pure gas	11.1	0.15	0.65	73.9	17.2
	Mix(CO_2/CH_4)	12.7	0.14	-	87.9	-
	Mix(CO_2/N_2)	13.6	-	0.52	-	26.2
6FDA-DABA-350	Pure gas	22.5	0.25	0.93	90.4	24.3
	Mix(CO_2/CH_4)	22.5	0.24	-	93.9	-
	Mix(CO_2/N_2)	26.6	-	0.95	-	28.6
6FDA-DABA-400	Pure gas	146.7	6.1	9.8	24.1	15.0
	Mix(CO_2/CH_4)	161.8	4.8	-	39.3	-
	Mix(CO_2/N_2)	179.5	-	9.4	-	21.5

Table 6-5 shows the contributions of gas solubility and diffusivity to membrane permeability and selectivity as a function of annealing temperature. For both CO_2 and N_2, it is clear that the very strong enhancement in gas permeability for 6FDA-DABA-400 results from a substantial increase in both solubility and diffusivity compared to the other membranes. This is a direct result of pronounced decarboxylation cross-linking, causing more FFV to occur. When the membrane is heated from 100 °C to 350 °C a more subtle change in permeation behavior is noted. As mentioned earlier, both the CO_2 and N_2 solubility increase for 6FDA-DABA-350 in comparison with 6FDA-DABA-100. However, while the diffusivity of CO_2 only shows a minor reduction after heating to 350 °C (-11%), the N_2 diffusivity of 6FDA-DABA-350 is severely affected, constituting a loss of 92% compared to 6FDA-DABA-100. Logically, this is also visible in the solubility and diffusivity selectivity difference between 6FDA-DABA-100 and 6FDA-DABA-350. Diffusivity selectivities were calculated to be 1.69, 2.90 and 1.57, respectively. Increasing the annealing temperature from 100 °C to 350 °C thus results in a reduction of solubility selectivity of 58% and a gain in diffusivity selectivity of +25%. These results point towards a relatively stronger size sieving effect for 6FDA-DABA-350, causing the higher overall CO_2/N_2 selectivity. It should be noted that the solubility selectivity for the CO_2/N_2 experiment is still significantly larger than the diffusivity selectivity and is comparable with those found for other PI membranes such as 6FDA-DAM[264] and Matrimid[265,266].

Even though no quantitative sorption data could be obtained for CH_4, it is hypothesized that the strong enhancement in CO_2/CH_4 selectivity is also due to an increased size sieving, which would be more pronounced for CO_2/CH_4 than for CO_2/N_2 as a result of a larger difference in kinetic diameter. The sorption data further confirm the trends previously shown by density experiments, XRD and gas permeation. For 6FDA-DABA-350, the simultaneous rise in diffusion selectivity and FFV might seem contradictory at first sight but possibly points towards a membrane structure with concentrated domains of high selectivity due to size sieving (as a result of polymer tightening) and domains in which the polymer tightening has been compromised by cross-linking, resulting in more FFV. Similar use of so-called segmental separation behavior has been reported for rigid 6FDA-based polypyrrolone membranes, in which polymer packing was controlled by systematically incorporating chain-disrupting segments and flat, packable segments in the polymer backbone[267].

Table 6-5: Permeability P (Barrer), solubility S (cm^3 (STP)/cm^3 cmHg), diffusivity D (x10^{-8} cm^2/s), ideal CO_2/N_2 selectivity α (-), CO_2/N_2 solubility selectivity S/S (-) and CO_2/N_2 diffusivity D/D (-) of 6FDA-DABA membranes annealed at 100 °C, 350 °C and 400 °C.

	P(CO_2)	S(CO_2)	D(CO_2)	P(N_2)	S(N_2)	D(N_2)	α	S/S	D/D
6FDA-DABA-100	18.6	0.0797	2.33	0.83	0.0060	1.38	22.4	13.3	1.69
6FDA-DABA-350	22.5	0.1080	2.08	0.93	0.0129	0.72	24.2	8.37	2.90
6FDA-DABA-400	146.7	0.1528	9.60	9.80	0.0160	6.13	15.0	9.55	1.57

Based on the permeation and characterization data, it seems that two mechanisms with opposing effects define the membrane performance. On one hand, physical tightening, caused by polymer rearrangement and improved polymer chain stacking at higher annealing temperatures, results in a better separation factor. On the other hand, decarboxylation-cross-linking generates a more open structure by forming interchain covalent cross-links that sterically hinder efficient chain stacking. While the membranes annealed at 250 °C or below only profit from the tightening effect and thus an enhanced separation factor and decreased gas permeability, decarboxylation cross-linking dilates the polymer structure of 6FDA-DABA-400, resulting in a 10-fold increase in permeability but no separation factor improvement. However, for 6FDA-DABA-350, a synergy is observed between the dilation effect of decarboxylation (as confirmed by XRD and density) and, at the same time, the tightening effect (as confirmed by fluorescence spectroscopy), resulting in a strongly enhanced separation performance.

6.3.4 Effect of plasticization and temperature on gas permeation

CO_2-induced plasticization takes place when large concentrations of the highly condensable CO_2 swell the membrane polymers, resulting in higher mobility of polymer chain segments. Consequently, the diffusivity of all gases is increased and a lower selectivity and higher gas permeability is perceived[11]. Mixed-gas pressure dependency experiments on 6FDA-DABA-100 and 6FDA-DABA-350 were conducted to investigate the membrane performance and plasticization behavior at high pressure (Figure 6-9). Both 6FDA-DABA-100 and 6FDA-DABA-350 show a strong initial decline in CO_2 permeability when the pressure is elevated from 5 to 10 bar (-37% and -39%, respectively), which is explained by an equally significant diminution in solubility. Although the permeation data are measured under mixed-gas conditions while solubility data are for pure CO_2, the substantially lower CO_2 solubility (-40% and -51%, respectively) at 10 bar can be considered as a good indication for the mixed-gas solubility. After the initial decrease, the CO_2 permeability of 6FDA-DABA-100 further declines with increasing feed pressure up to a minimal permeability at roughly 15 bar, after which a rise in permeability is observed at 20 bar. This permeability response as a function of pressure concurs with typical dual-mode sorption predictions: first a reduced CO_2 permeability is observed with increasing pressure, in agreement with the dual mode sorption, followed by an upturn in CO_2 permeability due to plasticization[21]. Assuming that dense, non-porous membranes with a high Young's modulus do not experience compaction, a decreasing CO_2/CH_4 separation factor with increasing feed pressure suggests that the solubility of the most condensable gas CO_2 is more affected by a higher pressure than the solubility of CH_4, as was confirmed by sorption measurements (Table S6-2). Furthermore, Figure 6-9 shows that the permeability data of 6FDA-DABA-350 do not reveal a plasticization point within the feed pressure range tested, indicating that the cross-linked membrane obtained an improved resistance to plasticization.

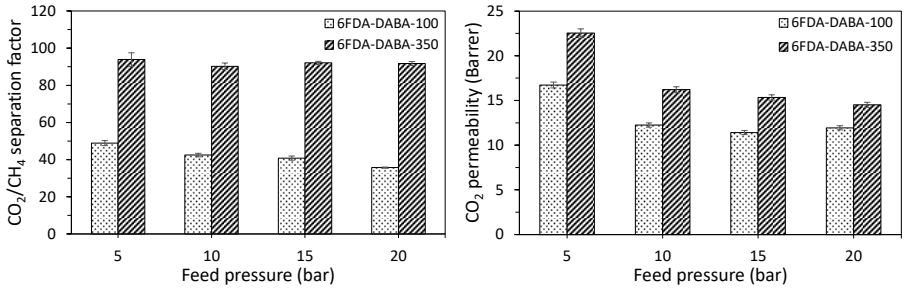

Figure 6-9: Effect of feed pressure on CO_2/CH_4 separation factor (left) and CO_2 permeability (right). Gas filtrations were performed at 30 °C and 50v%/50v% CO_2/CH_4 feed.

Furthermore, Figure 6-10 shows that the CO_2/CH_4 separation factor decreases with increasing temperature, in agreement with the temperature dependency of gas solubility and diffusivity in the polymer matrix[10]. Both 6FDA-DABA-100 and 6FDA-DABA-350 show a similar decline in separation factor while CO_2 permeability increases at higher measuring temperatures. In addition, gas permeability of the membrane can be expressed as a function of temperature (Equation 6.7):

$$P = P_0 \times exp(-\frac{E_P}{RT}) \quad (6.7)$$

with P_0 a pre-exponential factor (Barrer), E_p the activation energy for permeation and R the universal gas constant.

An Arrhenius plot of the permeability as a function of temperature allows calculation of the activation energy for CO_2 permeation in both membranes. The calculated activation energy for 6FDA-DABA-350 (6.0 kJ/mol) is lower than that of 6FDA-DABA-100 (9.4 kJ/mol), indicating a lower energy barrier that needs to be overcome for CO_2 permeation in the 6FDA-DABA-350 membrane.

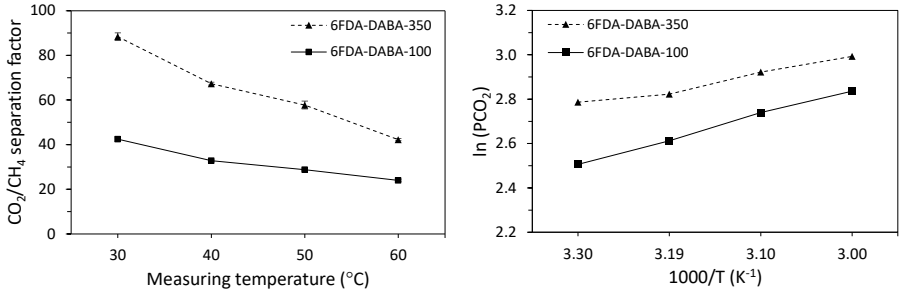

Figure 6-10: Effect of measuring temperature on CO_2/CH_4 separation factor (left) and CO_2 permeability (right). Gas filtrations were performed at 10 bar feed pressure and 50v%/50v% CO_2/CH_4 feed.

6.3.5 Comparison with state-of-the-art

The obtained separation performances were compared with literature and defined upper bounds for single and pure gas data[39,55,61,240,262]. The 6FDA-DABA membranes in this work compare well to those reported in literature (Figure 6-11). As mentioned above, the choice for a low permeability/high selectivity starting material eventually results in a membrane (6FDA-DABA-350), which crosses the 2018 upper bound and is close to the 2008 Robeson upper bound. Furthermore, 6FDA-DABA-400 performs very similarly to cross-linked membranes that started from more permeable precursors. However, it should be noted that the 6FDA-DABA-400 membranes were very brittle and thus limited in their applicability potential.

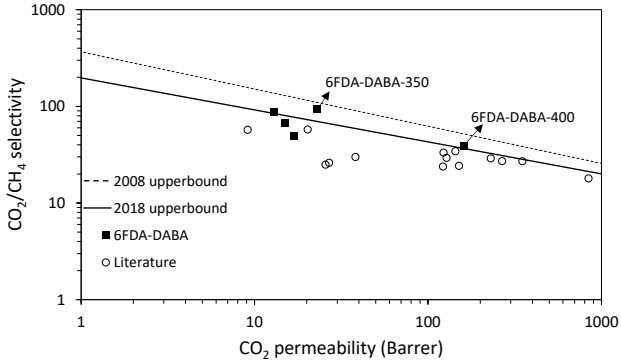

Figure 6-11: Comparison of the obtained data with literature and state-of-the-art in a selectivity-permeability plot. The full black line represents the 2018 mixed-gas upper bound for CO_2/CH_4[61] while the dotted black line represents the 2008 Robeson upper bound[55].

6.4 Conclusions

Thermal treatment of 6FDA-DABA membranes was conducted at different temperatures and the resulting membranes were tested for their CO_2 removal capacity. In agreement with literature, decarboxylation cross-linking was induced for the membranes annealed at 350 °C and 400 °C. It was found that the separation performance of the membranes is defined by two counteracting effects. On one hand, physical tightening of the membrane caused by enhanced polymer rearrangement and chain packing was confirmed by fluorescence spectroscopy and density measurements and resulted in higher CO_2/CH_4 separation factors with increasing curing temperature. 6FDA-DABA-350 reached a CO_2/CH_4 separation factor of 94, which constitutes an improvement of almost 100% compared to the reference membrane. On the other hand, decarboxylation cross-linking, starting from ~330 °C, forms covalent bonds between 6FDA-DABA polymer chains, resulting in a more open polymer structure. Evidence for the occurrence of decarboxylation cross-linking and the open polymer structure was established by a combination of ATR-FTIR, TGA-MS, DSC, EDX, XRD and density measurements. Consequently, a CO_2 permeability enhancement was observed for 6FDA-DABA-350 (+40% compared to the pristine membrane) while 6FDA-DABA-400 reached a 10 times higher CO_2 permeability at approximately the same separation factor. However, the severely increased brittleness of 6FDA-DABA-400 might hamper further development of this membrane. Being a borderline case, 6FDA-DABA-350 profits from both higher CO_2/CH_4 separation factor and an improved CO_2 permeability, resulting in a separation performance close to the 2008 Robeson upper bound. Finally, the cross-linked 6FDA-DABA-350 showed an increased resistance to CO_2 plasticization.

6.5 Acknowledgements

R.T. is grateful for his FWO-SB fellowship (1S63317N).

6.6 Supplementary information to Chapter 6

Table S6-1: Heating profiles of the different 6FDA-DABA membranes.

	Stage I	Stage II	Stage III
6FDA-DABA-100	60 °C, 1 h	N/A	100 °C, 6 h
6FDA-DABA-180	110 °C, 1 h	N/A	180 °C, 6 h
6FDA-DABA-250	180 °C, 1 h	N/A	250 °C, 6 h
6FDA-DABA-350	180 °C, 1 h	280 °C, 1 h	350 °C, 6 h
6FDA-DABA-400	180 °C, 1 h	300 °C, 1 h	400 °C, 6 h

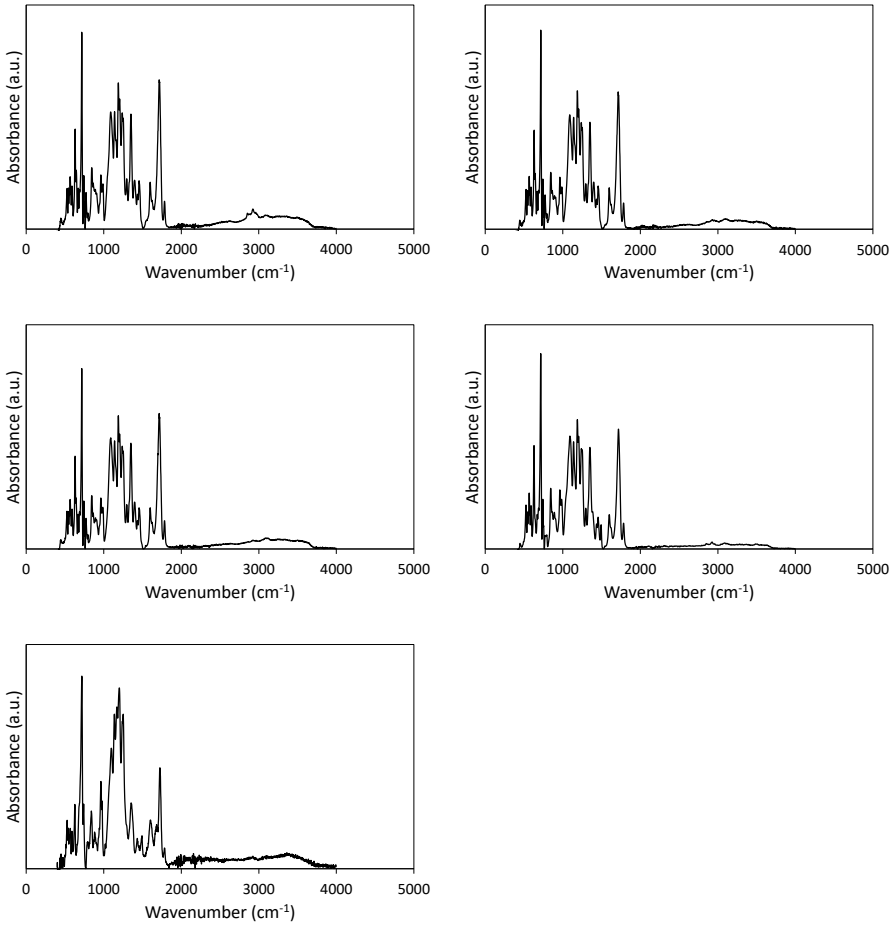

Figure S6-1: ATR-FTIR data of 6FDA-DABA membranes annealed at 100 °C (top, left), 180 °C (top, right), 250 °C (middle, left), 350 °C (middle, right) and 400 °C (bottom, left).

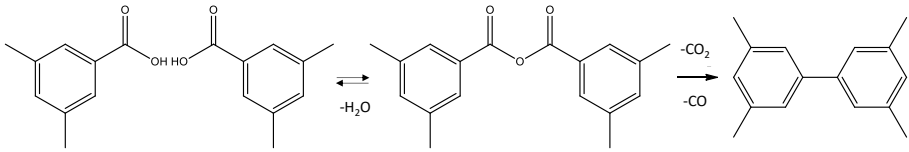

Figure S6-2: Cross-linking mechanism during decarboxylation as proposed by Qiu *et al.*[39].

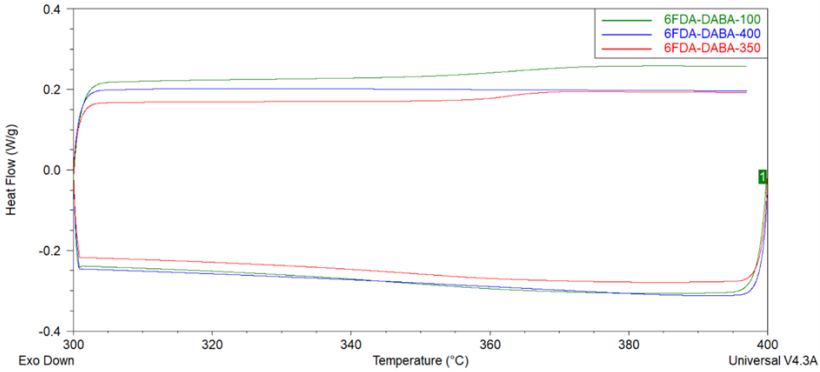

Figure S6-3: DSC plot of 6FDA-DABA-100, 6FDA-DABA-350 and 6FDA-DABA-400.

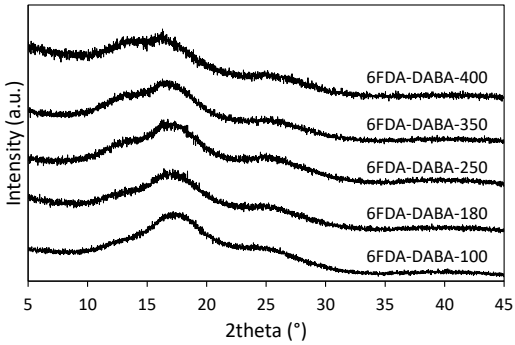

Figure S6-4: XRD spectra of 6FDA-DABA membranes annealed at 100 °C, 180 °C, 250 °C, 350 °C and 400 °C.

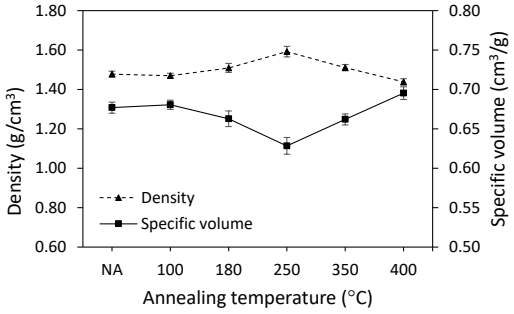

Figure S6-5: Density and specific volume data for all 6FDA-DABA membranes. NA = not annealed.

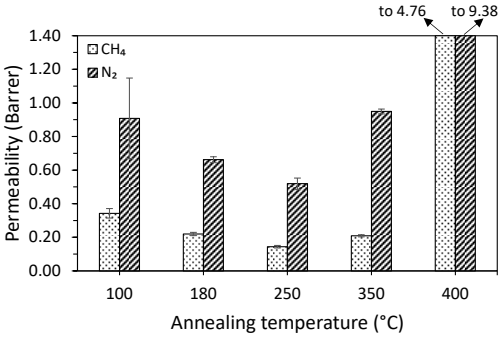

Figure S6-6: CH_4 and N_2 mixed-gas permeability of 6FDA-DABA membranes annealed at different temperatures. Gas filtrations were performed at 30 °C, 5 bar feed pressure and 50v%/50v% CO_2/CH_4 and CO_2/N_2 feed.

Table S6-2: Solubility (S) of CO_2 and N_2 in 6FDA-DABA-100, 6FDA-DABA-350 and 6FDA-DABA-400. S_{CO2}/S_{N2} constitutes the CO_2/N_2 solubility selectivity. Measurements were conducted at 30 °C and varying pressures (see table).

Pressure (bar)	Membrane	S_{N2}	S_{CO2}	S_{CO2}/S_{N2}
5	6FDA-DABA-100	0.0060	0.0797	13.2
	6FDA-DABA-350	0.0129	0.1080	8.36
	6FDA-DABA-400	0.0160	0.1528	9.53
10	6FDA-DABA-100	0.0069	0.0571	8.26
	6FDA-DABA-350	0.0106	0.0713	6.73
	6FDA-DABA-400	0.0136	0.0999	7.32
15	6FDA-DABA-100	0.0063	0.0479	7.61
	6FDA-DABA-350	0.0093	0.0555	5.99
	6FDA-DABA-400	0.0117	0.0773	6.58
20	6FDA-DABA-100	0.0070	0.0416	5.95
	6FDA-DABA-350	0.0087	0.0465	5.36
	6FDA-DABA-400	0.0110	0.0641	5.81
25	6FDA-DABA-100	0.0064	0.0379	5.94
	6FDA-DABA-350	0.0078	0.0407	5.18
	6FDA-DABA-400	0.0098	0.0555	5.68

Chapter 7

Second generation high-throughput set-up for testing of gas separation membranes under industrially relevant conditions

Raymond Thür, Ivo F.J. Vankelecom

Centre for Membrane Separations, Adsorption, Catalysis and Spectroscopy for Sustainable Solutions (cMACS), KU Leuven, Celestijnenlaan 200F, Box 2454, 3001 Heverlee, Belgium

Abstract

A second generation high-throughput (HT) gas separation (GS) set-up (HTGS-2) was developed and built for testing membranes under industrially relevant conditions. HTGS-2 allows quick testing of 8 membranes at the same time, significantly speeding up the process of membrane development and optimization compared to conventional single cell analysis. It is equipped for testing membranes with 7 different gases or gas mixtures, relevant for e.g. CO_2 capture, natural gas/bio gas upgrading and olefin/paraffin separation. As the feed composition can be freely tuned in terms of temperature (up to 100 °C) and pressure (up to 34.5 bar), controlled and accurate mimicking of industrial operating conditions can be achieved to yield realistic membrane performance. Dense lab-made membranes, consisting of different relevant polymers for gas separation (6FDA-DAM, Pebax MH 1657, 6FDA-DABA), were prepared and used to proof test HTGS-2. These membranes were subjected to the full range of temperature and pressure in mixed-gas conditions. It was found that the separation factors of all membranes were accurate and well in line with literature and measurements on HTGS-1. The mixed-gas permeability however was systematically higher than reported values. To map this problem, three membranes with strongly varying permeances (polysulfone, 6FDA-DAM and PAN-PDMS) were tested for their pure gas permeability with five different gases (N_2, CH_4, CO_2, propane and propylene) at different feed pressures (2.5 bar, 5 bar and 10 bar) on both HTGS-1 and HTGS-2. It was observed that test conditions, resulting in low gas flux through the membrane (e.g. slow gas, low pressure and polysulfone membranes), caused high and fluctuating permeability offsets between HTGS-1 and HTGS-2. When the gas flux was increased (e.g. by switching to a fast gas or increasing the pressure), the permeability offset was smaller and more constant. For PAN-PDMS composite membranes tested at 2 bar N_2 the offset was nearly constant. Several potential solutions for the permeability offset were proposed, including minimizing the downstream volume, redesigning the measuring cylinder concept and repositioning the pressure sensor.

Contributions

Raymond Thür: design of set-up, coordination, building and proof testing of set-up, membrane preparation, gas permeation experiments, data analysis, manuscript writing and redaction. Ivo Vankelecom: design of set-up, manuscript correction and redaction.

7.1 Introduction

Over the past decades, membrane-based gas separation has emerged as an alternative for traditional purification technologies, such as amine absorption and adsorption processes[7]. CO_2 removal and capture from several industrial gas streams (such as bio gas/natural gas, syn gas and exhaust gas) and olefin/paraffin separation are often identified as potential, large, new target applications for membranes[8]. However, one of the problems and limitations currently encountered in early-stage membrane development is the lack of adequate testing under relevant conditions[22]. Consequently, a discrepancy still exists between lab-scale and industrial-scale testing of membranes. In industry, composite membranes are subjected to long term use at high pressure and temperature in presence of complex streams, containing impurities such as H_2O, H_2S, or BTX (benzene, toluene, xylene)[13]. At lab-scale, and for sure in academia, membranes are mostly tested as dense films at relatively low pressure for a short period of time, with pure gases or with gas mixtures of pure gases, not taking into account the effect of trace impurities. Even though these tests are definitely useful, a clear need for testing promising membranes under more industrially relevant conditions exists[22].

Our research group applied the concept of high-throughput (HT) membrane testing (i.e. parallel testing of multiple membranes) on both liquid and gaseous feeds by developing various HT tools for membrane screening[123,268,269]. A custom-made HT gas separation set-up (HTGS) was built in 2010, allowing the simultaneous testing of 16 membranes with pure streams or mixtures of N_2, CH_4, CO_2, O_2 and H_2 up to 15 bar[123]. Nevertheless, this set-up partially lacks the testing options needed to map membrane performance under realistic and more demanding conditions. This work presents the development and proof testing of a second generation HTGS (HTGS-2, Figure 7-1), which allows users to accurately mimic industrial streams, like flue gas (N_2, CO_2, H_2O) and natural/bio gas (CH_4, CO_2, H_2O, ethane, ethylene, propane, propylene) to gain better insight in the real separation performance of the membranes. Membranes can be tested at pressures up to 34 bar and, specifically for olefin/paraffin separation, up to 25 bar. Proof testing of the set-up was done by means of a case study in which the separation behavior of various relevant polymer membranes was tested under various conditions.

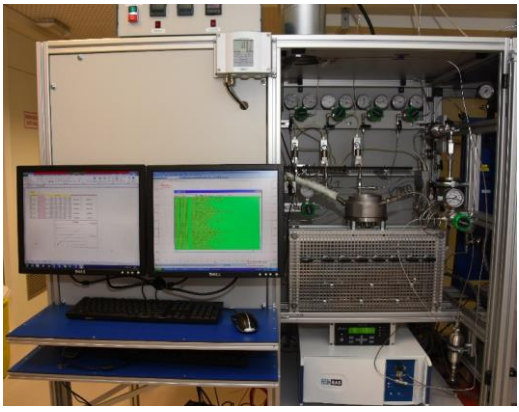

Figure 7-1: Picture of the HTGS-2 set-up.

7.2 Materials and methods

7.2.1 Chemicals

6FDA-DAM and 6FDA-DABA polymer as well as polyacrylonitrile (PAN) porous supports coated with a 600 nm polydimethylsiloxane (PDMS) selective layer were kindly provided by Fujifilm Manufacturing Europe B.V. (Tilburg, the Netherlands). Pebax MH1657 (Pebax) pellets were kindly provided by Arkema. Tetrahydrofuran (THF, >99%) and ethanol were purchased from Acros. CO_2, N_2, CH_4, He, propane and propylene were purchased from Air Liquide (Belgium) and used as delivered. Polysulfone films (Udel©, 25 µm) were purchased from Goodfellow and degassed in a vacuum oven at 50 °C before use.

7.2.2 Membrane synthesis

6FDA-DAM and 6FDA-DABA (0.42 g) were dried overnight in an oven at 100 °C and consequently dissolved in 5.58 g of THF, resulting in a 7 wt.% polymer solution. After stirring overnight, the solution was cast in a Teflon Petri dish under nitrogen atmosphere at room temperature. Plastic funnels were inversely placed over the Petri dishes to reduce the solvent evaporation rate. The dry polymer film was then transferred to an oven and annealed at 180 °C for 6 h. 6FDA-DABA membranes were annealed at 75 °C for 6 h. A polymer solution was prepared by dissolving 4.17 g Pebax in 100 g solvent (70/30 v%/v% EtOH and deionized water) at 80 °C for 2 h. Then, 6 g of polymer solution was cast in a Teflon Petri dish. The resulting membranes were placed in a vacuum oven at 60 °C overnight to remove residual solvent after which the membranes were tested. An overview of the different polymers used is given in Table 7-1.

Table 7-1: Overview of the polymer membranes used for proof testing of HTGS-2.

Polymer	Polymer chemical structure	Average selective layer thickness (µm)
6FDA-DAM	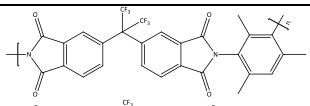	144
6FDA-DABA	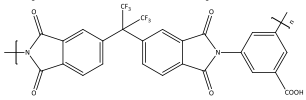	103
PAN supported PDMS		0.6
Pebax	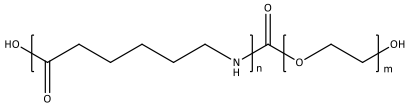	59
Polysulfone	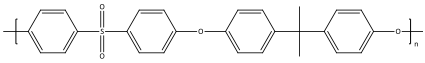	27

7.3 Results and discussion

7.3.1 Equipment design

7.3.1.1 Flow scheme

HTGS-2 is a semi-automated, constant-volume gas permeation set-up, which allows simultaneous performance testing of 8 membrane coupons. Table 7-2 gives an overview of the characteristics of HTGS-2 and compares with the original set-up (HTGS-1). Whereas the purpose of HTGS-1 was to create a testing unit that can quickly and accurately scan a large set of membranes in mixed-gas conditions, HTGS-2 aims at membrane testing under more industrially relevant conditions. It therefore allows a wider test range of both temperature and pressure, a more varied choice of relevant gas types and the possibility to add impurities (H_2O, BTX, ethane, propane). Furthermore, all tests are done in HT mode, which makes rapid screening of new membranes also possible for HTGS-2.

Table 7-2: Overview of HTGS-2 features and comparison to HTGS-1. RT = room temperature, BTX = benzene, toluene, xylene.

	HTGS-1	HTGS-2
Feed pressure range (bar)	1-15	1-34,5
Temperature range (°C)	RT-55	RT-100
Gases installed in the prototype set-up*	N_2, CH_4, CO_2, O_2, H_2	N_2, CH_4, CO_2, ethane, ethylene, propane, propylene
Effective membrane area per coupon (cm^2)	1,91	1,91
Humidifier	No	Yes
HT	Yes	Yes
Automated selectivity analysis	Yes	Yes
Accumulation volume (cm^3)	75	150
Mixed-gas	Yes	Yes
Permeate displacement	Vacuum	Vacuum
Number of membrane coupons	16	8

*Any gas type can be installed, provided the appropriate and correctly calibrated mass flow controllers (MFCs) are installed and the correct column for analysis is present in the on-line GC.

A simplified flow scheme is presented in Figure 7-2. A maximum of 8 membranes is placed in the pressure module (Figure 7-3), which is then sealed and pressurized. The module contains a stirrer, which helps minimizing concentration polarization. HTGS-2 is equipped with 5 MFCs, one for every gas type. For olefin/paraffin separation, one MFC is calibrated for both ethane and propane and one other for both ethylene and propylene. Flexible preparation of numerous gas mixtures is thus realized in a wide range of mixture compositions. As water is an important component in e.g. bio gas and flue gas, the resulting gas mixture can optionally be led to a humidifier, containing a 150 mL stainless steel cylinder filled with water. The relative humidity (RH) is measured by a RH sensor (Vaisala, HMT338). Analogously, the liquid-containing cylinder can also be applied for saturation of the gas stream with BTX (benzene, toluene, xylene) for natural gas mimicking. The feed stream is then introduced to the membrane module in cross-

flow mode, with Viton® rings ensuring that gas molecules only permeate from feed to permeate through the membranes. The module temperature is regulated by means of an electrical resistance embedded in the bottom plate of the module. Both gas stream and membrane module can be heated from room temperature to 100 °C, permitting elaborate temperature dependency studies. Moreover, a maximum feed pressure of 34.5 bar can be achieved in the prototype set-up, which enables better simulation of the conditions at which membranes for e.g. CO_2 removal from natural gas are tested in industry. Higher testing pressures can be reached if appropriate back-pressure controllers with higher pressure ranges are installed.

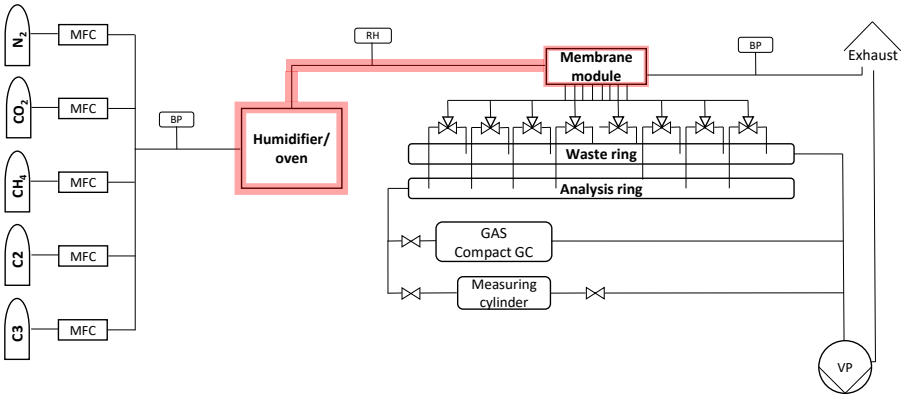

Figure 7-2: Simplified flow scheme of HTGS-2. MFC = mass flow controller, BP = back-pressure controller, RH = relative humidity sensor, GC = gas chromatograph, VP = vacuum pump, C2 = ethane and ethylene, C3 = propane and propylene. Set-up areas with temperature control are indicated in red.

On the permeate side, a vacuum is applied to facilitate displacement of the permeated gas. A two-ring system is used to permit simultaneous conditioning of all 8 membranes. The analysis ring collects the permeate of the membrane which is to be analyzed, which is subsequently led to either a gas chromatograph (GC) for compositional analysis (see section 7.3.1.4) or to the measuring cylinder for determination of permeance/permeability (see section 7.3.1.3). The waste ring is directly connected to the vacuum pump and merely serves for continuously conditioning of the 7 membranes that are not being analyzed at that moment. A set of 8 three-way valves allows straightforward switching between analysis and waste ring. By doing so, HTGS-2 can quickly change between different membrane positions for analysis (as all membranes are constantly kept in steady state), intensifying the HT principle.

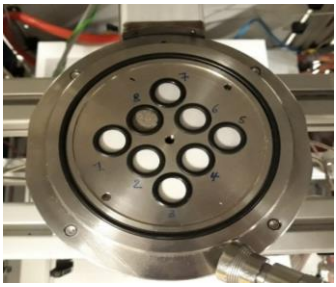

Figure 7-3: Picture of the HTGS-2 membrane module. Eight membranes can be placed and tested at the same time.

7.3.1.2 Hardware and software

Pressure reducers (0-68 bar), back-pressures (0-34.5 bar), 1/8" tubing, valves and pressure cylinders were acquired from Swagelok. All parts are made from 316L stainless steel to withstand corrosion by CO_2. MFCs were ordered from Gefran (Bronkhorst). For CH_4, N_2, ethane, propane, ethylene and propylene, standard F-201CV thermal MFCs were applied while CO_2 required a special Coriolis MFC. All MFCs have a minimal flow range of 0-250 mL/min, which is sufficient to give a gradual rise in pressure build-up throughout the set-up. The humidifier is custom-made and entails a 316L cylinder (150 mL) and a diffusion stone for gas sparging. Heating of the humidifier is performed inside an oven (max. temperature = 120 °C, Binder BF-56). RH of the feed stream is measured by a HMT 338 humidity and temperature transmitter (Vaisala, pressure limit = 40 bar).

Gas analysis is performed in a gas chromatograph (Compact $GC^{4.0}$, Interscience). A standard thermal conductivity detector (TCD) is used for detection, based on the difference in thermal conductivity of the applied gases. Helium is selected as carrier gas since it has a high thermal conductivity and can thus be used to accurately differentiate with other gases (Table 7-3). The permeate gas mixture is separated on a Rt-Q-Bond column (polyimide coated, fused silica outer tubing with a non-polar, stationary phase of divinylbenzene) of 20 m (diameter 0.32 mm, film thickness 5 µm). At the set conditions of flow and pressure, CO_2, CH_4 and N_2 elude within 2 min from the GC column while propane, propylene, ethane and ethylene diffuse through the column in less than 9 min. The down-stream pressure is measured with a pressure transducer (MKS Baratron, type 627F12MBC1B) with a measuring range of 0.1-200 mbar. The real-time pressure can be read on a display (MKS, PR4000BF2V2), connected to the pressure sensor and the PC. Finally, a rotation vacuum pump (Edwards, RV3, 220V/50Hz) is used to maintain vacuum at the permeate side. All MFCs are controlled via FlowBus software, including a FlowDDE package for communication between PC and MFCs and a FlowView package per MFC, which enables the user to set specific gas flows. The GC is operated by Chromeleon 7 software (Interscience). Permeance and permeability are measured with Lab-View executables.

Table 7-3: Thermal conductivity of all used gases in HTGS-2 (at 300 K)[270].

Gas	Thermal conductivity (mW/m.K)
He	155.7
CH_4	34.4
N_2	26.0
Ethane	21.2
Ethylene	20.6
H_2O	18.6
Propane	18.5
Propylene	17.0
CO_2	16.8

7.3.1.3 Permeability and permeance analysis

For gas permeability and permeance measurements, a constant-volume-varying-pressure method is applied. The two-way valve behind the accumulation cylinder is closed and the change in pressure as a function of time is monitored by the MKS Baratron vacuum sensor, which is connected to a desktop computer. The real-time pressure is shown on the pressure display. The rate of the change in pressure (dp/dt, expressed in Torr/s) is then used to calculate gas permeability by using Equation 7.1. Figure 7-4 shows the Excel plot, which is obtained after measuring the increase in pressure.

$$P_i = 10^{10} \times \frac{y_i \times V \times V_m \times L}{x_i \times p_{up} \times A \times R \times T} \times \frac{dp}{dt} \quad (7.1)$$

with P_i the gas permeability (Barrer), y_i the mole fraction of the component in the permeate, x_i the mole fraction of the component in the feed, V the downstream volume (75 cm^3), V_m the molar volume (L/mol), A the membrane permeation area (1.91 cm^2), L the membrane thickness (µm), T the operating temperature (K), p_{up} the upstream pressure (bar), R the gas constant (0.082 L atm/mol K) and dp/dt the pressure increase (Torr/s). For pure gas experiments y_i and x_i equal 1.

The permeance Q is then given by:

$$Q_i = \frac{P_i}{L} \quad (7.2)$$

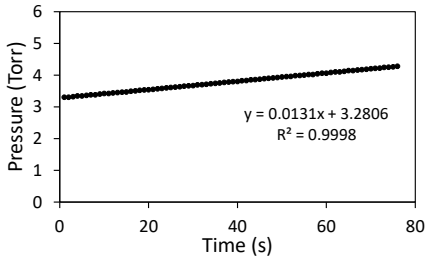

Figure 7-4: Example of the determination of the dp/dt slope for calculation of the membrane permeability.

7.3.1.4 Gas compositional analysis

The separation factor α^*_{ij} of the membranes is calculated by determination of the permeate composition (Equation 7.3):

$$\alpha^*_{ij} = \frac{y_i / y_j}{x_i / x_j} \tag{7.3}$$

where y_i and y_j are the mole fractions of gas i and gas j in the permeate, x_i and x_j the mole fractions of gas i and j in the feed.

The ratio y_i/y_j is determined from the chromatogram peak areas corresponding with the different gases present in the permeate, while x_i/x_j is determined by the MFC feed settings.

7.3.2 Set-up for proof testing

7.3.2.1 Stage-cut and concentration polarization

The stage-cut (SC) is an operational process parameter defined as the ratio of the permeate flow over the feed flow:

$$SC = \frac{Permeate\ flow}{Feed\ flow} \tag{7.4}$$

Two other process parameters, i.e. CO_2 recovery and permeate purity, heavily depend on the choice of SC. CO_2 recovery entails the percentage of feed CO_2 that is recovered in the permeate and permeate purity is defined as the concentration of CO_2 in the permeate. For an identical membrane, choosing a low SC results in a relatively high purity and low recovery while high SC will overall lead to low purity and high recovery. Table 7-4 shows the anticipated SC for three different polymer membranes (6FDA-DAM, 6FDA-DABA and Pebax) tested in HTGS-2. The set-up SC is calculated based on the total permeate flow of 8 membrane coupons (feed stream consisting of 250 mL/min CO_2 and 250 mL/min CH_4, 5 bar, 500 mL/min total feed flow). As can be observed in Table 7-4, the expected SC for all dense membranes is well below 1%. Experimentally, this indicates that 8 coupons can be tested at the same time without concentration polarization occurring. Furthermore, no problems in feed pressure build-up are expected.

Table 7-4: Overview of the anticipated stage-cut for all membranes used.

Polymer	CO_2 permeability (Barrer)*	Anticipated total permeate flow (mL/min)	Anticipated stage-cut
6FDA-DAM	~1000	2.4×10^{-1}	0.0038
6FDA-DABA	~20	6.7×10^{-3}	0.0001
Pebax	~75	4.3×10^{-2}	0.0007

*for 50v%/50v% CO_2/CH_4 feed at 5 bar.

7.3.2.2 Stability over time and equivalence of positions

Figure 7-5 shows the variation in CO_2/CH_4 separation factor of a 6FDA-DAM membrane over time. The separation factor initially strongly decreases per time unit, but stabilizes after roughly 120 min once the gas permeation through this ~140 µm thick membrane reaches steady state.

After steady state, the membrane performance remains constant for a period of 24 h, indicating the stability of the GC measurement over time.

The HT principle applied in HTGS-2 involves that all membranes positioned in the set-up are exposed to the same feed conditions. As a result, all membranes can be simultaneously conditioned. Once the membranes have reached steady state, this allows a swift, consecutive screening of all membranes, severely reducing the measuring time. To demonstrate this and to confirm the equal performance at each module position, all positions were loaded with 6FDA-DAM membrane coupons. The membranes were allowed to reach steady state and were then consecutively measured. Figure 7-5 displays that in general all membranes give very similar and constant performances. The CO_2/CH_4 separation factor for all membranes varies between 22.0 and 24.2, which can be considered as normal performance deviations related to differences between the membrane coupons. Moreover, these values agree very well with the ones reported in literature[168]. Also for the CO_2 permeability measurements, no differences can be observed between the positions. The variation noted in permeabilities between coupons (ranging from 1850 till 2080 Barrer) are again attributed to the membranes themselves. Yet, all permeability values measured are substantially higher than generally reported for similar membranes (~1000 Barrer).

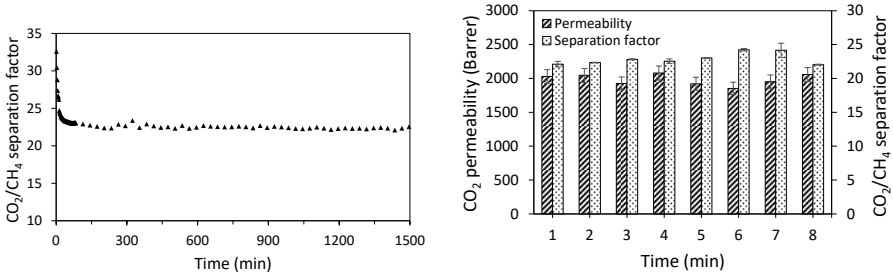

Figure 7-5: Left: Steady state separation factor for the 6FDA-DAM membrane is reached after approximately 60 min during a CO_2/CH_4 separation at 5 bar, 25 °C. For time = 0 till time = 84 min, sampling time between two measurements is 1.7 min. Afterwards, sampling time is 30 min. Right: Comparison of mixed-gas CO_2/CH_4 selectivity and CO_2 permeability between all 8 positions in HTGS-2. 6FDA-DAM membranes were used as test case.

7.3.2.3 Mixed-gas performance of various membranes

Next, the mixed-gas separation performance of 6FDA-DAM, 6FDA-DABA and Pebax membranes at varying pressures and temperatures for all available gases were tested. Table 7-5 confirms the good reliability of the GC measurements for determination of the separation factor. For all gas feeds and for all membranes, the separation factors observed are accurately in line with literature reports and show low standard deviations between 2-3%[47,143,262,271]. Although the standard deviations for the permeability measurements are low as well, the absolute CO_2 and propylene permeability values are systematically higher than reported in literature.

Table 7-5: CO_2/CH_4, CO_2/N_2 and propylene(C3=)/propane(C3) separation factor and CO_2 and propylene permeability of 6FDA-DAM, 6FDA-DABA and Pebax membranes as tested on HTGS-2. Gas filtrations were performed with 50v%/50v% CO_2/CH_4 and CO_2/N_2 mixtures at 5 bar and 30 °C.

Polymer	$\alpha^*_{CO2/CH4}$	P_{CO2} (Barrer)	$\alpha^*_{CO2/N2}$	P_{CO2} (Barrer)	$\alpha^*_{C3=/C3}$	$P_{C3=}$ (Barrer)
6FDA-DAM	22.9±1.1	2050±91	24.2±1.7	2044.9±84	6.7±0.1	136±19
6FDA-DABA	31.5±1.1	43.0±1.7	-	-	-	-
Pebax	14.1±0.0	163±9.1	45.7±2.2	171±9.7	-	-

Subsequently, a pressure-dependency test on 6FDA-DAM membranes was carried out in a broad feed pressure range, as displayed in Figure 7-6. The steady permeability decrease is in agreement with the dual-mode sorption model[21]. Nonetheless, the absolute permeability values are again higher than reported. Above 20 bar, the CO_2 permeability increases as a result of plasticization. The plasticization pressure found here corresponds well with literature as a similar plasticization pressure was found by Qiu *et al.*[262]. Evolution of the CO_2/CH_4 separation factor depends on the relative change in permeability between CO_2 and CH_4. A decreasing CO_2/CH_4 separation factor suggests that the permeation behavior of CO_2 is more affected by the changing pressure than CH_4 permeation. Both solubility and diffusivity can be at the base of this behavior but since dense membranes with high Young modulus were tested, compaction and thus large changes in gas diffusivity seem unlikely. In previous work, it was shown that the reduction in separation factor can largely be attributed to a relatively stronger decrease in CO_2 solubility than in CH_4 solubility[208].

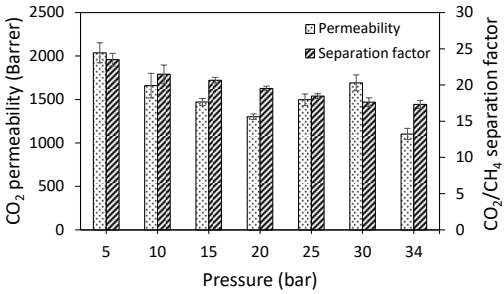

Figure 7-6: Pressure dependency experiments performed on 6FDA-DAM membranes. Gas filtrations were performed with a 50v%/50v% CO_2/CH_4 feed composition at 30 °C.

Also the temperature dependency of the 6FDA-DAM membranes was studied by gradually increasing the measuring temperature from 30 °C till 100 °C (Figure 7-7). Both CO_2/CH_4 separation factor and CO_2 permeability decrease with increasing temperature. It is believed that diffusion of gases increases at higher temperatures due to enhanced rotational movement of the polymer chains, eventually resulting in lowered separation factor. As permeability is a product of both gas solubility and diffusivity, the balance between the two will dictate whether the overall permeability will decrease or increase with temperature. Furthermore, the activation energy for CO_2 permeation (E_p) can be calculated since transport through a dense

membrane can be presented as an activated process with an Arrhenius-like permeability behavior. Following Equation 7.5, the permeability can be expressed as a function of temperature. From Equation 7.5 follows that the activation energy for CO_2 permeation in 6FDA-DAM is -4.9 kJ/mol, which is well in line with literature (e.g. -3.3 kJ/mol for CO_2 permeation in related 6FDA-TMPDA membranes)[272].

$$P = P_0 \times \exp(-\frac{E_P}{RT}) \quad (7.5)$$

with P the permeability, P_0 a pre-exponential factor, E_p the activation energy for permeation, T the temperature and R the universal gas constant.

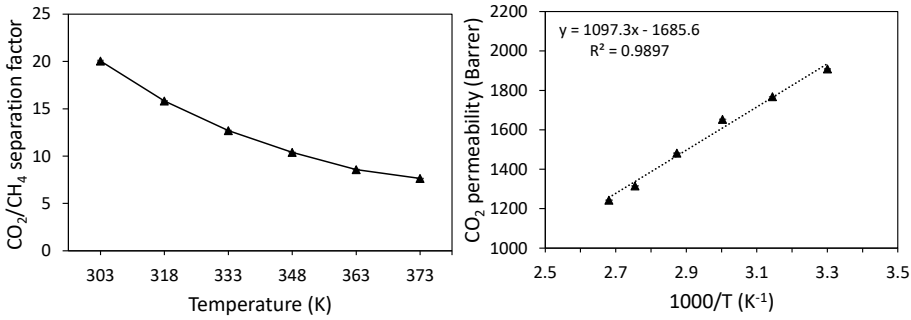

Figure 7-7: Temperature dependency of the CO_2/CH_4 separation factor and CO_2 permeability of a 6FDA-DAM membranes.

7.3.2.4 Comparison with HTGS-1

Finally, the membranes used for proof testing HTGS-2 were placed in HTGS-1 and both permeation results were compared (Table 7-6). On one hand, a good agreement can be observed between both data sets with respect to the separation factor. For both low- and high-permeable membranes, a low standard deviation indicates a good consistency between membrane coupons while the corresponding absolute values for separation factor are very similar. On the other hand, the CO_2 permeability for all membranes is systematically higher with HTGS-2. The permeability offset strongly varies between coupons, with the highest offset observed for Pebax membranes (120%).

Table 7-6: Comparison of separation factor ($\alpha^*_{CO2/CH4}$, $\alpha^*_{CO2/N2}$) and CO_2 permeability (Barrer) of dense 6FDA-DAM, 6FDA-DABA and Pebax membranes measured on HTGS-1 and HTGS-2 for CO_2/CH_4 and CO_2/N_2 mixed-gas filtrations.

	HTGS-1	HTGS-2	HTGS-1	HTGS-2	HTGS-1	HTGS-2	HTGS-1	HTGS-2
Polymer	P_{CO2} (CO_2/CH_4)		P_{CO2} (CO_2/N_2)		$\alpha^*_{CO2/CH4}$		$\alpha^*_{CO2/N2}$	
6FDA-DAM	1168±95	2050±91	1102±23	2044±84	21.7±0.2	22.9±1.1	20.8±0.9	24.2±1.7
6FDA-DABA	23.1±3.5	43.0±1.7	-	-	32.0±0.8	31.5±1.1	-	-
Pebax	74.4±0.5	163±9	76.4±0.8	171±9	14.7±1.2	14.1±0.0	43.5±2.4	45.7±2.2

7.3.2.5 Preliminary conclusions

Even though the obtained separation factor values agree very well with both literature and measurements conducted with HTGS-1, it is clear that CO_2 permeability values obtained with HTGS-2 are systematically too high. In the next section, this problem is mapped in more detail by measuring gas permeation through various membranes while varying gas type and feed pressure on both HTGS-1 and HTGS-2.

7.3.3 Mapping the permeability problem

Three polymer membranes with strongly varying permeance are chosen to map the HTGS-2 permeability problems: dense polysulfone films with low permeance (~25 µm thickness), dense 6FDA-DAM membranes with medium permeance (average thickness of 144 µm) and thin-film composite PDMS membranes with high gas permeance (~0.6 µm thickness). For each membrane type, three coupons were systematically measured with HTGS-1 and HTGS-2. All membranes were tested with three different gases (N_2, CH_4 and CO_2) at three different pressures (2.5 bar, 5 bar and 10 bar). A permeability offset is defined to allow comparison between both set-ups and between measuring conditions:

$$Permeability\ offset = \left(\frac{permeability\ HTGS-2}{permeability\ HTGS-1} - 1\right) \times 100\% \tag{7.6}$$

For example, a 6FDA-DAM membrane with a CO_2 permeability of 2050 Barrer measured on HTGS-2 and 1170 Barrer measured on HTGS-1 will have a permeability offset of 75%.

7.3.3.1 Polysulfone membranes

Figure S7-1 shows the average N_2, CH_4 and CO_2 permeability measured for the polysulfone coupons with HTGS-1 and HTGS-2. As measured with HTGS-1, the CO_2 permeability of polysulfone varied between 7 and 10 Barrer depending on the pressure, making polysulfone a low-permeable polymer. At the lowest pressure (2.5 bar), the average CH_4, N_2 and CO_2 permeances of the polysulfone membranes were 0.016, 0.013 and 0.38 GPU, respectively. The permeability offsets for the examined polysulfone membranes are given in Figure 7-8. In general, high offsets up to 250-260% are observed for the 'slow' gases N_2 and CH_4, especially at low pressure (2.5 and 5 bar). Switching to a fast gas (CO_2) and applying a higher pressure decreases the permeability offset, indicating that the gas flux through the membrane determines the accuracy of the measurement. It is thus noted that the permeability offset is not constant and strongly fluctuates depending on the gas type and feed pressure. Furthermore, the ideal selectivities for CO_2/N_2 and CO_2/CH_4 were determined and are displayed in Figure S7-2. Both CO_2/N_2 and CO_2/CH_4 ideal selectivity determined on HTGS-1 follow a clear decreasing trend with increasing feed pressure, similar to previous observations for pressure dependency experiments with glassy polymers[95,208]. In strong contrast, the ideal selectivities measured on HTGS-2 seem to evolve randomly, indicating that the offset trends between gases are not the same.

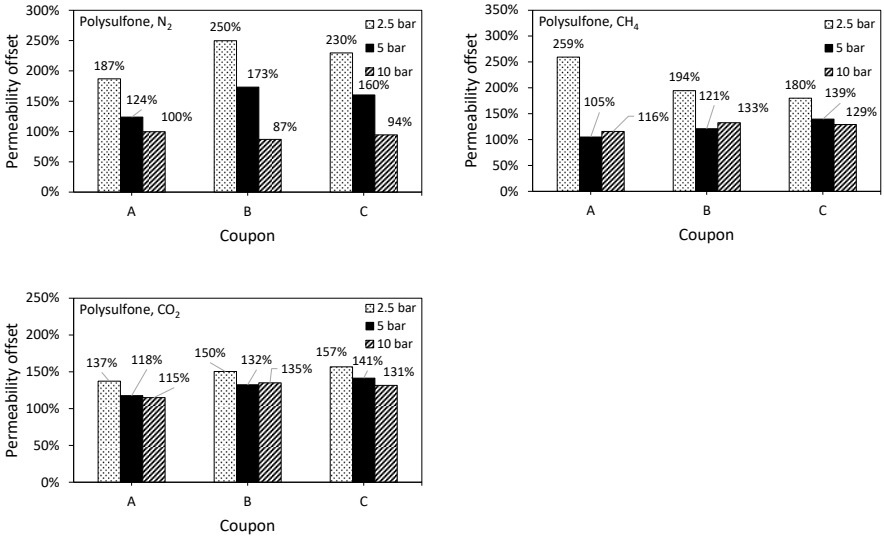

Figure 7-8: Permeability offsets of three polysulfone coupons (A, B, C) for N_2, CH_4 and CO_2 pure gas filtrations at 2.5, 5 and 10 bar.

7.3.3.2 6FDA-DAM membranes

The average N_2, CH_4 and CO_2 permeabilities obtained at HTGS-1 and HTGS-2 for 6FDA-DAM membranes are given in Figure S7-3. The 6FDA-DAM membranes showed a medium CO_2 permeability of around 1100 Barrer. At 2.5 bar feed pressure, the average CH_4, N_2 and CO_2 permeances were 0.52, 0.61 and 10.26 GPU, respectively. Similar to polysulfone, high and strongly varying offsets are observed for N_2 and CH_4, albeit less pronounced (Figure 7-9). Again, a more uniform and lower offset is observed when measuring CO_2 or when applying higher pressures. These data further confirm the hypothesis that high-flux conditions are beneficial for the sensitivity of the measurement. Also for the ideal selectivity, similar trends are observed compared to polysulfone membranes (Figure S7-4).

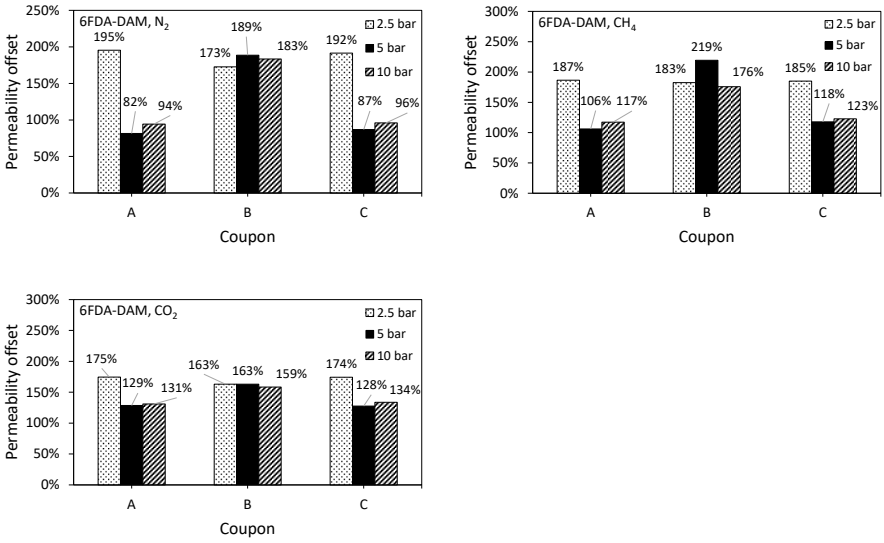

Figure 7-9: Permeability offsets of three 6FDA-DAM coupons (A, B, C) for N_2, CH_4 and CO_2 pure gas filtrations at 2.5, 5 and 10 bar.

7.3.3.3 PAN-PDMS membranes

Similarly, PAN-PDMS composite membranes were tested on HTGS-1 and HTGS-2. The high permeances of the PAN-PDMS membranes were found to lay outside the measuring range of HTGS-1. Consequently, no comparison could be made with HTGS-2 under the standard feed conditions and gas types. Yet, at 2 bar N_2 and 25 °C, the rate of N_2 permeation through the PAN-PDMS membrane was low enough to conduct a permeance measurement on HTGS-1 (Figure S7-5). The N_2 permeance averaged around 126 GPU for HTGS-1 while HTGS-2 recorded an average of 491 GPU. In contrast to the polysulfone and 6FDA-DAM membranes, the permeance offset between HTGS-1 and HTGS-2 is relatively constant (even at low feed pressure), ranging from 285% till 302% (Figure 7-10). When the PAN-PDMS membranes are tested on HTGS-2 in the same conditions as the polysulfone and 6FDA-DAM membranes (N_2, CH_4, CO_2 at 2.5-10 bar), consistent data are thus obtained albeit roughly 300% too high. However, the trends with respect to pressure dependency and gas type are in line with expectations as the permeance decreases at higher pressures for all gas types (Figure 7-10) and the permeation rate increases from $N_2 < CH_4 < CO_2$.

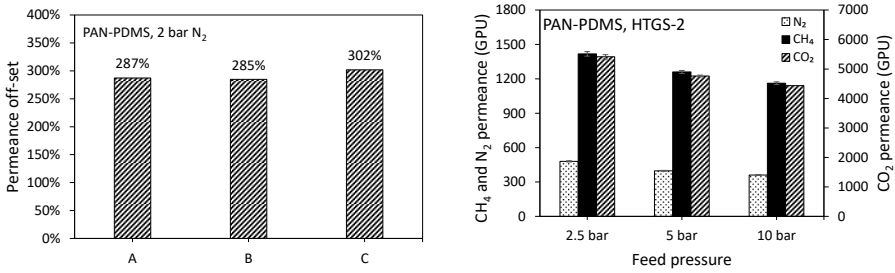

Figure 7-10: Left: Permeance offsets of three PAN-PDMS coupons (A, B, C) for N_2 pure gas filtration at 2 bar. Right: average CO_2, N_2 and CH_4 permeability measured on HTGS-2 for PAN-PDMS membranes at 2.5, 5 and 10 bar.

7.3.4 Discussion

The results obtained from the permeation experiments with different membranes clearly show that HTGS-2 currently faces two problems that need to be resolved. First of all, the permeabilities and permeances obtained with HTGS-2 are structurally too high compared to permeabilities measured on HTGS-1 and literature reports. Furthermore, the offset between HTGS-1 and HTGS-2 strongly fluctuates depending on the membrane type, gas type and feed pressure and thus cannot be considered constant. In general, higher and more varying offsets are observed for low-flow conditions (i.e. low-permeable polymer, slow gas and low feed pressure). In other words, the set-up struggles to accurately measure gas permeation in these conditions. In high-flow conditions (for example PAN-PDMS membranes), the offset is high but relatively constant and permeation trends are observed as expected based on the solution-diffusion model. So far, additional leak testing, recalibration of the vacuum pressure sensor and the use of a secondary vacuum pressure sensor could not resolve or identify the root of the problem. Several future mitigation strategies with a strong focus on the downstream part of the set-up are proposed to fix this problem:

- The measuring time can be increased when acquiring data in low-flux conditions, elongating the averaging time.
- In the current configuration, the downstream tubing and measuring cylinder constitute a total volume of approximately 180 cm^3. A smaller downstream volume would induce higher vacuum pressures and thus a more accurate measurement. For this purpose, the downstream measuring cylinder can be replaced by several smaller cylinders with two-way valves in between (Figure 7-11). As such, the total volume of 150 cm^3 can be divided into one of 25 cm^3, one of 50 cm^3 and one of 75 cm^3, ensuring for a flexible downstream volume that can be modified depending on the anticipated membrane and flux.
- The vacuum pressure sensor and measuring cylinder can be repositioned to minimize dead-volume between the membranes and the sensor. Currently, the gas needs to migrate through approximately 2 m of 1/8" tubing before it reaches the pressure sensor and the measuring cylinder. In a future design of the set-up, the sensor and

measuring cylinder can be attached directly to the analysis ring, albeit still in parallel with the GC (Figure 7-11).

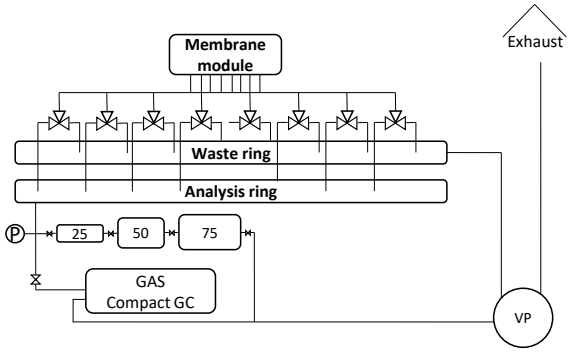

Figure 7-11: Modified downstream configuration of HTGS-2.

7.4 Conclusions

A second generation HTGS set-up was developed and built to overcome the currently existing gap between lab-scale and industrial membrane testing. HTGS-2 builds on the HT principle of membrane testing, which allows rapid assessment of 8 membranes in one experiment. It is equipped for testing membranes at high pressure (up to 34 bar) and temperature (up to 100 °C) with a wide variety of gases (N_2, CH_4, CO_2, ethane, propane, ethylene and propylene). Lab-made 6FDA-DAM, Pebax and 6FDA-DABA membranes with high, intermediate and low permeability, respectively, were used to proof-test the set-up over a broad range of membrane performances. GC measurements for determination of the separation factor proved to be stable over a time period of 24 h. Membranes placed in the 8 different positions of HTGS-2 performed statistically identical. The acquired separation factors of the different membrane types for CO_2/CH_4, CO_2/N_2 and propylene/propane separations were in excellent agreement with values previously reported in literature and measured on HTGS-1. Furthermore, low standard deviations indicated good reproducibility of the results. However, mixed-gas permeabilities measured during proof testing were systematically too high in comparison with permeabilities obtained on HTGS-1. For this reason, three polymer membranes (PAN-PDMS, 6FDA-DAM, polysulfone) with strongly varying gas permeability and permeance were used to map the permeability problem. Measuring these membranes with pure gas streams of N_2, CH_4, CO_2, propane and propylene at three different pressures (2.5, 5 and 10 bar) revealed that low-flux conditions (low-permeable polymer, slow gas and/or low pressure) resulted in high permeability offsets between HTGS-1 and HTGS-2. Furthermore, the variation on the offset was also high, making it impossible to identify trends. These observations suggested that the sensitivity of the set-up in the current configuration is too low to accurately measure low-permeable membranes with feeds at low pressure and slowly permeating gases. For high flux conditions (highly permeable polymer, fast gas and/or high pressure), the offset decreased and was more constant. PAN-PDMS coupons showed a relatively constant offset of 280-300% for a pure N_2 feed at 2 bar. Several potential solutions for the permeability offset were proposed, including minimizing the downstream volume, redesigning the measuring cylinder concept and repositioning the pressure sensor.

7.5 Acknowledgements

R.T. is grateful to FWO Vlaanderen for his FWO SB grant (1S63317N).

7.6 Supplementary information to Chapter 7

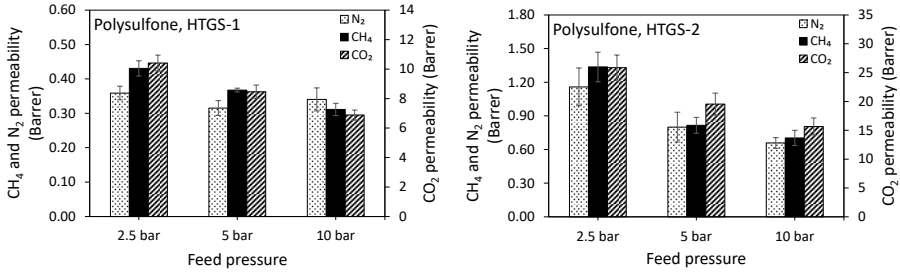

Figure S7-1: Average CO_2, N_2 and CH_4 permeability measured on HTGS-1 (left) and HTGS-2 (right) for polysulfone membranes at 2.5, 5 and 10 bar.

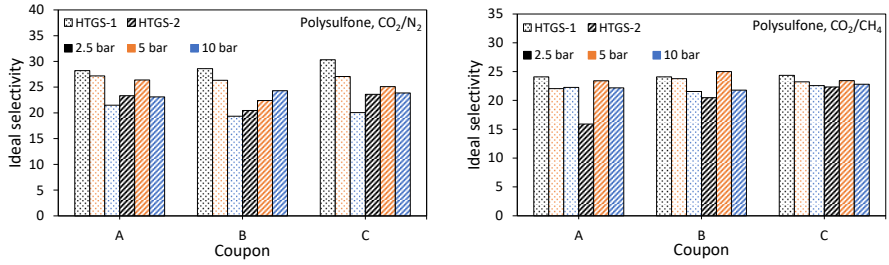

Figure S7-2: CO_2/N_2 and CO_2/CH_4 ideal selectivities of three polysulfone coupons (A, B, C) for filtrations at 2.5, 5 and 10 bar.

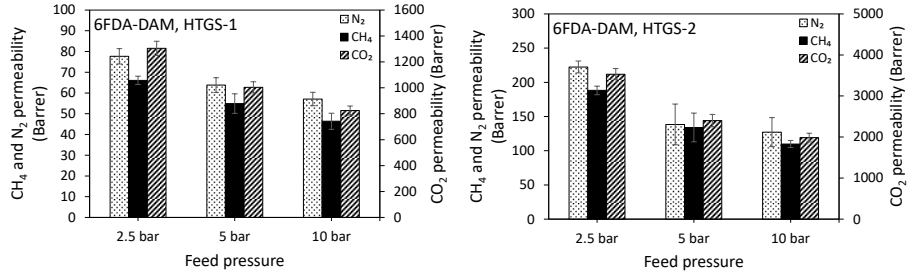

Figure S7-3: Average CO_2, N_2 and CH_4 permeability measured on HTGS-1 (left) and HTGS-2 (right) for 6FDA-DAM membranes at 2.5, 5 and 10 bar.

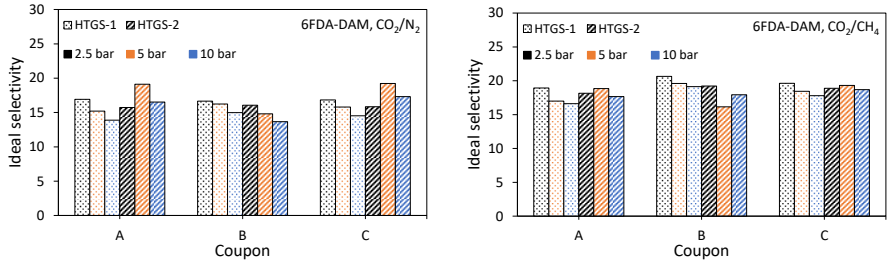

Figure S7-4: CO_2/N_2 and CO_2/CH_4 ideal selectivities of three 6FDA-DAM coupons (A, B, C) for filtrations at 2.5, 5 and 10 bar.

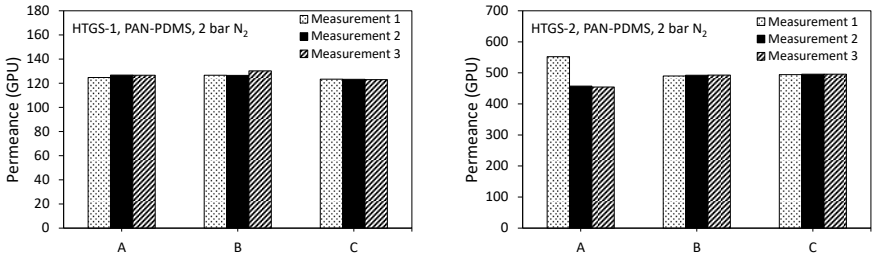

Figure S7-5: N_2 permeance at 2 bar feed pressure measured on HTGS-1 (left) and HTGS-2 (right) of three PAN-PDMS coupons (A, B, C). Each measurement was repeated three times.

Chapter 8

General conclusions and future perspectives

Raymond Thür, Ivo F.J. Vankelecom

Centre for Membrane Separations, Adsorption, Catalysis and Spectroscopy for Sustainable Solutions (cMACS), KU Leuven, Celestijnenlaan 200F, Box 2454, 3001 Heverlee, Belgium

8.1 General conclusions

This dissertation aimed to improve three important aspects of membrane development for CO_2 separations. In a first part, a strong focus on membrane development towards better membrane properties for separation of CO_2 from CH_4 and N_2 resulted in novel MMMs based on MOF-808 and UiO-67 and cross-linked 6FDA-DABA membranes with enhanced separation performance. Secondly, the conclusions drawn from the MMM research eventually gave rise to the question which fundamental MOF parameters can be used as indicators for MMM performance and can, as such, pave the road toward a smarter design of MMMs. Finally, a second generation HTGS equipment was designed and constructed for testing of membranes under realistic, industrial conditions. In this way, the true potential of the membrane should become clear earlier in the development stage. The integrated conclusions from this dissertation are formulated below.

Chapter 1 gave an introduction to membrane-based gas separation, including a short historical overview of important membrane events, relevant membrane terminology, performance indicators and transport mechanisms. Commonly used polymer membranes in industry and academia were shortly discussed along with possible new routes towards improved membranes. MMMs were introduced with special attention for their opportunities and challenges.

In **Chapter 3**, novel MMMs based on zirconium MOF UiO-67 and Matrimid were developed. The standard BPDC linkers of UiO-67 were replaced with BPYDC linkers in varying concentrations in an attempt to increase the CO_2-philicity of the MOF and hence of the MMM. Higher CO_2 uptake and affinity were observed for the MOF when more BPYDC linker was incorporated, which was attributed to the Lewis basic nitrogen functionalities in the BPYDC linker. Upon incorporation of the MOF in Matrimid membranes, a strong enhancement in both CO_2/CH_4 separation factor and CO_2 permeability was realised. PALS showed that the increased CO_2 permeability was a result of more free volume in the membrane while the improved separation factor was linked to the higher CO_2 affinity of the UiO-67-BPYDC MOF and to polymer rigidification at the polymer-MOF interphase. Although the UiO-67-BPDYC MMMs were a success in terms of separation performance, the UiO-67 MOF showed limited stability and was considered relatively expensive due to the high cost of the BPYDC linker.

In **Chapter 4**, UiO-67 was replaced by the far more stable MOF-808, consisting of the same zirconium-oxo clusters but connected with tritopic BTC linkers instead of ditopic BPDC. MOF-808 was introduced as a platform MOF for MMM functionalization since the unique structure of MOF-808 allows incorporation of CO_2-philic modulators during a simple and cheap in-situ MOF functionalization method (MoFu). The presented MoFu concept was exemplified by using fluorinated carboxylic acids as modulator during MOF-808 synthesis. In a first section, the dependency of the MMM performance on the MOF particle size was studied by incorporating TFAA modulated MOF-808 with average particle sizes around 150 nm, 550 nm and 1300 nm. In contrast to literature, it was found that a minor improvement in permeability and separation factor could be achieved for the smallest MOF particles. This was mainly attributed to the

prevention of particle agglomeration by using a 'wet synthesis' method for MMM preparation. In a second part, the MoFu concept was expanded and a series of fluorinated and non-fluorinated carboxylic acids were used to modulate MOF-808 synthesis. With exception of HFBA, all modulators (both the non-fluorinated and the fluorinated) yielded microporous and highly crystalline MOFs. The fluorinated MOFs showed a higher affinity for CO_2 than the non-fluorinated MOFs, owing to the strongly polarized nature of the C-F modulator bonds. Eventually, incorporation of the fluorinated MOFs resulted in excellent MMM CO_2/CH_4 separation performance for TFAA and PFPA modulated MOF-808. Interestingly, an improved solubility selectivity seemed to be at the base of the better performance of MMM-PFPA compared to MMM-TFAA. For HFBA modulated MOF-808, the performance was partially compromised, which was hypothesized to be due to bad interaction between the polymer chains and the long hydrophobic modulators on the MOF surface. Nonetheless, the fluorinated MOF MMMs crossed the 2018 mixed-gas upper bound, proving their excellent performance.

Chapter 5 continued on the findings of Chapter 4. More particularly, the apparent lack of structural link between MOF CO_2 uptake and MMM performance in Chapter 4 gave rise to the question which MOF parameters can be used as MMM performance indicators. In an attempt to correlate intrinsic MOF parameters to the performance of the corresponding MMM, the platform ability of MOF-808 was again exploited to make a series of isostructural MOFs with different ligands (TFAA, histidine, GA, BA, FA and Li_2SO_4) attached to the MOF cluster. In this way, a broad range of values for traditional MOF parameters such as CO_2 uptake, BET surface area and pore volume was obtained. Moreover, to more accurately quantify the CO_2 affinity of the MOFs, the CO_2 heat of adsorption (Q_{st}) was determined for all MOFs. Next, MMMs were prepared from all MOFs and tested for their CO_2/N_2 separation performance under different feeds with varying CO_2 content. Correlation coefficients between the four MOF parameters (CO_2 uptake, CO_2 Q_{st}, BET surface area and pore volume) on one hand and the corresponding MMM gas separation performance on the other hand were calculated. As expected, BET surface area and pore volume showed only weak correlation with the MMM separation factor and moderate correlation with CO_2 permeability. Surprisingly, MOF CO_2 uptake proved to be a poor indicator for MMM performance in contrast to general assumptions in literature. Q_{st} at high CO_2 loadings yielded the highest correlation with the CO_2/N_2 separation factor, albeit still with only moderate correlation strength. The best indicator for CO_2 permeability proved to be Q_{st} as well at high CO_2 loadings, which was the only parameter to display high correlation coefficients with CO_2 permeability. The surprising lack of correlation of MMM performance with CO_2 uptake and the strong correlation with CO_2 Q_{st} once more underlined the difficulty to rationally design MMMs and, more importantly, emphasized the need for more research focused on finding consistent relationships between MOF and MMM structures and ultimate membrane performance.

In **Chapter 6**, 6FDA-DABA membranes were annealed at different temperatures (100 °C, 180 °C, 250 °C, 350 °C and 400 °C) and tested for their CO_2 removal capacity from CO_2/N_2 and CO_2/CH_4 model mixtures. ATR-FTIR, DSC and TGA-MS showed that, starting from ~330 °C, decarboxylation cross-linking occurred, resulting in the formation of covalent bonds between the polymer chains for 6FDA-DABA-350 and 6FDA-DABA-400. Furthermore, EDX suggested that

(at least part of) the polymer backbone of 6FDA-DABA-400 had been oxidized by the thermal treatment. Thorough characterization showed that the separation performance of the 6FDA-DABA membranes was governed by two counteracting mechanisms. On one hand, higher annealing temperatures resulted in a more efficient polymer chain packing, causing a steady increase in CO_2/CH_4 separation factor with increased annealing temperature till 350 °C. For 6FDA-DABA-350, the CO_2/CH_4 separation factor was almost doubled compared to the reference membrane. On the other hand, it was observed that decarboxylation cross-linking, occurring only for 6FDA-DABA-350 and 6FDA-DABA-400, resulted in a more open polymer structure with more FFV, as confirmed by XRD and density measurements. As a result of this dilated polymer structure, an enhanced CO_2 permeability was realized for 6FDA-DABA-350 (+40%) while 6FDA-DABA-400 even reached a 10 times higher CO_2 permeability than 6FDA-DABA-100 at constant separation factor. However, the mechanical properties of 6FDA-DABA-400 were severely compromised, hampering the application potential of this membrane. Being a borderline case, 6FDA-DABA-350 profits from both effects, resulting in a simultaneous increase in both permeability and separation factor. Finally, following from the cross-linking, an improved resistance to CO_2 plasticization was achieved for 6FDA-DABA-350, as demonstrated in pressure-dependency experiments.

Chapter 7 discussed the design and assembly of a second generation HT membrane testing set-up (HTGS-2). The direct incentive for the development of HTGS-2 was the currently existing gap between academic and industrial membrane testing, where membranes in academia are often tested and evaluated in conditions that are far from industrial reality. HTGS-2 builds on the principle of HT membrane testing and is equipped to simultaneously test 8 membranes at high pressure (up to 34 bar), high temperature (up to 100 °C), with 7 available gases (CO_2, CH_4, N_2, propane, ethane, propylene and ethylene) and the optional addition of gas impurities (e.g. water) to the feed streams. These testing conditions allow HTGS-2 to accurately mimic industrial gas streams, such as natural gas, bio gas or flue gas and olefin/paraffin streams. After assembly, the set-up was proof tested with three lab-made polymer membranes (6FDA-DAM, Pebax and 6FDA-DABA). The membrane separation factors and gas permeabilities acquired on HTGS-2 were compared to literature reports and values obtained on HTGS-1. The separation factors of the different membranes for CO_2/CH_4, CO_2/N_2 and propylene/propane separation were found to be highly accurate and well in agreement with literature and HTGS-1 data. Low standard deviations indicated good reproducibility of the results. Moreover, it was proven that the separation factor measurements were stable over time and were not affected by module position. In contrast, it was observed that the mixed-gas permeabilities of the membranes used during proof testing were systematically too high. Consequently, three polymer membranes with strongly varying permeances (commercial PAN-PDMS, commercial polysulfone and lab-made 6FDA-DAM) were used to map this permeability problem and identify the root cause. The membranes were tested with pure gas streams of N_2, CH_4, CO_2, propane and propylene at 2.5, 5 and 10 bar on both HTGS-1 and HTGS-2. Two important conclusions could be drawn from these experiments. First of all, the comparison between HTGS-1 and HTGS-2 revealed that low-flux conditions (low-permeable polymer, slow gas and low transmembrane pressure) caused high permeability offsets. Secondly, the observed permeability offsets were not constant within

a series of membrane type, gas type or pressure. Especially for low-flux conditions strongly fluctuating offsets were observed while the offsets were found to be more stable for high-flux conditions (e.g. PAN-PDMS coupons showed a relatively constant offset of 280-300% for a pure N_2 feed at 2 bar). As a result, no trends in permeability offset could be observed. These observations suggested that the sensitivity of the set-up in the current configuration is too low for accurately measuring low-permeable membranes with feeds at low pressure and slow gases. Several potential solutions for the permeability offset were proposed, including minimizing the downstream volume, redesigning the measuring cylinder concept and repositioning the pressure sensor.

8.2 Future work and outlook

Membrane-based CO_2 separation has matured over the past decades into a viable alternative for conventional separation techniques such as amine scrubbing and cryogenic distillation. Exceptional performance improvements have been reported for so-called breakthrough materials, such as MMMs, PIMs, TRs and facilitated transport membranes, potentially unlocking new applications (e.g. CO_2 capture). With regard to this dissertation, focus has mainly been on development of CO_2-selective MOF-808 MMMs and polymeric 6FDA-DABA membranes and on the design of a new membrane testing set-up. Future research suggestions for all of these are listed below.

8.2.1 Future work

8.2.1.1 MOF-808 MMMs

MOF-808 has proven to be an attractive candidate for MOF-based MMM development as it yields a broad range of appealing properties relevant for MMM synthesis. It shows excellent chemical, mechanical and economical features combined with straightforward upscaling and synthesis pathways based on water instead of toxic solvents. Moreover, MOF-808 can act as a platform material, allowing very easy functionalization with just about all chemicals bearing a carboxylic acid group. This functionalization versatility allows to tune MOF and MMM performance towards both high solubility, high diffusivity selectivity or even a combination of both. First of all, the overall permeability of the MMMs prepared in this doctorate should be increased. The target membrane performances for CO_2/CH_4 applications are believed to entail a separation factor of 20-30 (under real conditions) combined with a CO_2 permeance of more than 100 GPU[8]. A simple calculation shows that for a selective layer thickness of 500 nm (which is reasonable for a defect free thin-film MMM), an up-scaled version of the MMMs would have a CO_2 permeance of 40 GPU. A first and straightforward option here would be to use of a more permeable starting polymer, which can significantly improve permeance but probably at the expense of selectivity, owing to the selectivity-permeability trade-off. Good candidates would be 6FDA-DAM or 6FDA-based copolymers with DAM and DABA moieties. PIM materials could also be considered but have a bad reputation as MMM polymer, owing to the high probability of interfacial defects around the particles as a result of the polymer's rigidity. Functionalisation of these PIMs with carboxylic acid groups is relatively simple and could offer a solution for possible problems with interfacial compatibility[273]. Moreover, MOF-808 optimization towards enhanced CO_2 diffusivity or solubility is a relevant option. Based on the conclusions of this dissertation, ligands with heterocyclic nitrogen (for example isonicotinic acid) and fluorine atoms are the most attractive candidates to achieve improved solubility selectivity. Albeit cumbersome and less straightforward, enhanced diffusivity selectivity for CO_2 over N_2 or CH_4 could be realized by narrowing down the pore size with bulky ligands to create a size sieving effect between the gases[274]. Furthermore, MOF-808 MMM properties need to be investigated in thin-film capacity instead of thick films. Notwithstanding the importance of thin-film research, only a limited number of reports on thin-film MMMs has been published over the years, mostly in the context of interfacially polymerized polyamide membranes[275]. With regard

to the description of structure-property relationships for MMMs, defining MMM performance indicators based on simple MOF parameters can be considered a step in the right direction, although a lot of room for improvement exists. Other interesting research topics that need to be elucidated for MOF-808 MMMs specifically are MOF-polymer compatibility, polymer rigidity at the interphase and its effect on performance and cluster interaction with CO_2 and its contribution to separation factor and permeability.

8.2.1.2 6FDA-DABA membranes

The investigated 6FDA-DABA membranes offer an exciting perspective for CO_2/CH_4 separations such as bio gas. Since decarboxylation cross-linking is only investigated at high temperature and after an annealing procedure of several hours, the exact time and temperature range necessary to induce decarboxylation should be specified to become an optimal synthesis method. Possibly, the decarboxylation reaction, which occurred in a temperature range of 330-350 °C, is linked to the polymer T_g (~350 °C). If the polymer chain mobility actually plays a central role in the enabling of the cross-linking reaction, another way to reduce the high annealing temperatures would be to consider polymers with lower T_g, which also bear a carboxylic acid group (e.g. polyetherimides with a T_g of ~200 °C). Exploiting the similarities in chemistry between sulfonated and carboxylated polymers might also be an interesting research option[276]. Once synthesis conditions are optimized, attention should shift from the preparation of thick, isotropic polymer films to the preparation of thin-film selective layers, either in the form of an asymmetric membrane prepared via phase inversion or by making thin-film composite membranes. Both pathways have their respective challenges. Phase inversion is simple but might prove to be too costly here as 6FDA-DABA is a relatively expensive polymer. Polymer blending might resolve this if a compatible polymer can be found that does not deteriorate performance. In thin-film composite membranes, where the selective layer is made from a different material than the support and gutter layer, only small amounts of 6FDA-DABA would be required. However, the support should be able to endure treatments at 350 °C without suffering from pore collapse and/or delamination from the selective layer. In both approaches, the high CO_2/CH_4 selectivity obtained in Chapter 6 is encouraging and gives some manoeuvring room as a loss of a certain percentage of selectivity to improve permeability is not problematic as such. The 6FDA-DABA-350 membrane prepared in this work has an intrinsic permeability of ~25 Barrer, corresponding with ~100 GPU for a 250 nm thin industrial membrane, which is just sufficient to meet the performance targets. Nonetheless, further improving the CO_2 permeability by a combination of 6FDA-DABA with MOF-808 would be an interesting research route. A good compatibility between MOF and filler is anticipated as the exposed zirconium clusters at the MOF surface have a high affinity for free carboxylic acids on the polymer backbone.

8.2.1.3 HTGS-2

During proof testing, HTGS-2 measured stable and reliable separation factors but too high and strongly fluctuating permeability values for various membranes. Obviously, the permeability problem should be resolved before reliable performance measurements can be conducted. On the short term, redesigning the analysis loop downstream of the membranes should do the

trick. A combination of replacing the 150 cm^3 measuring cylinder by three cylinders with smaller volume (e.g. 25 cm^3, 50 cm^3 and 75 cm^3) and minimizing the tubing volume should increase the measuring sensitivity of the set-up. A measuring cylinder consisting of three small volumes would allow to gradually increase or decrease the downstream volume, depending on the membrane type that is being measured. On the long term, MFCs with higher flow range could be considered to prevent concentration polarization when measuring highly selective composite membranes with high permeances.

8.2.2 Outlook

The publication of the first MOF-based MMM in 2004 marked the beginning of more than 15 years of intensive research on finding better MMMs with higher gas pair selectivity and higher gas permeability than their purely polymeric counterparts[277]. Despite all effort and time invested in MMMs, the discrepancy between the immense offer of novel polymer-MOF combinations described in academic literature and the lack of commercialization of MMMs is striking. Yet, open literature seemingly pays no or little attention to the reasons behind this phenomenon. Finding the right balance between MOF and polymer permeability during MMM material selection is of high importance and might explain part of the commercialization problem[278]. As described in Chapter 1, 90% of the MMMs reported in literature only display enhanced permeability while the remaining 10% is capable of improving both selectivity and permeability[67]. The bulk of the membranes belonging to the latter category (including those reported in this dissertation) consists of low-permeable polymer matrices[67,72,107,135,230,279]. Consequently, good relative improvements compared to the low-permeable mother membrane are observed and published, but the absolute permeability often remains too low to meet the performance requirements of industrial-grade membranes. In contrast, using polymers with high intrinsic permeability for MMM design guarantees relevant gas fluxes but is almost never accompanied by improved selectivities after MOF addition[280,281]. The choice of polymer thus seems to limit the applicability of the MMMs. Furthermore, MOF incorporation increases the membrane thickness by a factor of 1.5-3 (depending on MOF loading), meaning that a permeance improvement is only obtained when the permeability is enhanced by a factor higher than the relative thickness increase[95,154]. Additional research on MMMs in thin-film capacity is imperative for further development of the field. Thin-film nanocomposite (TFN) membranes have been sporadically reported for gas separation but not nearly in the same numbers as free-standing MMM publications[282]. A review on the challenges and opportunities for these TFN membranes can be found elsewhere[275].

With respect to the search for structure-performance relationships in MMMs, a critical question remains how to acquire the fundamental parameters linked to gas permeation in the MMMs. Chapter 5 demonstrated that general assumptions in literature (e.g. higher MOF CO_2 uptake equals higher MMM performance) are not always correct. Research questions should focus more on determination of the conceptual parameters, such as the optimal CO_2 adsorption enthalpy during permeation (probably depending on the MOF-polymer system) or the CO_2 concentration gradient in the membrane. Next to material selection and membrane design, the

upscaling of MMMs is notoriously challenging as well. The uniform dispersion of fillers in a thin yet still selective polymer layer with continuous coating techniques has proven to be a major roadblock so far[54]. MMMs have better processability than purely inorganic membranes but they are far more difficult to process than unfilled polymeric membranes[23]. The creation of large-surface-area MMMs with reproducible performance is a serious future engineering challenge, owing to the large number of process variables influencing the final membrane structure[54]. Finally, if MMMs are to be seriously considered for upscaling, reproducibility and repeatability studies, which are currently extremely scarce in MMM literature, will be required.

Membrane research in academics has had a strong focus on the characterization of dense, free-standing polymer films. Using these films as a rapid and easy way to screen new membrane materials for gas separation is definitely useful. Since they are free-standing, no support layer is required and a relatively straightforward synthesis procedure allows fast production of novel membranes. However, it is important to keep in mind that this is only the first stage of membrane development[8]. In the end, industrial-grade membranes should have selective layers with submicron thickness. The production of thin but selective, large-surface-area membrane modules therefore remains one of the biggest challenges (for both polymeric membranes and MMMs). For gas separations, defect densities must be less than 1 cm^2 of defects per 10^5 cm^2 of membrane area, which is a though target and often the main reason why the transition to thin films is not realised[54]. Nonetheless, thin active layers remain imperative for obtaining sufficient gas permeance. After all, higher permeance (through thin active layers or through high material permeability) is translated into lower required membrane area and thus lower capital cost. On the other hand, more selective membranes increase the product purity and reduce the operational cost and required energy input[52]. Ideally, membranes with both high permeability and high selectivity are thus desired. In real applications however, membrane process economics can limit the driving force that is applied for the separation. In such cases, more selective membranes result in no or only a small gain in product purity[54]. Especially for promising future applications limited by a low pressure ratio such as syn gas (H_2/CO_2) or flue gas (CO_2/N_2) treatment, obtaining membranes with high permeance/permeability is more relevant than synthesizing highly selective membranes[248]. For example, CO_2 capture can become an interesting market considering the recent, "positive" development in the cost of CO_2 emission. Albeit fundamentally a similar application as CO_2 removal from natural gas/bio gas, substantial practical differences between CO_2/CH_4 and CO_2/N_2 separation lead to different membrane requirements. Whereas upgraded natural or bio gas has an important economic value, the retentate stream in CO_2 capture applications would consist of CO_2 depleted flue gas (N_2), which can be emitted in the atmosphere. Moreover, the operating conditions that define the needed membrane performance differ significantly. Flue gas generally consists of large volumes of gas applied at 1-2 bar at elevated temperatures, while the feed pressure during natural gas treatment can be up to 80-100 bar[54]. Combination of the low feed pressure and the large volumes of flue gas that need to be treated renders high permeance membranes (1000-5000 GPU) to be preferred for this application[8,283]. One highly promising way to achieve such high permeances is interfacial polymerization, in which thin (<200 nm) but selective polymer layers are formed. The current generation of interfacially polymerized membranes academically

developed for gas separation is mainly based on the polyamide and polyamine membranes, similar to RO membranes. Field-trials on real flue gas with these membranes reported CO_2 permeances of ~1500 GPU combined with CO_2/N_2 separation factor of ~180[284]. However, the nitrogen chemistry, which is at the heart of these membranes, makes that these membranes are sensitive to carrier saturation and depend heavily on water in the feed stream to fuel the facilitated transport mechanism, responsible for the excellent performances[66]. An interesting alternative consists of interfacially polymerized poly(ether)epoxide membranes[285], in which EO segments are incorporated as CO_2-selective moieties, similar to the Polaris chemistry, while maintaining thin layers. Whereas soft materials (e.g. Pebax, Polyactive) or facilitated transport materials (e.g. polyamide/polyamine) render excellent CO_2/N_2 selectivities and use thin active layers to achieve sufficient gas permeance, semi-rigid nanoporous polymers (e.g. PIMs) are, despite their relatively low CO_2/N_2 selectivity, also promising for these applications, owing to their very high intrinsic permeability as a result of their intrinsic microporosity[7,61]. A series of benzotriptycene-based PIMs have recently been reported to provide exceptional gas separation performance for CO_2/CH_4 and CO_2/N_2 mixtures, far above the current state-of-the-art[286]. Isoporous membranes made from block copolymers offer an exciting perspective as well since they have very sharp free volume element size distributions, which makes them suitable candidates for achieving combined high selectivity and permeance. However, the current generation of these membranes is not yet able to create pores with sizes in the range of the kinetic diameters of gas molecules[287,288].

Although membrane-based natural gas sweetening (CO_2/CH_4 separation) is already an established market with a broad choice in commercial membranes, better membranes would allow to capture a larger market segment at the expense of the conventional technologies[8]. In addition, new methane sources like bio methane (from bio gas) are future application targets, in which membranes can be applied with relative ease[146]. Following from the relatively large difference in molecular size between CO_2 and CH_4, upcoming rigid materials with clear molecular sieving capacity are particularly interesting to acquire improved CO_2/CH_4 selectivity. TRs and modified PIMs have already proven that they can combine sufficiently high selectivities and permeabilities to reach industrial performance targets[7,61,245]. Ultra-rigid materials such as MOF or carbon molecular sieve (CMS) membranes deserve mention too. Presence of two types of pores (termed micropores and ultramicropores) gives these materials among the highest selectivity-permeability combinations reported. Crystalline MOF membranes induce high entropic selectivity due to their well-defined and ordered pore structure. Similarly, amorphous CMS membranes, typically synthesized by pyrolysis of a polymeric precursor, also create spatially confined environments, following from their slit-like ultramicropores[278]. Owing to their rigid pore structure and narrow pore size distribution, CMS membranes are the separation performance champions among membranes. CMS hollow fibre membranes based on a polyimide denoted a stunning CO_2/CH_4 selectivity of more than 3600 accompanied by a fair CO_2 permeability of 30 Barrer[289], while a 6FDA-based CMS recently reached a CO_2 permeability of more than 14000 Barrer at a CO_2/CH_4 selectivity of 54[290]. However, to date, scalability remains the most important issue for these ultra-rigid materials[278] although significant progress has been made[291].

The massive number of new membrane materials researched over the past years has provided the membrane community with important insights with regard to MMM design and mass transport. MOFs, ZIFs, COFs, POFs, graphene, carbon nanotubes and many other new materials have taken the MMM field by storm, framed in the rat race towards a gain in separation performance. However, the question rises whether there is still added value in pouring time, effort and resources into these kinds of new materials without sufficient techno-economic evidence for their potential usefulness. Performance improvements definitely remain relevant to unlock new applications, such as N_2/CH_4 separation or CO_2 capture, but there is more to membrane development than performance alone. Current breakthrough materials are able to reach and even surpass the performance targets set by industry. As a result, the actual research priority should lay with the identification of materials that retain their performance over time and show resilience when exposed to industrial conditions. Moreover, engineering the scalability and processability of these materials to form thin, yet selective membranes should be an important point of focus. Despite the discovery of countless new 'high-performant' CO_2-selective membrane materials over the past years, the polymers that currently form the backbone of the commercially available membranes are largely the same as 3 decades ago[8], indicating the need for an additional, functional paradigm to assess membrane performance.

In conclusion, I would like to pass on three basic rules of thumb for future membranologists when designing membranes for CO_2 separation: (1) properly sized free volume elements with a narrow distribution are key for simultaneously obtaining high diffusivity selectivity and gas permeability, (2) aim for strong affinity between CO_2 and the membrane but keep an eye on the CO_2 adsorption enthalpy and (3) thin selective layers are the end product[54]. May the driving force be with you and your membranes.

Bibliography

(1) Cox, P. M.; Betts, R. A.; Jones, C. D.; Spall, S. A.; Totterdell, I. J. Acceleration of Global Warming Due to Carbon-Cycle Feedbacks in a Coupled Climate Model. *Nature* **2000**, *408* (November), 184–187.

(2) Nakao, S.; Yogo, K.; Goto, K.; Kai, T.; Yamada, H. *Advanced CO2 Capture Technologies*; SpringerBriefs in Energy; Springer International Publishing, 2019. https://doi.org/10.1007/978-3-030-18858-0.

(3) Proost, S.; Baelmans, T.; Bruninx, K.; Delarue, E.; Driesen, J.; Meyers, J.; Muylaert, K.; Sintubin, M.; Vandevelde, A.; Van Acker, K.; et al. *"Een Duurzame Energie-Voorziening Voor België". Meta-Forum Visietekst 18*; Leuven, 2020.

(4) Merkel, T.; Kniep, J.; Hofmann, T. *Scale-Up and Testing of Advanced Polaris Membrane CO2 Capture Technology*; Pittsburgh, 2018.

(5) Xiao, Y.; Low, B. T.; Hosseini, S. S.; Chung, T. S.; Paul, D. R. The Strategies of Molecular Architecture and Modification of Polyimide-Based Membranes for CO2 Removal from Natural Gas-A Review. *Progress in Polymer Science (Oxford)*. June 2009, pp 561–580. https://doi.org/10.1016/j.progpolymsci.2008.12.004.

(6) Bernardo, P.; Drioli, E.; Golemme, G. Membrane Gas Separation: A Review/State of the Art. *Ind. Eng. Chem. Res.* **2009**, *48* (10), 4638–4663. https://doi.org/10.1021/ie8019032.

(7) Sanders, D. F.; Smith, Z. P.; Guo, R.; Robeson, L. M.; McGrath, J. E.; Paul, D. R.; Freeman, B. D. Energy-Efficient Polymeric Gas Separation Membranes for a Sustainable Future: A Review. *Polymer (Guildf).* **2013**, *54* (18), 4729–4761. https://doi.org/10.1016/j.polymer.2013.05.075.

(8) Galizia, M.; Chi, W. S.; Smith, Z. P.; Merkel, T. C.; Baker, R. W.; Freeman, B. D. Polymers and Mixed Matrix Membranes for Gas and Vapor Separation : A Review and Prospective Opportunities. *Macromolecules* **2017**, *50*, 7809–7843. https://doi.org/10.1021/acs.macromol.7b01718.

(9) Baker, R. W.; Lokhandwala, K. Natural Gas Processing with Membranes: An Overview. *Ind. Eng. Chem. Res.* **2008**, *47* (February), 2109–2121. https://doi.org/10.1021/ie071083w.

(10) Mulder, M. *Basic Principles of Membrane Technology*; 1996.

(11) Baker, R. W. *Membrane Technology and Applications*; John Wiley and Sons: London, 2004.

(12) Stannett, V. The Transport of Gases in Synthetic Polymeric Membranes - An Historic Perspective. *J. Memb. Sci.* **1978**, *3*, 97–115.

(13) Baker, R. W. Future Directions of Membrane Gas Separation Technology. *Ind. Eng. Chem. Res.* **2002**, *41* (6), 1393–1411.

(14) Graham, T. On the Absorption and Idalytic Separaiton of Gases by Colloid Septa. *Philos. Mag. J. Sci.* **1866**, *32* (4), 218.

(15) von Wroblewski, S. Ueber Die Abhängigkeit Der Constante Der Verbreitung Der Gase in Einer Flüssigkeit von Der Zähigkeit Der Letztern. *Wiedemann Ann. der Phys. und Chemie* **1879**, *243* (5), 11–23.

(16) Barrer, R. M.; Rideal, E. Activated Diffusion in Membranes. *Trans. Faraday Soc.* **1939**, *35*, 628.

(17) Maeres, P. The Diffusion of Gases through Polyvinyl Acetate. *J. Am. Chem. Soc.* **1954**, *76* (13), 3415–3422.

(18) Loeb, S. The Loeb-Sourirajan Membrane: How It Came About. *ACS Symp. Ser.* **1981**, *153*, 1–9.

(19) Fritzmann, C.; Löwenberg, J.; Wintgens, T.; Melin, T. State-of-the-Art of Reverse Osmosis Desalination. *Desalination* **2007**. https://doi.org/10.1016/j.desal.2006.12.009.

(20) Bollinger, W. A.; Maclean, D. L.; Narayan, R. S. Separation Systems for Oil Refining. *Chem. Eng. Prog.* **1982**, *78:10*.

(21) Matteucci, S.; Yampolskii, Y.; Freeman, B. D.; Pinnau, I. Transport of Gases and Vapors in Glassy and Rubbery Polymers. In *Materials Science of Membranes for Gas and Vapor Separation*; 2006; pp 1–48.

(22) Baker, R. W.; Low, B. T. Gas Separation Membrane Materials: A Perspective. *Macromolecules* **2014**, *47* (20), 6999–7013. https://doi.org/10.1021/ma501488s.

(23) Ismail, A. F.; Khulbe, K. C.; Matsuura, T. *Gas Separation Membranes*, 1st ed.; Springer International Publishing, 2015.

(24) Wijmans, J. G. H.; Baker, R. W. *The Solution-Diffusion Model: A Unified Approach to Membrane Permeation*; 2006. https://doi.org/10.1002/047002903X.ch5.

(25) Paul, D. R.; Paciotti, D. J. Driving Force for Hydraulic and Pervaporation Transport in Homogeneous Membranes. *J. Polym. Sci. Polym. Phys. Ed.* **1975**, *13*, 1201. https://doi.org/https://doi.org/10.1002/pol.1975.180130612.

(26) Paul, D. R.; Paciotti, D. J.; Ebra-Lima, O. M. Hydraulic Permeation of Liquids through Swollen Polymeric Networks. *J. Appl. Polym. Sci.* **1975**, *19*, 1837. https://doi.org/https://doi.org/10.1002/app.1975.070191011.

(27) Rosenbaum, S.; Cotton, O. Steady-State Distribution of Water in Cellulose Acetate Membrane. *J. Polym. Sci.* **1969**, *7*, 101. https://doi.org/https://doi.org/10.1002/pol.1969.150070110.

(28) Kim, S. N.; Kammermeyer, K. Actual Concentration Profiles in Membrane Permeation. *Sep. Sci.* **1970**, *5*, 679. https://doi.org/https://doi.org/10.1080/00372367008055530.

(29) Tanaka, K.; Kita, H.; Okano, M.; Okamoto, K. Permeability and Permselectivity of Gases in Fluorinated and Non-Fluorinated Polyimides. *Polymer (Guildf).* **1992**, *33* (3), 585–

592.

(30) Smit, E.; Mulder, M. H. V.; Smolders, C. A.; Karrenbeld, H.; van Eerden, J.; Feil, D. Modelling of the Diffusion of Carbon Dioxide in Polyimide Matrices by Computer Simulation. *J. Memb. Sci.* **1992**, *73* (2–3), 247–257.

(31) Kesting, R. *Synthetic Polymer Membranes - a Structural Perspective*, 2nd ed.; Finch, C. A., Ed.; John Wiley & Sons: Chichester & New York, 1986; Vol. 18. https://doi.org/https://doi.org/10.1002/pi.4980180318.

(32) Donohue, M. D.; Minhas, B. S.; Lee, S. Y. Permeation Behavior of Carbon Dioxide-Methane Mixtures in Cellulose Acetate Membranes. *J. Memb. Sci.* **1989**, *42* (3), 197–214.

(33) Pandey, P.; Chauchan, R. S. Membranes for Gas Separation. *Prog. Polym. Sci.* **2001**, *26* (6), 853–893. https://doi.org/https://doi.org/10.1016/S0079-6700(01)00009-0.

(34) Vanherck, K.; Koeckelberghs, G.; Vankelecom, I. F. J. Crosslinking Polyimides for Membrane Applications: A Review. *Prog. Polym. Sci.* **2013**, *38* (6), 874–896. https://doi.org/10.1016/j.progpolymsci.2012.11.001.

(35) Marti, A. M.; Venna, S. R.; Roth, E. A.; Culp, J. T.; Hopkinson, D. P. Simple Fabrication Method for Mixed Matrix Membranes with in Situ MOF Growth for Gas Separation. *ACS Appl. Mater. Interfaces* **2018**, *10*, 24787–24790. https://doi.org/10.1021/acsami.8b06592.

(36) Scholes, C. A.; Chen, G. Q.; Tao, W. X.; Bacus, J.; Anderson, C.; Stevens, G. W.; Kentish, S. E. The Effects of Minor Components on the Gas Separation Performance of Membranes for Carbon Capture. *Energy Procedia* **2011**, *4*, 681–687. https://doi.org/10.1016/j.egypro.2011.01.105.

(37) Shahid, S.; Nijmeijer, K. High Pressure Gas Separation Performance of Mixed-Matrix Polymer Membranes Containing Mesoporous Fe(BTC). *J. Memb. Sci.* **2014**, *459*, 33–44. https://doi.org/10.1016/j.memsci.2014.02.009.

(38) Zhang, Y.; Musselman, I. H.; Ferraris, J. P.; Balkus Jr, K. J. Gas Permeability Properties of Matrimid Membranes Containing the Metal-Organic Framework Cu–BPY–HFS. *J. Memb. Sci.* **2008**, *313*, 170–181. https://doi.org/10.1016/j.memsci.2008.01.005.

(39) Qiu, W.; Chen, C.-C.; Xu, L.; Cui, L.; Paul, D. R.; Koros, W. J. Sub-Tg Cross-Linking of a Polyimide Membrane for Enhanced CO2 Plasticization Resistance for Natural Gas Separation. *Macromolecules* **2011**, *44*, 6046–6056. https://doi.org/10.1021/ma201033j.

(40) Tian, Z.; Cao, B.; Li, P. Effects of Sub-Tg Cross-Linking of Triptycene-Based Polyimides on Gas Permeation, Plasticization Resistance and Physical Aging Properties. *J. Memb. Sci.* **2018**, *560* (March), 87–96. https://doi.org/10.1016/j.memsci.2018.05.018.

(41) Shahid, S.; Nijmeijer, K. Performance and Plasticization Behavior of Polymer – MOF Membranes for Gas Separation at Elevated Pressures. *J. Memb. Sci.* **2014**, *470*, 166–177. https://doi.org/10.1016/j.memsci.2014.07.034.

(42) Staudt-Bickel, C.; Koros, W. J. Improvement of CO2/CH4 Separation Characteristics of Polyimides by Chemical Crosslinking. *J. Memb. Sci.* **1999**, *155*, 145–154.

(43) Tien-Binh, N.; Vinh-Thang, H.; Chen, X. Y.; Rodrigue, D.; Kaliaguine, S. Crosslinked MOF-Polymer to Enhance Gas Separation of Mixed Matrix Membranes. *J. Memb. Sci.* **2016**, *520*, 941–950. https://doi.org/10.1016/j.memsci.2016.08.045.

(44) Guo, R. Aromatic Polyethers, Polyetherketones, Polysulfides, and Polysulfones. *McGrath, J.E.* **2012**, *5*, 377–430. https://doi.org/https://doi.org/10.1016/B978-0-444-53349-4.00153-9.

(45) McHattie, J. S.; Koros, W. J.; Paul, D. R. Gas Transport Properties of Polysulphones: 3. Comparison of Tetramethyl-Substituted Bisphenols. *Polymer (Guildf).* **1992**, *33* (8), 1701–1711.

(46) Aitken, C. L.; Koros, W. J.; Paul, D. R. Gas Transport Properties of Biphenol Polysulfones. *Macromolecules* **1992**, *25* (14), 3651–3658.

(47) Didden, J.; Thür, R.; Volodin, A.; Vankelecom, I. F. J. Blending PPO-Based Molecules with Pebax MH 1657 in Membranes for Gas Separation. *J. Appl. Polym. Sci.* **2018**, *135*, 46433. https://doi.org/10.1002/app.46433.

(48) Harrigan, D. J.; Lawrence III, J. A.; Reid, Harrison, W.; Rivers, J. B.; O'Brien, Jeremy, T.; Sharber, Seth, A.; Sundell, B. J. Tunable Sour Gas Separations: Simultaneous H2S and CO2 Removal from Natural Gas via Crosslinked Telechelic Poly(Ethylene Glycol) Membranes. *J. Memb. Sci.* **2020**, *602*, 117947.

(49) Kim, N. U.; Park, B. J.; Guiver, M. D.; Kim, J. H. Use of Non-Selective, High-Molecular-Weight Poly(Ethylene Oxide) Membrane for CO2 Separation by Incorporation of Comb Copolymer. *J. Memb. Sci.* **2020**, *605*, 118092.

(50) Lin, H.; He, Z.; Sun, Z.; Vu, J.; Ng, A.; Mohammed, M.; Kniep, J.; Merkel, T. C.; Wu, T.; Lambrecht, R. C. CO2-Selective Membranes for Hydrogen Production and CO2 Capture – Part I: Membrane Development. *J. Memb. Sci.* **2014**, *457*, 149–161. https://doi.org/10.1016/j.memsci.2014.01.020.

(51) Merkel, T.; Freeman, B. *Membranes: An Emerging CO2 Capture Technology*; 2017.

(52) Freeman, B. D. Basis of Permeability/Selectivity Tradeoff Relations in Polymeric Gas Separation Membranes. *Macromolecules* **1999**, *32*, 375–380. https://doi.org/10.1021/ma9814548.

(53) Robeson, L. M. Correlation of Separation Factor versus Permeability for Polymeric Membranes. *J. Memb. Sci.* **1991**, *62*, 165–185.

(54) Park, H. B.; Kamcev, J.; Robeson, L. M.; Elimelech, M.; Freeman, B. D. Maximizing the Right Stuff: The Trade-off between Membrane Permeability and Selectivity. *Science (80-.).* **2017**, *356*, 1137. https://doi.org/10.1126/science.aab0530.

(55) Robeson, L. M. The Upper Bound Revisited. *J. Memb. Sci.* **2008**, *320* (1–2), 390–400. https://doi.org/10.1016/j.memsci.2008.04.030.

(56) Balçık, M.; Tantekin-Ersolmaz, S. B.; Ahunbay, M. G. Interfacial Analysis of Mixed-Matrix Membranes under Exposure to High-Pressure CO2. *J. Memb. Sci.* **2020**, *607* (January), 118147. https://doi.org/10.1016/j.memsci.2020.118147.

(57) Xia, J.; Chung, T. S.; Li, P.; Horn, N. R.; Paul, D. R. Aging and Carbon Dioxide Plasticization of Thin Polyetherimide Films. *Polymer (Guildf).* **2012**, *53*, 2099–2108.

(58) Rowe, B. W.; Freeman, B. D.; Paul, D. R. Physical Aging of Ultrathin Glassy Polymer Films Tracked by Gas Permeability. *Polymer (Guildf).* **2009**, *50* (23), 5565–5575. https://doi.org/10.1016/j.polymer.2009.09.037.

(59) Low, Z.-X.; Budd, P. M.; Mckeown, N. B.; Patterson, D. A. Gas Permeation Properties, Physical Aging and Its Mitigation in High Free Volume Glassy Polymers. *Chem. Rev.* **2018**, *118* (12), 5871–5911.

(60) Makhloufi, C.; Roizard, D.; Favre, E. Reverse Selective NH3/CO2 Permeation in Fluorinated Polymers Using Membrane Gas Separation. *J. Memb. Sci.* **2013**, *441*, 63–72. https://doi.org/10.1016/j.memsci.2013.03.048.

(61) Wang, Y.; Ma, X.; Ghanem, B. S.; Alghunaimi, F.; Pinnau, I.; Han, Y. Polymers of Intrinsic Microporosity for Energy-Intensive Membrane-Based Gas Separations. *Mater. Today Nano* **2019**, *3* (2018), 69–95. https://doi.org/10.1016/j.mtnano.2018.11.003.

(62) Moon, J. D.; Bridge, A. T.; D'Ambra, C.; Freeman, B. D.; Paul, D. R. Gas Separation Properties of Polybenzimidazole/Thermally-Rearranged Polymer Blends. *J. Memb. Sci.* **2019**, *582* (March), 182–193. https://doi.org/10.1016/j.memsci.2019.03.067.

(63) Wang, M.; Wang, Z.; Li, S.; Zhang, C.; Wang, J.; Wang, S. A High Performance Antioxidative and Acid Resistant Membrane Prepared by Interfacial Polymerization for CO2 Separation from Flue Gas. *Energy Environ. Sci.* **2013**, *6* (2), 539–551. https://doi.org/10.1039/C2EE23080A.

(64) He, W.; Wang, Z.; Li, W.; Li, S.; Bai, Z.; Wang, J.; Wang, S. Cyclic Tertiary Amino Group Containing Fixed Carrier Membranes for CO2 Separation. *J. Memb. Sci.* **2015**, *476*, 171–181. https://doi.org/10.1016/j.memsci.2014.11.039.

(65) Chen, K. K.; Salim, W.; Han, Y.; Wu, D.; Ho, W. S. W. Fabrication and Scale-up of Multi-Leaf Spiral-Wound Membrane Modules for CO2 Capture from Flue Gas. *J. Memb. Sci.* **2020**, *595*, 117504. https://doi.org/10.1016/j.memsci.2019.117504.

(66) Li, Y.; Wang, S.; He, G.; Wu, H.; Pan, F.; Jiang, Z. Facilitated Transport of Small Molecules and Ions for Energy-Efficient Membranes. *Chem. Soc. Rev.* **2015**, *44*, 103–118. https://doi.org/10.1039/c4cs00215f.

(67) Seoane, B.; Coronas, J.; Gascon, I.; Benavides, M. E.; Karvan, O.; Caro, J.; Kapteijn, F.; Gascon, J. Metal–Organic Framework Based Mixed Matrix Membranes: A Solution for Highly Efficient CO2 Capture? *Chem. Soc. Rev.* **2015**, *44*, 2421–2454. https://doi.org/10.1039/C4CS00437J.

(68) Bastani, D.; Esmaeili, N.; Asadollahi, M. Polymeric Mixed Matrix Membranes Containing Zeolites as a Filler for Gas Separation Applications: A Review. *J. Ind. Eng. Chem.* **2013**, *19* (2), 375–393. https://doi.org/10.1016/j.jiec.2012.09.019.

(69) Nejad, M. N.; Asghari, M.; Afsari, M. Investigation of Carbon Nanotubes in Mixed Matrix Membranes for Gas Separation: A Review. *ChemBioEng Rev.* **2016**, No. 6, 276–298. https://doi.org/10.1002/cben.201600012.

(70) Yuan, S.; Li, X.; Zhu, J.; Zhang, G.; Van Puyvelde, P.; Van der Bruggen, B. Covalent Organic Frameworks for Membrane Separation. *Chem. Soc. Rev.* **2019**, *48*, 2665–2681. https://doi.org/10.1039/c8cs00919h.

(71) Dong, G.; Li, H.; Chen, V. Challenges and Opportunities for Mixed-Matrix Membranes for Gas Separation. *J. Mater. Chem. A* **2013**, *1* (15), 4610–4630. https://doi.org/10.1039/C3TA00927K.

(72) Lewis, J.; Al-sayaghi, M. A. Q.; Buelke, C.; Alshami, A. Activated Carbon in Mixed-Matrix Membranes. *Sep. Purif. Rev.* **2019**. https://doi.org/DOI: 10.1080/15422119.2019.1609986.

(73) Shi, F.; Sun, J.; Wang, J.; Liu, M.; Wang, S.; Cao, X.; Yan, Z.; Li, Y.; Nunes, S. P. Exploration of the Synergy Between 2D Nanosheets and a Non-2D Filler in Mixed Matrix Membranes for Gas Separation. *Front. Chem.* **2020**, *8* (February), 1–12. https://doi.org/10.3389/fchem.2020.00058.

(74) Rodenas, T.; Luz, I.; Prieto, G.; Seoane, B.; Miro, H.; Corma, A.; Kapteijn, F.; Llabrés i Xamena, F. X.; Gascon, J. Metal–Organic Framework Nanosheets in Polymer Composite Materials for Gas Separation. *Nat. Mater.* **2015**, *14* (November 2014), 48–55. https://doi.org/10.1038/NMAT4113.

(75) Lin, R.; Hernandez, B. V.; Ge, L.; Zhu, Z. Metal Organic Framework Based Mixed Matrix Membranes: An Overview on Filler/Polymer Interfaces. *J. Mater. Chem.* **2018**, *6* (October 2014), 293–312. https://doi.org/10.1039/C7TA07294E.

(76) Wong, K. C.; Goh, P. S.; Ismail, A. F. Thin Film Nanocomposite: The next Generation Selective Membrane for CO2 Removal. *J. Mater. Chem. A* **2016**, *4* (41), 15726–15748. https://doi.org/10.1039/C6TA05145F.

(77) Lin, R.; Hernandez, B. V.; Ge, L.; Zhu, Z. Metal Organic Framework Based Mixed Matrix Membranes: An Overview on Filler/Polymer Interfaces. *J. Mater. Chem. A* **2018**, *6*, 293–312. https://doi.org/10.1039/C7TA07294E.

(78) Tien-Binh, N.; Vinh-Thang, H.; Chen, X. Y.; Rodrigue, D.; Kaliaguine, S. Polymer Functionalization to Enhance Interface Quality of Mixed Matrix Membranes for High CO2/CH4 Gas Separation. *J. Mater. Chem.* **2015**, *3*, 15202–15213. https://doi.org/10.1039/c5ta01597a.

(79) Qian, Q.; Wu, A. X.; Chi, W. S.; Asinger, P. A.; Lin, S.; Hypsher, A.; Smith, Z. P. Mixed-Matrix Membranes Formed from Imide-Functionalized UiO-66-NH2 for Improved Interfacial Compatibility. *ACS Appl. Mater. Interfaces* **2019**, *11*, 31257–31269. https://doi.org/10.1021/acsami.9b07500.

(80) Venna, S. R.; Lartey, M.; Li, T.; Spore, A.; Kumar, S.; Nulwala, H. B.; Luebke, D. R.; Rosi, L.; Albenze, E. Fabrication of MMMs with Improved Gas Separation Properties Using Externally-Functionalized MOF Particles. *J. Mater. Chem. A* **2015**, *3*, 5014–5022. https://doi.org/10.1039/C4TA05225K.

(81) Anjum, M. W.; Vermoortele, F.; Khan, A. L.; Bueken, B.; Vos, D. E. De; Vankelecom, I. F. J. Modulated UiO-66-Based Mixed-Matrix Membranes for CO2 Separation. *ACS Appl. Mater. Interfaces* **2015**, *7*, 25193–25201. https://doi.org/10.1021/acsami.5b08964.

(82) Jiang, L. Y.; Chung, T. S. Fabrication of Mixed Matrix Hollow Fibers with Intimate Polymer–Zeolite Interface for Gas Separation. *AIChE J.* **2006**, *52* (8), 2898–2908. https://doi.org/10.1002/aic.

(83) Duan, P.; Moreton, J. C.; Tavares, S. R.; Semino, R.; Maurin, G.; Cohen, S. M.; Schmidt-Rohr, K. Polymer Infiltration into Metal-Organic Frameworks in Mixed- Matrix Membranes Detected in Situ by NMR. *J. Am. Chem. Soc.* **2019**, *141*, 7589–7595. https://doi.org/10.1021/jacs.9b02789.

(84) Ozcan, A.; Semino, R.; Maurin, G.; Yazaydin, A. O. Modeling of Gas Transport through Polymer/MOF Interfaces: A Microsecond-Scale Concentration Gradient-Driven Molecular Dynamics Study. *Chem. Mater.* **2020**, *32*, 1288–1296. https://doi.org/10.1021/acs.chemmater.9b04907.

(85) Hwang, S.; Semino, R.; Seoane, B.; Zahan, M.; Chmelik, C.; Valiullin, R.; Bertmer, M.; Haase, J.; Kapteijn, F.; Gascon, J.; et al. Revealing the Transient Concentration of CO2 in a Mixed-Matrix Membrane by IR Microimaging and Molecular Modeling. *Angew. Chemie - Commun.* **2018**, *6900*, 5156–5160. https://doi.org/10.1002/anie.201713160.

(86) Tavares, S. R.; Ramsahye, N. A.; Adil, K.; Eddaoudi, M.; Maurin, G.; Semino, R. Computationally Assisted Assessment of the Metal-Organic Framework/Polymer Compatibility in Composites Integrating a Rigid Polymer. *Adv. Theory Simulations* **2019**, *2* (1900116), 1–9. https://doi.org/10.1002/adts.201900116.

(87) Mahdi, E. M.; Tan, J.-C. Mixed-Matrix Membranes of Zeolitic Imidazolate Framework (ZIF-8)/Matrimid Nanocomposite: Thermo-Mechanical Stability and Viscoelasticity Underpinning Membrane Separation Performance. *J. Memb. Sci.* **2016**, *498*, 276–290. https://doi.org/10.1016/j.memsci.2015.09.066.

(88) Flyagina, I. S.; Mahdi, E. M.; Titov, K.; Tan, J.-C. Thermo-Mechanical Properties of Mixed- Matrix Membranes Encompassing Zeolitic Imidazolate Framework-90 and Polyvinylidine Difluoride: ZIF-90/PVDF Nanocomposites. *APL Mater.* **2017**, *5*, 086104. https://doi.org/10.1063/1.4986565.

(89) Rodenas, T.; Dalen, M. van; Serra-Crespo, P.; Kapteijn, F.; Gascon, J. Mixed Matrix Membranes Based on NH2-Functionalized MIL-Type MOFs: Influence of Structural and Operational Parameters on the CO2/CH4 Separation Performance. *Microporous Mesoporous Mater.* **2014**, *192*, 35–42. https://doi.org/10.1016/j.micromeso.2013.08.049.

(90) Basu, S.; Cano-Odena, A.; Vankelecom, I. F. J. Asymmetric Matrimid/[Cu3(BTC)2] Mixed-Matrix Membranes for Gas Separations. *J. Memb. Sci.* **2010**, *362* (1–2), 478–487. https://doi.org/10.1016/j.memsci.2010.07.005.

(91) Ren, H.; Jin, J.; Liu, H. Affinity between Metal–Organic Frameworks and Polyimides in Asymmetric Mixed Matrix Membranes for Gas Separations. *Ind. Eng. Chem. Res.* **2012**, *51* (30), 10156–10164.

(92) Li, T.; Pan, Y.; Peinemann, K.-V.; Lai, Z. Carbon Dioxide Selective Mixed-Matrix Composite Membrane Containing ZIF-7 Nano-Fillers. *J. Memb. Sci.* **2013**, *425–426*, 235–242.

(93) Yang, E.; Goh, K.; Chuah, C. Y.; Wang, R.; Bae, T.-H. Asymmetric Mixed-Matrix Membranes Incorporated with Nitrogen-Doped Graphene Nanosheets for Highly Selective Gas Separation. *J. Memb. Sci.* **2020**, 118293. https://doi.org/10.1016/j.memsci.2020.118293.

(94) Sánchez-Laínez, J.; Zornoza, B.; Friebe, S.; Caro, J.; Cao, S.; Sabetghadam, A.; Seoane, B.; Gascon, J.; Kapteijn, F.; Le Guillouzer, C.; et al. Influence of ZIF-8 Particle Size in the Performance of Polybenzimidazole Mixed Matrix Membranes for Pre-Combustion CO2 Capture and Its Validation through Interlaboratory Test. *J. Memb. Sci.* **2016**, *515*, 45–53. https://doi.org/10.1016/j.memsci.2016.05.039.

(95) Thür, R.; Van Velthoven, N.; Lemmens, V.; Bastin, M.; Smolders, S.; De Vos, D. De; Vankelecom, I. F. J. Modulator-Mediated Functionalization of MOF-808 as a Platform Tool to Create High-Performance Mixed-Matrix Membranes. *ACS Appl. Mater. Interfaces* **2019**. https://doi.org/10.1021/acsami.9b19774.

(96) Kertik, A.; Khan, A. L.; Vankelecom, I. F. J. Mixed Matrix Membranes Prepared from Non-Dried MOFs for CO2/CH4 Separations. *RSC Adv.* **2016**, *6*, 114505–114512. https://doi.org/10.1039/c6ra23013j.

(97) Knebel, A.; Bavykina, A.; Datta, S. J.; Sundermann, L.; Garzon-Tovar, L.; Lebedev, Y.; Durini, S.; Ahmad, R.; Kozlov, S. M.; Shterk, G.; et al. Solution Processable Metal-Organic Frameworks for Mixed Matrix Membranes Using Porous Liquids. *Nat. Mater.* **2020**. https://doi.org/10.1038/s41563-020-0764-y.

(98) Qian, Q.; Asinger, P. A.; Lee, M. J.; Han, G.; Rodriguez, K. M.; Lin, S.; Benedetti, F. M.; Wu, A. X.; Chi, W. S.; Smith, Z. P. MOF-Based Membranes for Gas Separations. *Chem. Rev.* **2020**, *120* (16), 8161. https://doi.org/10.1021/acs.chemrev.0c00119.

(99) Monsalve-Bravo, G. M.; Bhatia, S. K. Modeling Permeation through Mixed-Matrix Membranes: A Review. *Processes* **2018**, *6*, 172. https://doi.org/10.3390/pr6090172.

(100) Vinh-Thang, H.; Kaliaguine, S. A Comprehensive Computational Strategy for Fi Tting Experimental Permeation Data of Mixed Matrix Membranes. *J. Memb. Sci.* **2014**, *452*, 271–276. https://doi.org/10.1016/j.memsci.2013.10.020.

(101) Harold, J.; Staudt, C.; Janiak, C. Metal-Organic Frameworks in Mixed-Matrix Membranes for Gas Separation. *Dalt. Trans. Trans.* **2012**, *41*, 14003–14027. https://doi.org/10.1039/c2dt31550e.

(102) Bueken, B.; Van Velthoven, N.; Krajnc, A.; Smolders, S.; Taulelle, F.; Mellot-Draznieks, C.; Mali, G.; Bennett, T. D.; De Vos, D. Tackling the Defect Conundrum in UiO-66: A Mixed-Linker Approach to Engineering Missing Linker Defects. *Chem. Mater.* **2017**, *29* (24), 10478–10486. https://doi.org/10.1021/acs.chemmater.7b04128.

(103) Bai, Y.; Dou, Y.; Xie, L.-H.; Rutledge, W.; Li, J.-R.; Zhou, H.-C. Zr-Based Metal-Organic Frameworks: Design, Synthesis, Structure, and Applications. *Chem. Soc. Rev.* **2016**, *45*, 2327–2367. https://doi.org/10.1039/C5CS00837A.

(104) Li, L.; Tang, S.; Wang, C.; Lv, X.; Jiang, M.; Wu, H.; Zhao, X. High Gas Storage Capacities and Stepwise Adsorption in a UiO Type Metal–Organic Framework Incorporating Lewis Basic Bipyridyl Sites. *Chem. Commun.* **2014**, *50* (18), 2304. https://doi.org/10.1039/c3cc48275h.

(105) Cavka, J. H.; Jakobsen, S.; Olsbye, U.; Guillou, N.; Lamberti, C.; Bordiga, S.; Lillerud, K. P. A New Zirconium Inorganic Building Brick Forming Metal Organic Frameworks with Exceptional Stability. *J. Am. Chem. Soc. Commun.* **2008**, *130*, 13850–13851.

(106) Katz, M.; Brown, Z.; Colon, Y.; Siu, P.; Scheidt, K.; Snurr, R.; Hupp, J.; Farha, O. K. A Facile Synthesis of UiO-66, UiO-67 and Their Derivatives. *Chem. Commun.* **2013**, *49*, 9449–9451. https://doi.org/10.1039/c3cc46105j.

(107) Castarlenas, S.; Téllez, C.; Coronas, J. Gas Separation with Mixed Matrix Membranes Obtained from MOF UiO-66- Graphite Oxide Hybrids. *J. Memb. Sci.* **2017**, *526*, 205–211. https://doi.org/10.1016/j.memsci.2016.12.041.

(108) Shen, J.; Liu, G.; Huang, K.; Li, Q.; Guan, K.; Li, Y.; Jin, W. UiO-66-Polyether Block Amide Mixed Matrix Membranes for CO 2 Separation. *J. Memb. Sci.* **2016**, *513*, 155–165. https://doi.org/10.1016/j.memsci.2016.04.045.

(109) Dechnik, J.; Sumby, C. J.; Janiak, C. Enhancing Mixed-Matrix Membrane Performance with Metal − Organic Framework Additives. *Cryst. Growth Des.* **2017**, *17*, 4467–4488. https://doi.org/10.1021/acs.cgd.7b00595.

(110) Tien-Binh, N.; Rodrigue, D.; Kaliaguine, S. In-Situ Cross Interface Linking of PIM-1 Polymer and UiO-66-NH2for Outstanding Gas Separation and Physical Aging Control. *J. Memb. Sci.* **2018**, *548* (November 2017), 429–438. https://doi.org/10.1016/j.memsci.2017.11.054.

(111) Tu, T. N.; Nguyen, M. V; Nguyen, H. L.; Yuliarto, B.; Cordova, K. E.; Demir, S. Designing Bipyridine-Functionalized Zirconium Metal – Organic Frameworks as a Platform for Clean Energy and Other Emerging Applications. *Coord. Chem. Rev.* **2018**, *364*, 33–50. https://doi.org/10.1016/j.ccr.2018.03.014.

(112) Song, Y.; Yang, D.; Yu, S.; Teng, X.; Chang, Z.; Pan, F.; Bu, X.; Jiang, Z.; Wang, B.; Wang, S.; et al. Hybrid Membranes with Cu (II) Loaded Metal Organic Frameworks for Enhanced Desulfurization Performance. *Sep. Purif. Technol.* **2019**, *210* (July 2018), 258–267. https://doi.org/10.1016/j.seppur.2018.08.018.

(113) Wu, G.; Li, Y.; Geng, Y.; Lu, X.; Jia, Z. Adjustable Pervaporation Performance of Zr-MOF / Poly (Vinyl Alcohol) Mixed Matrix Membranes. *J. Chem. Technol. Biotechnol.* **2018**, *93* (10). https://doi.org/10.1002/jctb.5846.

(114) Nasir, R.; Mukhtar, H.; Man, Z.; Mohshim, D. F. Material Advancements in Fabrication of Mixed-Matrix Membranes. *Chem. Eng. Technol.* **2013**, *36* (5), 717–727. https://doi.org/10.1002/ceat.201200734.

(115) Nik, O. G.; Chen, X. Y.; Kaliaguine, S. Functionalized Metal Organic Framework-Polyimide Mixed Matrix Membranes for CO2/CH4 Separation. *J. Memb. Sci.* **2012**, *413–414*, 48–61. https://doi.org/10.1016/j.memsci.2012.04.003.

(116) Trickett, C. A.; Helal, A.; Al-maythalony, B. A.; Yamani, Z. H.; Cordova, K. E.; Yaghi, O. M. The Chemistry of Metal–Organic Frameworks for CO2 Capture, Regeneration and Conversion. *Nature* **2017**, *2*, 1–16. https://doi.org/10.1038/natrevmats.2017.45.

(117) Rouquerol, F.; Rouquerol, J.; Sing, K. *Adsorption by Powders and Porous Solids*, 11th ed.; Academic Press: San Diego, 1999.

(118) Walton, K. S.; Snurr, R. Q. Applicability of the BET Method for Determining Surface Areas of Microporous Metal-Organic Frameworks. *J. Am. Chem. Soc.* **2007**, *129* (27), 8552–8556. https://doi.org/10.1021/ja071174k.

(119) Tao, S. J. Positronium Annihilation in Molecular Substances. *J. Chem. Phys.* **1972**, *56*, 5499–5510.

(120) Eldrup, M.; Lightbody, D.; Sherwood, J. N. The Temperature Dependence of Positron Lifetimes in Solid Pivalic Acid. *Chem. Phys.* **1981**, *63* (1–2), 51–58. https://doi.org/10.1016/0301-0104(81)80307-2.

(121) Verbeke, R.; Gómez, V.; Koschine, T.; Eyley, S.; Szymczyk, A.; Dickmann, M.; Stimpel-Lindner, T.; Egger, W.; Thielemans, W.; Vankelecom, I. F. J. Real-Scale Chlorination at PH4 of BW30 TFC Membranes and Their Physicochemical Characterization. *J. Memb. Sci.* **2018**, *551* (September 2017), 123–135. https://doi.org/10.1016/j.memsci.2018.01.019.

(122) Kirkegaard, P.; Olsen, J. V.; Eldrup, M. M. *PALSfit3: A Software Package for Analysing Postiron Lifetime Spectra*; Kongens Lyngby, 2017.

(123) Khan, A. L.; Basu, S.; Cano-odena, A.; Vankelecom, I. F. J. Novel High Throughput Equipment for Membrane-Based Gas Separations. *J. Memb. Sci.* **2010**, *354* (1–2), 32–39. https://doi.org/10.1016/j.memsci.2010.02.069.

(124) Fei, H.; Cohen, S. M. A Robust, Catalytic Metal–Organic Framework with Open 2,2'-Bipyridine Sites. *Chem. Commun.* **2014**, *50* (37), 4810–4812. https://doi.org/10.1039/C4CC01607F.

(125) Schaate, A.; Roy, P.; Godt, A.; Lippke, J.; Waltz, F.; Wiebcke, M.; Behrens, P. Modulated Synthesis of Zr-Based Metal – Organic Frameworks: From Nano to Single Crystals. *Chem. - A Eur. J.* **2011**, *17* (24), 6643–6651. https://doi.org/10.1002/chem.201003211.

(126) Chavan, S.; Vitillo, J. G.; Gianolio, D.; Zavorotynska, O.; Civalleri, B.; Jakobsen, S.; Nilsen, M. H.; Valenzano, L.; Lamberti, C.; Lillerud, K. P.; et al. H2 Storage in Isostructural UiO-67 and UiO-66 MOFs. *Phys. Chem. Chem. Phys.* **2012**, *14* (5), 1614–1626. https://doi.org/10.1039/C1CP23434J.

(127) Le, N. L.; Wang, Y.; Chung, T. S. Synthesis, Cross-Linking Modifications of 6FDA-NDA/DABA Polyimide Membranes for Ethanol Dehydration via Pervaporation. *J. Memb. Sci.* **2012**, *415–416*, 109–121. https://doi.org/10.1016/j.memsci.2012.04.042.

(128) Gutterød, E. S.; Øien-ØDegaard, S.; Bossers, K.; Nieuwelink, A. E.; Manzoli, M.; Braglia, L.; Lazzarini, A.; Borfecchia, E.; Ahmadigoltapeh, S.; Bouchevreau, B.; et al. CO2 Hydrogenation over Pt-Containing UiO-67 Zr-MOFs - The Base Case. *Ind. Eng. Chem. Res.* **2017**, *56* (45), 13206–13218. https://doi.org/10.1021/acs.iecr.7b01457.

(129) Øien, S.; Agostini, G.; Svelle, S.; Borfecchia, E.; Lomachenko, K. A.; Mino, L.; Gallo, E.; Bordiga, S.; Olsbye, U.; Lillerud, K. P.; et al. Probing Reactive Platinum Sites in Uio-67 Zirconium Metal-Organic Frameworks. *Chemistry of Materials*. 2015, pp 1042–1056. https://doi.org/10.1021/cm504362j.

(130) Li, J.-R.; Kuppler, R. J.; Zhou, H.-C. Selective Gas Adsorption and Separation in Metal–Organic Frameworks. *Chem. Soc. Rev.* **2009**, *38* (5), 1477. https://doi.org/10.1039/b802426j.

(131) Ge, L.; Zhou, W.; Rudolph, V.; Zhu, Z. Mixed Matrix Membranes Incorporated with Size-Reduced Cu-BTC for Improved Gas Separation. *J. Mater. Chem. A* **2013**, *1*, 6350–6358. https://doi.org/10.1039/c3ta11131h.

(132) Smith, B. C. *Infrared Spectral Interpretation: A Systematic Approach*; CRC Press LLC, 1998.

(133) Kertik, A.; Wee, L. H.; Pfannmoeller, M.; Bals, S.; Martens, J.; Vankelecom, I. F. J. Highly Selective Gas Separation Membrane Using In-Situ Amorphised Metal-Organic Frameworks. *Energy Environ. Sci.* **2017**, *10*, 2342–2351. https://doi.org/10.1039/C7EE01872J.

(134) Okamoto, K. ichi; Tanaka, K.; Katsube, M.; Sueoka, O.; Ito, Y. Positronium Formation in Various Polyimides. *Radiat. Phys. Chem.* **1993**, *41* (3), 497–502. https://doi.org/10.1016/0969-806X(93)90011-I.

(135) Chung, T. S.; Jiang, L. Y.; Li, Y.; Kulprathipanja, S. Mixed Matrix Membranes (MMMs) Comprising Organic Polymers with Dispersed Inorganic Fillers for Gas Separation. *Prog. Polym. Sci.* **2007**, *32* (4), 483–507. https://doi.org/10.1016/j.progpolymsci.2007.01.008.

(136) Ahn, J.; Chung, W. J.; Pinnau, I.; Song, J.; Du, N.; Robertson, G. P.; Guiver, M. D. Gas Transport Behavior of Mixed-Matrix Membranes Composed of Silica Nanoparticles in a Polymer of Intrinsic Microporosity (PIM-1). *J. Memb. Sci.* **2010**, *346* (2), 280–287. https://doi.org/10.1016/j.memsci.2009.09.047.

(137) Rezakazemi, M.; Ebadi Amooghin, A.; Montazer-Rahmati, M. M.; Ismail, A. F.; Matsuura, T. State-of-the-Art Membrane Based CO2separation Using Mixed Matrix Membranes (MMMs): An Overview on Current Status and Future Directions. *Prog. Polym. Sci.* **2014**, *39* (5), 817–861. https://doi.org/10.1016/j.progpolymsci.2014.01.003.

(138) Chau, J. Y. H.; Freeman, H. C.; Le, R.; Narayana, D. Dipole Moments of Pyridine, Quinoline, and Isoquinoline. *J. Chem. Soc.* **1956**, *0*, 1405–1411.

(139) Chen, L.; Cao, F.; Sun, H. Ab Initio Study of the π-π Interactions between CO2 and Benzene, Pyridine, and Pyrrole. *Int. J. Quantum Chem.* **2013**, *113* (20), 2261–2266. https://doi.org/10.1002/qua.24444.

(140) Torrisi, A.; Mellot-Draznieks, C.; Bell, R. G. Impact of Ligands on CO2 Adsorption in Metal-Organic Frameworks: First Principles Study of the Interaction of CO2 with Functionalized Benzenes. I. Inductive Effects on the Aromatic Ring. *J. Chem. Phys.* **2009**, *130* (19). https://doi.org/10.1063/1.3120909.

(141) Japip, S.; Wang, H.; Xiao, Y.; Chung, T. S. Highly Permeable Zeolitic Imidazolate Framework (ZIF)-71 Nano-Particles Enhanced Polyimide Membranes for Gas Separation. *J. Memb. Sci.* **2014**, *467*, 162–174. https://doi.org/10.1016/j.memsci.2014.05.025.

(142) Ahmad, M. Z.; Navarro, M.; Lhotka, M.; Zornoza, B.; Téllez, C.; Vos, W. M. De; Benes, N. E.; Konnertz, N. M.; Visser, T.; Semino, R.; et al. Enhanced Gas Separation Performance of 6FDA-DAM Based Mixed Matrix Membranes by Incorporating MOF UiO-66 and Its Derivatives. *J. Memb. Sci.* **2018**, *558* (March), 64–77. https://doi.org/10.1016/j.memsci.2018.04.040.

(143) Ahmad, M. Z.; Navarro, M.; Lhotka, M.; Zornoza, B.; Téllez, C.; Fila, V.; Coronas, J. Enhancement of CO2/CH4 Separation Performances of 6FDA-Based Co-Polyimides Mixed Matrix Membranes Embedded with UiO-66 Nanoparticles. *Sep. Purif. Technol.* **2018**, *192* (October 2017), 465–474. https://doi.org/10.1016/j.seppur.2017.10.039.

(144) Jiang, Y.; Liu, C.; Caro, J.; Huang, A. A New UiO-66-NH2 Based Mixed-Matrix Membranes with High CO2/CH4 Separation Performance. *Microporous Mesoporous Mater.* **2019**, *274* (July 2018), 203–211. https://doi.org/10.1016/j.micromeso.2018.08.003.

(145) Khdhayyer, M. R.; Esposito, E.; Fuoco, A.; Monteleone, M.; Giorno, L.; Jansen, J. C.; Attfield, M. P.; Budd, P. M. Mixed Matrix Membranes Based on UiO-66 MOFs in the Polymer of Intrinsic Microporosity PIM-1. *Sep. Purif. Technol.* **2017**, *173*, 304–313. https://doi.org/10.1016/j.seppur.2016.09.036.

(146) Basu, S.; Khan, A. L.; Cano-Odena, A.; Liu, C.; Vankelecom, I. F. J. Membrane-Based Technologies for Biogas Separations. *Chem. Soc. Rev.* **2010**, *39* (2), 750–768. https://doi.org/10.1039/B817050A.

(147) Katayama, Y.; Bentz, K. C.; Cohen, S. M. Defect-Free MOF-Based Mixed-Matrix Membranes Obtained by Corona Cross-Linking. *ACS Appl. Mater. Interfaces* **2019**, *11*, 13029–13037. https://doi.org/10.1021/acsami.9b02539.

(148) Liu, G.; Labreche, Y.; Chernikova, V.; Shekhah, O.; Zhang, C.; Belmabkhout, Y.; Eddaoudi, M.; Koros, W. J. Zeolite-like MOF Nanocrystals Incorporated 6FDA-Polyimide Mixed-Matrix Membranes for CO2/CH4 Separation. *J. Memb. Sci.* **2018**, *565* (August), 186–193. https://doi.org/10.1016/j.memsci.2018.08.031.

(149) Perez, E. V; Balkus Jr, K. J.; Ferraris, J. P.; Musselman, I. H. Mixed-Matrix Membranes Containing MOF-5 for Gas Separations. *J. Memb. Sci.* **2009**, *328*, 165–173. https://doi.org/10.1016/j.memsci.2008.12.006.

(150) Ma, C.; Urban, J. J. Enhanced CO2 Capture and Hydrogen Purification by Hydroxy Metal–Organic Framework/Polyimide Mixed Matrix Membranes. *ChemSusChem* **2019**, *12*, 1–8. https://doi.org/10.1002/cssc.201902248.

(151) Prasetya, N.; Donose, B. C.; Ladewig, B. P. A New and Highly Robust Light-Responsive Azo-UiO-66 for Highly Selective and Low Energy Post-Combustion CO2 Capture and Its Application in a Mixed-Matrix Membrane for CO2/N2 Separation. *J. Mater. Chem. A* **2018**, *6*, 16390–16402. https://doi.org/10.1039/c8ta03553a.

(152) Sutrisna, P.; Hou, J.; Zulkifli, M.; Li, H.; Zhang, Y.; Liang, W.; D'Alesandro, D.; Chen, V. Surface Functionalized UiO-66/Pebax-Based Ultrathin Composite Hollow Fiber Gas Separation Membranes. *J. Mater. Chem. A* **2018**, *6*, 918–931. https://doi.org/10.1039/C7TA07512J.

(153) Mautschke, H.; Drache, F.; Senkovska, I.; Kaskel, S.; Llabrés i Xamena, F. X. Catalytic Properties of Pristine and Defect-Engineered Zr-MOF-808 Metal Organic Frameworks. *Catal. Sci. Technol.* **2018**, *8* (14), 3610–3616. https://doi.org/10.1039/c8cy00742j.

(154) Thür, R.; Van Velthoven, N.; Slootmaekers, S.; Didden, J.; Verbeke, R.; Smolders, S.; Egger, W.; Dickmann, M.; De Vos, D.; Vankelecom, I. F. J. Bipyridine-Based UiO-67 as Novel Filler in Mixed-Matrix Membranes for CO2-Selective Gas Separation. *J. Memb. Sci.* **2019**, *576* (15 April 2019), 78–87. https://doi.org/10.1016/j.memsci.2019.01.016.

(155) Furukawa, H.; Gándara, F.; Zhang, Y.-B.; Jiang, J.; Queen, W. L.; Hudson, M. R.; Yaghi, O. M. Water Adsorption in Porous Metal−Organic Frameworks and Related Materials. *J. Am. Chem. Soc.* **2014**, *136*, 4369–4381. https://doi.org/10.1021/ja500330a.

(156) Velthoven, N. Van; Waitschat, S.; Chavan, S. M.; Liu, P.; Smolders, S.; Vercammen, J.; Bueken, B.; Bals, S.; Lillerud, K. P.; Stock, N.; et al. Single-Site Metal–Organic Framework Catalysts for the Oxidative Coupling of Arenes via C–H/C–H Activation. *Chem. Sci.* **2019**. https://doi.org/10.1039/c8sc05510f.

(157) Jiang, J.; Gándara, F.; Zhang, Y.-B.; Na, K.; Yaghi, O. M.; Klemperer, W. G. Superacidity in Sulfated Metal − Organic Framework-808. *J. Am. Chem. Soc.* **2014**, *136*, 12844–12847. https://doi.org/10.1021/ja507119n.

(158) Jia, C.; Cirujano, F. G.; Bueken, B.; Claes, B.; Jonckheere, D.; Van Geem, K. M.; De Vos, D. Geminal Coordinatively Unsaturated Sites on MOF-808 for the Selective Uptake of Phenolics from a Real Bio-Oil Mixture. *ChemSusChem* **2019**, *101*, 1256–1266. https://doi.org/10.1002/cssc.201802692.

(159) Zheng, H.-Q.; Liu, C.-Y.; Zeng, X.-Y.; Chen, J.; Lu, J.; Lin, R.-G.; Cao, R.; Lin, Z.; Su, J. MOF-808: A Metal–Organic Framework with Intrinsic Peroxidase-Like Catalytic Activity at Neutral PH for Colorimetric Biosensing. *Inorg. Chem.* **2018**, *57*, 9096–9104. https://doi.org/10.1021/acs.inorgchem.8b01097.

(160) Howarth, A. J.; Liu, Y.; Li, P.; Li, Z.; Wang, T. C.; Hupp, J.; Farha, O. K. Chemical, Thermal and Mechanical Stabilities of Metal-Organic Frameworks. *Nat. Rev. | Mater.* **2016**, No. 15018, 1–15. https://doi.org/10.1038/natrevmats.2015.18.

(161) Reinsch, H.; Waitschat, S.; Chavan, S. M.; Lillerud, K. P.; Stock, N. A Facile "Green" Route for Scalable Batch Production and Continuous Synthesis of Zirconium MOFs. *Eur. J. Inorg. Chem.* **2016**, *2016* (27), 4490–4498. https://doi.org/10.1002/ejic.201600295.

(162) Deria, P.; Mondloch, J. E.; Tylianakis, E.; Ghosh, P.; Bury, W.; Snurr, R. Q.; Hupp, J. T.; Farha, O. K. Perfluoroalkane Functionalization of NU-1000 via Solvent-Assisted Ligand Incorporation: Synthesis and CO2 Adsorption Studies. *J. Am. Chem. Soc.* **2013**, *14*, 16801–16804. https://doi.org/10.1021/ja408959g.

(163) Beg, M. A. A.; Clark, H. C. Chemistry of the Trifluoromethyl Group: PART V. Infrared Spectra of Some Phosphorus Compounds Containing CF3. *Can. J. Chem.* **1962**, *40* (3),

393–398. https://doi.org/https://doi.org/10.1139/v62-063.

(164) Bueken, B.; Van Velthoven, N.; Willhammar, T.; Stassin, T.; Stassen, I.; Keen, D. A.; Baron, G. V; Denayer, J. F. M.; Ameloot, R.; Bals, S.; et al. Gel-Based Morphological Design of Zirconium Metal-Organic Frameworks. *Chem. Sci.* **2017**, *8*, 3939–3948. https://doi.org/10.1039/c6sc05602d.

(165) Yoreo, J. J. De; Vekilov, P. G. Principles of Crystal Nucleation and Growth. *Rev. Mineral. Geochemistry* **2003**, *54* (1), 57–93. https://doi.org/https://doi.org/10.2113/0540057.

(166) Xue, D.-X.; Cairns, A. J.; Belmabkhout, Y.; Wojtas, L.; Liu, Y.; Alkordi, M. H.; Eddaoudi, M. Tunable Rare-Earth Fcu-MOFs: A Platform for Systematic Enhancement of CO2 Adsorption Energetics and Uptake. *J. Am. Chem. Soc.* **2013**, *135*, 7660–7667. https://doi.org/10.1021/ja401429x.

(167) Cho, H.-Y.; Yang, D.-A.; Kim, J.; Jeong, S.-Y.; Ahn, W.-S. CO2 Adsorption and Catalytic Application of Co-MOF-74 Synthesized by Microwave Heating. *Catal. Today* **2012**, *185* (1), 35–40. https://doi.org/10.1016/j.cattod.2011.08.019.

(168) Etxeberria-Benavides, M.; David, O.; Johnson, T.; Magdalena, M. Ł.; Orsi, A.; Wright, P. A.; Mastel, S.; Hillenbrand, R.; Kapteijn, F.; Gascon, J. High Performance Mixed Matrix Membranes (MMMs) Composed of ZIF-94 Filler and 6FDA-DAM Polymer. **2018**, *550* (August 2017), 198–207. https://doi.org/10.1016/j.memsci.2017.12.033.

(169) Cece, A.; Jureller, S. H.; Kerschner, J. L.; Moschner, K. F. Molecular Modeling Approach for Contrasting the Interaction of Ethane and Hexafluoroethane with Carbon Dioxide. *J. Phys. Chem.* **1996**, *3654* (95), 7435–7439. https://doi.org/10.1021/jp953627q.

(170) Fried, J. R.; Hu, N. The Molecular Basis of CO2 Interaction with Polymers Containing Fluorinated Groups: Computational Chemistry of Model Compounds and Molecular Simulation of Poly[Bis(2,2,2-Trifluoroethoxy)Phosphazene]. *Polymer (Guildf).* **2003**, *44*, 4363–4372. https://doi.org/10.1016/S0032-3861(03)00285-4.

(171) Paul, D. R. Gas Sorption and Transport in Glassy Polymers. *Berichte der Bunsengesellschaft für Phys. Chemie* **1979**, *83* (4), 294–302. https://doi.org/https://doi.org/10.1002/bbpc.19790830403.

(172) Zahn, G.; Albert, H.; Lippke, J.; König, S.; Sazama, U.; Fröba, M.; Behrens, P. A Water-Born Zr-Based Porous Coordination Polymer: Modulated Synthesis of Zr-Fumarate MOF. *Microporous Mesoporous Mater.* **2015**, *203*, 186–194. https://doi.org/10.1016/j.micromeso.2014.10.034.

(173) Crowder, G. A. Infrared Spectra of Heptafluorbutyric Acid and Some of Its Esters. *J. Fluor. Chem.* **1973**, *3* (2), 133–140. https://doi.org/https://doi.org/10.1016/S0022-1139(00)84158-5.

(174) Zhang, Y.; Balkus Jr, K. J.; Musselman, I. H.; Ferraris, J. P. Mixed-Matrix Membranes Composed of Matrimid® and Mesoporous ZSM-5 Nanoparticles. *J. Memb. Sci.* **2008**, *325*, 28–39. https://doi.org/10.1016/j.memsci.2008.04.063.

(175) Ren, H.; Jin, J.; Hu, J.; Liu, H. Affinity between Metal − Organic Frameworks and Polyimides in Asymmetric Mixed Matrix Membranes for Gas Separations. *Ind. Eng.*

Chem. Res. **2012**, *51*, 10156–10164. https://doi.org/10.1021/ie300553k.

(176) Li, W.; Pan, F.; Song, Y.; Wang, M.; Wang, H.; Walker, S.; Wu, H.; Jiang, Z. Construction of Molecule-Selective Mixed Matrix Membranes with Confined Mass Transfer Structure. *Chinese J. Chem. Eng.* **2017**, *25* (11), 1563–1580. https://doi.org/10.1016/j.cjche.2017.04.015.

(177) Sabetghadam, A.; Seoane, B.; Keskin, D.; Duim, N.; Rodenas, T.; Shahid, S.; Sorribas, S.; Guillouzer, C. Le; Clet, G.; Tellez, C.; et al. Metal Organic Framework Crystals in Mixed-Matrix Membranes: Impact of the Filler Morphology on the Gas Separation Performance. *Adv. Funct. Mater.* **2016**, *26*, 3154–3163. https://doi.org/10.1002/adfm.201505352.

(178) Carter, D.; Tezel, F. H.; Kruczek, B.; Kalipcilar, H. Investigation and Comparison of Mixed Matrix Membranes Composed of Polyimide Matrimid with ZIF–8 , Silicalite , and SAPO–34. *J. Memb. Sci.* **2017**, *544* (May), 35–46. https://doi.org/10.1016/j.memsci.2017.08.068.

(179) Liang, C. Z.; Chung, T.-S.; Lai, J.-Y. A Review of Polymeric Composite Membranes for Gas Separation and Energy Production. *Prog. Polym. Sci.* **2019**, *97*, 101141. https://doi.org/10.1016/j.progpolymsci.2019.06.001.

(180) Li, H.; Haas-Santo, K.; Schygulla, U.; Dittmeyer, R. Inorganic Microporous Membranes for H2 and CO2 Separation — Review of Experimental and Modeling Progress. *Chem. Eng. Sci.* **2015**, *127*, 401–417. https://doi.org/10.1016/j.ces.2015.01.022.

(181) Tsapatsis, M. Toward High-Throughput Zeolite Membranes. *Science (80-.).* **2011**, *334* (November), 767–769. https://doi.org/10.1126/science.1205957.

(182) Qian, Q.; Chi, W. S.; Han, G.; Smith, Z. P. Impact of Post-Synthetic Modification Routes on Filler Structure and Performance in Metal−Organic Framework-Based Mixed-Matrix Membranes. *Indust* **2020**, *59*, 5432–5438. https://doi.org/10.1021/acs.iecr.9b04820.

(183) Chi, W. S.; Sundell, B. J.; Zhang, K.; Harrigan, D. J.; Hayden, S. C.; Smith, Z. P. Mixed-Matrix Membranes Formed from Multi-Dimensional Metal–Organic Frameworks for Enhanced Gas Transport and Plasticization Resistance. *ChemSusChem* **2019**, *02139*, 2355–2360. https://doi.org/10.1002/cssc.201900623.

(184) Shahid, S.; Nijmeijer, K. Performance and Plasticization Behavior of Polymer-MOF Membranes for Gas Separation at Elevated Pressures. *J. Memb. Sci.* **2014**, *470*, 166–177. https://doi.org/10.1016/j.memsci.2014.07.034.

(185) Ahmad, M. Z.; Peters, T. A.; Konnertz, N. M.; Visser, T.; Téllez, C.; Coronas, J.; Fila, V.; de Vos, W. M.; Benes, N. E. High-Pressure CO2/CH4 Separation of Zr-MOFs Based Mixed Matrix Membranes. *Sep. Purif. Technol.* **2020**, *230* (June 2019), 115858. https://doi.org/10.1016/j.seppur.2019.115858.

(186) Van Essen, M.; Montrée, E.; Houben, M.; Borneman, Z.; Nijmeijer, K. Magnetically Aligned and Enriched Pathways of Zeolitic Imidazolate Framework 8 in Matrimid Mixed Matrix Membranes for Enhanced CO 2 Permeability. *Membranes (Basel).* **2020**, *10* (7), 155.

(187) Rodenas, T.; Van Dalen, M.; García-Pérez, E.; Serra-Crespo, P.; Zornoza, B.; Kapteijn, F.; Gascon, J. Visualizing MOF Mixed Matrix Membranes at the Nanoscale: Towards Structure-Performance Relationships in CO2/CH4 Separation Over NH2-MIL-53 (Al)@PI. *Adv. Funct. Mater.* **2014**, *24*, 249–256. https://doi.org/10.1002/adfm.201203462.

(188) Kang, Z.; Peng, Y.; Hu, Z.; Qian, Y.; Chi, C.; Yeo, L. Y.; Tee, L.; Zhao, D. Mixed Matrix Membranes Composed of Two-Dimensional Metal–Organic Framework Nanosheets for Pre-Combustion CO2 Capture: A Relationship Study of Fi Ller Morphology versus Membrane. *J. Mater. Chem. A* **2015**, *3*, 20801–20810. https://doi.org/10.1039/c5ta03739e.

(189) Chen, K.; Xu, K.; Xiang, L.; Dong, X.; Han, Y.; Wang, C.; Sun, L.; Pan, Y. Enhanced CO2/CH4 Separation Performance of Mixed-Matrix Membranes through Dispersion of Sorption-Selective MOF Nanocrystals. *J. Memb. Sci.* **2018**, *563* (March), 360–370. https://doi.org/10.1016/j.memsci.2018.06.007.

(190) Cheng, Y.; Ying, Y.; Zhai, L.; Liu, G.; Dong, J.; Wang, Y.; Christopher, M. P.; Long, S.; Wang, Y.; Zhao, D. Mixed Matrix Membranes Containing MOF@COF Hybrid Fillers for Efficient CO2/CH4 Separation. *J. Memb. Sci.* **2019**, *573* (November 2018), 97–106. https://doi.org/10.1016/j.memsci.2018.11.060.

(191) Yu, G.; Li, Y.; Wang, Z.; Xiaoteng, T.; Zhu, G.; Zou, X. Mixed Matrix Membranes Derived from Nanoscale Porous Organic Frameworks for Permeable and Selective CO2 Separation. *J. Memb. Sci.* **2019**, *591* (August), 117343. https://doi.org/10.1016/j.memsci.2019.117343.

(192) Van Velthoven, N.; Henrion, M.; Dallenes, J.; Krajnc, A.; Bugaev, A. L.; Liu, P.; Bals, S.; Soldatov, A. V; Vos, D. E. De. S,O-Functionalized Metal–Organic Frameworks as Heterogeneous Single-Site Catalysts for the Oxidative Alkenylation of Arenes via C–H Activation. *ACS Catal.* **2020**, *10*, 5077–5085. https://doi.org/10.1021/acscatal.0c00801.

(193) LoPachin, R. M.; Gavin, T.; DeCaprio, A.; Barber, D. S. Application of the Hard and Soft, Acids and Bases (HSAB) Theory to Toxicant-Target Interactions. *Chem. Res. Toxicol.* **2012**, *25* (2), 239–251.

(194) Baek, J.; Rungtaweevoranit, B.; Pei, X.; Park, M.; Fakra, S. C.; Liu, Y.-S.; Matheu, R.; Alshmimri, S. A.; Alshehri, S.; Trickett, C. A.; et al. Bioinspired Metal–Organic Framework Catalysts for Selective Methane Oxidation to Methanol. *J. Am. Chem. Soc.* **2018**, *140*, 18208–18216. https://doi.org/10.1021/jacs.8b11525.

(195) Park, H. J.; Suh, M. P. Enhanced Isosteric Heat, Selectivity and Uptake Capacity of CO2 Adsorption in a Metal-Organic Framework by Impregnated Metal Ions. *Chem. Sci.* **2013**, *4* (3), 685–690. https://doi.org/10.1039/c2sc21253f.

(196) Hutter, J.; Iannuzzi, M.; Schiffmann, F.; VandeVondele, J. Cp2k: Atomistic Simulations of Condensed Matter Systems. *WIREs Comput. Mol. Sci.* **2013**, *4* (1), 15–25.

(197) Perdew, J. P.; Burke, K.; Ernzerhof, M. Generalized Gradient Approximation Made Simple. *Phys. Rev. Lett.* **1996**, *77* (3), 3865–3868.

(198) Grimme, S.; Antony, J.; Ehrlich, S.; Krieg, H. A Consistent and Accurate Ab Initio Parametrization of Density Functional Dispersion Correction (DFT-D) for the 94 Elements H-Pu. *J. Phys. Chem.* **2010**, *132*, 154104.

(199) Grimme, S.; Ehrlich, S.; Goerigk, L. Effect of the Damping Function in Dispersion Corrected Density Functional Theory. *J. Comput. Chem.* **2011**, *32* (7), 1456–1465.

(200) VandeVondele, J.; Hutter, J. Gaussian Basis Sets for Accurate Calculations on Molecular Systems in Gas and Condensed Phases. *J. Chem. Phys.* **2007**, *127* (11), 114105.

(201) Goedecker, S.; Teter, M.; Hutter, J. Separable Dual-Space Gaussian Pseudopotentials. *Phys. Rev. B* **1996**, *54*, 1703–1710.

(202) Dubbeldam, D.; Calero, S.; Ellis, D. E.; Snurr, R. Q. RASPA: Molecular Simulation Software for Adsorption and Diffusion in Flexible Nanoporous Materials. *Mol. Simulations* **2016**, *42* (2), 81–101.

(203) Potoff, J. J.; Siepmann, J. I. Vapor-Liquid Equilibria of Mixtures Containing Alkanes, Carbon Dioxide, and Nitrogen. *AlChE J.* **2004**, *47* (7), 1676–1682.

(204) Verstraelen, T.; Vandenbrande, S.; Heidar-Zadeh, F.; Vanduyfhuys, L.; Van Speybroeck, V.; Waroquier, M.; Ayers, P. W. Minimal Basis Iterative Stockholder: Atoms in Molecules for Force- Field Development. *J. Chem. Theory Comput.* **2016**, *12*, 3894–3912. https://doi.org/10.1021/acs.jctc.6b00456.

(205) Mayo, S. L.; Olafson, B. D.; Goddard, W. A. DREIDING: A Generic Force Field for Molecular Simulations. *J. Phys. Chem.* **1990**, *94* (26), 8897–8909.

(206) Vandenbrande, S.; Verstraelen, T.; Gutiérrez-Sevillano, J. J.; Waroquier, M.; Van Speybroeck, V. Van. Methane Adsorption in Zr-Based MOFs: Comparison and Critical Evaluation of Force Fields. *J. Phys. Chem. C* **2017**, *121* (45), 25309–25322. https://doi.org/10.1021/acs.jpcc.7b08971.

(207) Rappe, A. K.; Casewit, C. J.; Colwell, K. S.; Goddard III, W. A.; Skiff, W. M. UFF, a Full Periodic Table Force Field for Molecular Mechanics and Molecular Dynamics Simulations. *J. Am. Chem. Soc.* **1992**, *114* (25), 10024–10035.

(208) Thür, R.; Lemmens, V.; Van Havere, D.; van Essen, M.; Nijmeijer, K.; Vankelecom, I. F. J. Tuning 6FDA-DABA Membrane Performance for CO2 Removal by Physical Densification and Decarboxylation Cross-Linking during Simple Thermal Treatment. *J. Memb. Sci.* **2020**, *610*, 118195. https://doi.org/10.1016/j.memsci.2020.118195.

(209) Hafizovic, J.; Bjørgen, M.; Olsbye, U.; Dietzel, P. D. C.; Bordiga, S.; Prestipino, C.; Lamberti, C.; Lillerud, K. P. The Inconsistency in Adsorption Properties and Powder XRD Data of MOF-5 Is Rationalized by Framework Interpenetration and the Presence of Organic and Inorganic Species in the Nanocavities. *J. Am. Chem. Soc.* **2007**, No. 7, 3612–3620. https://doi.org/10.1021/ja0675447.

(210) Øien-ØDegaard, S.; Shearer, G. C.; Wragg, D. S.; Lillerud, K. P. Pitfalls in Metal–Organic Framework Crystallography: Towards More Accurate. *Chem. Soc. Rev.* **2017**, *46*, 4867–4876. https://doi.org/10.1039/c6cs00533k.

(211) Chen, B.; Wang, X.; Zhang, Q.; Xi, X.; Cai, J.; Qi, H.; Shi, S.; Wang, J.; Yuan, D.; Fang, M. Synthesis and Characterization of the Interpenetrated MOF-5 †. *J. Mater. Chem.* **2010**, *20*, 3758–3767. https://doi.org/10.1039/b922528e.

(212) Xuan, K.; Pu, Y.; Li, F.; Luo, J.; Zhao, N.; Xiao, F. Metal-Organic Frameworks MOF-808-X as Highly Efficient Catalysts for Direct Synthesis of Dimethyl Carbonate from CO2 and Methanol. *Chinese J. Catal.* **2019**, *40*, 533–566. https://doi.org/doi:10.1016/S1872-2067(19)63291-2.

(213) Kumar, S.; Rai, A. K.; Rai, S. B.; Rai, D. K. Infrared and Raman Spectra of Histidine: An Ab Initio DFT Calculations of Histidine Molecule and Its Different Protonated Forms. *Indian J. Phys.* **2010**, *84*, 563–573. https://doi.org/doi:10.1007/s12648-010-0039-6.

(214) Stepanian, S. G.; Reva, I. D.; Radchenko, E. D.; Sheina, G. G. Infrared Spectra of Benzoic Acid Monomers and Dimers in Argon Matrix. *Vib. Spectrosc.* **1996**, *11*, 123–133. https://doi.org/doi:10.1016/0924-2031(95)00068-2.

(215) Williams, R.; Jencks, W. P.; Westheimer, F. H. *PKa Data Compiled by R. Williams*.

(216) Fan, G.; Liu, Y.; Wang, H. Identification of Thermophilic Proteins by Incorporating Evolutionary and Acid Dissociation Information into Chou's General Pseudo Amino Acid Composition. *J. Theor. Biol.* **2016**, *407*, 138–142. https://doi.org/10.1016/j.jtbi.2016.07.010.

(217) Xu, J.; Liu, J.; Wang, X.; Xu, Y.; Chen, S.; Wang, X. Optimized Synthesis of Zr(IV) Metal Organic Frameworks (MOFs-808) for Efficient Hydrogen Storage. *New J. Chem.* **2019**, *43* (2), 4092–4099. https://doi.org/10.1039/c8nj06362a.

(218) Wendy, S.; Queen, L. An Experimental and Computational Study of CO2 Adsorption in the Sodalite-Type M-BTT (M ¼ Cr, Mn, Fe, Cu) Metal–Organic Frameworks Featuring Open Metal Sites. *Chem. Sci.* **2018**, *9*, 4579. https://doi.org/10.1039/c8sc00971f.

(219) Arstad, B.; Fjellvåg, H.; Kongshaug, K. O.; Swang, O.; Blom, R. Amine Functionalised Metal Organic Frameworks (MOFs) as Adsorbents for Carbon Dioxide. *Adsorption* **2008**, *14*, 755–762. https://doi.org/10.1007/s10450-008-9137-6.

(220) Mason, J. A.; Sumida, K.; Herm, Z. R.; Krishna, R.; Long, J. R. Evaluating Metal – Organic Frameworks for Post-Combustion Carbon Dioxide Capture via Temperature Swing Adsorption †. *Energy Environ. Sci.* **2011**, *4*, 3030–3040. https://doi.org/10.1039/c1ee01720a.

(221) Hossain, M. I.; Cunningham, J. D.; Becker, T. M.; Grabicka, B. E.; Walton, K. S.; Rabideau, B. D.; Glover, T. G. Impact of MOF Defects on the Binary Adsorption of CO2 and Water in UiO-66. *Chem. Eng. Sci.* **2019**, *203*, 146–357. https://doi.org/doi:10.1016/j.ces.2019.03.053.

(222) Koutsianos, A.; Kazimierska, E.; Barron, A. R.; Taddei, M.; Andreoli, E. A New Approach to Enhancing the CO2 Capture Performance of Defective UiO-66 via Post-Synthetic Defect Exchange. *Dalt. Trans.* **2019**, *48*, 3349–3359. https://doi.org/10.1039/c9dt00154a.

(223) Plonka, A. M.; Grissom, T. G.; Musaev, D. G.; Balboa, A.; Gordon, W. O.; Collins-

Wildman, D. L.; Ghose, S. K.; Tian, Y.; Ebrahim, A. M.; Mitchell, M. B.; et al. Effect of Carbon Dioxide on the Degradation of Chemical Warfare Agent Simulant in the Presence of Zr Metal Organic Framework MOF-808. *Chem. Mater.* **2019**, *31*, 9904–9914. https://doi.org/10.1021/acs.chemmater.9b04565.

(224) Luconi, L.; Mercuri, G.; Islamoglu, T.; Fermi, A.; Bergamini, G.; Giambastiani, G.; Rossin, A. Benzothiazolium-Functionalized NU-1000: A Versatile Material for Carbon Dioxide Adsorption and Cyanide Luminescence Sensing. *J. Mater. Chem. C* **2020**. https://doi.org/10.1039/d0tc01436b.

(225) Grissom, T. G.; Driscoll, D. M.; Troya, D.; Sapienza, N. S.; Usov, P. M.; Morris, A. J.; Morris, J. R. Molecular-Level Insight into CO2 Adsorption on the Zirconium-Based Metal−Organic Framework, UiO-66: A Combined Spectroscopic and Computational Approach. *J. Phys. Chem. C* **2019**, *123*, 13731–13738. https://doi.org/10.1021/acs.jpcc.9b02513.

(226) Lau, C. H.; Babarao, R.; Hill, M. R. A Route to Drastic Increase of CO2 Uptake in Zr Metal Organic Framework UiO-66. *Chem. Commun.* **2013**, *49* (207890), 3634–3637. https://doi.org/10.1039/c3cc40470f.

(227) Dingel, T.; Tessema, M.; Venna, S. R.; Dahe, G.; Hopkinson, D. P.; El-kaderi, H. M.; Sekizkardes, A. K. Incorporation of Benzimidazole Linked Polymers into Matrimid to Yield Mixed Matrix Membranes with Enhanced CO2/N2 Selectivity. *J. Memb. Sci.* **2018**, *554* (January), 90–96. https://doi.org/10.1016/j.memsci.2018.02.054.

(228) Shan, M.; Seoane, B.; Pustovarenko, A.; Wang, X.; Liu, X. Benzimidazole Linked Polymers (BILPs) in Mixed-Matrix Membranes: Influence of Filler Porosity on the CO2/N2 Separation Performance. *J. Memb. Sci.* **2018**, *566* (May), 213–222. https://doi.org/10.1016/j.memsci.2018.08.023.

(229) Ross, S. *Introduction to Probability and Statistics for Engineers and Scientists*, 4th editio.; 2009.

(230) Vinoba, M.; Bhagiyalakshmi, M.; Alqaheem, Y.; Alomair, A. A.; Pérez, A.; Rana, M. S. Recent Progress of Fillers in Mixed Matrix Membranes for CO2 Separation: A Review. *Sep. Purif. Technol.* **2017**, *188*, 431–450. https://doi.org/10.1016/j.seppur.2017.07.051.

(231) Paul, D. R.; Koros, W. J. Effect of Partially Immobilizing Sorption on Permeability and the Diffusion Time Lag. *J. Polym. Sci.* **1976**, *14*, 675–685.

(232) Frisch, M. J.; Trucks, G. W.; Schlegel, H. B.; Scuseria, G. E.; Robb, M. A.; Cheeseman, J. R.; Scalmani, G.; Barone, V.; Petersson, G. A.; Nakatsuji, H.; et al. *Gaussian 16 Revision C.01*; Inc., G., Ed.; Wallingford CT, 2016.

(233) Becke, A. D. Density-functional Thermochemistry. III. The Role of Exact Exchange. *J. Chem. Phys.* **1993**, *98*, 5648.

(234) Krishnan, R.; Binkley, J. S.; Seeger, R.; Pople, J. A. Self-consistent Molecular Orbital Methods. XX. A Basis Set for Correlated Wave Functions. *J. Chem. Phys.* **1980**, *72*, 650.

(235) Hay, P. J.; Wadt, W. R. Ab Initio Effective Core Potentials for Molecular Calculations.

Potentials for the Transition Metal Atoms Sc to Hg. *J. Chem. Phys.* **1985**, *82*, 270.

(236) Enkovaara, J.; Rostgaard, C.; Mortensen, J. J.; Chen, J.; Dulak, M.; Ferrighi, L.; Gavnholt, J.; Glinsvad, C.; Haikola, V.; Lehtovaara, L.; et al. Electronic Structure Calculations with GPAW: A Real-Space Implementation of the Projector Augmented-Wave Method. *Joural Phys. Condens. Matter* **2010**, *22*, 253202. https://doi.org/10.1088/0953-8984/22/25/253202.

(237) Chen, J.; Martınez, T. J. QTPIE : Charge Transfer with Polarization Current Equalization. A Fluctuating Charge Model with Correct Asymptotics. *Chem. Phys. Lett.* **2007**, *438*, 315–320. https://doi.org/10.1016/j.cplett.2007.02.065.

(238) Mukherjee, S.; Manna, B.; Desai, A. V.; Yin, Y.; Krishna, R.; Babarao, R.; Ghosh, S. K.; Kitagawa, S.; Kitaura, R.; Noro, S. -i.; et al. Harnessing Lewis Acidic Open Metal Sites of Metal–Organic Frameworks: The Foremost Route to Achieve Highly Selective Benzene Sorption over Cyclohexane. *Chem. Commun.* **2016**, *52* (53), 8215–8218. https://doi.org/10.1039/C6CC03015G.

(239) Smith, Z. P.; Sanders, D. F.; Ribeiro, C. P.; Guo, R.; Freeman, B. D.; Paul, D. R.; McGrath, J. E.; Swinnea, S. Gas Sorption and Characterization of Thermally Rearranged Polyimides Based on 3,3'-Dihydroxy-4,4'-Diamino-Biphenyl (HAB) and 2,2'-Bis-(3,4-Dicarboxyphenyl) Hexafluoropropane Dianhydride (6FDA). *J. Memb. Sci.* **2012**, *416*, 558–567. https://doi.org/10.1016/j.memsci.2012.05.050.

(240) Zhang, C.; Li, P.; Cao, B. Decarboxylation Crosslinking of Polyimides with High CO2/CH4 Separation Performance and Plasticization Resistance. *J. Memb. Sci.* **2017**, *528* (January), 206–216. https://doi.org/10.1016/j.memsci.2017.01.008.

(241) Kratochvil, A. M.; Koros, W. J. Decarboxylation-Induced Cross-Linking of a Polyimide for Enhanced CO2 Plasticization Resistance. *Macromolecules* **2008**, *41*, 7920–7927.

(242) Kim, Y. K.; Lee, J. M.; Park, H. B.; Lee, Y. M. The Gas Separation Properties of Carbon Molecular Sieve Membranes Derived from Polyimides Having Carboxylic Acid Groups. **2004**, *235*, 139–146. https://doi.org/10.1016/j.memsci.2004.02.004.

(243) Yerzhankyzy, A.; Ghanem, B. S.; Wang, Y.; Alaslai, N.; Pinnau, I. Gas Separation Performance and Mechanical Properties of Thermally-Rearranged Polybenzoxazoles Derived from an Intrinsically Microporous Dihydroxyl-Functionalized Triptycene Diamine-Based Polyimide. *J. Memb. Sci.* **2020**, *595* (June 2019), 117512. https://doi.org/10.1016/j.memsci.2019.117512.

(244) Lee, J.; Kim, J. S.; Moon, S.; Park, C. Y.; Kim, J. F.; Lee, Y. M. Dimensionally-Controlled Densification in Crosslinked Thermally Rearranged (XTR) Hollow Fiber Membranes for CO2 Capture. *J. Memb. Sci.* https://doi.org/10.1016/j.memsci.2019.117535.

(245) Park, H. B.; Jung, C. H.; Lee, Y. M.; Hill, A. J.; Pas, S. J.; Mudie, S. T.; Van Wagner, E.; Freeman, B. D.; Cookson, D. J. Polymers with Cavities Tuned for Fast Selective Transport of Small Molecules and Ions. *Science (80-.).* **2007**, *318* (October), 254–259.

(246) Zhang, C.; Cao, B.; Li, P. Thermal Oxidative Crosslinking of Phenolphthalein-Based Cardo Polyimides with Enhanced Gas Permeability and Selectivity. *J. Memb. Sci.* **2018**, *546* (May 2017), 90–99. https://doi.org/10.1016/j.memsci.2017.10.015.

(247) Qiu, W.; Chen, C.; Kincer, M. R.; Koros, W. J. Thermal Analysis and Its Application in Evaluation of Fluorinated Polyimide Membranes for Gas Separation. *Polymer (Guildf).* **2011**, *52* (18), 4073–4082. https://doi.org/10.1016/j.polymer.2011.07.002.

(248) Huang, Y.; Merkel, T. C.; Baker, R. W. Pressure Ratio and Its Impact on Membrane Gas Separation Processes. *J. Memb. Sci.* **2014**, *463*, 33–40. https://doi.org/10.1016/j.memsci.2014.03.016.

(249) Wieneke, J. U.; Staudt, C. Thermal Stability of 6FDA-(Co-) Polyimides Containing Carboxylic Acid Groups. *Polym. Degrad. Stab.* **2010**, *95* (4), 684–693. https://doi.org/10.1016/j.polymdegradstab.2009.11.041.

(250) Mrsevic, M. Nanopartikel-Komposite Aus Titandioxid-Nanopartikeln Und Schwefelhaltigen Polyimiden Für Optische Anwendungen, Heinrich-Heine-Universität Düsseldorf, 2009.

(251) Karunaweera, C.; Musselman, I. H.; Balkus Jr, K. J.; Ferraris, J. P. Fabrication and Characterization of Aging Resistant Carbon Molecular Sieve Membranes for C3 Separation Using High Molecular Weight Crosslinkable. *J. Memb. Sci.* **2019**, *581* (October 2018), 430–438. https://doi.org/10.1016/j.memsci.2019.03.065.

(252) Giroux, L.; Charland, J.; Macphee, J. A. Application of Thermogravimetric Fourier Transform Infrared Spectroscopy (TG-FTIR) to the Analysis of Oxygen Functional Groups in Coal. *Energy & Fuels* **2006**, *20* (6), 1988–1996. https://doi.org/10.1021/ef0600917.

(253) Cervantes-Uc, J. M.; Cauich-Rodriguez, J. V.; Vazques-Torres, H.; Licea-Claverie, A. TGA/FTIR Study on Thermal Degradation of Polymethacrylates Containing Carboxylic Groups. *Polym. Degrad. Stab.* **2006**, *91*, 3312–3321. https://doi.org/10.1016/j.polymdegradstab.2006.06.005.

(254) Turk, S. C. H. J.; Kloosterman, W. P.; Ninaber, D. K.; Kolen, K. P. A. M.; Knutova, J.; Suir, E.; Schu, M.; Raemakers-franken, P. C.; Mu, M.; Wildeman, S. M. A. De; et al. Metabolic Engineering toward Sustainable Production of Nylon - 6. **2016**. https://doi.org/10.1021/acssynbio.5b00129.

(255) Charati, S. G.; Houde, A. Y.; Kulkarni, S. S.; Kulkarni, M. G. Transport of Gases in Aromatic Polyesters: Correlation with WAXD Studies. *J. Polym. Sci. Part B* **1991**, *29* (8), 921–931.

(256) Park, S.-H.; Kim, K.-J.; So, W.-W.; Moon, S.-J.; Lee, S.-B. Gas Separation Properties of 6FDA-Based Polyimide Membranes with a Polar Group. *Macromol. Res.* **2003**, *11* (3), 157–162.

(257) Saberi, M.; Rouhi, P.; Teimoori, M. Estimation of Dual Mode Sorption Parameters for CO2 in the Glassy Polymers Using Group Contribution Approach. *J. Memb. Sci.* **2020**, *595* (September 2019), 117481. https://doi.org/10.1016/j.memsci.2019.117481.

(258) Kim, J. H.; Koros, W. J.; Paul, D. R. Physical Aging of Thin 6FDA-Based Polyimide Membranes Containing Carboxyl Acid Groups. Part II. Optical Properties. *Polymer (Guildf).* **2006**, *47*, 3104–3111. https://doi.org/10.1016/j.polymer.2006.02.079.

(259) Hasegawa, M.; Kochi, M.; Mita, I.; Yokota, R. Molecular Aggregation and Fluorescence Spectra of Aromatic Polyimides. *Eur. Polym. J.* **1989**, *25* (4), 349–354.

(260) Wachsman, E. D.; Frank, C. W. Effect of Cure History on the Morphology of Polyimide: Fluorescence Spectroscopy as a Method for Determining the Degree of Cure. *Polymer (Guildf).* **1988**, *29* (July), 1191–1197.

(261) Tang, H.; Feng, H.; Luo, H.; Dong, L.; Feng, Z. The Aggregation State of Polyimide. *Eur. Polym. J.* **1997**, *33* (4), 519–523.

(262) Qiu, W.; Xu, L.; Chen, C.; Paul, D. R.; Koros, W. J. Gas Separation Performance of 6FDA-Based Polyimides with Different Chemical Structures. *Polymer (Guildf).* **2013**, *54* (22), 6226–6235. https://doi.org/10.1016/j.polymer.2013.09.007.

(263) Esposito, E.; Mazzei, I.; Monteleone, M.; Fuoco, A.; Carta, M.; Mckeown, N. B.; Malpass-evans, R.; Jansen, J. C. Highly Permeable Matrimid/PIM-EA(H2)-TB Blend Memmbrane for Gas Separation. *Polymers (Basel).* **2019**, *11*, 1–14. https://doi.org/10.3390/polym11010046.

(264) Liu, Y.; Liu, G.; Zhang, C.; Qiu, W.; Yi, S.; Chernikova, V.; Chen, Z.; Belmabkhout, Y.; Shekhah, O.; Eddaoudi, M.; et al. Enhanced CO2/CH4 Separation Performance of a Mixed Matrix Membrane Based on Tailored MOF-Polymer Formulations. *Adv. Sci.* **2018**, *5*, 1800982. https://doi.org/10.1002/advs.201800982.

(265) Ricci, E.; Minelli, M.; De Angelis, M. G. A Multiscale Approach to Predict the Mixed Gas Separation Performance of Glassy Polymeric Membranes for CO2 Capture: The Case of CO2/CH4 Mixture. *J. Memb. Sci.* **2017**, *539* (March), 88–100. https://doi.org/10.1016/j.memsci.2017.05.068.

(266) Chung, T.-S.; Chang, S. S.; Wang, R.; Lu, Z.; He, C. Characterization of Permeability and Sorption in Matrimid/C60 Mixed Matrix Membranes. *J. Memb. Sci.* **2003**, *211*, 91–99.

(267) Zimmerman, C. M.; Koros, W. J. Polypyrrolones for Membrane Gas Separations. I. Structural Comparison of Gas Transport and Sorption Properties. *J. Polym. Sci. Part B Polym. Phys.* **1998**, *37* (December), 1235–1249.

(268) Bilad, M. R.; Declerck, P.; Piasecka, A.; Vanysacker, L.; Yan, X.; Vankelecom, I. F. J. Development and Validation of a High-Throughput Membrane Bioreactor. *J. Memb. Sci.* **2011**, *379* (1–2), 146–153. https://doi.org/10.1016/j.memsci.2011.05.052.

(269) Vandezande, P.; Gevers, L. E. M.; Paul, J. S.; Vankelecom, I. F. J.; Jacobs, P. A. High Throughput Screening for Rapid Development of Membranes and Membrane Processes. *J. Memb. Sci.* **2005**, *250*, 305–310. https://doi.org/10.1016/j.memsci.2004.11.002.

(270) Huber, M. L.; Harvey, A. H. Thermal Conductivity of Gases. In *CRC Handbook of Chemistry and Physics*; Haynes, W., Lide, D., Bruno, T., Eds.; Taylor and Francis Group: New York, 2012; pp 240–241.

(271) Yave, W.; Car, A.; Peinemann, K.-V. Nanostructured Membrane Material Designed for Carbon Dioxide Separation. *J. Memb. Sci.* **2010**, *350*, 124–129. https://doi.org/10.1016/j.memsci.2009.12.019.

(272) Duthie, X.; Kentish, S.; Powell, C.; Nagai, K.; Qiao, G.; Stevens, G. Operating Temperature Effects on the Plasticization of Polyimide Gas Separation Membranes. *J. Memb. Sci.* **2007**, *294*, 40–49. https://doi.org/10.1016/j.memsci.2007.02.004.

(273) Rodriguez, K. M.; Wu, A. X.; Qian, Q.; Han, G.; Lin, S.; Benedetti, F. M.; Lee, H.; Chi, W. S.; Doherty, C. M.; Smith, Z. P. Facile and Time-Efficient Carboxylic Acid Functionalization of PIM-1: Effect on Molecular Packing and Gas Separation Performance. *Macromolecules* **2020**, *53*, 6220–6234. https://doi.org/10.1021/acs.macromol.0c00933.

(274) Ghalei, B.; Wakimoto, K.; Wu, C. Y.; Isfahani, A. P.; Yamamoto, T.; Sakurai, K.; Higuchi, M.; Chang, B. K.; Kitagawa, S.; Sivaniah, E. Rational Tuning of Zirconium Metal – Organic Framework Membranes for Hydrogen Purification. *Angew. Chemie* **2019**, *32001*, 19034–19040. https://doi.org/10.1002/anie.201911359.

(275) Wong, K. C.; Goh, P. S.; Ismail, A. F. Thin Film Nanocomposite: The next Generation Selective Membrane for CO2 Removal. *J. Mater. Chem. A* **2016**, *4*, 15726–15748. https://doi.org/10.1039/c6ta05145f.

(276) Xu, R.; Li, L.; Hou, M.; Xue, J.; Liu, Y.; Pan, Z.; Song, C.; Wang, T. Enhanced CO2 Permeability of Thermal Crosslinking Membrane via Sulfonation/Desulfonation of Phenolphthalein-Based Cardo Poly (Arylene Ether Ketone). *J. Memb. Sci.* **2020**, *598* (January), 117824. https://doi.org/10.1016/j.memsci.2020.117824.

(277) Yehia, H.; Pisklak, T. J.; Ferraris, J. P.; Balkus, K. J.; Musselman, I. H. Methane Facilitated Transport Using Copper (II) Biphenyl Dicarboxylate-Triethylenediamine Poly(3-Acetoxyethylthiophene) Mixed Matrix Membranes. *Polym. Prepr.* **2004**, *45*, 35–36.

(278) Koros, W. J.; Zhang, C. Materials for Next-Generation Molecularly Selective Synthetic Membranes. *Nat. Mater.* **2017**, *16* (3), 289–297. https://doi.org/10.1038/nmat4805.

(279) Noble, R. D. Perspectives on Mixed Matrix Membranes. *J. Memb. Sci.* **2011**, *378* (1–2), 393–397. https://doi.org/10.1016/j.memsci.2011.05.031.

(280) Ghalei, B.; Sakurai, K.; Kinoshita, Y.; Wakimoto, K.; Isfahani, A. P.; Song, Q.; Doitomi, K.; Furukawa, S.; Hirao, H.; Kusuda, H.; et al. Enhanced Selectivity in Mixed Matrix Membranes for CO2 Capture through Efficient Dispersion of Amine-Functionalized MOF Nanoparticles. *Nat. Energy* **2017**, *17086* (June). https://doi.org/10.1038/nenergy.2017.86.

(281) Liu, G.; Chernikova, V.; Liu, Y.; Zhang, K.; Belmabkhout, Y.; Shekhah, O.; Zhang, C.; Yi, S.; Eddaoudi, M.; Koros, W. J. Mixed Matrix Formulations with MOF Molecular Sieving for Key Energy-Intensive Separations. *Nat. Mater.* **2018**, *17*, 283–289. https://doi.org/10.1038/s41563-017-0013-1.

(282) Wong, K. C.; Goh, P. S.; Ismail, A. F. Gas Separation Performance of Thin Film Nanocomposite Membranes Incorporated with Polymethyl Methacrylate Grafted Multi-Walled Carbon Nanotubes. *Int. Biodeterior. Biodegrad.* **2015**, *102*, 339–345. https://doi.org/10.1016/j.ibiod.2015.02.007.

(283) Merkel, T. C.; Lin, H.; Wei, X.; Baker, R. Power Plant Post-Combustion Carbon Dioxide Capture: An Opportunity for Membranes. *J. Memb. Sci.* **2010**, *359* (1–2), 126–139.

https://doi.org/10.1016/j.memsci.2009.10.041.

(284) Han, Y.; Salim, W.; Chen, K. K.; Wu, D.; Ho, W. S. W. Field Trial of Spiral-Wound Facilitated Transport Membrane Module for CO2 Capture from Flue Gas. *J. Memb. Sci.* **2019**, *575* (December 2018), 242–251. https://doi.org/10.1016/j.memsci.2019.01.024.

(285) Verbeke, R.; Arts, W.; Dom, E.; Dickmann, M.; Egger, W.; Koeckelberghs, G.; Szymczyk, A.; Vankelecom, I. F. J. Transferring Bulk Chemistry to Interfacial Synthesis of TFC-Membranes to Create Chemically Robust Poly (Epoxyether) Films. *J. Memb. Sci.* **2019**, *582* (February), 442–453. https://doi.org/10.1016/j.memsci.2019.02.016.

(286) Comesana-Gandara, B.; Chen, J.; Bezzu, C. G.; Carta, M.; Rose, I.; Ferrari, M.-C.; Esposito, E.; Fuoco, A.; Jansen, J. C.; Mckeown, N. B. Redefining the Robeson Upper Bounds for CO2/ CH4 and CO2/N2 Separations Using a Series of Ultrapermeable Benzotriptycene-Based Polymers of Intrinsic Microporosity. *Energy Environ. Sci.* **2019**, *12*, 2733–2740. https://doi.org/10.1039/c9ee01384a.

(287) Wickramasinghe, S. R.; Bower, S. E.; Chen, Z.; Mukherjee, A.; Husson, S. M. Relating the Pore Size Distribution of Ultrafiltration Membranes to Dextran Rejection. *J. Memb. Sci.* **2009**, *340*, 1–8. https://doi.org/10.1016/j.memsci.2009.04.056.

(288) Bai, J.; Zhong, X.; Jiang, S.; Huang, Y.; Duan, X. Graphene Nanomesh. *Nat. Nanotechnol.* **2010**, *5*, 190–194. https://doi.org/https://doi-org.kuleuven.ezproxy.kuleuven.be/10.1038/nnano.2010.8.

(289) Zhang, C.; Koros, W. J. Ultraselective Carbon Molecular Sieve Membranes with Tailored Synergistic Sorption Selective Properties. *Adv. Mater.* **2017**, *1701631*, 1–6. https://doi.org/10.1002/adma.201701631.

(290) Qiu, W.; Zhang, K.; Li, F. S.; Zhang, K.; Koros, W. J. Gas Separation Performance of Carbon Molecular Sieve Membranes Based on 6FDA-MPDA/DABA (3:2) Polyimide. *ChemSusChem* **2014**, *7*, 1186–1194. https://doi.org/10.1002/cssc.201300851.

(291) Koros, W. J.; Zhang, C. Ultra-Selective Carbon Molecular Sieve Membranes and Methods of Making. WO2016196595A1, 2016.